HAL
open science

Acoustic metamaterials for underwater applications : homogenisation methods, design optimisation and experimental characterisation

Laëtitia Roux

To cite this version:

Laëtitia Roux. Acoustic metamaterials for underwater applications : homogenisation methods, design optimisation and experimental characterisation. Acoustics [physics.class-ph]. Université de Lille, 2021. English. NNT : 2021LILUN015 . tel-03626959

HAL Id: tel-03626959

https://theses.hal.science/tel-03626959

Submitted on 1 Apr 2022

HAL is a multi-disciplinary open access archive for the deposit and dissemination of scientific research documents, whether they are published or not. The documents may come from teaching and research institutions in France or abroad, or from public or private research centers.

L'archive ouverte pluridisciplinaire **HAL**, est destinée au dépôt et à la diffusion de documents scientifiques de niveau recherche, publiés ou non, émanant des établissements d'enseignement et de recherche français ou étrangers, des laboratoires publics ou privés.

UNIVERSITÉ de LILLE
École doctorale Sciences Pour l'Ingénieur
IEMN - Institut d'électronique, de microélectronique et de nanotechnologie

Thesis defended by:

Laetitia ROUX

On the 7th September 2021

In order to become Doctor from Université de Lille, in the academic field of Micro et Nano-Technologies, Acoustique et Télécommunications

ACOUSTIC METAMATERIALS FOR UNDERWATER APPLICATIONS: HOMOGENISATION THEORY, DESIGN OPTIMISATION AND EXPERIMENTAL CHARACTERISATION

Thesis prepared at:

CNRS, Univ. Lille, UMR 8520-IEMN, Lille (FRANCE),
School of Mechanical and Manufacturing Engineering, UNSW, Sydney (AUSTRALIA),
Naval Group Research, Ollioules (FRANCE).

Committee members

President:	Olivier BOU MATAR	Professeur, École Centrale de Lille, France
Reviewers :	Thomas BRUNET	Maître de conférences, I2M Bordeaux, France
	Valentin LEROY	Directeur de Recherche, LMSC Paris, France
Examiners :	Bertrand HABERT	Direction Générale de l'Armement, France
	Alex SKVORTSOV	Defence Science and Technology Group, Australia
Guests :	Jean DASSÉ	Thales - Defense Mission Systems, France
	Charles CROËNNE	Chargé de Recherche, IEMN Lille, France
Supervisor :	Anne-Christine HLADKY	Directrice de Recherche, IEMN Lille, France
Co-supervisors :	Christian AUDOLY	HDR, Naval Group Research, France
	Nicole KESSISSOGLOU	Professor, UNSW Sydney, Australia

UNIVERSITÉ de LILLE
École doctorale Sciences Pour l'Ingénieur
IEMN - Institut d'électronique, de microélectronique et de nanotechnologie

Thèse soutenue par:

Laetitia Roux

Le 7 Septembre 2021

Pour le titre de Docteur de l'Université de Lille, spécialité Micro et Nano-Technologies, Acoustique et Télécommunications

Métamatériaux Acoustiques pour Applications Sous-marines: Methodes d'Homogénéisation, Optimisation de Designs et Caractérisation Expérimentale

Thèse préparée à:

CNRS, Univ. Lille, UMR 8520-IEMN, Lille (FRANCE),
School of Mechanical and Manufacturing Engineering, UNSW, Sydney (AUSTRALIA),
Naval Group Research, Ollioules (FRANCE).

Membres du Jury

Président:	Olivier Bou Matar	Professeur, École Centrale de Lille, France
Rapporteurs :	Thomas Brunet	Maître de conférences, I2M Bordeaux, France
	Valentin Leroy	Directeur de Recherche, LMSC Paris, France
Examinateurs :	Bertrand Habert	Direction Générale de l'Armement, France
	Alex Skvortsov	Defence Science and Technology Group, Australia
Invités :	Jean Dassé	Thales - Defense Mission Systems, France
	Charles Croënne	Chargé de Recherche, IEMN Lille, France
Directrice :	Anne-Christine Hladky	Directrice de Recherche, IEMN Lille, France
Co-superviseurs :	Christian Audoly	HDR, Naval Group Research, France
	Nicole Kessissoglou	Professor, UNSW Sydney, Australia

Abstract

Designing efficient hull coatings for acoustic stealth of submerged vehicles remains a challenge that evolves along with improvements in sonar performance. Low frequency performance is particularly important for military applications, due to the long range propagation properties of low frequency signals in the sea. Acoustic metamaterials are now widely recognised as promising candidates for such underwater coatings. The aim of this research is to study metamaterials for underwater applications, from theoretical analysis to experimental characterisation.

This thesis presents analytical or semi-analytical models based on a transfer matrix formalism to homogenise periodic structures. These methods are then used in a computationally efficient optimisation approach to obtain metamaterial designs that meet a goal in terms of their anechoism coefficient, hull decoupling coefficient, or both. The entirety of this approach is first carried out for multilayered structures then extended to metamaterials with macro-inclusions to which a degree of complexity is added. Finally, measurement methods in a water tank facility are implemented and validated. They are then used for the experimental characterisation of panels manufactured within the framework of the thesis.

Acknowledgements

To begin with, I would like to express my gratitude to the members of my defense committee, Valentin Leroy, Thomas Brunet, Bertrand Habert, Alex Skvortsov, Jean Dassé, Charles Croënne, Olivier Bou Matar and my 3 supervisors, for their presence at the defense and for the interesting exchanges that followed. In particular, I would like to thank the two reviewers, Valentin Leroy and Thomas Brunet, for their careful reading of the manuscript and for their valuable feedback.

Since I spent half the time of my doctorate in France and the other half in Australia, I must continue my thanks in both languages.

Naval Group, Ollioules

Je commence avec la France, et plus particulièrement dans le sud, où j'ai passé les 6 premiers mois de ma thèse dans les locaux de Naval Group, à Ollioules. Je tiens particulièrement à remercier Christian Audoly, mon superviseur industriel, pour avoir mis en place ce projet pour m'avoir donné la chance de réaliser cette thèse. Son investissement et son regard avisé ont été d'une aide précieuse tout au long de la thèse.

Je souhaite aussi remercier mes collègues de Naval Group qui étaient là dès mes débuts et qui m'ont chaleureusement accueilli, Rania, Valentin, Ygaäl, Patrick, Gilles. Merci encore pour ce poster de Lorie qui m'a suivi jusqu'en Australie, et qui est désormais l'effigie de l'open space du CEMIS/AC. Je remercie aussi Pierre et Arthur, du CESMAN, pour leur aide à la réalisation des panneaux acoustiques.

UNSW, Sydney

I then flew to Sydney, where I was warmly welcomed by my supervisor Nicole Kessissoglou. I am deeply grateful for her support and comments, which have helped me a lot with my editing style. I would also like to thank the group of Nicole: Daniel, Gyani, David, Mahmoud and Jeffrey, with whom I enjoyed chatting from time to time around the open space. Among those I met at UNSW, I especially want to thank Sean, for the enjoyable discussions around a coffee in the morning. Above all, thanks to Jeoffrey, who was friendly from day one and who made my integration in Sydney so much easier and more fun.

My stay in Sydney wouldn't have been the same without the good friends I have made.

Thank you to all the Frenchies! And my deepest thanks to the amazing Tatjana, Iris and Beeh, for the support and the great times we spent together.

IEMN, Lille

De retour en France pour ma dernière année de thèse, j'ai été chaleureusement accueillie par l'équipe d'acoustique de l'ISEN de Lille, que je remercie ! En particulier, je remercie Charles Croenne, pour les échanges toujours pertinents et intéressants et pour m'avoir tant aidé à prendre du recul sur mon travail. Je tiens aussi à remercier Monique Pouille et sa bonne humeur qui ont fait des journées de mesures des moments intenses mais agréables, où j'ai beaucoup appris. Enfin, j'adresse un immense merci à Anne-Christine Hladky, pour son encadrement plein d'énergie, de gentillesse, d'idées pertinentes et de connaissance scientifique. Son enthousiasme dans nos discussions m'a aidé à rester motivée et dévouée jusqu'à la fin de la thèse. Un grand merci !

Enfin, je remercie mes amis de longues dates, Lucie, Audette, Jordane, mes pompoms, qui m'ont toujours apporté leur soutien et bonne humeur malgré la distance. Je remercie aussi mes nouveaux collègues du CEMIS/AC et amis de l'aire Toulonnaise pour leur soutien et encouragement au quotidien lors de la dernière ligne droite. Je tiens aussi tout particulièrement à remercier ma famille, et notamment mes parents et à ma sœur pour avoir fait le voyage jusqu'en Australie pour passer Noël à mes côtés. Je peux enfin dire fièrement : « Papa, je ne suis plus étudiante ! ». Pour finir, je remercie infiniment Stu pour sa patience, ses encouragements quotidiens et son soutien sans faille toutes ces dernières années.

Contents

Abstract **3**

Acknowledgements **5**

1 Introduction and Literature Review **11**
1.1 Context : Underwater Discretion and Stealth 12
1.2 Thesis Overview 14
1.2.1 Goals 14
1.2.2 Plan 14
1.3 Literature Review 16
1.3.1 Concept of Acoustic Metamaterial 16
1.3.2 Determination of Effective Properties 19
1.3.3 Materials for Underwater Applications 22
1.3.4 Experimental Studies 26
1.4 Notes on Concepts and Notations 30
1.4.1 Time Convention 30
1.4.2 Longitudinal and Shear Waves 30
1.4.3 Material Damping Representation 30
1.4.4 Homogenisation 31
1.4.5 Passivity Constraint 31
1.4.6 Acoustic Performance 31

I MULTILAYERED DESIGNS **33**

2 Homogenisation **35**
2.1 Transfer Matrix 36
2.1.1 Definition 36
2.1.2 Expression 36
2.1.3 Calculation 37
2.2 Homogenisation 38
2.2.1 Fluid Homogenisation Model 38
2.2.2 Willis Fluid Homogenisation Model 39
2.3 Scattering Coefficients 42
2.3.1 Multilayered Medium 42

2.3.2 Effective Medium . . . 43
2.4 Quasi-static Approach . . . 44
2.5 Numerical Results . . . 45
2.5.1 Designs . . . 45
2.5.2 Effective Parameters . . . 46
2.5.3 Scattering Coefficients . . . 50
2.6 Summary . . . 53

3 Optimisation **55**
3.1 Presentation of the Optimisation Approach . . . 56
3.1.1 Introduction . . . 56
3.1.2 Methodology . . . 57
3.1.3 Algorithm . . . 57
3.2 Results for Anechoism . . . 61
3.2.1 Objective Functions . . . 61
3.2.2 Validation . . . 62
3.2.3 Results . . . 64
3.3 Results for Hull Decoupling . . . 68
3.4 Results for Anechoism and Hull Decoupling . . . 71
3.4.1 Objective Functions . . . 71
3.4.2 Results . . . 71
3.5 Summary . . . 74

4 Experiments **75**
4.1 3-Point Method . . . 76
4.1.1 Conventional Set-up . . . 76
4.1.2 Methodology . . . 77
4.1.3 Experimental Facilities . . . 79
4.2 Method Validation . . . 81
4.2.1 Application on a Test Panel . . . 81
4.2.2 Validity Limits . . . 85
4.2.3 Pressure Mapping . . . 87
4.3 Experimental Speed of Sound Determination . . . 90
4.3.1 Measurements . . . 90
4.3.2 Retrieval Approach 1 . . . 91
4.3.3 Retrieval Approach 2 . . . 92
4.3.4 Verification . . . 94
4.4 Multilayered Medium Measurements . . . 95
4.4.1 Panel and Experimental Set-up . . . 95
4.4.2 Measurements . . . 96
4.4.3 Calculation of the Anechoism Coefficient . . . 99
4.5 Summary . . . 101

II DESIGNS WITH MACRO-INCLUSIONS 103

5 Homogenisation for Symmetric Designs 105
5.1 Methodology . . . 107
5.1.1 Fluid Homogenisation Model . . . 107
5.1.2 Direct Inversion Method . . . 107
5.1.3 Differential Method . . . 109
5.2 Implementation . . . 115
5.3 Validation . . . 116
5.4 Case Study: Hard Inclusions . . . 118
5.4.1 Design . . . 118
5.4.2 Effective Parameters . . . 118
5.4.3 Influence of the Number of Unit Cells . . . 123
5.4.4 Scattering Predictions . . . 124
5.5 Case Study: Voided Inclusions . . . 127
5.5.1 Effective Parameters . . . 127
5.5.2 Scattering Predictions . . . 129
5.6 Summary . . . 131

6 Homogenisation for Non-symmetric Designs 133
6.1 Methodology . . . 134
6.1.1 Willis Fluid Homogenisation Model . . . 134
6.1.2 Direct Inversion Method . . . 134
6.1.3 Differential Method . . . 136
6.2 Case study: Hard Inclusions . . . 139
6.2.1 Design . . . 139
6.2.2 Homogenisation . . . 140
6.2.3 Parametric Study . . . 143
6.3 Case study: Voided Inclusions . . . 147
6.3.1 Homogenisation . . . 147
6.3.2 Variant Approach . . . 149
6.4 Summary . . . 155

7 Optimisation 157
7.1 Optimisation Approach . . . 158
7.2 Database . . . 160
7.2.1 Presentation . . . 160
7.2.2 Influence of the Inclusion Shape . . . 161
7.2.3 Influence of the Inclusion Size . . . 164
7.3 Results for Anechoism . . . 167
7.3.1 Approach Validation . . . 167
7.3.2 Low Frequencies . . . 169
7.4 Performance Levels . . . 174
7.5 Summary . . . 175

8 Experiments **177**
8.1 Experimental Characterisation of Diffraction Gratings . . . 178
8.1.1 Grating Diffraction Phenomenon . . . 178
8.1.2 Challenges . . . 180
8.2 Measurements of the Alberich . . . 181
8.2.1 Presentation of the panel . . . 181
8.2.2 Below the Cut-off Frequency . . . 181
8.2.3 Above the Cut-off Frequency . . . 187
8.3 Summary . . . 197

9 Conclusion and Perspectives **199**
9.1 Thesis Summary . . . 200
9.2 Perspectives for Future Work . . . 203

Appendix **203**

A Transfer Matrix **205**
A.1 Definition . . . 205
A.2 Expression with S-parameters . . . 205
A.3 Expression with Material Properties . . . 208
A.4 Expression for Determination of Willis-parameters . . . 209

B Effective Wavenumber **211**
B.1 Expression . . . 211
B.2 Representation . . . 213

C Acoustic Performance **215**
C.1 S-parameters . . . 215
C.2 Anechoism Coefficient . . . 216
C.3 Hull Decoupling Coefficient . . . 217

D Panel Edge-diffraction **219**

E Performance Maps and Frequency Paths **221**
E.1 Mapping Approach . . . 222
E.1.1 Presentation . . . 222
E.1.2 Analysis . . . 225
E.2 Frequency Path . . . 235
E.2.1 Introduction . . . 235
E.2.2 Quadrant Driven Design . . . 236
E.2.3 Performance Driven Design . . . 241

Bibliography **245**

Chapter 1

Introduction and Literature Review

In this introduction, the concepts of underwater acoustic discretion and stealth are introduced and some of the current challenges are highlighted. In this context, acoustic metamaterials occur to be promising candidates to improve the discretion and stealth performances of underwater vehicles. A literature review is then conducted, focusing on the concept of metamaterials and some of their specific uses in an underwater environment. Following the literature review, the definition for concepts employed in this thesis are given. Finally, the thesis overview states the main goals of the current research and presents the thesis plan.

Contents

1.1 Context : Underwater Discretion and Stealth 12

1.2 Thesis Overview 14

1.2.1 Goals 14

1.2.2 Plan 14

1.3 Literature Review 16

1.3.1 Concept of Acoustic Metamaterial 16

1.3.2 Determination of Effective Properties 19

1.3.3 Materials for Underwater Applications 22

1.3.4 Experimental Studies 26

1.4 Notes on Concepts and Notations 30

1.4.1 Time Convention 30

1.4.2 Longitudinal and Shear Waves 30

1.4.3 Material Damping Representation 30

1.4.4 Homogenisation 31

1.4.5 Passivity Constraint 31

1.4.6 Acoustic Performance 31

1.1 Context : Underwater Discretion and Stealth

For navies and naval industries, underwater sound has always been a crucial matter. In the deep seas or oceans, sound is the main navigation and communication mean for submerged vehicles. Acoustic waves are also used for mine warfare, sea floor characterisation and submarine detection with the help of SONAR (SOund NAvigation and Ranging) systems. Such SONAR systems may be used for passive detection or active etection operations, both concepts being illustrated in Figure 1.1.

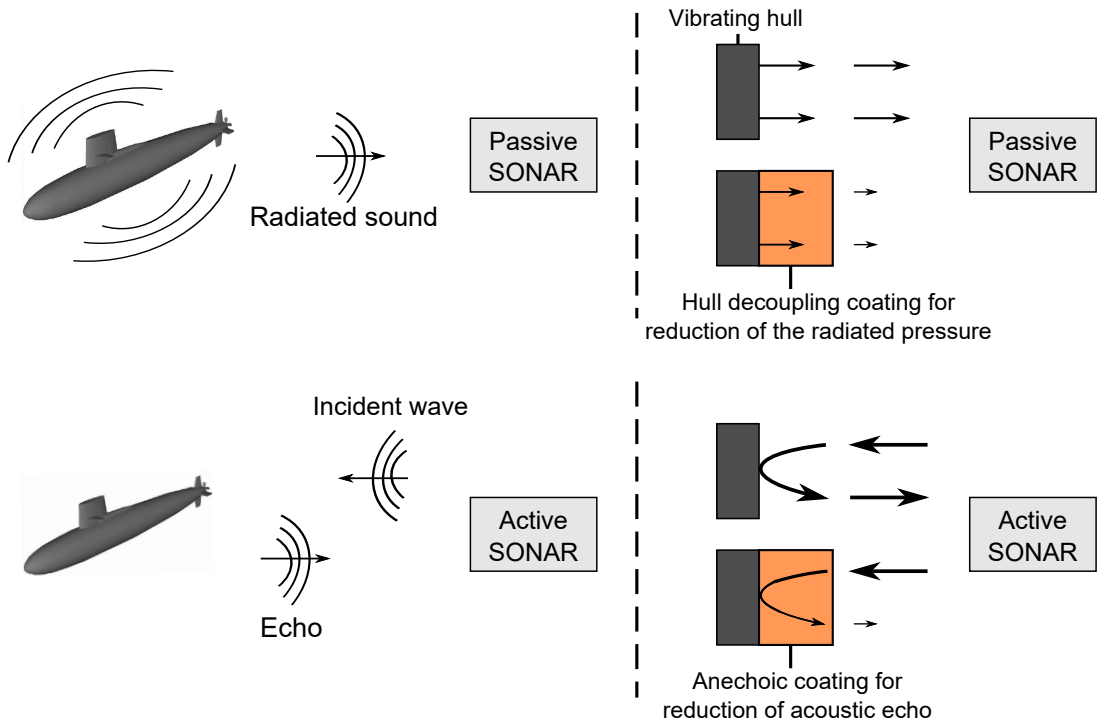

Figure 1.1 – Concepts of passive and active detection. To avoid detection by passive sonar, a hull decoupling coating can be used. To avoid detection by active sonar, anechoic coating to reduce the back-scattered energy can be used.

Underwater passive detection consists in analysing ambient sound in order to recognise characteristic sounds from a submarine or marine vessel. Those sounds mainly originate from vibrations of items of machinery, engines and propellers, which overall result in radiated noise that can be detected by an adverse passive SONAR system. Against such a threat, the discretion of a submarine or underwater vehicle is crucial. A solution, amongst others, is to place hull decoupling coatings on the submarine, which significantly reduce noise radiated from the hull.

Active detection is the other main acoustic threat, consisting in an acoustic wave sent in the underwater environment and in the detection of the potential reflected waves from an obstacle, thus informing on its presence and location. The vehicle stealth is thus also essential. Target strength, defined as the ratio between the back-scattered acoustic energy and the incident acoustic energy, can be reduced by adapting the external shape, by using acoustic deflectors or by applying anechoic coatings made of absorbing materials on the submarine outer hull in order to minimise back-scattered echoes.

Anechoic and hull decoupling coatings have been developed and used since World War II, starting with the Alberich-type design which consists of lattices of resonant cavities in an elastomer or rubber matrix, as represented in Figure 1.2. The cavities' diameters are tuned to maximise absorption for several specific frequencies. Nevertheless, there are also some non-acoustic requirements for the design of coatings, such as the weight and the total thickness. In particular, the static compressibility and stability of acoustic performances as a function of depth in the ocean must be taken into account in the design process of a coating. Hence, some coatings such as Alberich coatings can lead to interesting acoustic performances. However, their performance is often limited to specific frequencies, and in addition they may not comply to non-acoustic requirements.

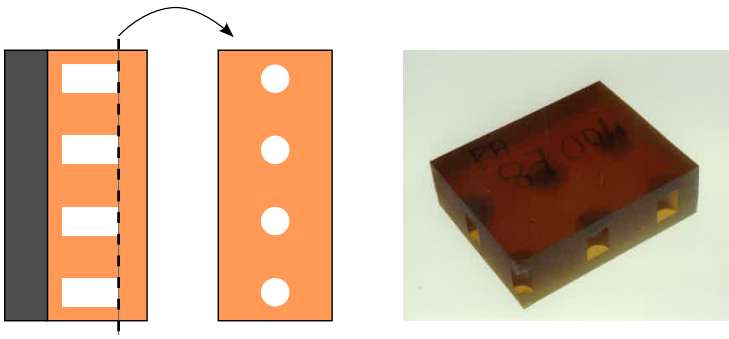

(a) (b) (c)

Figure 1.2 – (a) Section view, (b) top view and (c) sample picture [1] of a typical design of an acoustic coating comprising soft rubber embedded with voided inclusions.

Obtaining strong absorption coefficients over a broadband low frequency range (i.e. with deep sub-wavelength coatings) remains challenging. Very low frequency performance is especially important for military applications, since active detection systems usually use low frequency signals due to their long-range propagation properties in the sea. Acoustic metamaterials appear to be a potential solution to such a challenge, opening up new opportunities for the design of submarine coatings, mainly due to their strong acoustical effects at frequencies much lower than the ones corresponding to the typical coating thickness or inclusion sizes. In the following literature review, the concept of acoustic metamaterials is presented.

1.2 Thesis Overview

1.2.1 Goals

The aim of this research is to study, develop, implement and apply methods and tools that are useful to analyse and design metamaterials. More specifically, these tools and methods are to be used to examine structures for underwater applications, such as anechoic and hull decoupling coatings.

In this work, tools and methods are implemented for a full research and development process, from the theoretical analysis to the experimental characterisation of a structure. As such, analytical models or semi-analytical models need used or developed to theoretically study a design. Such analytical models or semi-analytical models are then to be used in a computationally efficient optimisation approach aiming to obtain ideal metamaterial designs for the anechoism, the hull decoupling, or both coefficients. Experimental validation are then carried out, for which measurement methods are developed and validated.

1.2.2 Plan

The manuscript is divided in two main parts. In Part I, multilayered designs are studied. They are simple but still interesting designs, for which the homogenisation, optimisation and experimental approaches are introduced. Designs of greater complexity with macro-inclusions are then considered in Part II. A summary of each Chapter is presented in what follows.

Chapter 2 introduces the notions of the transfer matrix and homogenisation models. In particular, it presents an effective medium theory based on a transfer matrix approach. This homogenisation process aims to effectively represent any multilayered arrangement as a fluid or a Willis-type fluid (depending on the symmetry of the medium). Effective properties, such as the effective wavenumber, impedance, density, bulk modulus, can be derived and used to characterise an effective medium of a given length. Such effective media can predict the scattering response of multilayered media of any length.

In **Chapter 3**, the effective medium method for multilayered media presented in Chapter 2 is used in an optimisation approach. The objective is to improve the anechoism performance or the hull decoupling performance by optimising the layer arrangement. Layers may be either steel or polyurethane with micro-balloons. The algorithm is first validated on a test case. Optimisation results are then analysed and a feature of performance is found for each coefficient. An asymmetric design is selected for its anechoic performance.

Chapter 4 aims at presenting the measurements for the selected configuration of Chapter 3. Beforehand, the principle of underwater measurements is exposed. An original method, referred to as the 3-point method, is also presented. The method's validity and robustness are assessed through measurements on an aluminium panel, for which edge-diffraction

effects are significant. The method is then applied to the polyurethane used in Chapter 3 in order to experimentally retrieve the effective speed of sound in the medium. Finally, the layer arrangement selected is measured and the anechoism coefficient is compared to the predictions.

Two retrieval methods, referred to as the direct inversion method and the differential method, are presented in **Chapter 5**. Both methods lead to the effective properties of a symmetric unit cell containing a macro-inclusion. These effective properties can then be used to characterise effective media, from which predictions of the scattering coefficients are made for designs comprising different numbers of unit cells. The retrieval methods are validated on a multilayered structure, for which the retrieved effective properties are found to be the same as those obtained using the transfer matrix model in Chapter 2. Two-dimensional designs comprising periodic cylindrical rigid or voided inclusions in a soft elastic matrix are then studied. Results led to the creation of an hybrid prediction method, which uses both the direct inversion method and the differential method, to predict the scattering response of a two-dimensional design of any length.

In **Chapter 6**, the two retrieval methods are extended for asymmetric structures with macro-inclusions. These extended methods are applied to an asymmetric variant of the locally resonant medium comprising steel inclusions, studied in Chapter 5. Effects of the asymmetry are investigated. A second case study considers an Alberich-type medium for which Willis coupling is introduced by combining two asymmetric layers to compare the results of the extended method to another approach that breaks the structure down in symmetric layers. It is shown that with such approach, unexpected results can be obtained.

Chapter 7, the two retrieval methods are used to create a database of effective properties associated to different unit cell designs. This database is used as an input into an optimisation algorithm that aims to optimise the unit arrangement of structures for anechoism performance. As such, each unit is seen as an effective layer, so the algorithm approach introduced in Chapter 3 is used. Complex structures with macro-inclusions can be therefore be optimised with short computation times. Moreover, similar performance features as in Chapter 3 are found using the effective impedance along the medium thickness.

In **Chapter 8**, the Alberich medium studied in Chapter 6 is experimentally analysed. For this purpose, the new challenges originated from the periodicity of the grating are highlighted. The 3-point method is tested on this non-homogeneous medium and extended for greater accuracy. Experimental results are then compared to predictions.

A general summary of the manuscript is finally proposed, in which of the main novelty and relevant results are summarised. Ideas for further work are also given.

1.3 Literature Review

1.3.1 Concept of Acoustic Metamaterial

Etymologically, *metamaterial* qualifies a material that *goes beyond* materials. The reason for such a term is found in the capacity of these artificial materials to exhibit properties that cannot be found for conventional materials. In the context of sinusoidal steady-state analysis for acoustic metamaterials, the dynamic material properties can reach negative values or strongly vary with frequency, contrarily to conventional materials. Hence, the most common accepted definition of an acoustic metamaterial is : "Artificial material with the capacity to exhibit unusual properties, that is to say with values or strong variations with frequency of the constitutive acoustic parameters not found for conventional materials. These unusual aspects arise from the collective manifestation of the internal constituent units in the structure, such as resonant inclusions arranged in a host matrix" [2]. Nevertheless, a clarification has to be added regarding these unusual acoustics properties. Due to the complex structure of acoustic metamaterials, the most common study scheme involves the use of an equivalent medium that reproduces the overall behaviour of the metamaterial. The equivalent medium is referred to as an *effective* medium, as shown in Figure 1.3. Effective properties of a metamaterial are thus the material properties of its effective medium. Such a homogenisation approach is usually valid if the scale of the constituent unit is much smaller than the wavelength. Nonetheless, efforts have been made to extend conventional effective medium theories to higher frequency regimes [3–5].

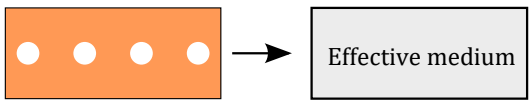

Figure 1.3 – Homogenisation approach, in which a composite material is represented by an effective medium.

Most acoustic metamaterial concepts' features rely on the behaviour of inclusions within a matrix, which may be arranged periodically or randomly distributed. It is then worth mentioning the distinction of a *phononic crystal*, which is a medium comprising of periodic arrangements of inclusions which produce wave phenomena resulting from the periodicity of the scatterers. If the inclusions are resonant, the medium may also be referred to as a locally resonant phononic crystal, and thus become a periodic metamaterial since the behaviour of the inclusion is involved [6].

Most research on metamaterials include the development or application of an homogenisation method to obtain one or several effective material properties, which are commonly the mass density, the bulk modulus or the refractive index. The wavenumber and impedance are also widely used. Acoustic metamaterials have been of great interest to the scientific community as unusual values and strong variations of these dynamic effective properties are a translation of physical phenomena occurring in the composite structure. For ex-

ample, a negative effective bulk modulus corresponds to a resonance that results in an expansion of the structure while loaded under a compressive force, as illustrated in Figure 1.4(a).

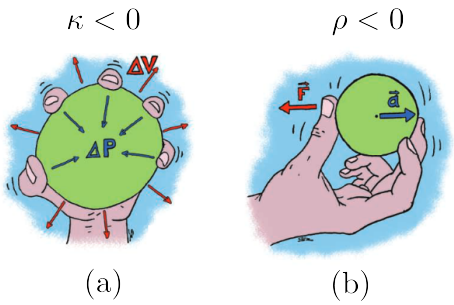

Figure 1.4 – Schematic illustrations of the dynamic behaviors of locally resonant materials with negative-valued effective parameters submitted to harmonic excitation. (a) A material possessing a negative effective bulk modulus ($\kappa < 0$) supports a volume expansion ($\Delta V > 0$) upon an isotropic compression ($\Delta P > 0$) (b) The acceleration a of a material possessing a negative effective mass density ($\rho < 0$) is opposite to the driving force F. [7].

A negative bulk modulus can be achieved by using a Helmholtz resonator, which creates the phenomenon of air resonance in a cavity [8], as shown in Figure 1.5(a). It can also be obtained using constituent units comprising side holes with both ends opened [9], as in Figure 1.5(b), or with periodic distributions of cylindrical boreholes in a waveguide [10], with balloon-like soft resonators [11], or even with some specific unit shapes resulting from an optimisation algorithm [12]. Broadly, the negative bulk modulus results from a monopolar resonance of the component units [13].

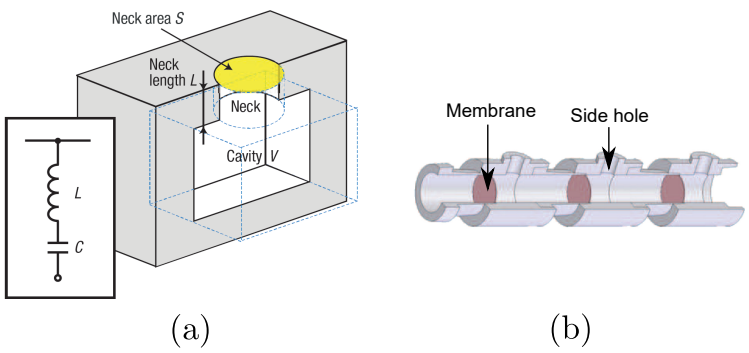

Figure 1.5 – (a) Schematic cross-sectional view of a Helmholtz resonator. The sample is made of aluminium, consisting of a rectangular cavity and a cylindrical neck. The cavity and neck are filled with water, and are connected at the same side to a square water duct. The inset illustrates the analogy between a Helmholtz resonator and an inductor–capacitor circuit, showing the fluidic inductance due to the neck, and the acoustic capacitance due to the cavity [8]. (b) Composite structure consisting of interspaced membranes and side holes [9].

Another typical metamaterial feature is an effective density that becomes negative. This is the result of a dipolar resonance of the building units [13]. The dipolar resonance corresponds to a resonance that leads to a motion of the centre of mass of the particle which is out of phase with an incident directional pressure field, as illustrated in Figure 1.4(b). With the appropriate polarisation, dipolar resonance can lead to significant transmission attenuation. The blocking effect capacity due to negative effective density can be easily demonstrated using a mass-spring structure [14], as shown in Figure 1.6(a). Nonetheless, the unusual low-frequency bandgaps observed in such negative density metamaterials are generally only present in a narrow bandwidth around resonant frequencies. Practically, dipolar resonances that lead to negative values of the effective density can appear using constituent units consisting of a heavy mass core surrounded by a soft polymer, both being arranged in a relatively rigid matrix [15] (Figure 1.6(b)). A similar effect can be achieved using, amongst others, membrane-type metamaterials [16], mass-spring systems [17] or anisotropic cylindrical scatterers penetrating in one of the rigid walls defining a 2D acoustic waveguide [18], as shown in Figure 1.6(c).

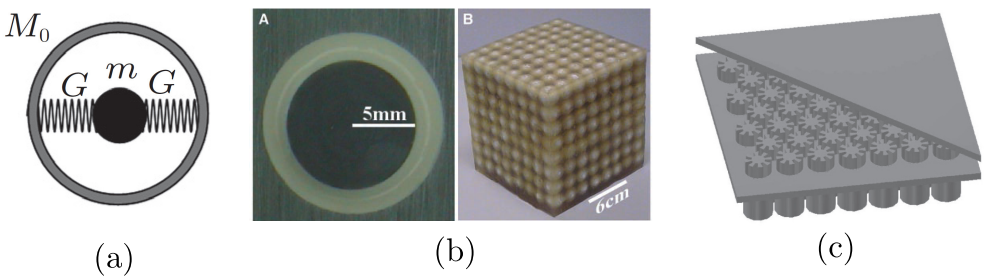

Figure 1.6 – (a) Mass-spring structure with negative effective mass [14]. (b) Cross section of a coated lead sphere that forms the basic structure unit [15]. (c) Schematic view of an array of anisotropic scatterers embedded in a 2D waveguide [18].

Therefore, local resonance of a constituent unit cell can lead to negative values and/or strong variations of either the bulk modulus or the effective density, which then add an imaginary part to the speed of sound. This in turn means that the acoustic wave amplitude dissipates with increasing distance. A considerable amount of research on acoustic metamaterials also aims at combining constitutive units leading to a monopolar resonance (negative bulk modulus) with resonant inclusions creating a dipolar resonance (negative mass density). As such, the phase speed is again a real-valued number, implying wave propagation, although with a twist: the energy and phase velocities are in opposite directions. This response provides metamaterials with the capability to produce unnatural effects like negative refraction. Some examples are metamaterials composed of membranes and side holes [9] or of Helmholtz and rod-spring resonators [19]. Another way to achieve the double negativity is to design hybrid resonators, producing a hybridisation between monopolar and dipolar resonances. Such resonators could be chiral microstructures (Figure 1.7(a) [20]) or a composite of soft rubber spheres suspended in water [13]. Other resonators can also create anti-resonances [21], quadrupolar resonances (Figure 1.7(b) [22]), or multiple resonances, for example the multi-mass resonating unit cell of Lai

et al. [23] shown in Figure 1.7(c) that leads to monopolar, dipolar and quadrupolar resonances, and results in novel elastic properties.

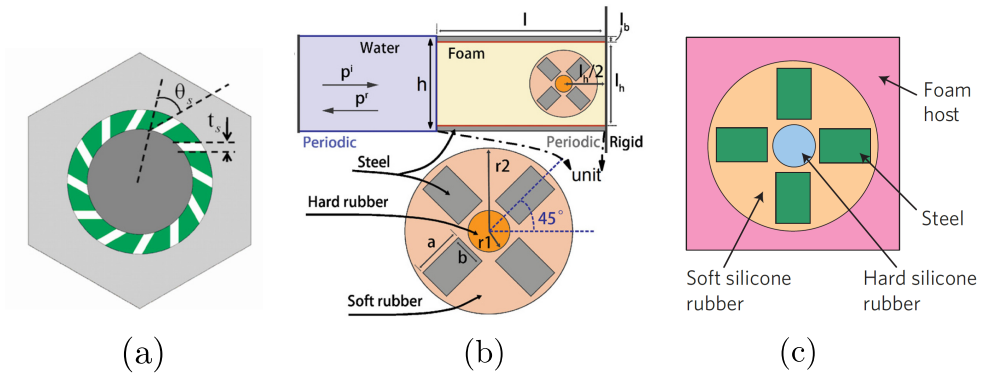

Figure 1.7 – (a) Unit cell of the 2D metamaterial made from solid media. The unit cell is composed of three-component continuum media by a chirally soft-coated heavy cylinder core embedded in a matrix [20]. (b) Inclusion composed of a soft rubber cylinder embedded with a hard rubber cylinder, surrounded by four rectangular steel rods in the shape of an X [22]. (c) Elastic metamaterial unit showing multiple resonances [23].

1.3.2 Determination of Effective Properties

Effective properties are therefore important for an in-depth analysis of a metamaterial design and its specific features. In the following section, a non-exhaustive overview of techniques to obtain effective properties is given.

Analytical Models

A range of analytical techniques have been employed to derive the effective properties of composite structures. For example, effective properties of multilayered structures are often derived using fully analytical models for one-dimensional wave propagation [24–26]. If the multilayered medium is periodic and symmetric, the derivation of the overall effective parameters can be reduced to the calculation of the effective properties for the constitutive unit [27]. For such cases, as presented in Figure 1.8(a), the transfer matrix method is found to be a suitable tool to characterise a multilayered structure [28]. However, most studies based on the the transfer matrix method are limited to the analysis of symmetric unit cells [29]. Multilayered media with non-symmetric units can still be using such an approach, but the investigation is limited to the dispersion curves [30, 31] or using an average density [24]. In recent works, several methods have been extended to take into account the asymmetry of a structure which may result in Willis coupling, as presented in the next subsection.

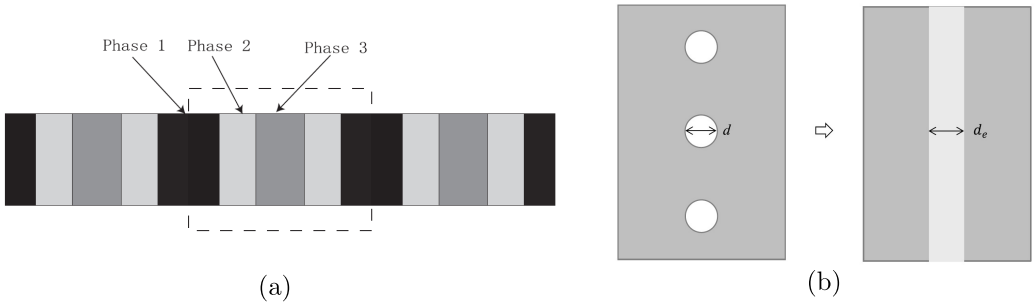

Figure 1.8 – (a) Schematic diagram of a multi-phase metamaterial. The dashed rectangle refers to a unit cell [28]. (b) Layer homogenisation applied to a PDMS medium with single layer of periodic voids [32].

Analytical models are also used to homogenise two-dimensional designs with macro-inclusions, such as periodically voided soft elastic media [32–34], as shown in Figure 1.8(b). Whilst analytical methods provide insight into physical mechanisms for wave propagation and are generally computationally efficient, they are limited to simple geometric designs.

Methods for the Study of Willis Structures

In recent literature, there has been a considerable effort to extend methods to determine the effective parameters to non-symmetric structures. The scope of possibilities for the design of metamaterials has thus been opened up with the consideration of the Willis-coupling, also referred to as acoustic bianisotropy [35]. In acoustics, a Willis material shows a pressure-velocity coupling [36], which arises from inherent asymmetry in the microstructure. More precisely, the asymmetry appears when the element center's of mass is misaligned with the centroid [37], as illustrated in Figure 1.9.

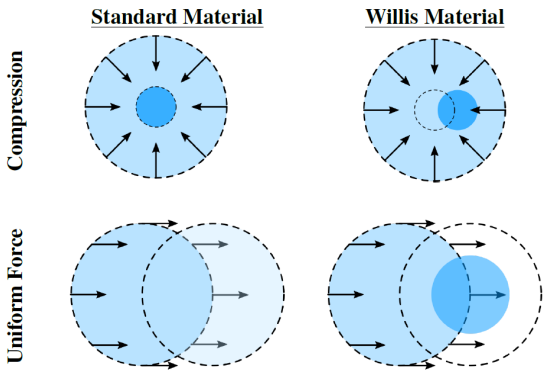

Figure 1.9 – Schematic description of the reaction of standard and Willis materials to compression and to a uniform force in one direction. The standard material under compression becomes smaller with the center unshifted, and under a uniform force translates without changing size. A Willis material, by contrast, both translates and changes size under both compression and a uniform force [38].

The acoustic bianisotropy can be optimised in order to be maximal at a subwavelength scale, which can lead to interesting properties resulting from the fact that both the dipole and monopole resonances can be excited by pressure and velocity fields [35]. However, neglecting bianisotropy in the effective material properties may result in parameters that may violate the principles of causality and passivity for an asymmetric unit cell [39–41]. To study such Willis metamaterials, extra parameters have to be determined compared to conventional symmetric materials. Muhlestein [40] and Amirkhizi [39] published methods to derive the effective properties for uniaxial Willis materials, which can be used to design unidirectional perfect absorbers [42] or bi-layer plate-type acoustic metamaterials [43].

Retrieval Methods

Retrieval methods are an alternative approach to derive effective properties that utilise scattering coefficients obtained on the incidence and transmission sides of the medium, as illustrated in Figure 1.10 [44, 45]. For such methods, the scattering coefficients have been obtained analytically for a periodic multilayered medium [46], numerically for periodic metamaterials [47, 48] or experimentally for acoustic metamaterials composed of split hollow spheres [49] or periodically arranged hollow tubes [50]. A retrieval method has also been extended for an asymmetric design [51]. Park et al. [52] also proposed a method to homogenise anisotropic metamaterial slabs by determining effective properties of the constitutive unit cell. Within the slab, the effective properties differ whether the unit cell is an edge cell or an inner cell. An advantage of retrieval methods is that they are not constrained to simple geometries.

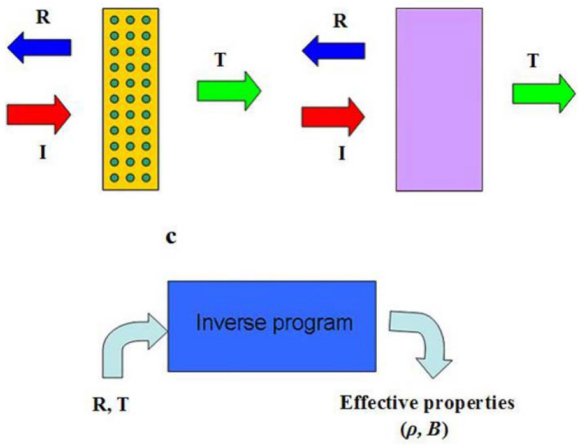

Figure 1.10 – Technique used for obtaining the effective properties of a metamaterial, with the structure as well as with incident, reflected, and transmitted plane waves. The effective material is also shown, along with the technique used for obtaining effective properties of a metamaterial [45].

1.3.3 Materials for Underwater Applications

Metamaterials have been developed for various underwater applications, such as carpet cloak [22,53] or a screen converting underwater cylindrical waves to plane waves [54]. This section reviews metamaterials used as coatings for underwater vehicles.

A simple way to improve wave attenuation is to use a large amount of absorbent material of a total thickness corresponding to several wavelengths. However, this is not suitable for the design of underwater coatings, which in practice can not exceed a certain thickness due to limitations related to naval architecture requirements for the vessel. In this context, metamaterials bring a new and promising perspective for thin coatings with good acoustic performance [55]. Some concepts applicable to underwater applications are reviewed here.

Elastomers as Matrix

For underwater applications, elastomers are widely used, providing good vibration energy dissipation due to their viscoelastic properties. In particular, they are very dispersive and dissipative for shear waves but not significantly for longitudinal waves. Elastomers are therefore widely used as a matrix material, in which elements are included to take advantage of these material properties. For example, a resonating inclusion may convert the longitudinal waves to shear waves, thus strongly dissipating the acoustic energy due to the shear material properties of the elastomer [56]. However, if the difference between the speed of sound in a resonating element and the surrounding elastomer is too high, the energy conversion may not occur [57].

In addition, the longitudinal sound velocity and density of an elastomer are generally close to the properties of water, resulting in impedance matching. An adequate impedance matching between the material interface and the surrounding water enhances coupling of the incident acoustic energy with the absorbers [58]. Hence, without good impedance matching at the interface, only a small proportion of the acoustic wave energy would be dissipated in the material. More generally, structures with gradient properties are a promising way to manipulate acoustic waves [59]. For example, Naify et al. [60] developed an underwater acoustic omnidirectional absorber based on a gradient index medium. However, that concept leads to thicknesses comparable to the wavelength, which may not comply with non-acoustic design criteria.

Micro-inclusion Materials

Micro-inclusion materials are elastomers comprising micro-cavities or soft-wall micro-balloons. There is usually a few percent volume fraction of these micro-inclusions, sometimes among other micro-inclusions such as carbon black or minerals in order to adjust the overall density. These inclusions of air bubbles or voids lower the effective speed of sound and provide better absorption. For high frequencies, micro-inclusion media

can be regarded as metamaterials [61, 62]. However, for low frequencies, the size of the micro-inclusions, generally of a few tens of microns, remains very small compared to the wavelength in water. Thus, a micro-inclusion medium can be considered as a homogeneous material. Further, the air cavities can deform under pressure, which could affect the performance of the coating [63].

Alberich Coatings

Alberich coatings, introduced in Figure 1.2, were developed by Erwin Meyer and his team, who were working on new absorbers of underwater sound in Berlin since 1945. At least one submarine of the German Navy, the U-480, was coated with this new technology as shown in Figure 1.11, making it the first stealth submarine [64]. Moreover, such a coating has the advantage of being significantly lighter than its counterpart with hard inclusions.

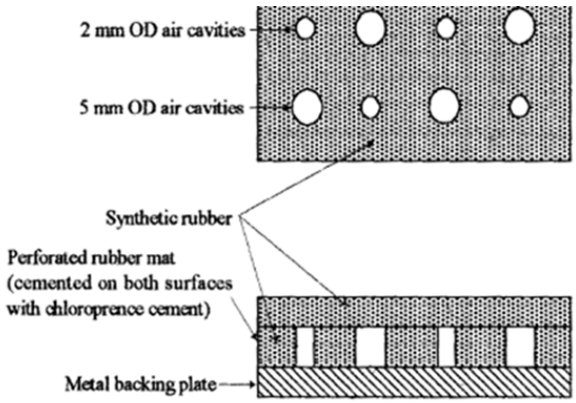

Figure 1.11 – Alberich acoustic absorption coating used on the German submarine U-480 [64].

In early work based on the finite element method (FEM), Hladky-Hennion and Decarpigny [33] developed a code to compute the sound transmission in a rubber medium submerged in water and embedded with periodic cylindrical cavities of finite height. A unit cell of the coating comprising a single cavity in rubber was simulated and periodicity of the geometry was implemented by applying classical Bloch conditions on the boundaries of the unit cell. Using the same finite element code, Langlet et al. [65] calculated the effective wavenumber of a periodically voided elastic medium under plane wave excitation.

Alberich coatings have latter been the subject of many studies to better understand their physical phenomena [66, 67]. Analytical [68, 69] and semi-analytical [32, 70] models have been developed to examine the acoustic performance of a periodically voided soft elastic medium. This type of coating can be derived in many ways, by modifying the shape of the cavities in other classical forms [71, 72] or in unusual new forms [73–77]. The use of pyramidal inclusions, as shown in Figure 1.12, helps with the impedance adaptation. It can also be achieved by cavities with gradient changes of radii and distances between

cavities in a soft elastic medium [77]. However, the resonance frequency of a cavity depends mainly on the volume of the cavity. It is therefore difficult to improve the absorption at low frequencies because the thickness of the anechoic layer is limited and the coating must also withstand hydrostatic pressure.

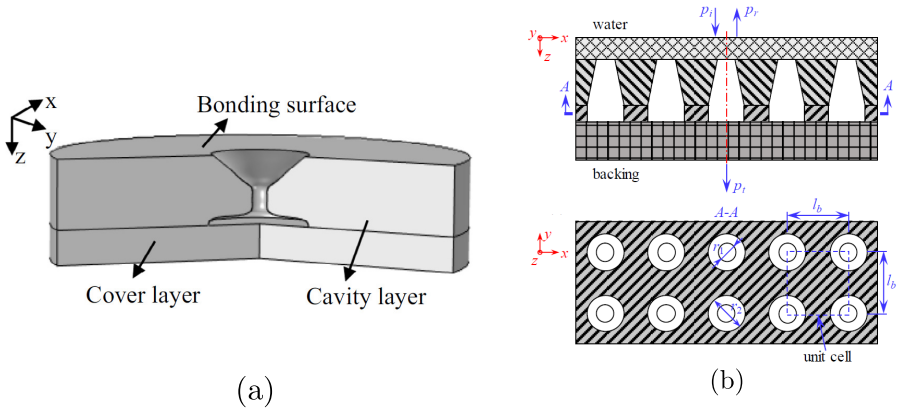

Figure 1.12 – Schematic diagrams of the coating with optimised cavities, from (a) [74] and (b) [75].

The steel support corresponding to the hull of the submarine also affects the performance of the coating as constructive interference can occur [70]. In addition, the mass of the steel support influences the low frequency absorption. An increase in the mass can decrease the frequency of the absorption peak [78].

Hard Inclusions

A metamaterial comprising hard inclusions embedded in a viscoelastic matrix is an ideal candidate as an external coating on the hull of an underwater vehicle, due to impedance matching of the viscoelastic medium with water and robustness of the hard scatterers under hydrostatic pressure [56, 79–81]. Scattering of sound waves by inclusions results in the conversion of longitudinal waves into shear waves, the latter being easily dissipated in a viscoelastic medium [56, 82]. An adaptation of the core-shell concept by Liu et al. [15] is shown in Figure 1.6(b) and consists of hard inclusions coated by a viscous rubber layer. This design has been shown to improve the acoustic performance of an underwater anechoic coating [57, 83, 84]. It has also been shown that an off-centred core leads to higher absorption [85, 86], as shown in Figure 1.13. Multiple layers of scatterers of different resonant frequency can also lead to broadband performance [87], which can also be achieved by the simultaneous use of voided and hard inclusions [88, 89].

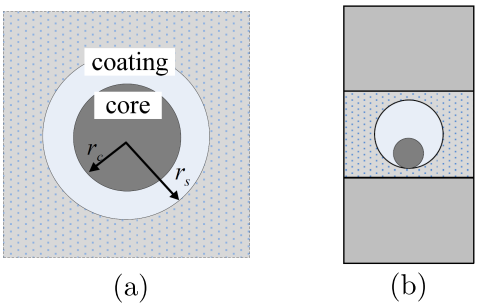

Figure 1.13 – (a) Cross section of one locally resonant core-shell unit, and (b) optimal core position [85].

Strong absorption can be obtained with the integration of resonant elements into a lossy viscoelastic material. The foremost simultaneous for energy dissipation is the presence of viscoelastic damping in at least one of the constituents [90]. It is nonetheless noted that the use of hard inclusions is sometimes limited by restrictions on the coating weight.

Multilayered Media

Despite their simple geometry, multilayered media may also lead to interesting acoustic performance. For example, sub-wavelength sound wave isolation has been achieved by utilising strong Gibbs-type oscillation in a finite periodic multilayered medium [26]. In addition, multilayered designs are easier to study and to homogenise than two- or three-dimensional structures. Multilayered media may also lead to negative parameters, such as effective density or effective bulk modulus, for a symmetric unit cell [91, 92]. However, examples of these structures for underwater applications are rare in the literature.

Other Designs

As mentioned previously, rubbers and polyurethane are the most commonly used matrix materials for underwater applications because of their ability to absorb incident sound wave energy. However, the elastic modulus of these materials increases with pressure. To cope with this constraint, Jiang and Wand [93] created the *phononic glass* for underwater applications, which includes a metal skeleton and polyurethane fillings with an inter-penetrating network structure, as shown in Figure 1.14(a). The physical connection between the locally resonant structure units is useful for exciting more modes, leading to a high sound absorption coefficient. In addition, the metal skeleton filled with polyurethane offers high mechanical strength and therefore has good resistance to hydrostatic pressure. However, with a metal skeleton, the total weight poses a difficulty for a coating application.

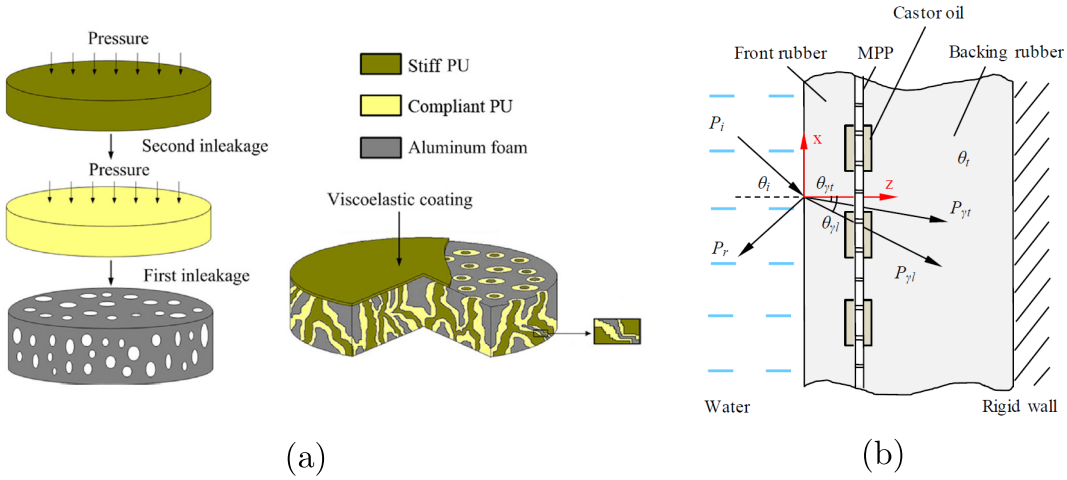

Figure 1.14 – (a) A schematic diagram of a synthesis and structure of phononic glass. [93] (b) Schematic diagram of the sandwich anechoic coating embedded with a micro-perforated panel in high-viscosity condition for underwater sound absorption [94].

Li and al. [94] recently designed a novel sandwich anechoic coating embedded with a castor-oil saturated micro-perforated panel as shown in Figure 1.14(b). It combines the low-frequency performance of a micro-perforated panel with the high-frequency performance of rubber, thus widening the absorption bandwidth .

1.3.4 Experimental Studies

The acoustic properties and acoustic performance of an elastomeric matrix or a the composite coating are often required to be obtained or verified experimentally. In what follows, experimental techniques for underwater panel characterisation are reviewed. Examples of underwater experimental studies are also given.

Experimental Techniques

Experimental characterisation of a panel requires the insonification of the sample by a known acoustic field. The reflection loss of a sample is obtained from the acoustic field reflected by the sample, while the transmission loss is calculated with the acoustic field passing through the sample [95]. The reflection and transmission coefficients can be measured in an impedance tube, a pressurised water tank or an open water tank [96]. The present review focuses on normal incidence characterisation techniques for panels in open water tanks.

One of the main difficulties of experimental measurements is the reproduction of the set of assumptions used for the theoretical or numerical calculations, which are difficult to implement in practice. For example, theoretical models or finite element calculations on periodic structures often consider infinite lateral dimensions, which is obviously impossible

to achieve in practice. The infinite panel assumption becomes particularly problematic for low frequency measurements. One of the main parasitic effects resulting from the finite lateral dimensions of the panel is the diffraction of acoustic waves by its edges. There exist techniques [97] and models [98, 99] to obtain direct evidence of the edge-diffraction phenomenon. It has even been shown that the importance of the edge diffraction perturbations is largely influenced by the material properties of the sample [100]. Edge diffraction may complicate measurements of the transmission loss for panels made of acoustically soft materials, since the amplitude of the transmitted waves can be very small compared to that of the diffracted waves. Moreover, if the speed of sound in the sample is rather low, the diffracted waves can overlap the reflected and transmitted signals in the time domain, which makes their differentiation difficult [101, 102]. Edge diffraction also significantly contaminates measurements on acoustically hard panels, for which the diffracted pattern shows strong variations in space within measurements planes [98].

Several methods have been developed to estimate the amplitude of diffracted waves. One method requires an air box to be placed in front of the panel (Figure 1.15(a)), for which the transmission loss is more than 60 dB. Thus, the signal received on the transmitted side is assumed to result from the sole contribution of the edge-diffracted waves [103]. An alternative technique has recently been presented which involves surrounding the panel in a reflective baffle so that its edges are less excited, thus reducing the contamination [104] (Figure 1.15(c)).

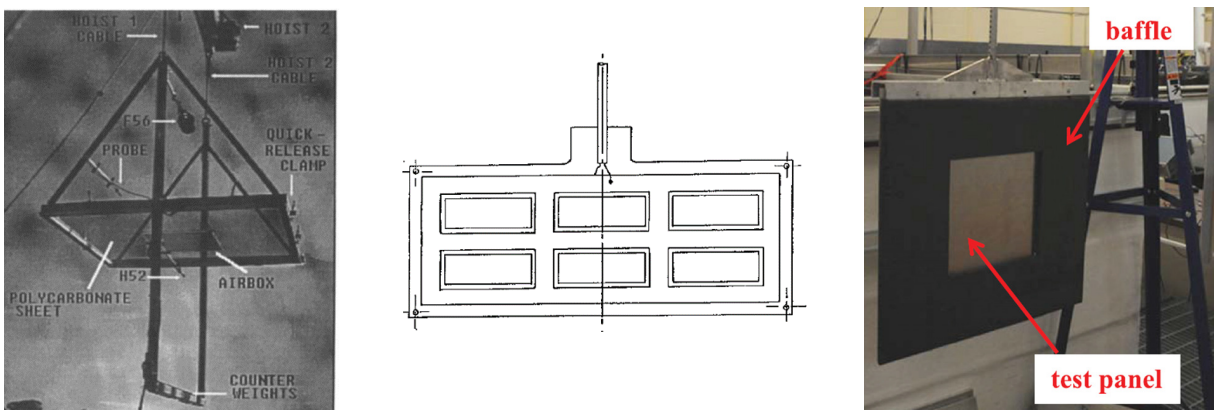

(a) (b) (c)

Figure 1.15 – (a) Measurement rig, sample and airbox [103]. (b) Surface hydrophone [99]. (c) Panel mounted in baffle [104].

Another experimental means of reducing the parasitic effects of edge diffraction is the use of a parametric array as the insonification is maximised at the centre of the panel and reduced at the edges [105]. The directivity of a parametric array for low-frequency waves is obtained by the interaction of high-frequency waves, which implies a non-linear mixing of the sound [106]. Nevertheless, it must be ensured that non-linear effects do not complicate or invalidate the measurement process [107], so a low-pass acoustic filter

is required in the measurement zone to attenuate the higher frequency primary waves. A surface receiver may also be used to reduce the scattered field perturbations on the transmission coefficient measurements (Figure 1.15(b)). This approach helps to reduce the effects of the edge-diffracted pressure assuming that the optimal size and position of the receiver have been found [99]. Perturbations caused by edge-diffracted waves can also be minimised as part of the post-processing by considering the transient-state reflected and transmitted signals, which are less contaminated. The transient-state signals are then extrapolated to obtain the steady-states used to derive the scattering coefficients. This process, known as the ONION method, has given good results for thick multilayered panels made of materials whose properties are known [102, 108, 109]. These techniques that have been implemented to reduce the edge diffraction effects. However, often these techniques have their own limitations, as they often require the manufacture or the use of some specific equipment or they may impose constraints on the panel design (thickness, material, etc.). Even with these techniques, a good compromise must still be found for the position of the hydrophones with respect to the panel. The hydrophones must be positioned close enough to reduce the detection of diffracted waves and far enough to avoid the overlap of the incident and reflected signals.

Experimental Study of Metamaterials

Experimental evidence of metamaterial features is not common in the literature, especially in an underwater environment. Bi et al. [53] designed and experimentally performed an underwater acoustic carpet cloak, comprising multiple layers of brass plates separated by layers of water. A soft 3D acoustic metamaterial with negative index has been developed by Brunet et al. [110]. Hladky et al. [111] experimentally demonstrated the negative refraction in water for medical imaging. These underwater achievements are interesting but such designs cannot be practically used as a coating as they do not consider all the related constraints such as thickness, hydrodynamics and weight.

There are only a handful of papers reporting the achievement of metamaterials with negative effective mass density in the water medium. Fok and Zhang [19] developed a negative acoustic index metamaterial in water that combines Helmholtz and rod-spring resonators to control effective bulk modulus and mass density, respectively. Effective properties from numerical simulations of their metamaterial design showed that negative real components of bulk modulus and density occur simultaneously, resulting in a negative real component of the acoustic index. Experimental measurements on a sample of their metamaterial design confirmed that the real components of the acoustic index and bulk modulus reach negative values, but the density does not become negative, attributed to the material loss. Popa et al. [112] also retrieved a positive effective mass density of an anisotropic acoustic metafluid, shown in Figure 1.16(a). This was achieved using an inverse method by measuring the reflected and transmitted fields on planes situated in front and behind the samples, and calculating the sample reflection and transmission coefficients based on the fields averaged along these planes. The coefficients were then inverted using a standard method proven to be very effective in acoustics. Chen et al. [50]

designed a 2D metamaterial with a simple design consisting of tubes on two pieces of epoxy. The tube was open and contained the water of the surrounding medium as shown in Figure 1.16(b). Effective properties extracted from experimental transmission and reflection coefficients showed that the effective density exhibits negative values for a narrowband frequency range.

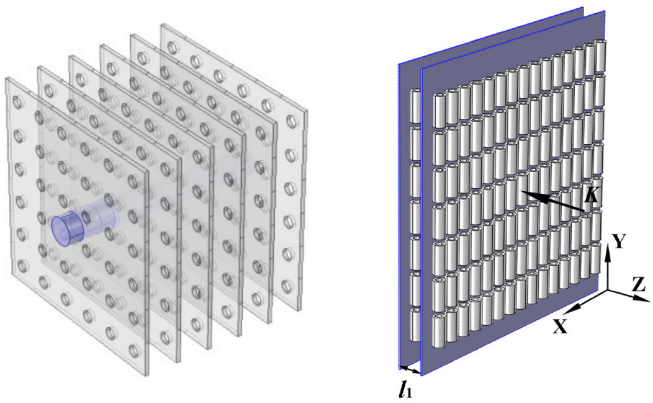

(a) (b)

Figure 1.16 – (a) Fluid-like structure made of perforated steel plates suspended in water. Plates are connected through solid spacers (purple) [112]. (b) Acoustic metamaterial with negative effective mass density in water, designed by periodically arranging hollow tube "meta-atoms" [50].

1.4 Notes on Concepts and Notations

1.4.1 Time Convention

In this manuscript, an incident wave refers to a harmonic plane wave excitation in a fluid domain that arrives under normal incidence on a medium. Using the notations of Figure 1.17, the sound propagates along the x-axis.

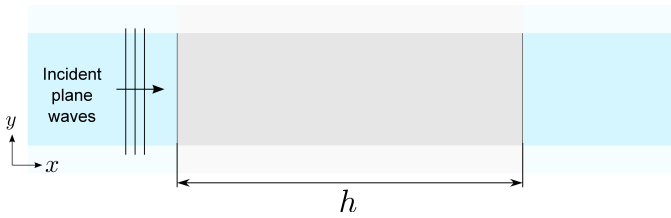

Figure 1.17 – Incident plane wave on a medium of thickness h.

The phase convention $e^{\mathrm{i}(\omega t - kx)}$ is used, where $\mathrm{i} = \sqrt{-1}$, ω is the angular frequency, k is the wavenumber, t is time and x defines the position on the x-axis.

1.4.2 Longitudinal and Shear Waves

In liquids or gases, only pressure waves can propagate. The propagation of a longitudinal wave is characterised by oscillations occurring in the direction of wave propagation. It thus corresponds to compression and expansion movements. In solids, longitudinal waves and shear waves can propagate. In the case of shear wave propagation, particles oscillate transversely to the direction of propagation.

For the study of a solid homogeneous medium at normal incidence, only the longitudinal waves are excited in the medium, provided that it is uniform in the lateral dimensions. Since there are only compression / expansion movements, as in a fluid, a fluid formalism is employed to study acoustic propagation in solids under these conditions. It is then applied for both a single layer of material and a multilayered structure.

1.4.3 Material Damping Representation

In acoustics, an isotropic material is commonly characterised by three parameters: mass density ρ, Young modulus E and Poisson ratio ν; or equivalently, mass density and longitudinal and shear speeds of sound denoted by c_{l} and c_{s}, respectively. Those parameters may depend on frequency or on environmental conditions, such as pressure and temperature. For elastomeric materials that have the ability to dissipate acoustic energy, an imaginary part can be added to given material properties. In such complex notations for damped material properties, the imaginary part represents the damping. It has to be noted that damping is physically represented by the imaginary part of the wavenumber. Nevertheless,

in this manuscript a complex speed of sound notation is used as $c_l = c_l^{'}(1 + i\eta)$, with $c_l^{'}$ corresponding to the real part of the longitudinal speed of sound and η the loss tangent.

1.4.4 Homogenisation

In this manuscript, the homogenisation process consists of applying a theoretical model to an effective medium so that its effective properties can be used to describe the far-field scattering response for normal incidence of a composite structure. Two models are considered. The first one, which happens to be the most commonly used in the literature, describes the effective medium as a fluid. The second model aims to describe asymmetric structures for which Willis-coupling effects may appear. The effective medium is then assumed to be a Willis fluid-like medium for which properties depend on the direction of wave propagation.

1.4.5 Passivity Constraint

Extreme effective properties can be obtained for a metamaterial. However, effective properties must comply with fundamental physical laws. For example, standard elastic materials and structures made of elastic materials are assumed to be passive. Implications of these restrictions were fully explored by Muhlestein [37], where a passive material is defined as a material that can not create mechanical energy.

In the present manuscript using the time convention $e^{i\omega t}$, passivity constraints set the sign of the wavenumber imaginary part to be negative, as shown in Section B.1 of Appendix B. Passivity also constrains the real part of the impedance to be positive, as described in [113].

1.4.6 Acoustic Performance

The acoustic performance of a structure is generally evaluated using the reflection and transmission coefficients for the structure placed between two semi-infinite fluid media. The reflection coefficient describes the amount of acoustic wave reflected by an impedance discontinuity created by the introduction of the structure in-between the surrounding media. It is equal to the ratio of the amplitude of the reflected wave to the incident wave. The transmission coefficient is a measure of the amount of acoustic energy passing through a structure. It is calculated from the ratio of the amplitude of the transmitted wave to the amplitude of the incident wave. For experimental determination of the reflection and transmission coefficients, free-field measurements on a test panel are used.

For underwater applications, the efficiency of an coating in reducing acoustic radiation from a structure is assessed using the hull decoupling coefficient C_{D}, while the stealth performance is evaluated with the anechoism coefficient C_{A}. For determination of the anechoism coefficient, the sample may be fixed on a steel plate. However, this approach is not practical at low frequencies as the steel backing plate might not be thick enough. The hull decoupling coefficient may be obtained by placing the sample on a vibrating support

and comparing results with and without the sample. This approach gives a qualitative comparison, but post-processing is complex [114].

In order to simplify the determination of the anechoism and hull decoupling coefficients, the common approach consists in conducting free-field measurements of the panel and then deriving these coefficients numerically using the reflection and transmission coefficients of the structure, as demonstrated in Appendix C.

Part I

MULTILAYERED DESIGNS

Chapter 2

Homogenisation

In this chapter, an analytical model based on a transfer matrix formalism is presented to characterise an effective medium that can effectively replace a multilayered medium and from which the reflection and transmission coefficients can be calculated. Two variants of the homogenisation method are proposed. The first method is specific to symmetric multilayered media whereas the second method can be applied to both asymmetric and symmetric designs. A quasi-static approach is also introduced to verify the homogenisation method at low frequencies. Numerical results are then presented for a case study consisting of a multilayered structure comprising alternating layers of acoustically rigid and soft materials.

Contents

2.1 Transfer Matrix **36**

2.1.1 Definition 36

2.1.2 Expression 36

2.1.3 Calculation 37

2.2 Homogenisation **38**

2.2.1 Fluid Homogenisation Model 38

2.2.2 Willis Fluid Homogenisation Model 39

2.3 Scattering Coefficients **42**

2.3.1 Multilayered Medium 42

2.3.2 Effective Medium 43

2.4 Quasi-static Approach **44**

2.5 Numerical Results **45**

2.5.1 Designs 45

2.5.2 Effective Parameters 46

2.5.3 Scattering Coefficients 50

2.6 Summary **53**

2.1 Transfer Matrix

2.1.1 Definition

In the context of one-dimensional propagation of waves in a fluid-like structure, the transfer matrix $\mathbf{M}$ relates the acoustic pressure p and the normal particle velocity v of the medium on the two sides of the layer. Based on the notations in Figure 2.1, the transfer matrix $\mathbf{M}$ is defined by:

$$\begin{pmatrix} p_{\text{left}} \\ v_{\text{left}} \end{pmatrix} = \mathbf{M} \begin{pmatrix} p_{\text{right}} \\ v_{\text{right}} \end{pmatrix}. \tag{2.1}$$

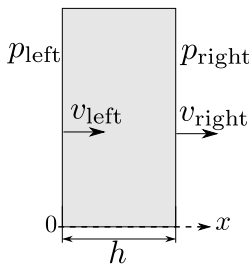

Figure 2.1 – Pressures and normal particle velocities at the inlet/outlet of a medium of thickness h, where the subscript left refers to the face on the left hand-side and the subscript right to the face on the right hand-side of the medium.

2.1.2 Expression

Expressions of the transfer matrix elements depend on the nature of the medium. Two cases are considered in what follows: classical fluid or Willis fluid. Details on how the expressions are derived are given in Appendix A.

Case 1: Fluid Medium

The simplest case considers a medium that can be assimilated to a fluid. With k the wavenumber and Z the acoustic impedance, the expression of the transfer matrix is given by:

$$\mathbf{M} = \begin{bmatrix} \cos(kh) & \mathrm{i}Z\sin(kh) \\ \mathrm{i}Z^{-1}\sin(kh) & \cos(kh) \end{bmatrix}, \tag{2.2}$$

where h is the thickness of the medium in the direction of the sound propagation. Since only harmonic plane waves at normal incidence on multilayered structures are considered in Part I, any homogeneous material can be approximated as a fluid medium and can thus be described by Equation (2.2).

Case 2: Willis Fluid Medium

The second case considers a fluid-like medium that is asymmetric, also referred to as a Willis fluid. Material properties thus depend on the wave propagation direction. For the one-dimensional wave propagation considered here, two directions are possible: waves are referred to as forward or backward propagating waves. The distinction is reflected on the effective impedance, since the wavenumber is the same for both directions [39]. The acoustic field can therefore be decomposed along these two directions, which leads to the transfer matrix form given by:

$$\mathbf{M} = \frac{1}{Z^+ - Z^-} \begin{bmatrix} Z^+ e^{\mathrm{i}kh} - Z^- e^{-\mathrm{i}kh} & Z^+ Z^- (e^{-\mathrm{i}kh} - e^{\mathrm{i}kh}) \\ e^{\mathrm{i}kh} - e^{-\mathrm{i}kh} & Z^+ e^{-\mathrm{i}kh} - Z^- e^{\mathrm{i}kh} \end{bmatrix}, \tag{2.3}$$

where k is the wavenumber and Z^+ and Z^- are the impedances for forward and backward propagating waves, respectively. It can be noted that for a symmetric medium, for which $Z^+ = -Z^- = Z$, the simplification of Equation (2.3) gives the transfer matrix given by Equation (2.2).

2.1.3 Calculation

When a plane wave arrives at normal incidence on a multilayered medium of infinite lateral dimensions, the acoustic fields at the interfaces are uniform. They may thus be described by only a scalar for the pressure and a scalar for the normal particle velocity, as shown in Figure 2.1. The use of transfer matrices is particularly suitable for the analysis of multilayered media as they can easily be connected to each other like a chain to represent a succession of layers. The technique that uses transfer matrices to study chained acoustic structures is also known as the transmission line method. As such, given the continuity of acoustic pressure and velocity at the interfaces between two layers, the total transfer matrix $\mathbf{M}_n$ of a multilayered medium comprising n layers is obtained by:

$$\mathbf{M}_n = \mathbf{m}_1 \mathbf{m}_2 ... \mathbf{m}_n, \tag{2.4}$$

where $\mathbf{m}_i$ denotes the transfer matrix of layer i. The transfer matrix $\mathbf{m}_i$ can be calculated using the transfer matrix given by Equation (2.2), assuming that each layer is a fluid-like medium with known material properties.

2.2 Homogenisation

The homogenisation approach described herein aims to replace a finite periodic multilayered structure by a fluid-like homogeneous medium that would have the same scattering response. For this purpose, the characteristic unit cell of the multilayered medium is defined as the smallest recurring unit. This unit cell is used to derive effective properties, such as the effective wavenumber and effective impedance, which are the material properties of an equivalent homogeneous unit cell, as illustrated in Figure 2.2.

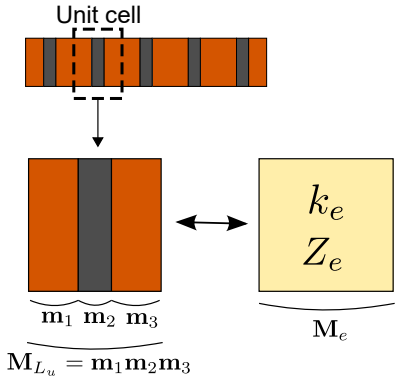

Figure 2.2 – Finite periodic multilayered medium characterised by a symmetric unit cell, for which a fluid effective medium is defined by an effective wavenumber and an effective impedance obtained using the transfer matrix M_{L_u} of the periodic unit.

In this manuscript, the notion of *effective medium* is therefore referring to a medium defined by an homogenisation model and which is intended to replace a given non-homogeneous medium. The simplest case is treated first, considering that the effective unit is a fluid that can replace a symmetric unit cell. Then, the case of non-symmetric unit cells is detailed, where effective properties are obtained using a Willis fluid homogenisation model.

2.2.1 Fluid Homogenisation Model

The transfer matrix of a unit cell of length L_u, denoted as $\mathbf{M}_{L_u}$, can be numerically computed since the properties for longitudinal wave propagation of the materials composing each layer of a multilayered unit are known. For this purpose, the transfer matrix for each layer is first calculated using Equation (2.2), and they are then multiplied according to Equation (2.4). For example, in the case presented in Figure 2.2, the transfer matrix of the unit $\mathbf{M}_{L_u}$ is $\mathbf{m}_1\mathbf{m}_2\mathbf{m}_3$, where $\mathbf{m}_i$ $(i = 1, 2, 3)$, are the transfer matrices for layers 1 to 3.

Another method of expressing the transfer matrix of the effective medium is as follows:

$$\mathbf{M}_e = \begin{bmatrix} \cos(k_e L_u) & \mathrm{i}Z_e \sin(k_e L_u) \\ \mathrm{i}Z_e^{-1}\sin(k_e L_u) & \cos(k_e L_u) \end{bmatrix}, \tag{2.5}$$

where L_u is the length of the medium, k_e is the effective wavenumber and Z_e is the effective impedance. As the effective medium aims to represent the multilayered structure, both transfer matrices $\mathbf{M}_{L_u}$ and $\mathbf{M}_e$ are the same, that is:

$$\mathbf{M}_{L_u} = \mathbf{M}_e. \tag{2.6}$$

Effective parameters can then be extracted from the elements of the transfer matrix $\mathbf{M}_e$. The effective wavenumber expression, derived in Appendix B.1, is given by:

$$k_e = \frac{\ln(\lambda)}{\mathrm{i}L_u} + \frac{2\pi m}{L_u}, \tag{2.7}$$

where m is an integer whose value is determined in such way that the effective wavenumber as a function of frequency is continuous, and λ is the eigenvalue of the transfer matrix $\mathbf{M}_{L_u}$, chosen so that the imaginary part of k_e is negative to comply with material passivity requirements (as mentioned in section 1.4.5 and in Appendix B).

The effective impedance Z_e can be directly extracted from the off-diagonal elements of the transfer matrix, using:

$$Z_e = \pm\sqrt{\frac{\mathbf{M}_e(1,2)}{\mathbf{M}_e(2,1)}}. \tag{2.8}$$

Material passivity requirements constrain the real part of the effective impedance Z_e to be positive.

With the effective wavenumber k_e and the effective impedance Z_e, the effective fluid-medium representing a given symmetric multilayered unit cell is fully characterised, given that the length of the effective medium in the direction of sound propagation is the same as the length of the unit cell, in this case, L_u. The effective medium approach described here is valid independently of the number of layers comprised in the unit cell, as long as it remains symmetric.

2.2.2 Willis Fluid Homogenisation Model

For a non-symmetric multilayered medium, the behaviour is different for a wave travelling towards $x = +\infty$ with respect to a wave travelling towards $x = -\infty$. In order to effectively represent non-symmetric media, the effective medium is now assumed to be an asymmetric fluid-like medium, also referred to as a Willis fluid. The effective medium approach follows the same scheme as before but it uses the more general form of the transfer matrix given by Equation (2.3).

One way to calculate the total transfer matrix for the unit cell of length L_u, defined as $\mathbf{M}_{L_u}$, is to take the product of the transfer matrices for each layer as per Equation (2.4).

The second method is to use the transfer matrix of the effective Willis fluid given as:

$$\mathbf{M}_e = \frac{1}{Z_e^+ - Z_e^-} \begin{bmatrix} Z_e^+ e^{\mathrm{i}k_e L_u} - Z_e^- e^{-\mathrm{i}k_e L_u} & Z_e^+ Z_e^- (e^{-\mathrm{i}k_e L_u} - e^{\mathrm{i}k_e L_u}) \\ e^{\mathrm{i}k_e L_u} - e^{-\mathrm{i}k_e L_u} & Z_e^+ e^{-\mathrm{i}k_e L_u} - Z_e^- e^{\mathrm{i}k_e L_u} \end{bmatrix}, \tag{2.9}$$

where k_e is effective wavenumber and $Z_e^\pm$ are the effective impedances for forward and backward propagating waves. The effective wavenumber is also given by Equation (2.7).

Effective impedances can be obtained by the direct identification ($\mathbf{M}_{L_u} = \mathbf{M}_e$), which yields:

$$Z_e^\pm = \frac{-(\mathbf{M}_{e2,2} - \mathbf{M}_{e1,1}) \pm \sqrt{(\mathbf{M}_{e2,2} - \mathbf{M}_{e1,1})^2 + 4\mathbf{M}_{e1,2}\mathbf{M}_{e2,1}}}{2\mathbf{M}_{e2,1}}, \tag{2.10}$$

where $\mathbf{M}_{ei,j}$ are the elements of the total transfer matrix $\mathbf{M}_e$. Due to the passivity material constraint, solutions are chosen in a way that the impedance for forward propagating waves Z_e^+ has a positive real part. The effective impedance Z_e^- then corresponds to the other branch.

The effective medium for a non-symmetric unit cell is now fully characterised with the effective wavenumber k_e and the effective impedances $Z_e^\pm$. It is worth noting that the effective medium approach for non-symmetric structures is also valid for symmetric structures, as the symmetry only implies some simplifications, such as the equality $\mathbf{M}_{e2,2} = \mathbf{M}_{e1,1}$, from Equation (2.2), which results in the simplification of Equation (2.10) into Equation (2.8).

Willis Parameters

As introduced by Mulhestein et al. [40], a Willis fluid may also be characterised using Willis parameters instead of impedances for forward and backward propagating waves. These parameters correspond to the asymmetry coefficient W and the characteristic impedance Z_W. The effective impedances $Z_e^\pm$ are linked to W and Z_W as per:

$$Z_e^\pm = Z_W(\pm 1 + \mathrm{i}W). \tag{2.11}$$

When the asymmetry coefficient W is equal to 0, the effective impedance Z_e is the same as the Willis characteristic impedance Z_W.

The asymmetry coefficient W and the characteristic impedance Z_W can be obtained from the transfer matrix form given by:

$$\mathbf{M}_e = \begin{bmatrix} \cos(k_e L_u) - W\sin(k_e L_u) & \mathrm{i}Z_W \sin(k_e L_u)(1 + W^2) \\ \mathrm{i}\sin(k_e L_u)/Z_W & \cos(k_e L_u) + W\sin(k_e L_u) \end{bmatrix}. \tag{2.12}$$

This expression is derived in Appendix A.4. Willis parameters are therefore given by:

$$W = \frac{-\mathrm{M}_{e1,1} + \cos(k_e L_u)}{\sin(k_e L_u)}, \tag{2.13}$$

$$Z_W = \sqrt{\frac{\mathrm{M}_{e1,2}}{\mathrm{M}_{e2,1}(1 + W^2)}}. \tag{2.14}$$

Effective material properties for a Willis fluid are then derived using the expressions:

$$\kappa = \frac{\omega Z_W}{k_e}, \tag{2.15}$$

$$\rho = \frac{k_e Z_W}{\omega}. \tag{2.16}$$

2.3 Scattering Coefficients

The scattering response of a multilayered medium here refers to the reflection and transmission coefficients defined as in a two-port network, where the ports correspond to the interfaces of the medium with the surrounding fluid (see Appendix A for the notion of two-port network and the definition of S-parameters). For a given multilayered structure, scattering coefficients can be calculated using (1) the total transfer matrix of the entire multilayered medium, or (2) the transfer matrix of an equivalent homogeneous medium. Both approaches are presented in what follows, based on Figure 2.3.

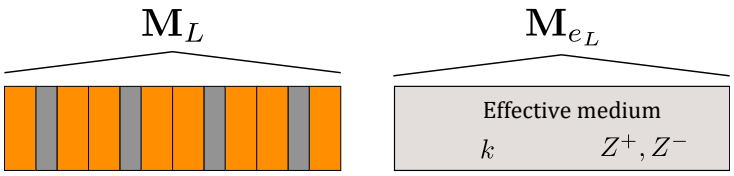

Figure 2.3 – Finite periodic multilayered medium of length L and effective medium of same length whose effective properties have been derived from the constituent unit cell.

2.3.1 Multilayered Medium

The transfer matrix $\mathbf{M}_L$ is analytically calculated by taking the product of the transfer matrix of each layer comprised in the multilayered medium, as per Equation (2.4). It is worth noting that this approach is still valid for non-periodic multilayered media. Elements $\mathbf{M}_{L_{i,j}}$ of the total transfer matrix are used to obtain the S-parameters as per:

$$S_{11} = \frac{\mathbf{M}_{L_{1,2}} + Z_{\mathrm{f}}(\mathbf{M}_{L_{1,1}} - \mathbf{M}_{L_{2,2}}) - Z_{\mathrm{f}}^2\mathbf{M}_{L_{2,1}}}{\Delta}, \tag{2.17}$$

$$S_{21} = \frac{2Z_{\mathrm{f}}}{\Delta}, \tag{2.18}$$

$$S_{22} = \frac{\mathbf{M}_{L_{1,2}} - Z_{\mathrm{f}}(\mathbf{M}_{L_{1,1}} - \mathbf{M}_{L_{2,2}}) - Z_{\mathrm{f}}^2\mathbf{M}_{L_{2,1}}}{\Delta}, \tag{2.19}$$

$$S_{12} = \frac{2Z_{\mathrm{f}}\mathrm{Det}(\mathbf{M}_L)}{\Delta}, \tag{2.20}$$

where Z_{f} is the impedance of the surronding fluid and Δ is:

$$\Delta = \mathbf{M}_{L_{1,2}} + Z_{\mathrm{f}}(\mathbf{M}_{L_{1,1}} + \mathbf{M}_{L_{2,2}}) + Z_{\mathrm{f}}^2\mathbf{M}_{L_{2,1}}. \tag{2.21}$$

Those expressions are derived in Appendix C.

2.3.2 Effective Medium

When a homogeneous effective medium is used to replace a multilayered medium, scattering coefficients can be obtained from its transfer matrix $\mathbf{M}_{e_L}$. This is achieved using Equations (2.17) to (2.20) by replacing the matrix elements $\mathbf{M}_{L_{i,j}}$ with the elements $\mathbf{M}_{e_{L_{i,j}}}$.

For an effective medium replacing a symmetric multilayered design of length L, S-parameters are obtained using the effective properties k_e and Z_e that have been derived for the symmetric unit cell, by calculating the transfer matrix $\mathbf{M}_{e_L}$ given by:

$$\mathbf{M}_{e_L} = \begin{bmatrix} \cos(k_e L) & \mathrm{i} Z_e \sin(k_e L) \\ \mathrm{i} Z_e^{-1} \sin(k_e L) & \cos(k_e L) \end{bmatrix}. \tag{2.22}$$

For a non-symmetric configuration, the transfer matrix of the effective medium of length L is:

$$\mathbf{M}_{e_L} = \frac{1}{Z_e^+ - Z_e^-} \begin{bmatrix} Z_e^+ e^{\mathrm{i}k_e L} - Z_e^- e^{-\mathrm{i}k_e L} & Z_e^+ Z_e^- (e^{-\mathrm{i}k_e L} - e^{\mathrm{i}k_e L}) \\ e^{\mathrm{i}k_e L} - e^{-\mathrm{i}k_e L} & Z_e^+ e^{-\mathrm{i}k_e L} - Z_e^- e^{\mathrm{i}k_e L} \end{bmatrix}. \tag{2.23}$$

2.4 Quasi-static Approach

At very low frequencies, values of the longitudinal wavenumber are very small. A quasi-static approach can be used to approximate effective parameters of a periodic unit cell. The quasi-static effective density is given by the average density for the various layers in the equivalent homogeneous medium as follows:

$$\rho_{\mathrm{QS}} = \frac{\sum_{i=1}^{N}(h_i \rho_i)}{h_u}, \tag{2.24}$$

where h_i and ρ_i respectively are the thickness and density of the layer i and $h_u = \sum_{i=1}^{N} h_i$ is the total thickness of the unit.

The effective wavenumber can be obtained using the dispersion relation given for a two layer unit [65], as follows:

$$\cos(k(h_1 + h_2)) = \cos(k_1 h_1)\cos(k_2 h_2) - \frac{1}{2}(\gamma + \frac{1}{\gamma})\sin(k_1 h_1)\sin(k_2 h_2), \tag{2.25}$$

where h_1, k_1, Z_1 and h_2, k_2, Z_2 are the thickness, wavenumber and impedance respectively, of material 1 and material 2 in the periodic unit, and $\gamma = Z_1/Z_2$. For low values of the wavenumber, a polynomial approximation of Equation (2.25) leads to:

$$k_{\mathrm{QS}}^2 (h_1 + h_2)^2 \simeq (k_1 h_1)^2 + (k_2 h_2)^2 + (\gamma + \frac{1}{\gamma}) k_1 h_1 k_2 h_2. \tag{2.26}$$

The quasi-static effective sound speed c_{QS} and the quasi-static effective impedance Z_{QS} are then given by:

$$c_{\mathrm{QS}} \simeq \frac{h_1 + h_2}{\sqrt{(\frac{h_1}{c_1})^2 + (\frac{h_2}{c_2})^2 + (\gamma + \frac{1}{\gamma})\frac{h_1 h_2}{c_1 c_2}}}, \tag{2.27}$$

$$Z_{\mathrm{QS}} = \rho_{\mathrm{QS}} c_{\mathrm{QS}}. \tag{2.28}$$

2.5 Numerical Results

2.5.1 Designs

Numerical results for periodic multilayered structures will now be presented. Media are formed by alternating layers of silicone rubber and aluminium. Material properties are given in Table 2.1.

	ρ (kg.m^{-3})	c_l (m.s^{-1})	η (%)
Silicone rubber	1250	1000	2
Aluminium	2700	6200	

Table 2.1 – Density ρ and longitudinal speed of sound c_l for the silicone and aluminium. Damping is expressed using the loss factor η as a percentage of the speed of sound.

Four different versions of the unit cell are considered, represented in Figure 2.4 and for which layer thicknesses are given in Table 2.2. Two of these designs are symmetric and the two other are non-symmetric. The total thickness of silicone is always 30mm and the total thickness of aluminium is 10mm.

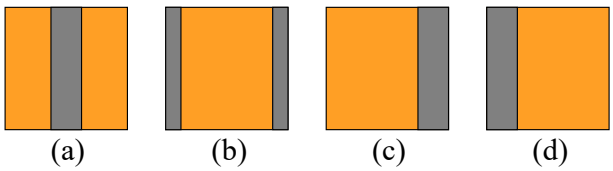

Figure 2.4 – Schematic diagram of the two symmetric unit cells (a) and (b) and the two asymmetric unit cells (c) and (d). Silicone rubber is represented by the orange layers and aluminium is represented by the grey layers.

	Layer 1	Layer 2	Layer 3
Version (a)	Silicone	Aluminium	Silicone
(mm)	15	10	15
Version (b)	Aluminium	Silicone	Aluminium
(mm)	5	30	5
Version (c)	Silicone	Aluminium	
(mm)	30	10	
Version (d)	Aluminium	Silicone	
(mm)	10	30	

Table 2.2 – Layer arrangements and thicknesses for the four versions of the unit cell, for which the total thickness is L_u

2.5.2 Effective Parameters

Effective Wavenumber

Since the effective wavenumber is independent of the unit cell version considered within those presented in Figure 2.4, thanks to the Bloch-Floquet relation, all four versions have the same dispersion curve, which is presented in Figure 2.5 in terms of the dimensionless wavenumber denoted $k_e L_u$. The concept of dispersion curve is briefly introduced in Appendix B.2. In order to visualise the effects of damping, the wavenumber $k_{e,\eta\%}$ is plotted for three different values of the loss factor η corresponding to 0%, 2% and 8%. Without losses ($\eta = 0\%$), the imaginary part of the effective wavenumber clearly gives the pass band and band gaps, as band gaps occur when the imaginary part is non-null and when the wrapped real part of the effective wavenumber is a multiple of π. Such Bragg band gaps are attributed to the fact that every aluminum-silicone interface in the structure generates partial wave reflections which can destructively interfere. For the frequency range considered, two complete band gaps appear, represented by the shaded areas. Within these band gaps and even in the presence of damping (η non null), the imaginary part of the wavenumber, which represents wave attenuation per unit distance, reaches a local maximum. This shows that there is a greater attenuation of acoustic waves in the band gaps than in the pass bands. Moreover, it can be seen that this maximum increases with higher loss factor η. For the real part of the reduced wavenumber, an increase of the damping η results in a more pronounced "smoothing" of the curve, which no longer meets the edges of the band gaps.

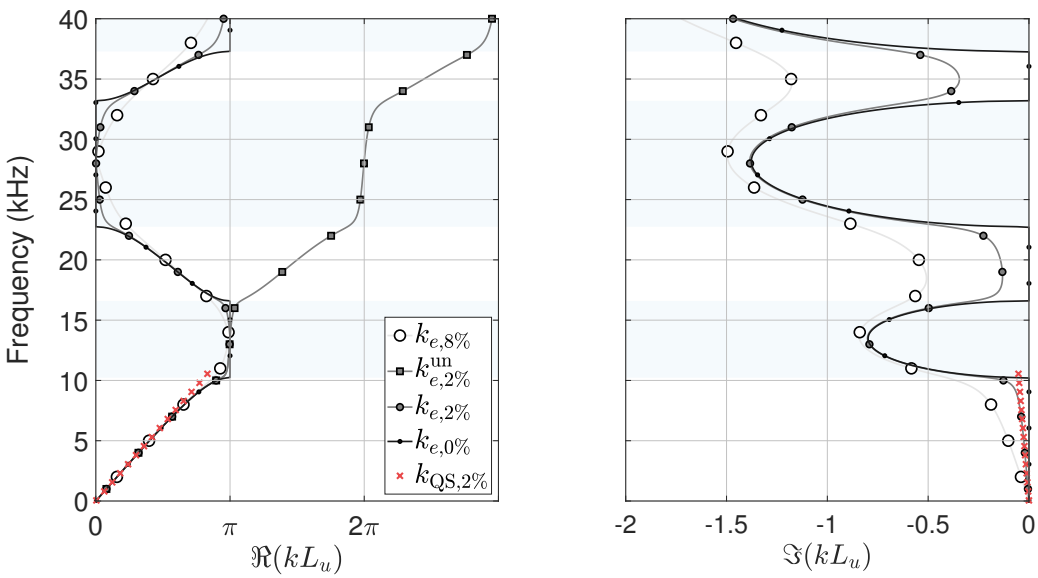

Figure 2.5 – Dispersion curve for the multilayered units comprising layers of silicone and aluminium, considering 0%, 2% and 8% loss factor in the silicone layer. For the case $\eta = 2\%$, the effective wavenumber is also unwrapped ($k^{\text{un}}_{e,2\%}$), as well as compared to the quasi-static value k_{QS}. The shaded areas represent band gaps defined using the wavenumber $k_{e,0\%}$

The real part of the wavenumber for $\eta = 2\%$ is unwrapped, represented by $k_{e,2\%}^{\text{un}}$, in order to illustrate the unwrapping process using the integer m introduced in Equation (2.7). This manipulation is only required if the effective wavenumber is then used to derive other effective parameters, such as the density and the bulk modulus, in order to get a continuous evolution with frequency.

Finally, the quasi-static wavenumber k_{QS}, obtained with Equation (2.26) and represented by the red crosses, is consistent with the effective wavenumber $k_{e,2\%}$ at low frequencies, thus validating the latter.

Effective Impedance

In contrast to the effective wavenumber, the effective impedance depends on the design of the unit cell. Considering $\eta = 2\%$ for the silicone, Figure 2.6 presents the real and imaginary parts of the effective impedances for units (a) to (d). Band gaps for zero damping are also shown by the shaded areas.

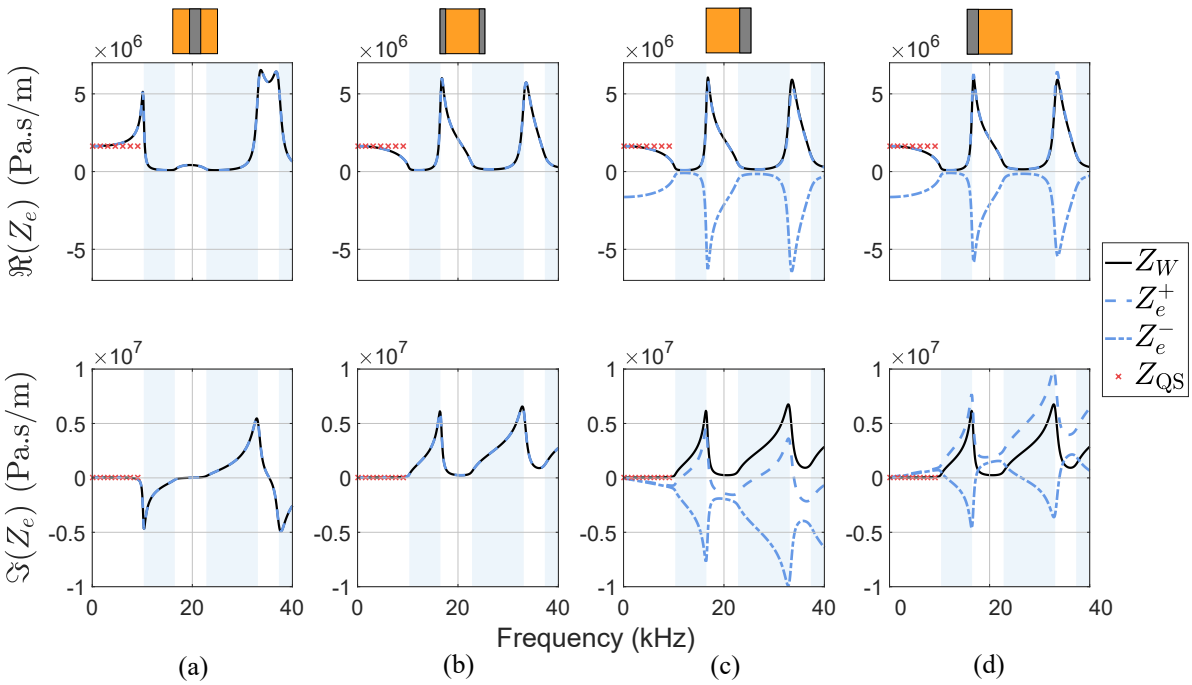

Figure 2.6 – Effective impedances for forward propagating waves (dashed blue lines) and backward propagating waves (dashed-dotted blue lines) as well as characteristic impedance Z_W (black lines) obtained for the unit designs shown in Figure 2.4(a) (first column), Figure 2.4(b) (second column), Figure 2.4(c) (third column) and Figure 2.4(d) (fourth column). The first line of graphics represents the real part of the effective impedances, while the second line corresponds to the imaginary part. The shaded areas represent the band gaps obtained using zero damping for silicone. The red crosses show the quasi-static effective impedance.

For the symmetric versions (a) and (b), the effective impedance is derived using Equation

(2.8) whereas for the two asymmetric units (c) and (d), Equation (2.10) is used, leading to the effective impedances for forward and backward propagating waves, respectively represented by the dashed and dashed-dotted blue lines. The black lines represent the characteristic impedance Z_W obtained using Equation (6.6). These plots first confirm that $Z_e = Z_W$ for the symmetric units (a) and (b). The quasi-static impedance, represented by the red crosses, is also consistent with the effective impedance obtained at low frequencies.

Differences in the effective impedances amongst the different unit cells are more visible for the imaginary part. For the two asymmetric versions (c) and (d), the real parts of the effective impedances are quite similar but the imaginary parts differ significantly. It is also important to note that the effective impedance for forward propagating waves Z_e^+ for one unit is the opposite of the effective impedance for backward propagating waves Z_e^- for the other (reverse) unit. In other words, $Z_{e,(\mathrm{c})}^+ = -Z_{e,(\mathrm{d})}^-$ and $Z_{e,(\mathrm{d})}^+ = -Z_{e,(\mathrm{c})}^-$. This observation can also be mathematically proven by inverting the transfer matrix. For these two asymmetric units, the characteristic impedance Z_W, given by Equation (2.11), differs from the effective impedance $Z_e^\pm$ as the asymmetry coefficient W is non-null.

The variations of the effective impedance for unit (a) greatly differs from the three others and even reaches negative values. In order to further study this difference, the effective density and bulk modulus are calculated in what follows.

Effective Density and Bulk Modulus

For the 4 unit cells, the effective density is plotted in Figure 2.7 using Equation (2.16). The effective bulk modulus is calculated using Equation (2.15) and is shown in Figure 2.8.

The real part of the effective density of version (a) reaches negative values in the first band gap. This specific metamaterial feature is usually the translation of a mass-spring resonance in most metamaterial studies. This observation can be made only for unit (a), where the heaviest layer (aluminium - mass) is placed in-between two soft and damped layers (silicone - spring). For all the other band gaps, the bulk modulus becomes negative, which is the translation of a compression-extensional motion. Hence, either a negative mass density or a negative bulk modulus is obtained for each band gap produced by the four unit versions. The version where the heavy layer is surrounded by the damped layer is the only one that can lead to a negative mass density.

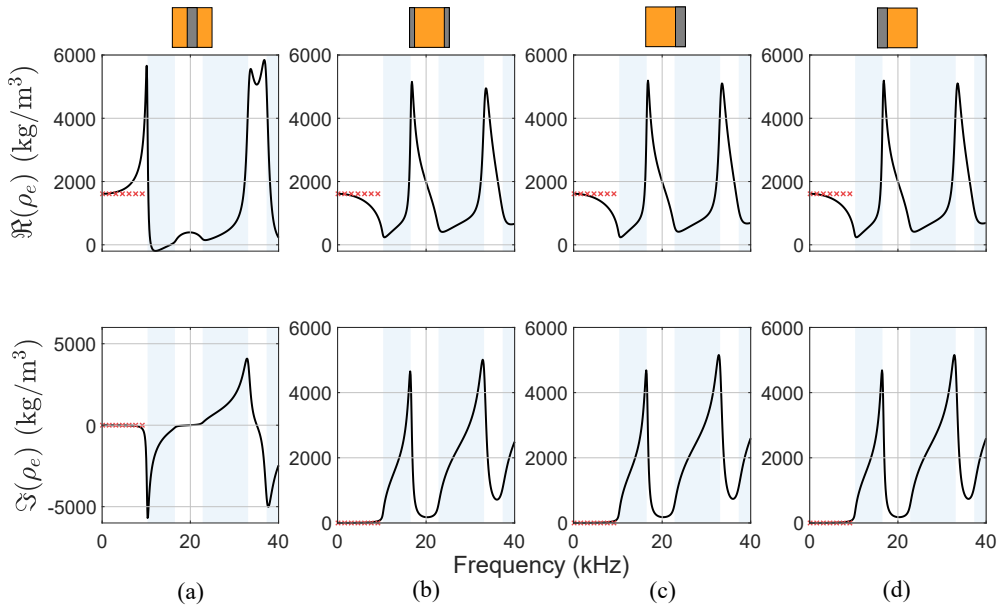

Figure 2.7 – Effective density obtained for the unit designs represented by Figure 2.4(a) (first column), Figure 2.4(b) (second column), Figure 2.4(c) (third column) and Figure 2.4(d) (fourth column). The top row shows the real part while the bottom row corresponds to the imaginary part. The shaded areas represent the band gaps obtained using zero damping for silicone.

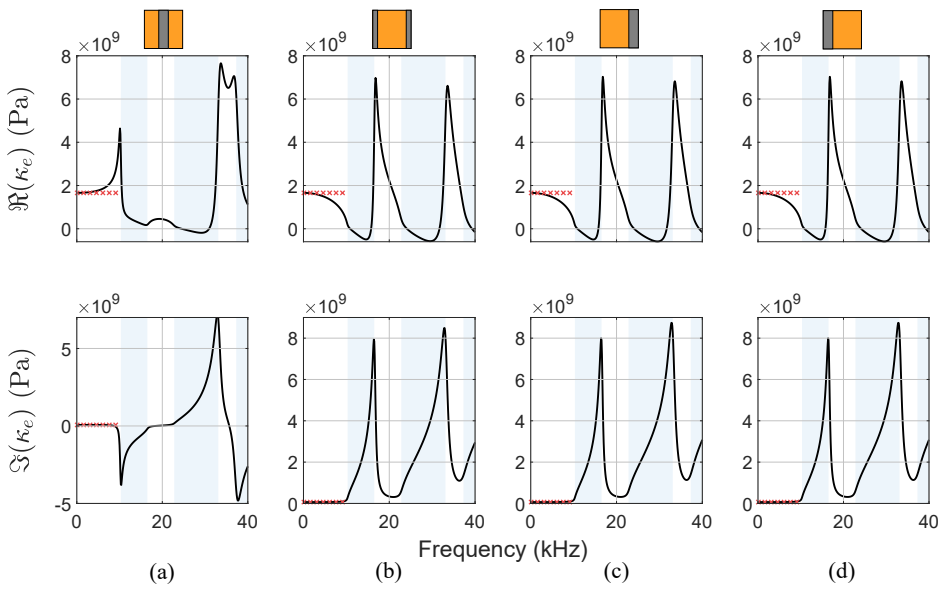

Figure 2.8 – Bulk modulus obtained for the unit designs represented by Figure 2.4(a) (first column), Figure 2.4(b) (second column), Figure 2.4(c) (third column) and Figure 2.4(d) (fourth column). The top row shows the real part while the bottom row corresponds to the imaginary part. The shaded areas represent the band gaps obtained using zero damping for silicone.

2.5.3 Scattering Coefficients

As presented in Section 2.3, two approaches are used to calculate the acoustic performance in terms of S-parameters for a medium of length $L = n \times L_u$. The first method to find the total transfer matrix $\mathbf{M}_L$ of the n-unit medium is calculated using the transfer matrix of each layer. Equations (2.17) to (2.20) are then used to derive the scattering coefficients.

For the second method, an effective homogeneous medium is also defined with the effective wavenumbers and impedances previously calculated. As illustrated in Figure 2.3, this effective medium has the same length L as the multilayered medium. Reflection and transmission coefficients are obtained from the transfer matrix $\mathbf{M}_{e_L}$ of the one-layer effective medium. Scattering coefficients are calculated for a length of $5 \times L_u$, for each of the unit versions (a) to (d), considering $\eta = 2\%$ for the silicone. Results are shown in Figure 2.9.

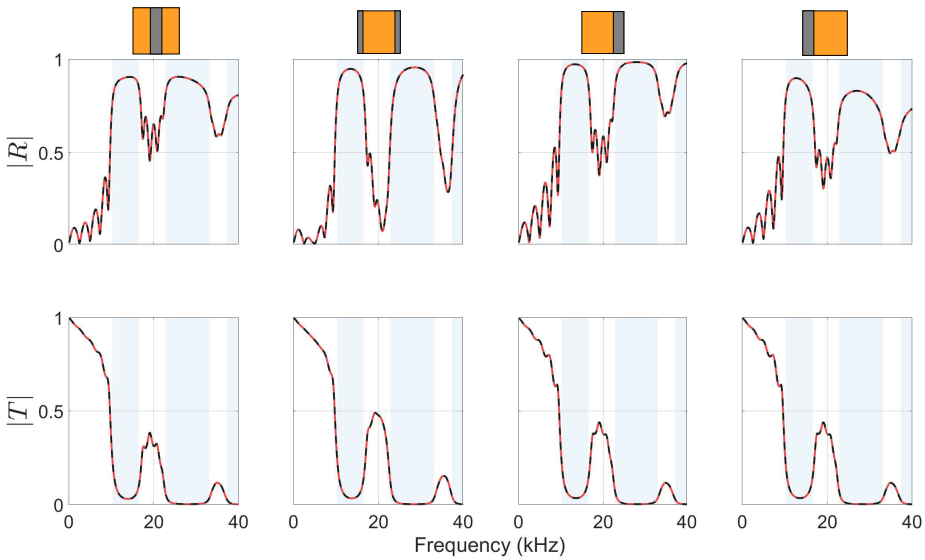

Figure 2.9 – Coefficients $R = S_{11}$ and $T = S_{12} = S_{21}$ of the four unit designs in Figure 2.4, obtained from the total transfer matrix for 5 unit cells (red lines) and from the effective media (black lines). The shaded areas represent the band gaps obtained with zero damping for silicone.

For all versions, the scattering coefficients of the effective medium (black lines) lead to the exact same reflection and transmission coefficients of the multilayered medium (red lines). The same observation has been made for larger structures, although results are not presented here to avoid repetition. As such, for these multilayered designs, the homogenisation approach introduced here is exact and multilayered media can therefore be accurately replaced by an effective medium to obtain the scattering coefficients using either a fluid or Willis fluid homogenisation model. In Figure 2.9, it can also be seen that the reflection and transmission coefficients differ depending on the unit cell, since the first layer is different. For better comparison, the coefficients are superimposed in Figure 2.10.

The transmission coefficient obtained for unit (c) is the same as that of unit (d), which is consistent with the equality $S_{12} = S_{21}$ as unit (c) is the reverse design of unit (d), and vice-versa. It is also observed that the reflection coefficient for the medium made of unit (b) is very low within the pass bands, even though this medium starts with a thin layer of aluminium.

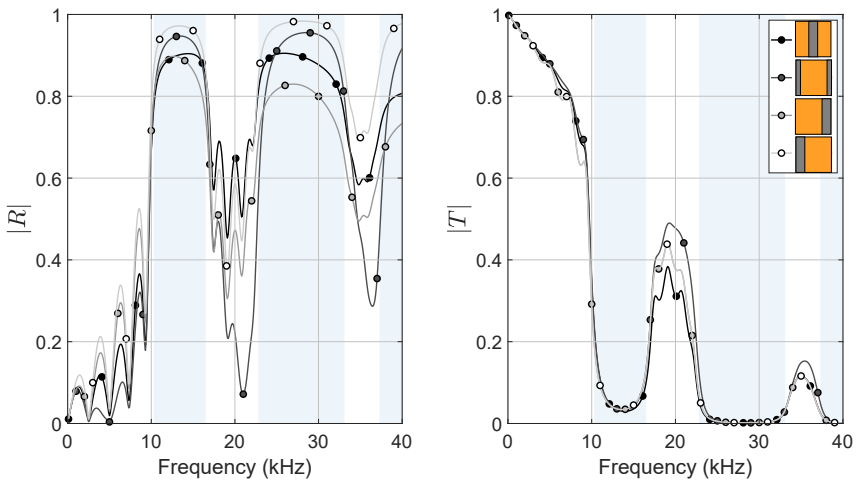

Figure 2.10 – Reflection and transmission coefficients of the forward scattering coefficients $R = S_{11}$ and $T = S_{12} = S_{21}$ obtained for the four unit designs of Figure 2.4.

These four versions of the multilayered medium are also compared for an increasing number of units in Figure 2.11 for the reflection coefficient and in Figure 2.12 for the transmission coefficient.

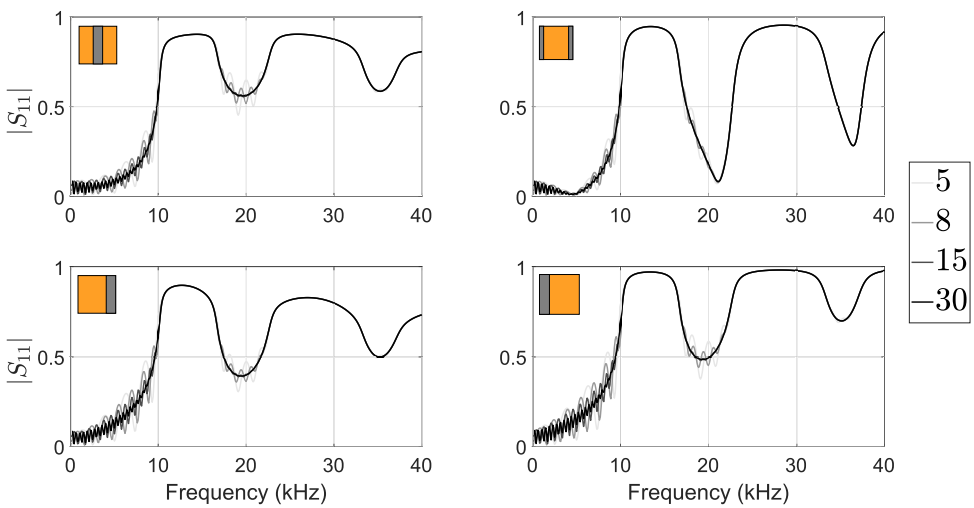

Figure 2.11 – Reflection coefficients $R = S_{11}$ for media comprising 5, 8, 15 or 30 units.

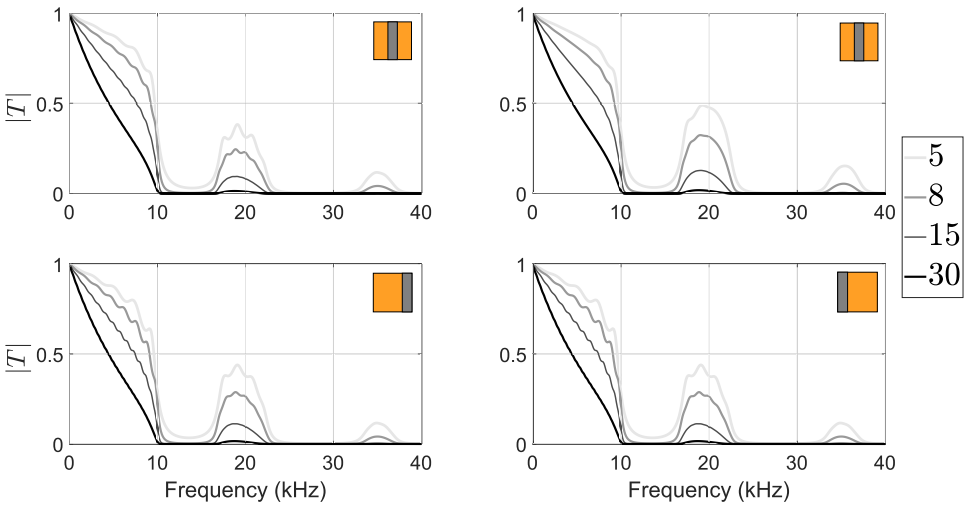

Figure 2.12 – Transmission coefficients T for media comprising 5, 8, 15 or 30 units.

There are very little changes in the reflection coefficient depending on the number of unit cells, and they are mostly found in the pass bands, where oscillations correspond to slack resonances. It shows that the reflection coefficient is mainly determined by the first unit. On the contrary, the transmission coefficient is significantly different depending on the number of unit cells, especially within the pass bands. The band gaps, associated to low transmission, are visible from 5 unit cells and are clearly defined for 8 unit cells and above.

2.6 Summary

In this chapter, a method has been presented to replace a given periodic multilayered medium by an equivalent homogeneous medium. The effective parameters that characterise the effective medium are obtained from the transfer matrix of the periodic unit. Two cases have been distinguished depending on the symmetry of the unit. If the unit is symmetric, the effective medium is assumed to be a fluid. For an asymmetric unit cell, the effective medium is a Willis fluid medium, characterised by impedances specific to forward and backward propagating waves, or by a characteristic impedance and an asymmetry coefficient.

The homogenisation approach has been applied to four variant designs of an unit cell. The effective medium approach leads to the effective wavenumber, identical for all variants, which gives the frequency ranges where wave propagation is strongly attenuated. The effective impedance highlights the necessity to adopt an homogenisation model that can describe an asymmetric structure. Effective density and effective bulk modulus have also been obtained and exhibit some of the specific features of metamaterials, that is, negative values of their real parts in some frequency bands. Effective parameters have been validated at low frequencies using a quasi-static approach.

It was also shown that the effective medium accurately predicts the reflection and transmission coefficients of a multilayered medium of any length multiple of the unit cell thickness. It is found that the scattering coefficients are noticeably different depending on the variant design chosen for the unit cell. Acoustic performance for increasing number of units has also been shown. As expected, it was observed that the reflection coefficient is mostly defined by the first unit.

Chapter 3

Optimisation

In this chapter, layer arrangements of one-dimensional multilayered structures are optimised to improve their broadband acoustic performance. The calculation of the acoustic performance is based on the transfer matrix approach introduced in Chapter 2. The controlled elitist genetic algorithm that has been implemented is first presented. It is then applied in order to improve (1) anechoic performance, (2) hull decoupling performance and (3) both coefficients. Selected designs are further investigated in order to draw out specific performance patterns.

Contents

3.1 Presentation of the Optimisation Approach 56

3.1.1 Introduction 56

3.1.2 Methodology 57

3.1.3 Algorithm 57

3.2 Results for Anechoism 61

3.2.1 Objective Functions 61

3.2.2 Validation 62

3.2.3 Results 64

3.3 Results for Hull Decoupling 68

3.4 Results for Anechoism and Hull Decoupling 71

3.4.1 Objective Functions 71

3.4.2 Results 71

3.5 Summary 74

3.1 Presentation of the Optimisation Approach

3.1.1 Introduction

The acoustic performance of any multilayered medium can be rapidly obtained using transfer matrices as presented in Chapter 2. As such, it is worth using this approach to optimise the layer arrangement of multilayered media. The figures of merit are the anechoism coefficient (Section 3.2), the hull decoupling coefficient (Section 3.3) and both coefficients combined (Section 3.4). The main objective of the optimisation study is to broaden the frequency range of effective acoustic performance through the layer arrangement. It may be found that non-periodic media, multi-periodic media or gradual media help reduce these coefficients better than an usual periodic medium.

For the layer optimisation in this Chapter, only two materials are considered : stainless steel or polyurethane with micro-balloons. The mass density for stainless steel is 7700 kg.m^{-3} and the longitudinal speed of sound is 5800 m.s^{-1}. Micro-balloons are introduced into a polyurethane matrix in order to tune the longitudinal speed of sound as needed. In particular, it is possible to obtain a lower speed of sound and a greater damping loss factor in matrices where the damping loss factor of longitudinal waves is usually very small. For the polyurethane with micro-balloons considered here, with 6% of micro-balloons, the estimated mass density is $\rho = 984$ kg.m^{-3}. The estimated speed of sound is given by $c = c_{\mathrm{L}} \times (1 + \mathrm{i}\eta)$, with the real part c_{L} and the damping η both plotted in Figure 3.1. These values have been experimentally derived as described in the following Chapter 4, for a temperature of 15°C.

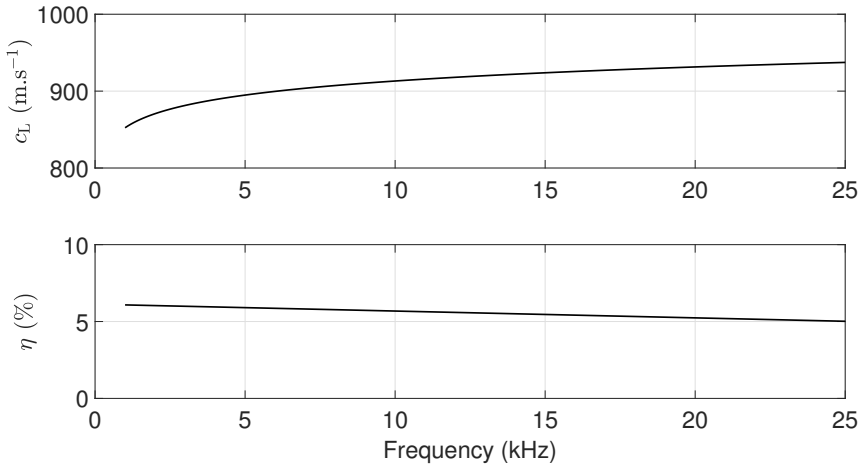

Figure 3.1 – Estimated complex speed of sound in the selected polyurethane matrix comprising 6% of micro-balloons.

Simple optimisation algorithms, such as a greedy algorithm, could thus be used for this layer optimisation. Nevertheless, the optimisation approach implemented here for multilayered media will also be applied to metamaterials with macro-inclusions using their effective properties in Chapter 7. The number of "material" possibilities will then be considerably higher than two. A controlled elitist genetic algorithm is thus selected. In what follows, the methodology to implement the optimisation problem is detailed.

3.1.2 Methodology

A genetic algorithm works on a population of individuals that are candidate solutions to an optimisation problem. These individuals are vectors made of several genes chosen amongst a set of given genes. For the present optimisation problem, the layer arrangement of multilayered media is optimised for a bi-objective function over a given frequency range. For this purpose, an individual is defined as a multilayered medium of n_l layers of thickness l, for a total length called L. For example, the multilayered configuration shown in Figure 3.2 comprises $n_l = 15$ layers, each being $l = 4$ mm-thick, for a total length of $L = 60$ mm. The algorithm selects a material from the available materials (genes) for each layer. In what follows, the various steps of the selected optimisation algorithm are presented.

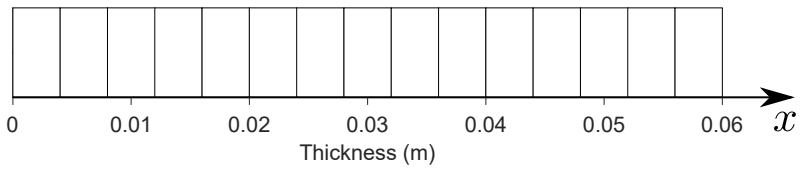

Figure 3.2 – Multilayered medium before the affectation of materials by the optimisation algorithm. Thicknesses are displayed in meters. The acoustic wave is incident on the face $x = 0$ whereas $x = 0.06$ corresponds to the transmission side. For the calculation of both the anechoism and hull decoupling coefficients, the hull is considered at on the right-hand side.

3.1.3 Algorithm

A controlled elitist genetic algorithm, variant of NSGA-II [115], is used through the MATLAB Global Optimization Toolbox. The search method operates on a population of potential solutions applying the principle of survival of the fittest to produce better individuals. At each generation, a new population is created by the process of selecting individuals according to their figures of merit and they are bred together using operators borrowed from natural genetics, such as selection, recombination and mutation. The bi-objective optimisation problem usually has no unique solution but a set of non-dominated solutions known as the Pareto-optimal set. The later is the result of a non-dominated ranking approach as illustrated in Figure 3.3, in which an individual i dominates an individual j if i is strictly better than j for at least one objective function and i is no worse than j for both objective functions. It is also possible to say that j is dominated by i or that i has a lower rank than j. As such, two individuals have the same rank if neither

dominates the other. The Pareto-front is defined as the group of best fit solutions, with the lowest rank.

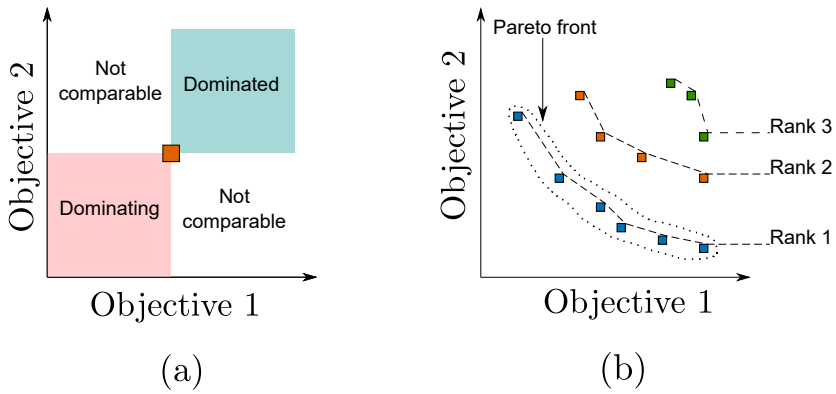

Figure 3.3 – (a) Schematic diagram showing how a solution divides the objective space into four quadrants for the non-dominated ranking approach. (b) Illustration of the Pareto front according to the non-dominated ranking system.

An elitist genetic algorithm always favors individuals with better fitness value (rank), whereas a controlled elitist genetic algorithm also favors individuals that can help increase the diversity of the population even if they have a lower fitness value. It is very important to maintain the diversity of the population in order to converge to an optimal Pareto front. Hence, to compute the next generation of the population, the non-dominated ranking system is used in the current generation. Individuals with equal rank are then compared using a crowding distance measure of individuals, that calculates the distance between the neighboring solution in order to help maintain diversity on a front by favoring individuals that are relatively far away from each other. As such, solutions are sorted according to the definition [115] : Solution i is better than solution j if $(i_{rank} < j_{rank})$ or $((i_{rank} = j_{rank})$ and $(i_{distance} > j_{distance}))$.

The optimisation process is detailed in what follows and illustrated on Figure 3.4 and described in what follows.

- (1) The algorithm randomly generates individuals to create the initial population, whose size N is fixed.
- (2) The optimisation process starts with the parents selection for the next generation. The set of parents is then transformed by means of two genetic transformations: crossover or mutation. A percentage of $C_{\%}$ of children is created by crossover and $(100 - C_{\%})$ is the result of mutation. Hence, in order to create the same amount of children than the number of individuals in the current population, the set of parents must contain $N \times (100 + C_{\%})$ individuals. For the parents' selection, a binary tournament is used, which chooses each parent by choosing two individuals at random and then choosing the best individual out of that set to be a parent.

- (3) Crossover operates on a pair of parents to produce new children by exchanging segments from the parents' vectors. In this work, the two-point crossover approach is used. The latter approach randomly generates two integers that will define segments within the pair of parents. The algorithm then concatenates these genes to form a single individual. In the case of mutation, a process comprised of two steps is applied. First, the algorithm selects a fraction of the vector entries of an individual for mutation, where each entry has a probability m of being mutated. In the second step, the algorithm replaces each selected entry by a random number selected uniformly from the range for that entry.

- (4) Those children created by crossover and mutation are then combined with the set of parents, resulting in a recombination of N_p individuals.

- (5) Each individual is then evaluated for both objective functions in order to establish the non-dominating ranking.

- (6) The choice of the individuals transferred into the next generation follows a controlled selection. The latter consists in restricting the number of individuals in the current best non-dominated rank and in maintaining a predefined distribution of individual numbers in each front. From the first rank, a ratio r_1 of the population N_p is kept and transferred into the next generation. For higher fronts, the maximum number of individuals n_i that can be retained from the front i is:

$$n_i = N_\mathrm{p} \frac{1-r}{1-r^K} r^{i-1}, \tag{3.1}$$

with K being the number of non-dominated fronts in the combined population of N_p individuals ($K = 4$ in the flow chart in Figure 3.4) and r is the geometric progression ratio, whose value is kept constant and equal 0.8. Therefore, the number of solutions kept in each front is exponentially reduced, so that solutions from all non-dominated fronts are forced to co-exist in the population.

- (7) The new generation is finally evaluated and repeats the entire optimisation process until the stopping criterion is met. Herein, the optimisation process stops when the maximum number of generations G_max is reached.

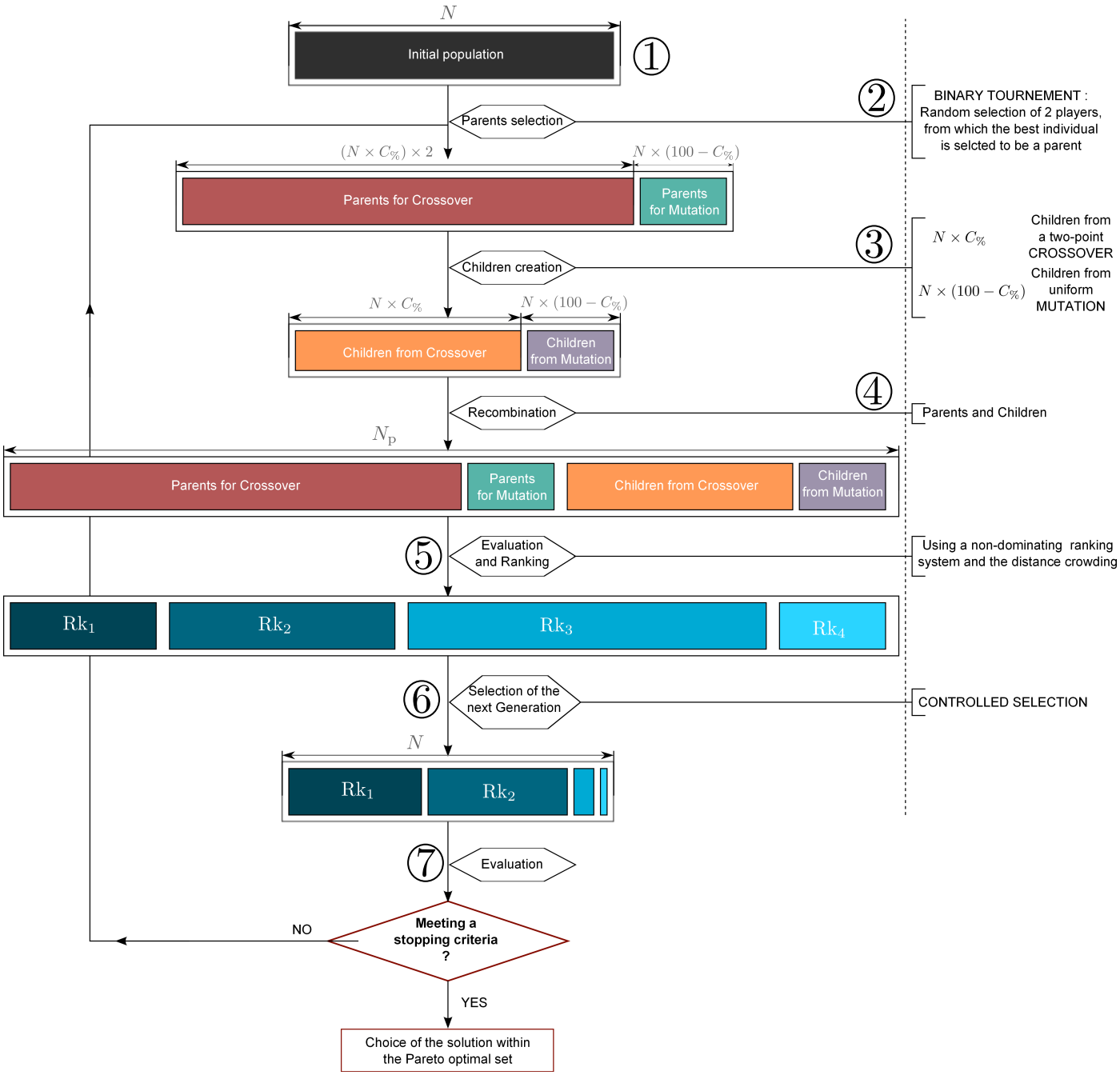

Figure 3.4 – Flow Chart for the Controlled Elitist Genetic Algorithm.

3.2 Results for Anechoism

3.2.1 Objective Functions

The optimisation process is first applied to minimise the anechoism coefficient C_A, given by:

$$C_A = S_{11} - \frac{S_{21}S_{12}}{S_{22} - 1}. \tag{3.2}$$

This expression is derived in Appendix C. The S-parameters of the entire multilayered medium are calculated using the transfer matrix method considering a water environment.

A bi-objective function is implemented in order to minimise the anechoism coefficient C_A over a finite number of frequencies n_{F}, each frequency f of the frequency range being indexed by i_{F}. The first component of the objective function aims to minimise the Root Mean Square (RMS) of the anechoism coefficient, referred to as $\overline{|C_A|}$ and given by:

$$\overline{|C_A|} = \sqrt{\frac{1}{n_{\mathrm{F}}} \sum_{i_{\mathrm{F}}=1}^{n_{\mathrm{F}}} |C_A(f(i_{\mathrm{F}}))|^2}. \tag{3.3}$$

This first objective function aims to reduce the values of the anechoism coefficient. The anechoism coefficient must also remain low over the entire frequency range of study and not only for narrow frequency ranges. The anechoism coefficient may indeed be very low for some specific frequencies, which would give a satisfactory $\overline{|C_A|}$, but that does not prevent the anechoism coefficient to be relatively high elsewhere, as illustrated in Figure 3.5.

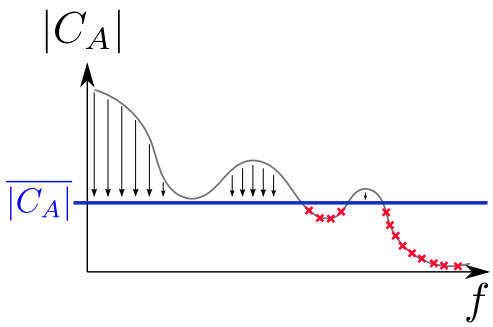

Figure 3.5 – Anechoism coefficient as function of frequency f, for which the root mean square, being the first objective function, is given by $\overline{|C_A|}$. The second objective function, σ_{C_A}, aims at lowering the values of the coefficient that are higher than $\overline{|C_A|}$, as shown by the downwards arrows. Values lower than $\overline{|C_A|}$, highlighted by the red crosses, are thus not considered.

Therefore, in order to avoid high peaks of the anechoism coefficient, a standard deviation is implemented for the second objective function. The standard deviation is customised

slightly, as values below $\overline{|C_A|}$ are replaced by $\overline{|C_A|}$ in order to cancel their effects in the standard deviation calculation. The reason for this manipulation is that it is acceptable to obtain values lower than $\overline{|C_A|}$ as it corresponds to better performance. The standard deviation is then normalised to reduce the effects of the values themselves, so that each deviation has the same weight in the minimisation process. Therefore, an intermediate function t_{C_A} is considered for each frequency $f(i_\mathrm{F})$, defined as:

$$t_{C_A}(f(i_\mathrm{F})) = \begin{cases} \overline{|C_A|} \text{ if } |C_A(f(i_\mathrm{F}))| < \overline{|C_A|} \\ |C_A(f(i_\mathrm{F}))| \text{ if } |C_A(f(i_\mathrm{F}))| > \overline{|C_A|} \end{cases} . \tag{3.4}$$

Using the intermediate function t_{C_A}, the normalised standard deviation (NSD), referred to as σ_{C_A}, is then given by:

$$\sigma_{C_A} = \frac{\mathrm{RMS}(t_{C_A} - \overline{|C_A|})}{\overline{|C_A|}}. \tag{3.5}$$

3.2.2 Validation

The algorithm is first validated for a case where all possible solutions can be calculated in order to check if the optimisation algorithm converges towards the best set of solutions. The parameters for the algorithm and for the multilayered medium to be optimised are given in Table 3.1. Six sets of parameters have been defined, where Set 1 is used for reference. In Sets 2 to 6, one parameter differs compared to Set 1 in order to assess its influence on the results. As such, using the notations in Figure 3.4, Set 2 is used to assess the influence of parameter N, Set 3 for $C_\%$, Set 4 for m, Set 5 for r_1, Set 6 for G_max.

Optimisation Parameter	Set 1	Set 2	Set 3	Set 4	Set 5	Set 6
Total thickness L (m)	0.06					
Layer thickness l (m)	0.004					
Number of layers n_l	15					
Frequency range (kHz)	$[3-20]$					
Population size N	150	**300**	150	150	150	150
Children created by Crossover $C_\%$ (%)	80	80	**60**	80	80	80
Children created by Mutation $100 - C_\%$ (%)	20	20	40	20	20	20
Mutation probability m	0.02	0.02	0.02	**0.005**	0.02	0.02
First rank ratio r_1	0.3	0.3	0.3	0.3	**0.5**	0.3
Maximum number of Generations G_max	300	300	300	300	300	**150**

Table 3.1 – Optimisation Parameters for the algorithm validation.

For this 15-layer configuration, there are 32768 possibilities. Scores for each one of these individuals are plotted in Figure 3.6, creating the cloud of grey dots. Scores of the Pareto front solutions are also given and are highlighted by the colored dots for sets 1 to 6.

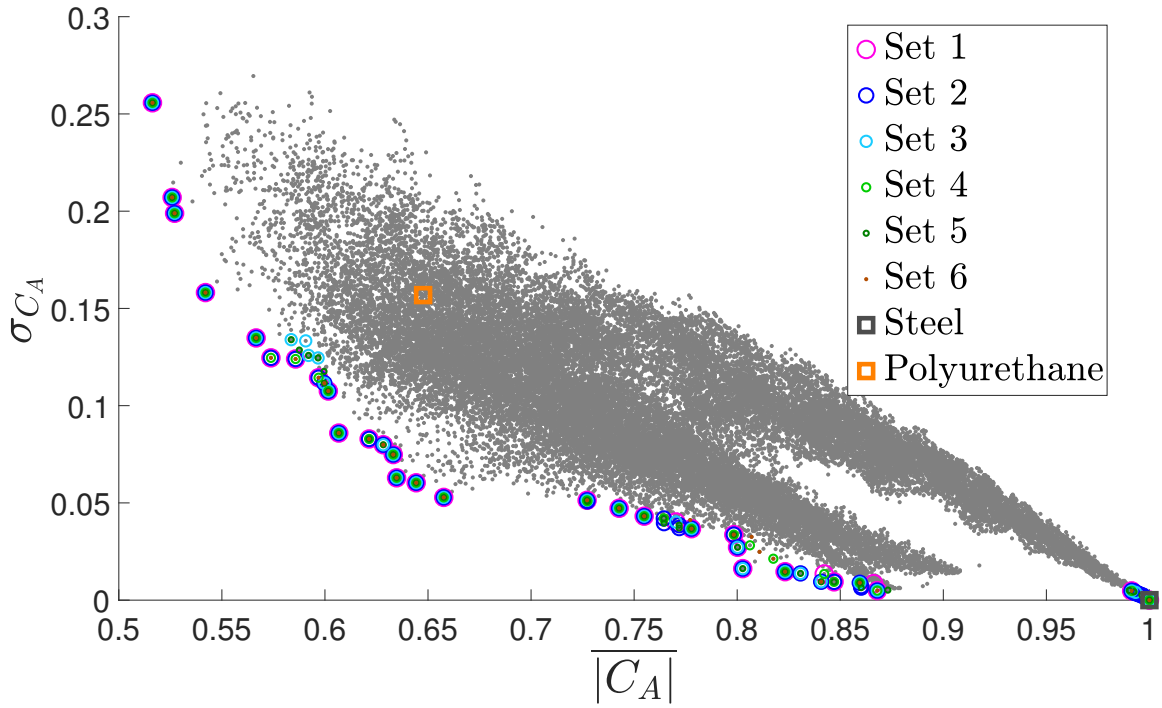

Figure 3.6 – Scores for all the possible layer arrangements for the configuration defined in Table 3.1. The colored dots represent the Pareto front for Sets 1 to 6. The orange square shows the score of a medium comprising only polyurethane layers, while the black square corresponds to the score of a stainless steel medium.

All Pareto fronts converge reasonably well towards the best solutions. Some solutions from Set 3 and Set 5 fail having the best solutions located around $\overline{|C_A|} = 0.6$. Results for Set 3 show that it is important to maintain a sufficient proportion of children created by crossover, since the rest of the children are created by mutation with a probability of 0.02. Results for Set 5 show that, when the algorithm is too elitist with $r_1 = 0.5$, then best solutions may be missing.

Around $\overline{|C_A|} = 0.8$, Set 4 and Set 6 do not lead to the absolute set of best solutions. For Set 4, mutation probability is too low, which hinders the creation of sufficiently diverse individuals. For Set 6, the maximum number of generations is relatively low, which does not guarantee the best set of solutions but still gives good results. Finally, only Set 1 and Set 2 lead to the exact set of best solutions, which shows that the parameters for Set 1 are adapted to the problem and there is no need to increase the population size.

In addition, the scores for a medium made entirely of polyurethane and for a medium entirely made of stainless steel are also visible, respectively shown by the orange and black squares. It shows that better acoustic performances are obtained by using both materials in a multilayered configuration.

3.2.3 Results

The optimisation process is now applied using parameters presented in Table 3.2. The objective here is to obtain layer arrangements that would be suitable for manufacturing and testing in a water tank. The maximum length of the medium is set to 4 cm, consisting of 40 layers.

Optimisation Parameter	Value
Total thickness	L = 0.04 m
Layer thickness	$l = 0.001$ m
Number of layers	$n_l = 40$
Frequency range	[3 kHz – 25 kHz]
Population size	$N = n_l \times 4 = 160$
Proportion of children created by Crossover	$C_{\%} = 80\%$
Proportion of children created by Mutation	$100 - C_{\%} = 20\%$
Mutation probability	$m = 0.02$
First rank ratio	$r_1 = 0.4$
Maximum number of Generations	$G_{\max} = 300$

Table 3.2 – Parameters to optimise the layer arrangement of a medium to lower the anechoism coefficient.

Figure 3.7 presents the population's scores over the generations, represented by the colored dots. The Pareto front obtained with the last generation is highlighted by the grey squares.

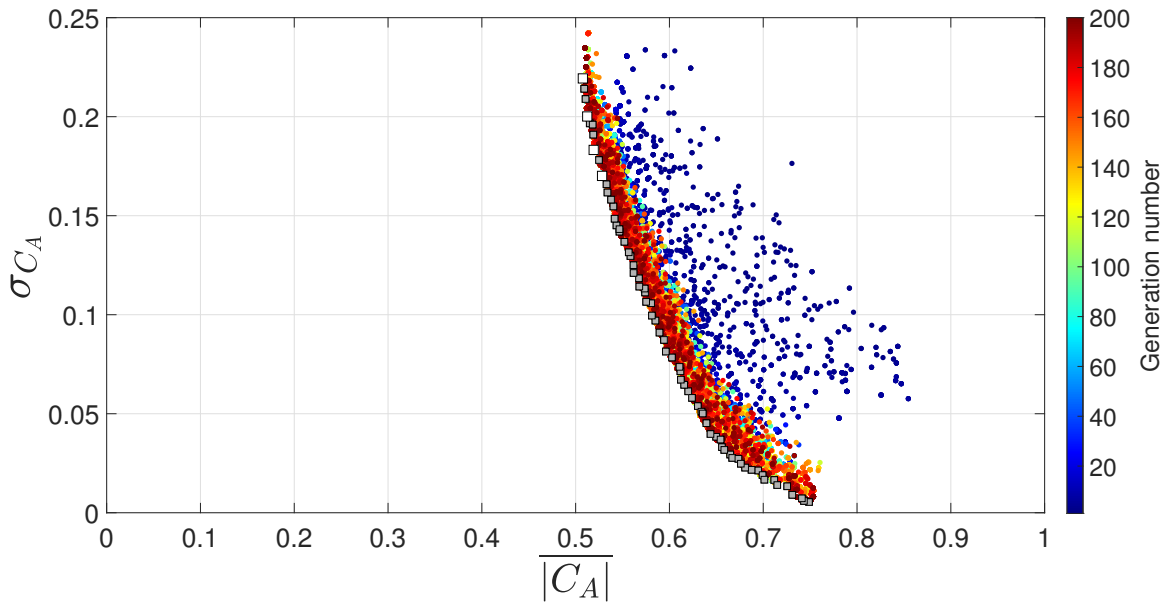

Figure 3.7 – Figures of merit for all individuals in the population, as a function of the generation number. Grey squares represent the Pareto front obtained at the last generation. White squares highlight the scores of 4 selected configurations.

The layer arrangement for each solution of the Pareto front is shown in Figure 3.8, where the orange color corresponds to polyurethane and the dark grey color to stainless steel. They are sorted from top to bottom in ascending $\overline{|C_A|}$ order. In all cases $x = 0$ corresponds to the water/metamaterial interface, and $x = 0.04$ to the metamaterial/rigid hull interface.

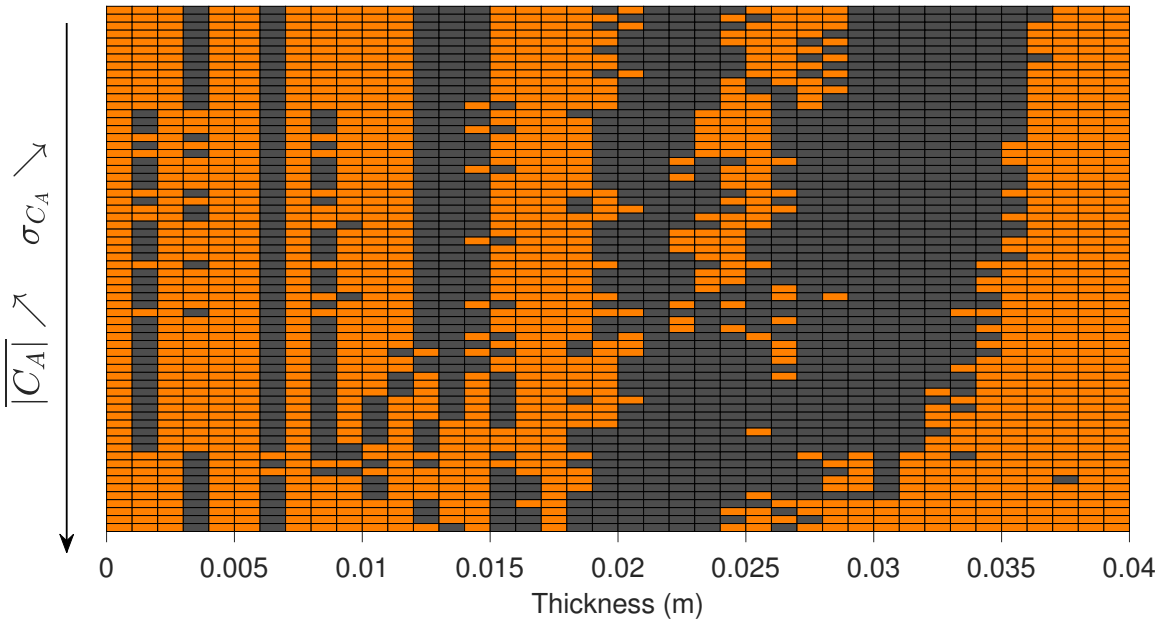

Figure 3.8 – Layer arrangement for all the solutions of the Pareto front, sorted according to decreasing σ_{C_A}, so increasing $\overline{|C_A|}$. The orange color represents polyurethane while the dark grey color corresponds to stainless steel.

In Figure 3.8, it is observed that some patterns are recurrent. For example, for the lowest values of $\overline{|C_A|}$ (i.e. arrangements at the top of the graph), there are about 11 layers, beginning and ending with a polyurethane layer. Moreover, for these arrangements, the first layer thickness is always the same, whereas the thicknesses of the other layers between $x = 0.015$ m and $x = 0.035$ m are more subject to variations. Overall, it seems that layers tend to get thicker as a function of their depth inside the arrangement, creating an impedance gradient. By going down along the Pareto front, it is then observed that the middle layers tend to disappear to form thicker layers. It can also be seen that non-periodic solutions are suitable here to minimise the anechoism coefficient on the wide frequency range, as none of these solutions is perfectly periodic.

Four of these arrangements are now selected for further investigation. After analysis of the solutions of the Pareto front, low values of $\overline{|C_A|}$ were preferred since these solutions do not show significant peaks. Their scores are shown by the white squares in Figure 3.7.

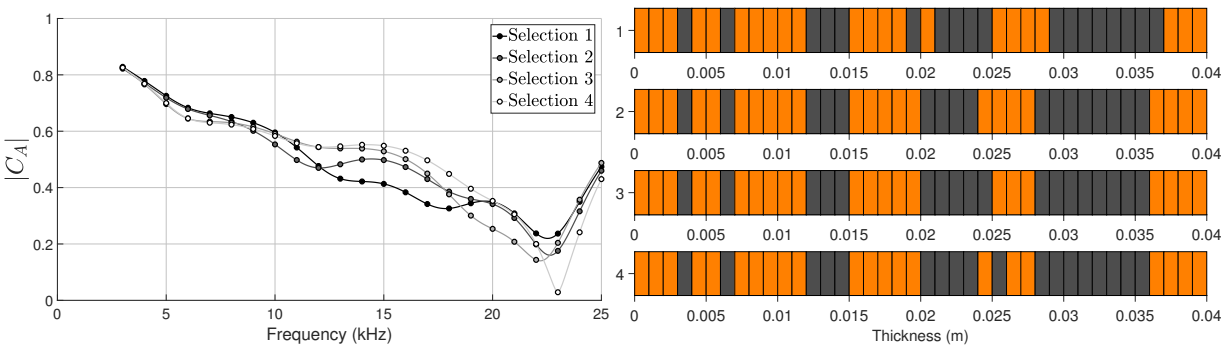

Figure 3.9 – Anechoism coefficient (left) and layer arrangement (right) for four selected solutions of the Pareto front.

For the four selected configurations, the anechoism coefficient as well as the layer arrangement are presented in Figure 3.9. Selection 4 corresponds to the configuration with the highest $\overline{|C_A|}$ from the selection and Selection 1 has the lowest $\overline{|C_A|}$, so the selection follows the Pareto front downward. Selection 1 gives a low anechoism coefficient from 12 kHz, but also have the highest values of $|C_A|$ for the lower frequencies. Selection 2 thus appears as a good compromise for low $\overline{|C_A|}$ for most frequencies and it is thus selected for measurements in a water tank. Moreover, this selection also has the advantage of being made of "thick layers", that is to say it does not include a polyurethane layer which is less than 2 millimetre thick which would be difficult to manufacture.

Selection 2 is now further analysed in order to determine features that make a medium satisfy both objective functions. As previously mentioned, most arrangements of the Pareto front are made of layers with gradually increasing average density as a function of depth inside the arrangement, just as a medium with gradient impedance. This feature can be observed with the moving average μ_{mov} of the individual layers' impedances, calculated along the medium's thickness. The average is realised on a maximum of 10 successive layers of minimal thickness l. It is represented as a function of the thickness in Figure 3.10, for the frequency 22.5 kHz since it corresponds to the frequency of lowest $|C_A|$.

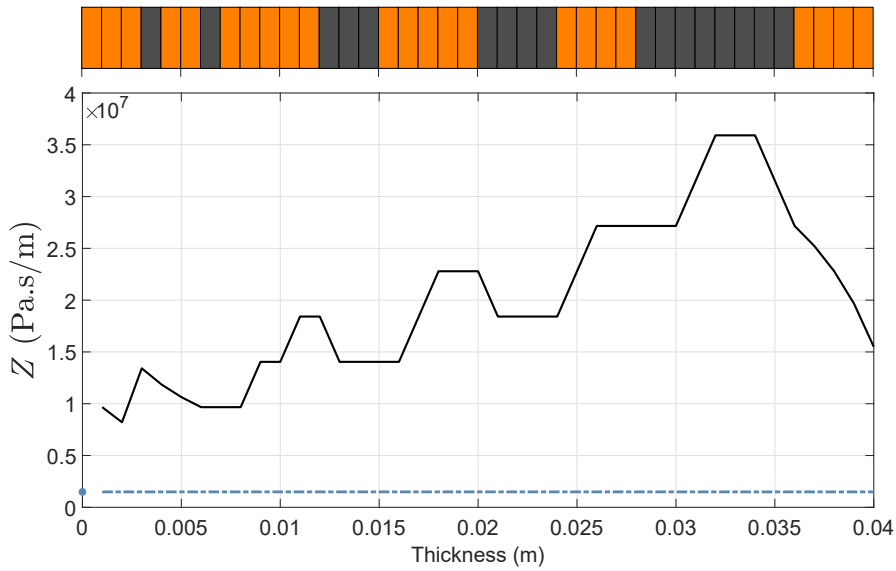

Figure 3.10 – Layer arrangement selected moving average μ_{mov} of the individual layers' impedances, calculated along the medium's thickness. The impedance of water is shown by the blue dotted line.

To summarise this optimisation for the anechoism coefficient, the optimisation algorithm was first validated, then applied to a case with more variables. The goal was to lower the mean of the anechoism coefficient (using $\overline{|C_A|}$) and keep its values low (using σ_{C_A}) over the frequency range of study. A design has been selected (Selection 2) for manufacturing and it will be measured in the next Chapter. A performance feature has also been found, which links the low anechoism coefficient to a specific impedance pattern.

3.3 Results for Hull Decoupling

The hull decoupling performance is optimised for a multilayered medium considering the exact same objective functions as for the anechoic performance, defined in Section 3.2.1. Equations (3.3) and (3.5) are thus used replacing C_A by C_D. The root mean square of the hull decoupling coefficient and the normalised standard deviation to this value are calculated. The hull decoupling coefficient is given by :

$$|C_D| = \frac{S_{12}}{-S_{22}+1}. \tag{3.6}$$

This expression is derived in Appendix C. The optimisation process is applied taking into account the same parameters as previously, displayed in Table 3.2, aiming to define a layer arrangement that would give a low hull decoupling coefficient over the frequency range from 3 kHz to 25 kHz.

Figure 3.11 presents the population's scores over the generations, represented by the colored dots. The Pareto front obtained with this last generation is highlighted by the grey squares. The layer arrangement for each solution of the Pareto front is shown in Figure 3.12, where the orange color corresponds to polyurethane and the dark grey color to stainless steel. The solutions are sorted from top to bottom in ascending $\overline{|C_D|}$ order. In all cases $x = 0$ corresponds to the water/metamaterial interface, and $x = 0.04$ to the metamaterial/rigid hull interface.

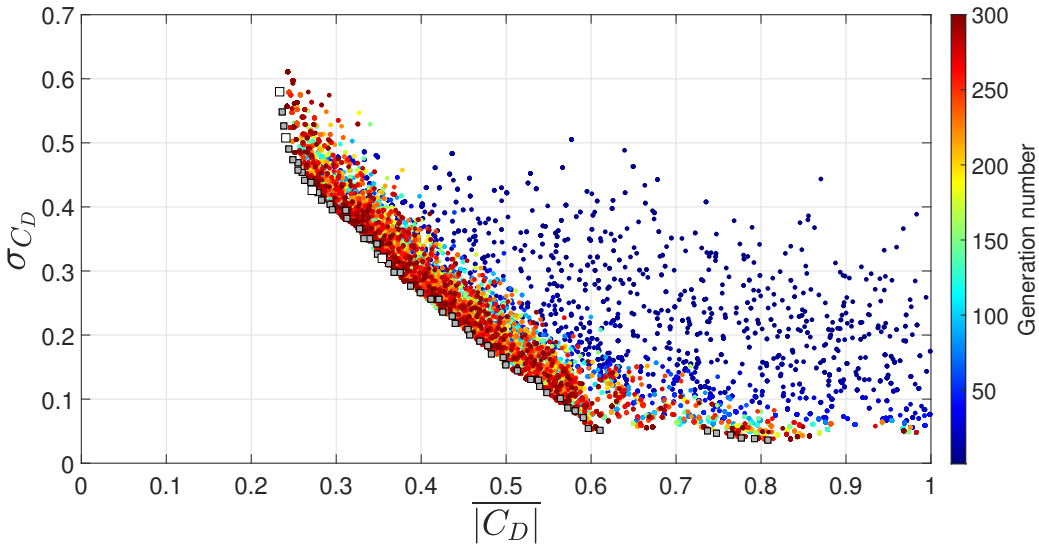

Figure 3.11 – Figures of merit for all individuals in the population, as a function of the generation number. Grey squares represent the Pareto front obtained at the last generation. White squares are the scores for a selection of four configurations.

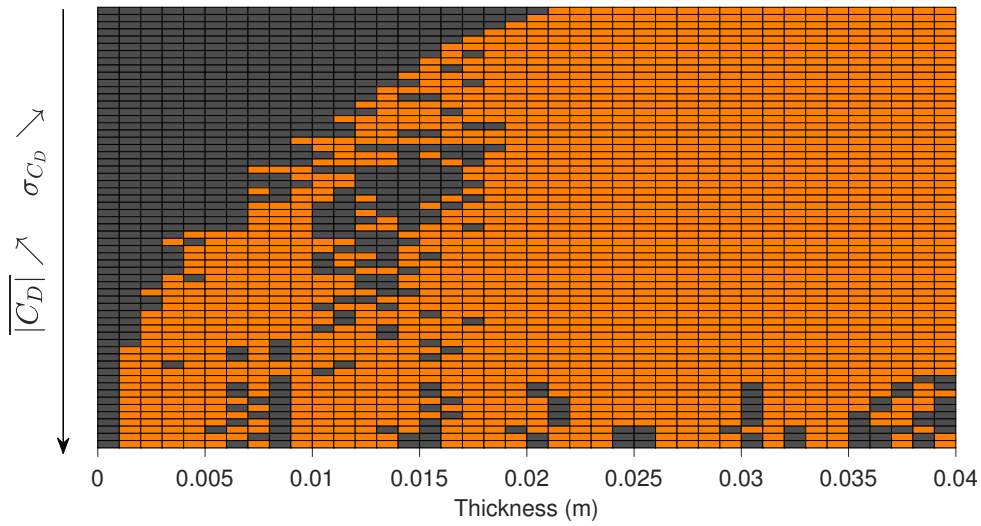

Figure 3.12 – Layer arrangement for all the solutions of the Pareto front, arranged according to decreasing σ_{C_D}, so increasing $\overline{|C_D|}$. The orange color represents the polyurethane while the dark grey color corresponds to the stainless steel.

In Figure 3.12, it can be seen that the first solutions are mostly made of two layers : one layer of stainless steel first, followed by one layer of polyurethane. Overall, most of the layer arrangements present a thick polyurethane layer to be placed on the vibrating hull. Four of these arrangements are now selected for further investigations. The scores of this selection are highlighted by the white squares in Figure 3.11. For the four selected configurations, the hull decoupling coefficient as well as the layer arrangement are presented in Figure 3.13.

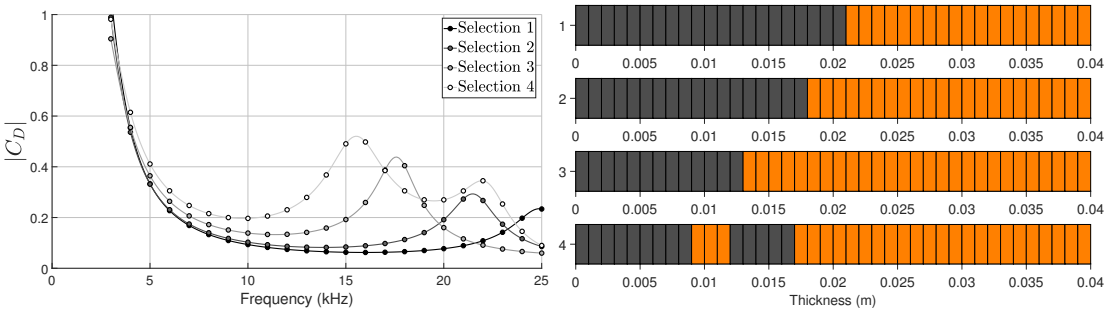

Figure 3.13 – Hull decoupling coefficient (left) and layer arrangement (right) for four selected solutions of the Pareto front.

Selection 1 corresponds to the configuration with the lowest $\overline{|C_D|}$ amongst the selected configurations, while Selection 4 has the highest $\overline{|C_D|}$. The hull decoupling coefficient is relatively similar for these four configurations. It is observed that the thickness of the two layers actually defines peaks of the coefficient. The first selection thus is preferable as this local maximum is at the edge of the frequency range of study.

It is interesting to note that the lowest $|C_D|$ values are obtained with some of the simplest arrangements, i.e. bi-layers. The first selection is further analysed to determine the origin of its superior performance. As for the anechoism coefficient, the effective impedance as a function of thickness is determined and is given in Figure 3.14.

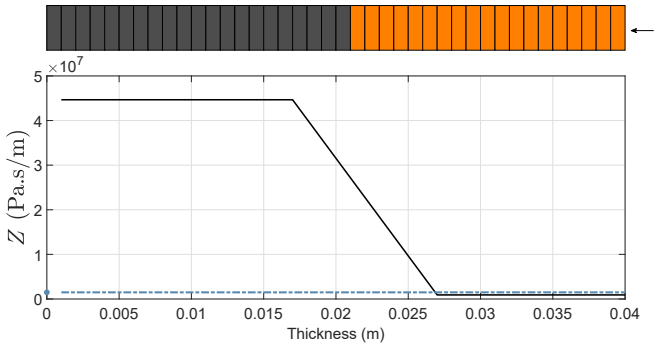

Figure 3.14 – Layer arrangement selected and moving mean μ_{mov} of the impedance. The impedance of water is shown by the blue dotted line

The moving mean μ_{mov} of the impedance simply shows an impedance break almost centred within the medium. Consequently, an efficient hull decoupling medium can be made of a thick layer of absorbing material followed by a thick layer of reflecting material. This design ensures that the waves remain trapped within the first layer, which dissipates the energy.

The optimisation study for the hull decoupling coefficient assisted in finding the impedance pattern leading to interesting performance. It is then observed that the ideal effective impedance for the hull decoupling coefficient is very different from that for the anechoism coefficient. In the next subsection, layer arrangements are optimised for both coefficients in order to analyse the evolution of the impedance patterns.

3.4 Results for Anechoism and Hull Decoupling

3.4.1 Objective Functions

The goal is herein to minimise both the anechoism and the hull decoupling coefficients so that they comply with the given required performance. For this purpose, the standard deviation functions are modified and performance levels are introduced. It is expected that the coefficients are less than 0.1, corresponding to −20dB. It should be noted that this level is arbitrary and is only given to develop and illustrate the optimisation approach. With this level requirement, the goal is now to minimise the deviation of the anechoism and hull decoupling coefficients according to the level, but only for higher values since lower values imply a better performance. As such, the first objective function is based on the normal standard deviation defined in Equation (3.5) and in Figure 3.5, but using the given level L instead of the root mean square of the coefficient. Therefore, an intermediary function l_{C_A} is considered for each frequency $f(i_\mathrm{F})$ in the frequency range of optimisation, defined as:

$$l_{C_A}(f(i_\mathrm{F})) = \begin{cases} L \text{ if } |C_A(f(i_\mathrm{F}))| < L \\ |C_A(f(i_\mathrm{F}))| \text{ if } |C_A(f(i_\mathrm{F}))| > L \end{cases} . \tag{3.7}$$

The level value is $L = 0.1$. The normalised standard deviation (NSD) according to the level requirements, referred to as $\sigma^L_{C_A}$, is then obtained with:

$$\sigma^L_{C_A} = \frac{\mathrm{RMS}(l_{C_A} - L)}{L}. \tag{3.8}$$

Hence, with this objective function, the compliance for a given acoustic performance is optimised. A similar function is considered for the hull decoupling coefficient C_D and the second objective function is therefore expressed as:

$$\sigma^L_{C_D} = \frac{\mathrm{RMS}(l_{C_D} - L)}{L}. \tag{3.9}$$

3.4.2 Results

Figure 3.15 presents the scores of the population over generations, represented by the colored dots. The Pareto front of the last generation is highlighted by the grey squares. It is observed that some of the solutions are close to level requirements for the hull decoupling coefficients since $\sigma^L_{C_D}$ reaches low values compared to $\sigma^L_{C_A}$. This observation is consistent with the two previous sections, that showed that the input parameters (materials and total length) are more suitable to the design of a hull decoupling coating than an anechoic coating.

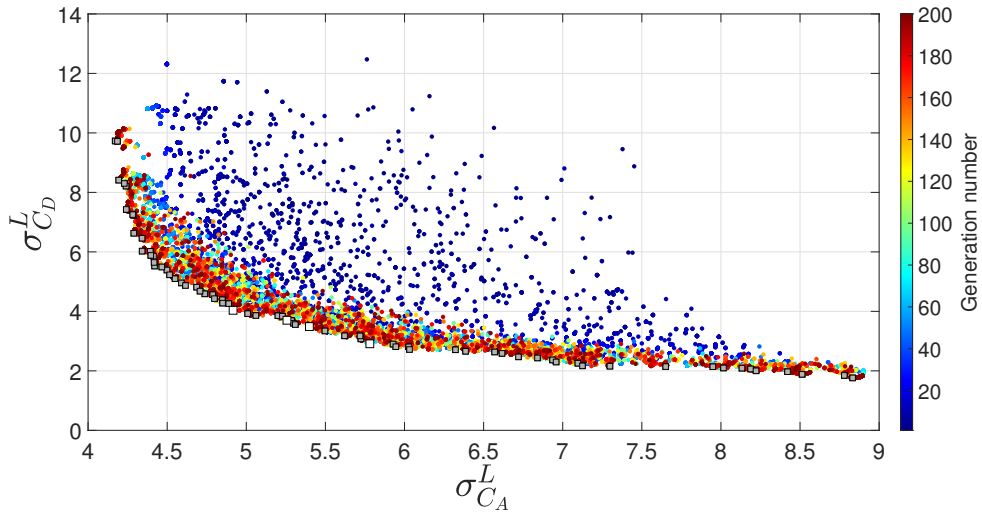

Figure 3.15 – Population's scores along generations. The grey squares represent the Pareto front obtained at the last generation, whereas the white squares are the scores of selected configurations.

All the layer arrangements of the Pareto front are given in Figure 3.16, noting that $x = 0$ corresponds to the water/coating interface, whereas $x = 0.04$ m would be the coating/hull interface. The main observations made in the two last sections are confirmed here: good anechoism performance is obtained with gradually increasing average density as a function of depth inside the arrangement, while the hull decoupling performance is better for a bi-layer design, whereby the layer at the coating/hull interface is polyurethane. As such, the layer at the interface $x = 0.04$ m tends to be thicker as the hull decoupling coefficient diminishes, so that the media comprising multiple layers converge to a 2-layer medium.

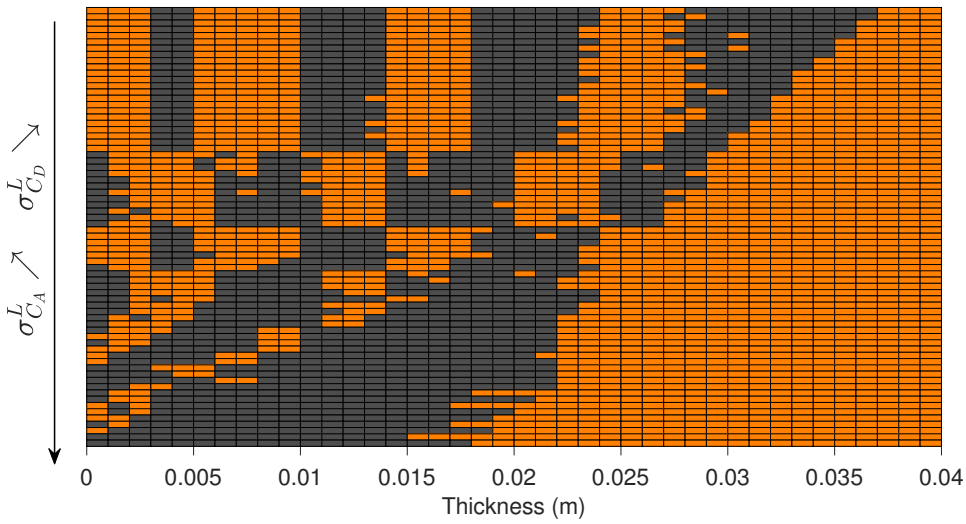

Figure 3.16 – Layer arrangements for all the solutions of the Pareto front, arranged according to decreasing $\sigma^L_{C_D}$, and thus increasing $\sigma^L_{C_A}$. The orange color represents the polyurethane while the dark grey color corresponds to the stainless steel.

Among these solutions, four configurations, presented in Figure 3.17, are selected, highlighted by the white squares in Figure 3.15. Anechoism and hull decoupling coefficients are presented in Figure 3.18.

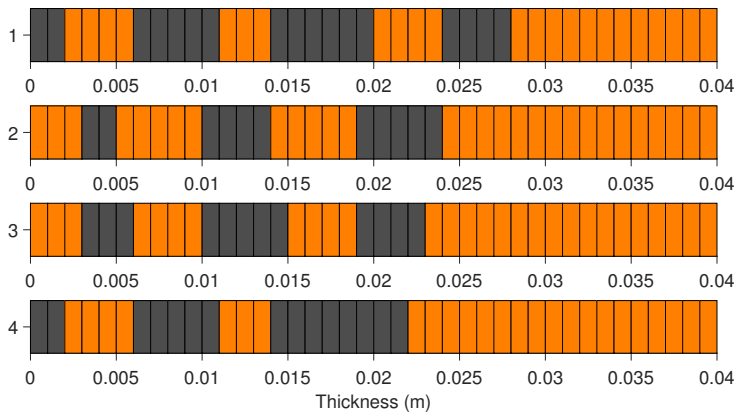

Figure 3.17 – Layer arrangement for four selected solutions of the Pareto front.

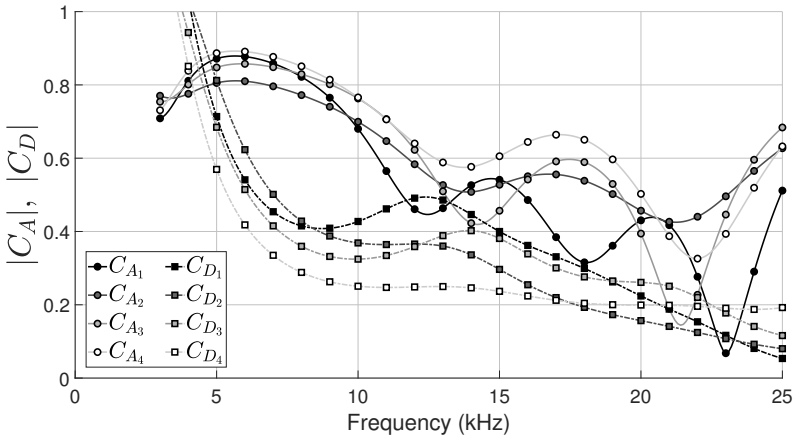

Figure 3.18 – Anechoism coefficient and hull decoupling coefficient for four selected solutions of the Pareto front.

It is observed that the anechoism coefficient at low frequency is higher than it was for its optimisation on its own, whereas the hull decoupling is higher for the entire frequency range, but remains relatively low. As such, improving the overall hull decoupling coefficient by increasing the last layer of polyurethane comes at the price of a poor anechoism performance at low frequency. The reverse observation is also verified here. Nonetheless, it is observed that both impedance patterns, associated with the anechoism coefficient and the hull decoupling coefficient are compatible.

3.5 Summary

In this chapter, an optimisation approach has been presented aiming to optimise the layer arrangement of multilayered media for the anechoic and hull decoupling performance. The optimisation algorithm has been validated on a test case.

Results were presented for the anechoic performance, which led mainly to media made of layers with gradually increasing average density as a function of depth inside the arrangement. A performance pattern has been drawn based on the effective impedance of the multilayered selection. In terms of a moving mean, a gradually increasing impedance along the medium thickness is obtained, which then drops close to the end of the medium (theoretically corresponding to the rigid end in an anechoic set up).

Results for the hull decoupling performance are simpler. It was shown that a simple bi-layer medium made of two thick layers with the soft layer placed on the hull performs best. The performance pattern for such a design shows a sudden and significant impedance change that creates strong reflection. Waves entering the coating from the soft layer are therefore trapped within this layer.

Finally, the optimisation algorithm was applied to simultaneously improve anechoism and hull decoupling figures of merit. The implemented optimisation approach thus appears as an efficient tool to optimise the layer arrangement of multilayered media for a variety of objective functions, materials and configurations.

Chapter 4

Experiments

The multilayered medium selected in Chapter 3 has been manufactured to be measured. In this chapter, a measurement method, referred to as the 3-point method, is presented and analysed. The 3-point method is first used to characterise the polyurethane comprised in the selected multilayered medium. Its effective speed of sound is experimentally retrieved from the underwater measurements. Finally, the multilayered medium is measured and experimental results are compared to the theoretical ones.

Contents

4.1 3-Point Method 76

4.1.1 Conventional Set-up 76

4.1.2 Methodology 77

4.1.3 Experimental Facilities 79

4.2 Method Validation 81

4.2.1 Application on a Test Panel 81

4.2.2 Validity Limits 85

4.2.3 Pressure Mapping 87

4.3 Experimental Speed of Sound Determination 90

4.3.1 Measurements 90

4.3.2 Retrieval Approach 1 91

4.3.3 Retrieval Approach 2 92

4.3.4 Verification 94

4.4 Multilayered Medium Measurements 95

4.4.1 Panel and Experimental Set-up 95

4.4.2 Measurements 96

4.4.3 Calculation of the Anechoism Coefficient 99

4.5 Summary 101

4.1 3-Point Method

4.1.1 Conventional Set-up

Panels are fully immersed in water and are characterised for a quasi-plane incident wavefront at normal incidence. In order to measure the acoustic pressure at a given frequency (in harmonic regime), a wave packet at the frequency of interest is used. The phase convention is $e^{\mathrm{i}(\omega t - kx)}$. One hydrophone is placed in front of the panel at position A to measure the sum of the reflected pressure p_r and the incident pressure p_i, whereas another hydrophone is located at position B behind the panel to obtain the transmitted pressure p_t, as shown in Figure 4.1.

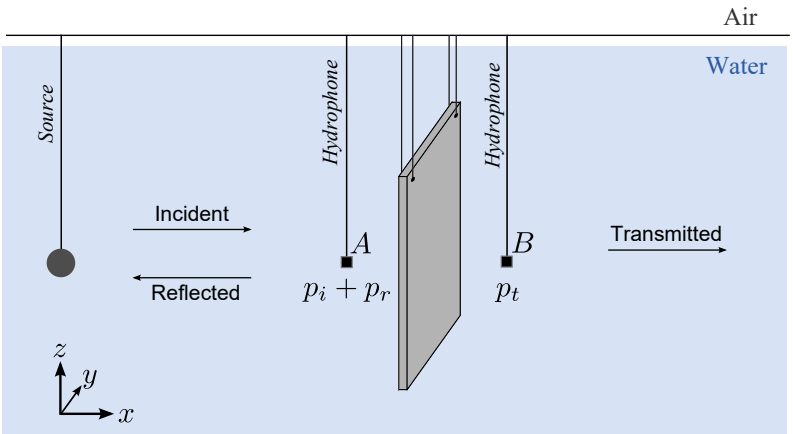

Figure 4.1 – Conventional set-up for panel measurements in an open water tank.

These pressures are used to calculate the reflection and transmission coefficients of a panel at positions A and B, as per:

$$R(A) = \frac{p_r(A)}{p_i(A)}, \tag{4.1}$$

$$T(B) = \frac{p_t(B)}{p_i(A)}. \tag{4.2}$$

A phase shift is then applied to these equations so that R corresponds to the reflection coefficient at the front face of the panel and T corresponds to the transmission coefficient between the front and the back faces, as per the two-port network configuration.

At position A, in front of the panel, it is often difficult to temporally distinguish the reflected pressure p_r from the incident pressure p_i, especially for low frequencies. The incident pressure can be obtained by measurement without the panel, or by calculation using several measurements as in the 3-point method described in this Chapter.

4.1.2 Methodology

In this section, a method is presented for acoustic panel measurements in water tanks. This method is based on a conventional measurement configuration consisting of the panel, an acoustic source and two hydrophones, one on either side of the panel. In the experimental set-up, only three different positions for the hydrophones are considered. This method, called the 3-point method, provides an estimation of the amplitude of the edge-diffracted waves as well as the amplitudes of the transmitted, reflected and incident waves. The method is detailed below, using Figure 4.2 to illustrate the experimental setup specific to the method.

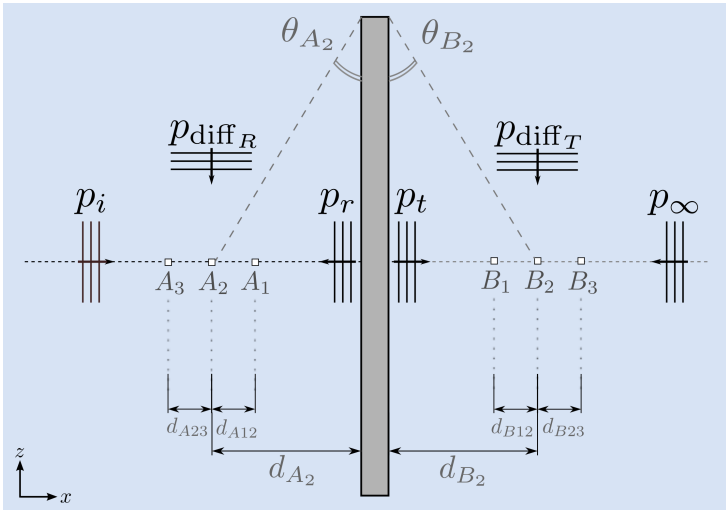

Figure 4.2 – Experimental set-up specific to the application of the 3-point method. Points A_1, A_2 and A_3 correspond to the three positions taken by the hydrophone on the reflection side, while points B_1, B_2 and B_3 are the positions of the hydrophone on the transmission side. Pressure contributions and geometric parameters are also presented.

On both sides of the panel, the total acoustic pressure is measured at three points. The 3-point method then treats the reflection and transmission sides in slightly different ways. For the determination of the reflection coefficient, the three points A_1, A_2 and A_3 are considered. The central position A_2 is taken as a reference, with the distances $d_{A12} = A_1A_2$ and $d_{A23} = A_2A_3$. At each point, the total pressure p can be expressed as a function of the contributions of the incident pressure p_i and the reflected pressure p_r at the central position as well as the diffracted pressure on the reflection side p_{diff_R}:

$$\begin{cases} p(A_1) = p_i(A_2)e^{-\mathrm{i}kd_{A12}} + p_r(A_2)e^{\mathrm{i}kd_{A12}} + p_{\mathrm{diff}_R}(A_1) \\ p(A_2) = p_i(A_2) + p_r(A_2) + p_{\mathrm{diff}_R}(A_2) \\ p(A_3) = p_i(A_2)e^{\mathrm{i}kd_{A23}} + p_r(A_2)e^{-\mathrm{i}kd_{A23}} + p_{\mathrm{diff}_R}(A_3) \end{cases} . \tag{4.3}$$

It is then assumed that the total contribution of the edge-diffracted pressure is equal at these three positions when the three points are placed close to each other on the x-axis.

To legitimise this hypothesis, the analytical model presented in Appendix D is used by comparing the edge-diffracted pressure in different positions. This hypothesis then leads to:

$$p_{\mathrm{diff}_R}(A_1) = p_{\mathrm{diff}_R}(A_2) = p_{\mathrm{diff}_R}(A_3) = p_{\mathrm{diff}_R}. \tag{4.4}$$

The system of equations given by Equation (4.3) can be simplified and written in a matrix form as follows:

$$\begin{pmatrix} p(A_1) \\ p(A_2) \\ p(A_3) \end{pmatrix} = \begin{bmatrix} e^{-\mathrm{i}kd_{A12}} & e^{\mathrm{i}kd_{A12}} & 1 \\ 1 & 1 & 1 \\ e^{\mathrm{i}kd_{A23}} & e^{-\mathrm{i}kd_{A23}} & 1 \end{bmatrix} \begin{pmatrix} p_i(A_2) \\ p_r(A_2) \\ p_{\mathrm{diff}_R} \end{pmatrix}. \tag{4.5}$$

By inverting Equation (4.5), the pressures $p_i(A_2)$, $p_r(A_2)$ and p_{diff_R} are obtained:

$$\begin{pmatrix} p_i(A_2) \\ p_r(A_2) \\ p_{\mathrm{diff}_R} \end{pmatrix} = \begin{bmatrix} e^{-\mathrm{i}kd_{A12}} & e^{\mathrm{i}kd_{A12}} & 1 \\ 1 & 1 & 1 \\ e^{\mathrm{i}kd_{A23}} & e^{-\mathrm{i}kd_{A23}} & 1 \end{bmatrix}^{-1} \begin{pmatrix} p(A_1) \\ p(A_2) \\ p(A_3) \end{pmatrix}. \tag{4.6}$$

Once the total pressures at points A_1, A_2 and A_3 are measured, the contribution of the incident, reflected and edge-diffracted pressures can be deduced using the previous system. The reflection coefficient at point A_2 is then obtained using Equation (4.1).

On the transmission side, the same approach is adopted, considering the three points B_1, B_2 and B_3 and the distances $d_{B12} = B_1B_2$ and $d_{B23} = B_2B_3$, where position B_2 is taken as the reference. In this case, the pressure field is decomposed into contributions of transmitted pressure p_t, diffracted pressure p_{diff_T} as well as pressure p_∞ called infinite pressure. The latter describes a wave coming from infinity in the direction of decreasing x. On the reflection side, this pressure would correspond to the contribution of reflected waves, but on the transmission side, only waves reflected on the water tank wall could be travelling in this direction. However, such waves are not recorded within the acquisition time window considered for the measurements. Thus, the infinite pressure is assumed to be zero. On the transmission side, the same hypothesis on the edge-diffracted pressure is used, so p_{diff_T} is also assumed to be equal for each of the three points. Total pressures at points B_1, B_2 and B_3 are therefore expressed by:

$$\begin{cases} p(B_1) = p_t(B_2)e^{\mathrm{i}kd_{B12}} + p_\infty(B_2)e^{-\mathrm{i}kd_{B12}} + p_{\mathrm{diff}_T} \\ p(B_2) = p_t(B_2) + p_\infty(B_2) + p_{\mathrm{diff}_T} \\ p(B_3) = p_t(B_2)e^{-\mathrm{i}kd_{B23}} + p_\infty(B_2)e^{\mathrm{i}kd_{B23}} + p_{\mathrm{diff}_T} \end{cases}. \tag{4.7}$$

The contributions of the transmitted, infinite and diffracted pressures are then calculated using:

$$\begin{pmatrix} p_t(B_2) \\ p_\infty(B_2) \\ p_{\mathrm{diff}_T} \end{pmatrix} = \begin{bmatrix} e^{\mathrm{i}kd_{B12}} & e^{-\mathrm{i}kd_{B12}} & 1 \\ 1 & 1 & 1 \\ e^{-\mathrm{i}kd_{B23}} & e^{\mathrm{i}kd_{B23}} & 1 \end{bmatrix}^{-1} \begin{pmatrix} p(B_1) \\ p(B_2) \\ p(B_3) \end{pmatrix}. \tag{4.8}$$

With the measurements of the total pressure at points B_1, B_2 and B_3, the contributions of the transmitted, infinite and edge-diffracted pressures can be deduced using the previous system. The transmission coefficient between A_2 and B_2 is then obtained using Equation(4.2).

4.1.3 Experimental Facilities

Measurements are conducted in a large open water tank, shown in Figure 4.3, which is 8 meters long, 6 meters wide and 7 meters deep. This facility is located in the academic laboratory ISEN, in Lille (France). An omnidirectional source is placed at a distance of approximately 3 m from the panel perpendicular to the panel surface and in its median plane. Two hydrophones are placed on either side of the panel, in symmetrical positions with respect to the central plane of the panel (parallel to its large surface). These hydrophones are fixed at the end of aluminium sections, which other end is fixed to a motor on the surface. The position of the receivers on the x-axis and y-axis can be easily modified using *Rexroth* motors able to move the sections, on which hydrophones are fixed with an accuracy of the order of one tenth of a millimetre. It is worth emphasising that such precision is valid on the surface. However, given that the hydrophones are placed about 3 meters deep, there is certainly a loss of accuracy in the position of the hydrophones in the water. Displacement along the z-axis must be done manually by changing the immersion of the panel.

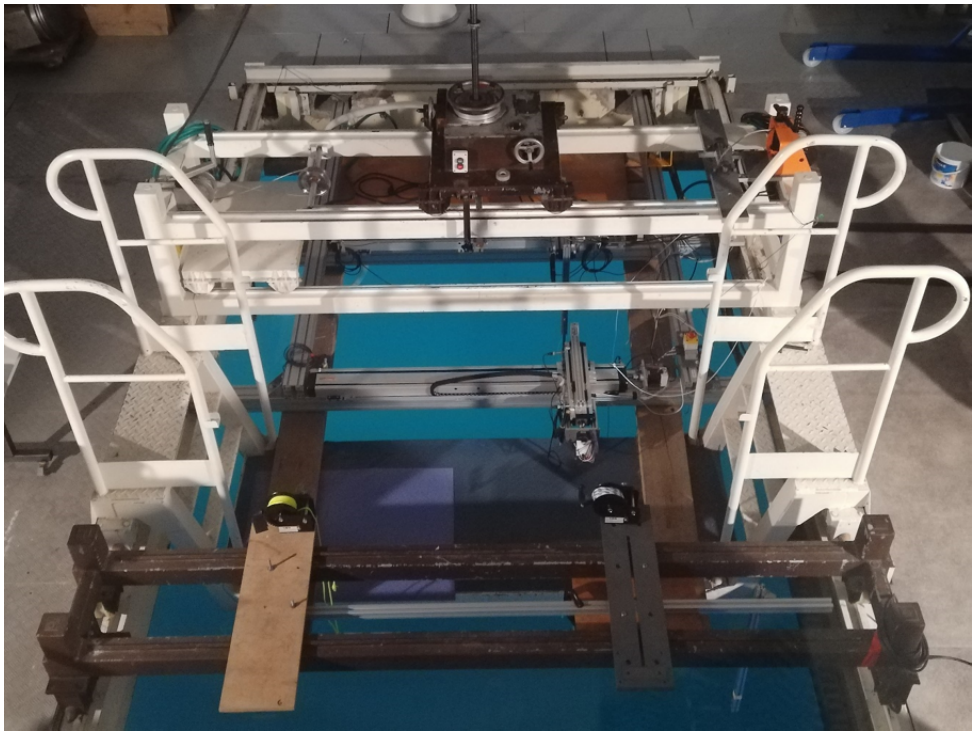

Figure 4.3 – Open Water Tank Facility of ISEN, Lille (France).

The experimental bench is fully controlled via a LabView interface, which has been coded in such a way that the user simply needs to indicate the frequency range as well as the different positions of the hydrophones along the x-axis. It is also possible to automatically change the hydrophone positions for each frequency, in order to define the distance between two positions in terms of wavelength λ instead of absolute distance.

The water temperature of 15.5°C remains stable for all measurements. Under such conditions, the speed of sound in water is estimated at 1489 m.s^{-1}.

The source emits a packet of sine waves at the frequency of interest for a duration of 2.2 ms. The signal received by each hydrophone is synchronised with this emitted signal. The signal received on each hydrophone is initially observed globally over a large time window using a conventional oscilloscope. This makes it possible to define the acquisition window to consider only the desired signals simultaneously (which will include the different pressures of interest) on each hydrophone using a picoscope. The choice of this window is made on several criteria: (1) it must be located before the reception of the own echo signals linked to the walls of the water tank, (2) it must start a little after the reception of the signal by each hydrophone once the signal is well established (without start-up bounce), and (3) it must be relatively homogeneous over the duration of the acquisition. A start of the window at 2.7 ms over a period of 1 ms is often a satisfactory setting for measurements carried out in the water tank given the classic positioning of the different elements and the size of the tank. As a result, measurements for frequencies below 3 kHz can be difficult because there is not enough level on the source side and not enough number of waves observed on the time side, before the arrival of the echoes.

Once this acquisition window is defined, the automatic acquisition program is launched and the picoscope records in this acquisition window for each hydrophone, the frequency, the modulus and the phase of the received signal. The quality of the measurement can be evaluated using the difference between the frequency measured on the hydrophones and that of the reference (imposed on the transmitter). A pre-processing step is thus always performed to check the quality of the recorded signals: pairs of positions X and frequencies f of unsteady-state signal are detected using the frequencies extracted from signals recorded in the acquisition window. When a retrieved frequency is significantly different from the reference frequency imposed on the transmitter, the pair (X, f) is not taken into account in the post-processing step.

4.2 Method Validation

4.2.1 Application on a Test Panel

The 3-point-method is applied on a reference panel made of 5083 aluminum alloy of dimensions 1 m × 1 m and of thickness 4 cm, as shown in Figure 4.4. In the water tank, the hydrophones and the projector are completely immersed to a depth of 2.73 m, corresponding to the position of the panel's center. The spherical projector is placed 2.87 m away from the panel. It is assumed that the incident wavefront is plane when it reaches the panel.

Figure 4.4 – Aluminium reference panel.

Hydrophone positions are always kept symmetrical about the panel, so notation X is used independently of the side for position $X = A$ or $X = B$. Positions of the hydrophones are given in Table 4.1. A distance of $\lambda/15$ is considered between the hydrophone positions, thus changing for each frequency within the frequency range [3 kHz − 13 kHz]. With this distance of $\lambda/15$ between the hydrophone positions, the edge-diffracted pressure level differs by less than 0.6% from one position to another, according to the analytical model in Appendix D. The configuration defined in Table 4.1 thus complies with the hypothesis

that the edge-diffracted pressure is equal in the three measurement positions, as per Equation (4.4). Moreover, with this distance, the total pressures at the three positions are sufficiently different (cf. Test 3 in 4.2.2).

d_{X_2} (cm)	$d_{X_{1,2}}$ (λ)	$d_{X_{2,3}}$ (λ)	θ (°)
8	$\lambda/15$	$\lambda/15$	9.1

Table 4.1 – Geometric parameters for validation of the 3-point method.

The total pressures recorded at the three positions on each side of the panel are plotted in Figure 4.5. As previously mentioned, the total pressure on the reflection side may reach local minima resulting from destructive interference. Pairs of positions / frequencies (X, f) that have been removed using the pre-processing step are highlighted with circles.

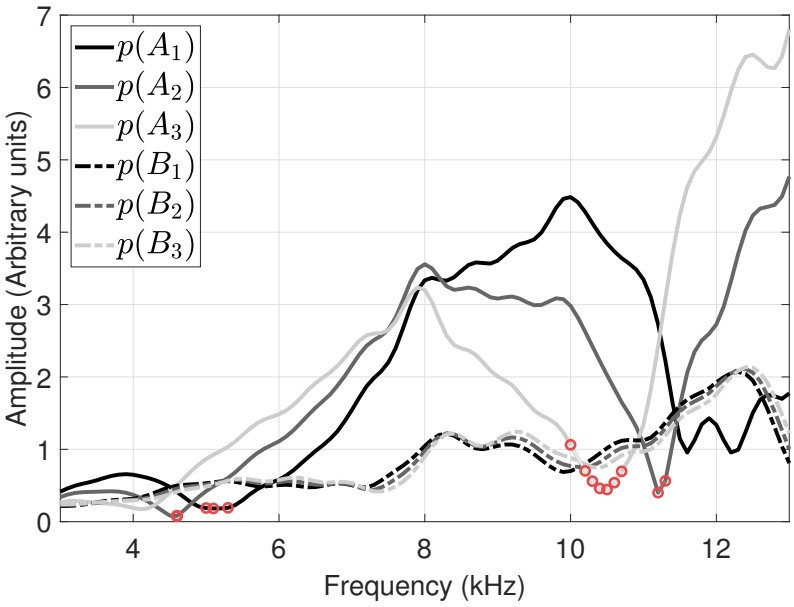

Figure 4.5 – Pressure amplitudes measured at the 3 positions A_1, A_2 and A_3 for the reflection side and at the 3 positions B_1, B_2 and B_3 for the transmission side. The circles represent (X, f) pairs of destructive interference.

On the reflection side, the total pressures are used to derive the incident pressure p_i, the reflected pressure p_r and the diffracted pressure on the reflection side p_{diff_R}. On the transmission side, the 3-point method leads to the transmitted pressure p_t as well as the diffracted pressure p_{diff_T}. Pressure p_∞ coming from infinity and travelling towards the negative x is also obtained for the transmission side. The fact that the infinite pressure must be zero can help to detect an invalid application of the method. All these deduced pressures are shown in Figure 4.6.

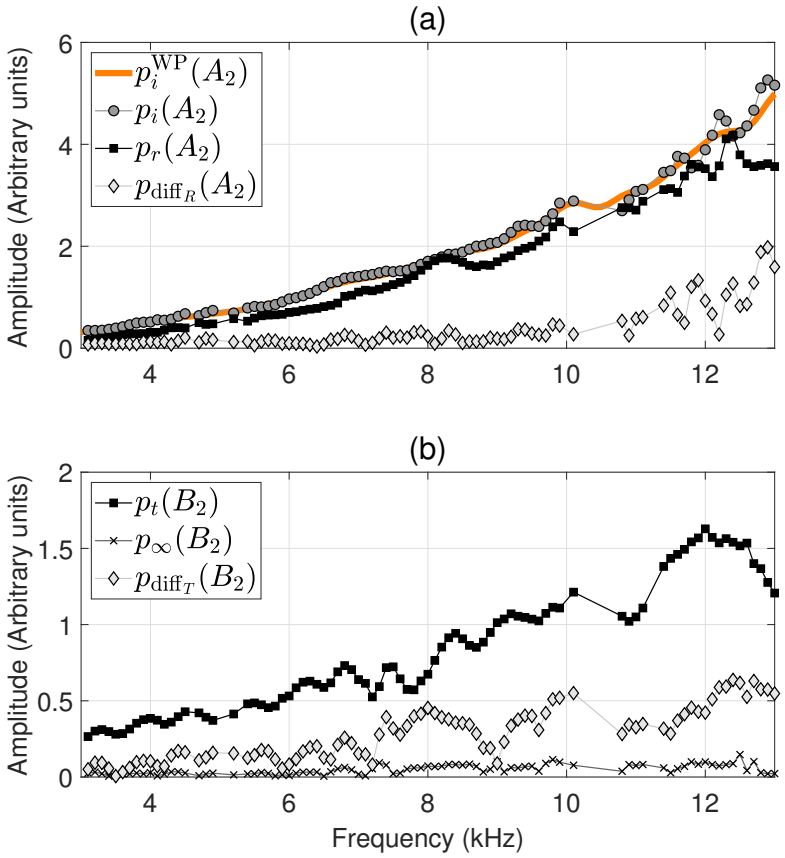

Figure 4.6 – (a) Incident pressure p_i, reflected pressure p_r and diffracted pressure p_{diff_R} at the central position A_2 on the reflection side. The incident pressure measured without panel (p_i^{WP}) is also plotted. (b) Transmitted pressure p_t, infinite pressure p_∞ and diffracted pressure p_{diff_T} at the central position B_2 on the transmission side.

The incident pressure is compared to that obtained by measurements without panel, referred to as p_i^{WP}. It can be observed that both measurements of the incident pressure with and without the panel are consistent over the whole frequency range, validating the estimation of the incident pressure provided by the 3-point method. In addition, the infinite pressure p_∞ is almost zero over the entire frequency range, which is expected when the 3-point method is valid and correctly implemented. It can also be noted that the diffracted pressure on both sides oscillates approximately between 2% and 70% of the total pressure, highlighting that the edge-diffraction effects cannot be neglected.

For comparison, the reflection and transmission coefficients can be obtained analytically for a medium of infinite lateral dimensions [116]. The material properties for aluminium are 2700 kg.m^{-3} for the mass density and 6183 m.s^{-1} for the longitudinal speed of sound. Since the 3-point method eliminates edge-diffraction contributions, the experimental coefficients can be directly compared to those of an infinite panel, as in Figure 4.7. Experimental coefficients have also been fitted to a quadratic curve. This fit weakens the few slight discrepancies which are mainly explained by the structural resonant modes of the finite panel, such as the plate bending modes [99]. Therefore, the 3-point method leads

to reflection and transmission coefficients that fit well with the ones calculated analytically for an infinite panel. Data recorded at the central position X_2 are also used to calculate the scattering coefficients, as per the direct conventional method using a single point. Results are different from the theoretical calculation, which highlights the benefit of using the 3-point method instead of direct measurements to remove the contribution of the edge-diffraction, since its effects are also strongly dependent on the hydrophone position, as shown latter in Section 4.2.3.

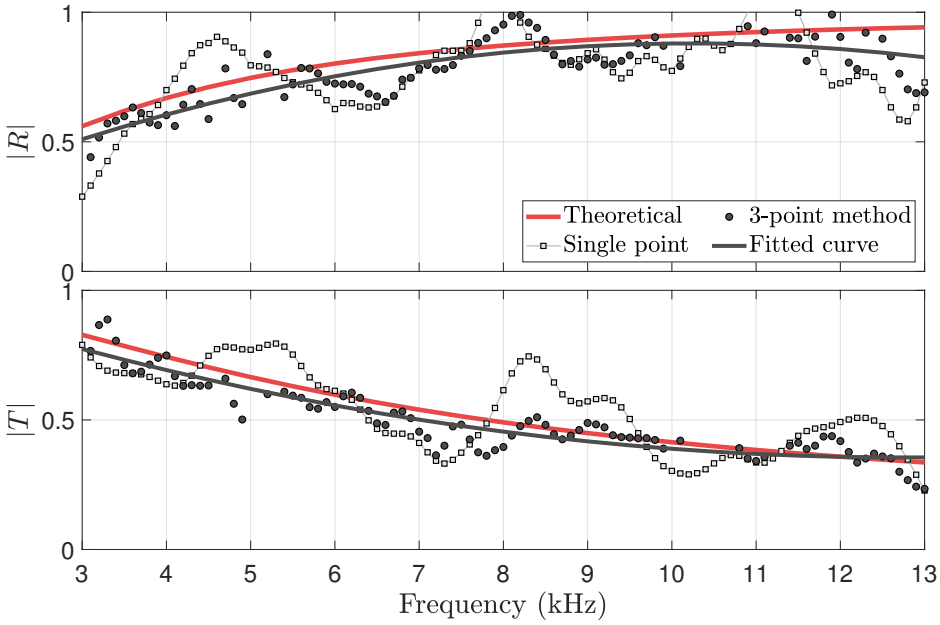

Figure 4.7 – Modulus of the reflection coefficient and the transmission coefficient obtained analytically for a panel of infinite lateral dimensions and measured with the direct single point method and with the 3-point method. Positions for the 3-point method are defined in Table 4.1 and the central position X_2 is used for the direct single point method. Results from the 3-point method are fitted to a quadratic curve.

The reflection and transmission coefficients given by the 3-point method are complex values, so their phase can be calculated. In Figure 4.8, phases of the coefficients derived from the 3-point method (dotted lines) are compared to the phases calculated theoretically. Phases obtained with the 3-point method were modified considering the distances hydrophone/panel $d_{X_2} + 2.2$cm for the reflection side and $d_{X_2} + 2.5$cm for the transmission side.. It can be seen that their variations are similar but they differ from one to another. This difference can be explain mainly by the uncertainty on the absolute position of the hydrophone relative to the panel. Indeed, as a hydrophone is fixed to a 3-meter-long section, it is unlikely that the position on the surface and in the water will be exactly the same. For instance, with a 3-meter-long section fixed at a right angle on a support, an offset of 1° of the support at the right angle would create a 5 cm displacement of the hydrophone in water. When the phase has to be shifted to the panel interface (for the calculation of the anechoism coefficient for instance) there is then a strong uncertainty

due to the lack of precision on the hydrophone/panel distance. However, it should be understood that this does not prevent the 3-point method from providing precise results (in modulus), as it only requires a relative position from one hydrophone to another and this displacement is precisely controlled by the motors.

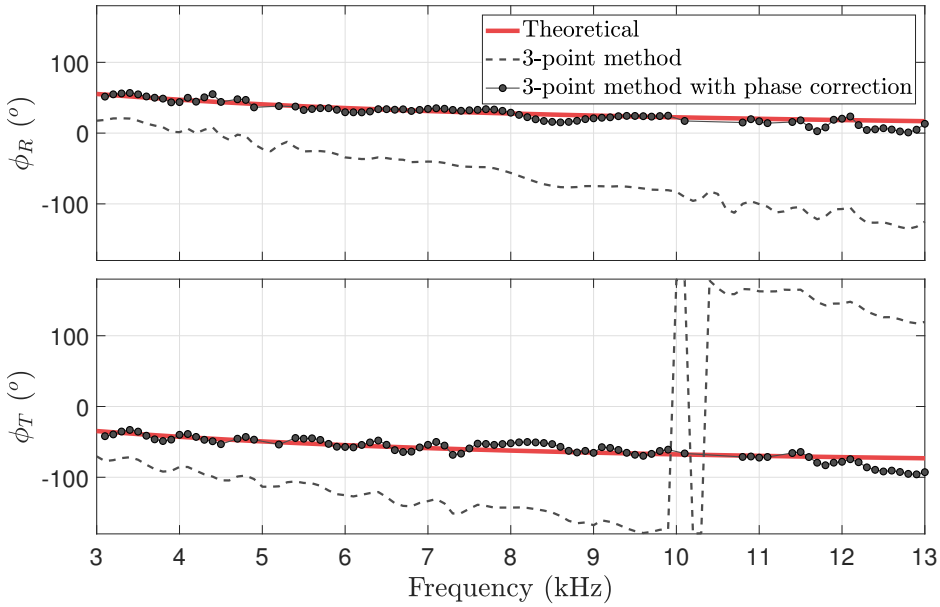

Figure 4.8 – Phase of the reflection coefficient and the transmission coefficient obtained analytically for a panel of infinite lateral dimensions and measured with the 3-point method. A distance correction is applied on the latter to retrieve the variation of the theoretical phase: Phases obtained with the 3-point method were modified considering the distances hydrophone/panel $d_{X_2} + 2.2$cm for the reflection side and $d_{X_2} + 2.5$cm for the transmission side.

4.2.2 Validity Limits

It has been shown with the previous example that when the hypothesis on the diffracted pressure is satisfied, the 3-point method leads to reflection and transmission coefficients that fit well with those of an infinite panel. The current section studies the limits of validity of the method based on three tests defined in Table 4.2. Measurements for these tests have been conducted between 1 kHz and 15 kHz. The first test considers three points close to each other (separated by 1 cm so that the hypothesis on the edge-diffracted pressure being equal in the 3 points is assumed to be satisfied) but far away from the panel, where the central position forms an angle $\theta = 25.6°$ with the panel face. In the second test, a significantly greater distance between hydrophone positions is considered using $d_{X_{1,2}} = d_{X_{2,3}} = 10$ cm, thus challenging the hypothesis on the edge-diffracted pressure equal in the three points. Finally, Test 3 considers three positions so that the angle θ is now equal to 5.7°, where hydrophone positions are separated from each other by only 0.5 cm. Test 3 then satisfies the hypothesis on the edge-diffracted waves.

	d_{X_2} (cm)	$d_{X_{1,2}}$ (cm)	$d_{X_{2,3}}$ (cm)	θ (°)
Test 1	24	1	1	25.6
Test 2	15	10	10	16.7
Test 3	5	0.5	0.5	5.7

Table 4.2 – Configuration parameters tested to assess limitations of the 3-point method.

For these three tests, the reflection and transmission coefficients given by the 3-point method are plotted in Figure 4.9. It is first observed that these experimental scattering coefficients are very different from those of an infinite panel obtained theoretically (lines without markers). Moreover, all of them reach values higher than one, which makes no sense physically for a passive material. Results for each test are further analysed.

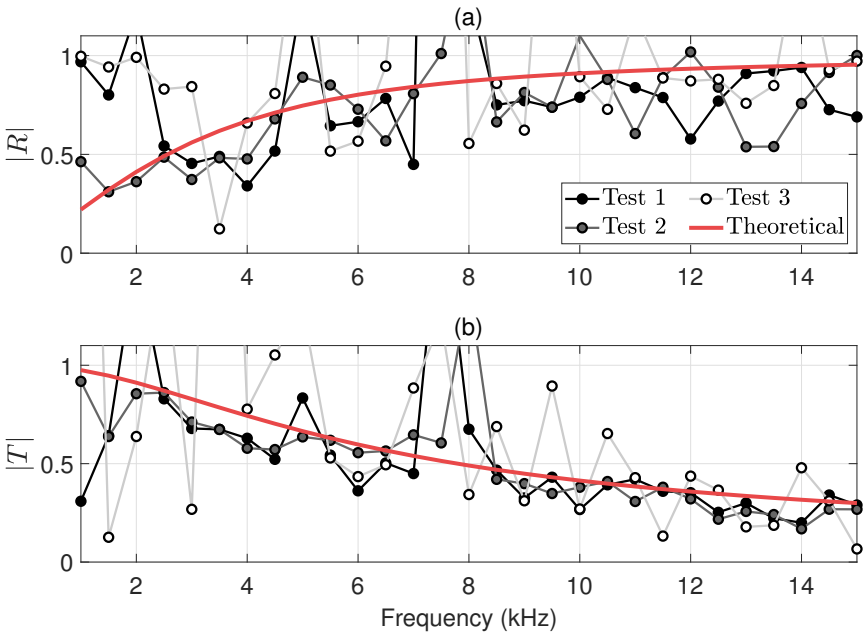

Figure 4.9 – Amplitude of (a) the reflection coefficient and (b) the transmission coefficient obtained with the 3-point method for the tests 1 to 3 defined in Table 4.2. Reflection and transmission coefficients obtained theoretically for a panel of infinite lateral dimensions are also presented (same as in Figure 4.7).

In Test 1, the relative difference between the edge-diffracted pressure levels in each point remains less than 1% according to the model in Appendix D. Even though the hypothesis on the edge-diffracted pressure can be considered as valid here, the experimental coefficients are very different from the theoretical ones because when the hydrophones are this far away from the panel, the signal may be polluted by waves other than those diffracted by the panel. The angle θ shall therefore remain less than 15°.

Test 2 considers a greater distance between hydrophone positions. This configuration gives acceptable results at very low frequencies, but leads to poor results at higher frequencies

as the distances d_X become too important in terms of wavelength. The relative difference between the edge-diffracted pressure levels is oscillating between 5% and 10% according to the analytical model in Appendix D. Poor quality results are thus obtained when the hydrophone set-up does not comply with the hypothesis on the hydrophone positions being close enough to each other so that the diffracted pressure is assumed identical for the three positions. Ideally, the distance between hydrophone positions should be lower than $\lambda/5$.

Finally, for Test 3, the distance $d_X = 0.5$ cm between hydrophone positions is equivalent to $\lambda/300$ at 1kHz and $\lambda/20$ at 15kHz. For this configuration, the hypothesis is satisfied and the relative difference is less than 0.1% according to the analytical model. Moreover, these three points are very close to the panel. However, the points are so close to each other that the total pressures measured are almost identical at the three points, which leads to results strongly dependent on measurement and numerical errors. Therefore, a compromise must be found to define three positions sufficiently close to each other and close to the panel, while being sufficiently spaced in terms of wavelength. It is thus preferable to maintain a minimum distance of $\lambda/20$ between two hydrophone positions.

The aforementioned criteria apply for the current aluminium panel and therefore will also generally apply to all panels of input impedance higher than the impedance of water. Nevertheless, it is worth noting that the behavior may be different in terms of the edge-diffracted signal, for a panel having an input impedance lower than the impedance of water [98]. For such a case, one has to make sure that measurements are made within an area where a diffracted signal exists at the 3 chosen positions so that it is accurately extracted from the total signal with the 3-point method.

4.2.3 Pressure Mapping

Acoustically hard panels are known for having a pronounced diffraction pattern. In order to evaluate and visualise the variations of the edge-diffracted pressure in a plane parallel to the panel, a pressure mapping is proposed. Both the analytical model in Appendix D and the 3-point method are applied for a pressure mapping along the y-axis.

Hydrophone positions along the x-axis defined in Table 4.1 are considered hereafter. Along the y-axis, 31 positions are considered, from $y = -15$ cm to $y = 15$ cm, with $y = 0$ cm corresponding to the panel's center. The distance between each y-position is then 1 cm. For frequencies 3.5 kHz, 5.5 kHz and 7.5 kHz, the calculated pressures on each side of the panel are plotted in Figure 4.10. For frequencies 14 kHz, 14.5 kHz and 15 kHz, the pressure mapping is given in Figure 4.11. Finally, variations of the edge-diffracted pressure given by the model in Appendix D are plotted in Figure 4.12. It should be noted that Figure 4.12 does not provide the amplitude of the edge-diffracted pressure, but only its variations.

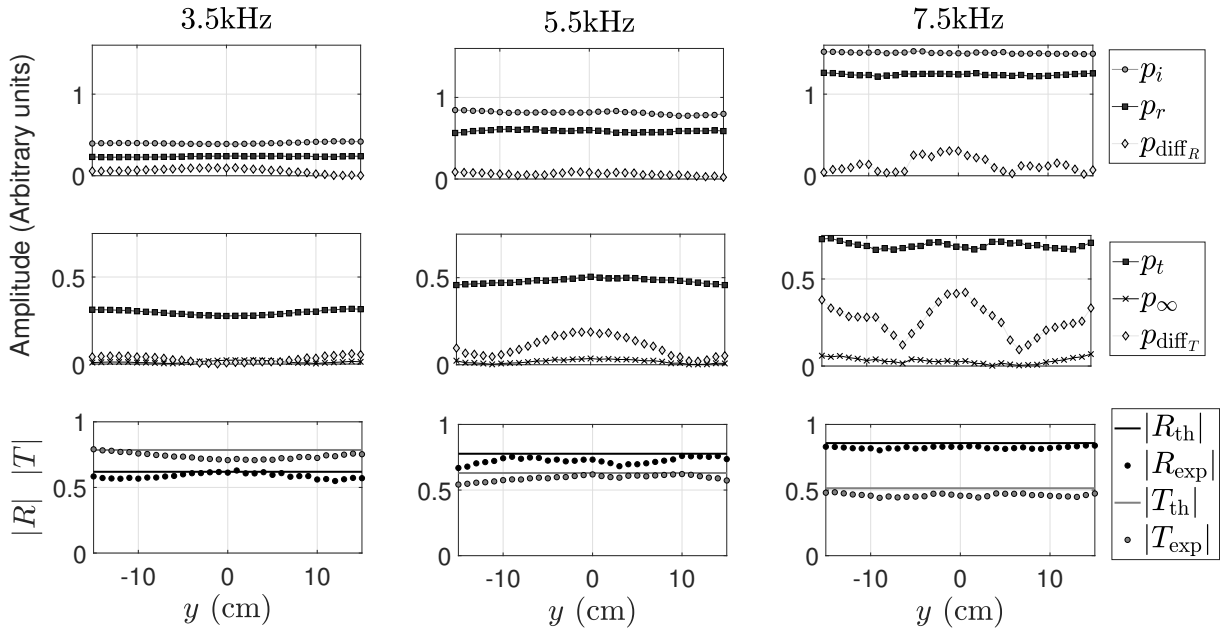

Figure 4.10 – Pressure mapping along the y-axis for 3.5 kHz, 5.5 kHz and 7.5 kHz. Experimental coefficients are also given and compared to the theoretical coefficients for a panel of infinite lateral dimensions.

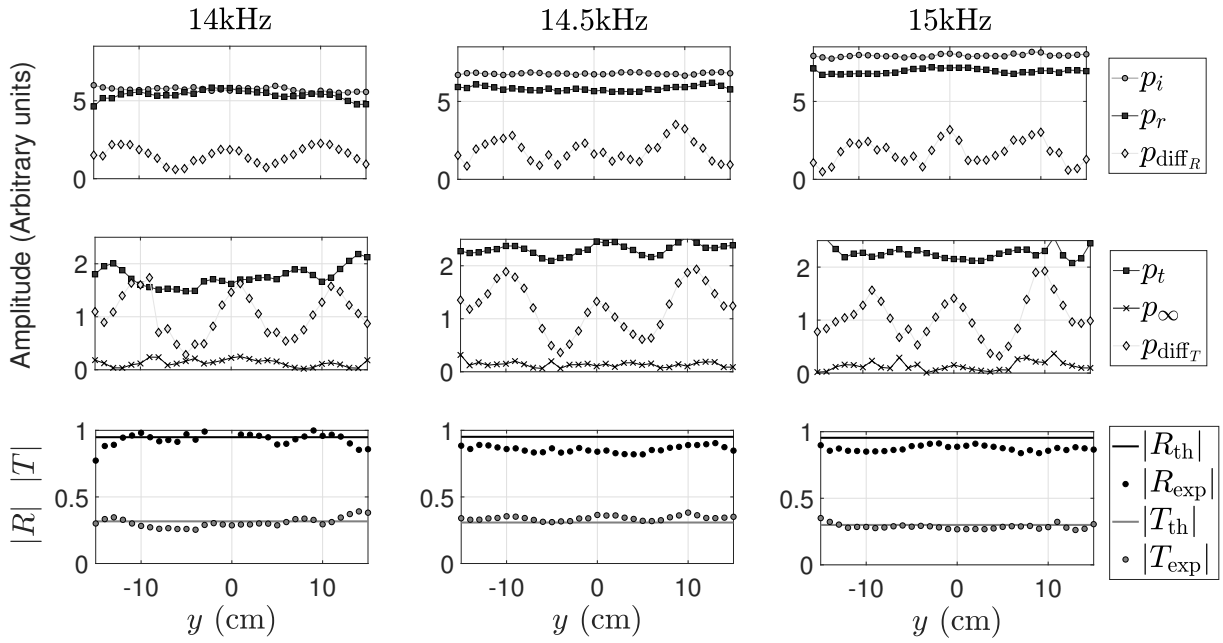

Figure 4.11 – Pressure mapping along the y-axis for 14 kHz, 14.5 kHz and 15 kHz. Experimental coefficients are also given and compared to the theoretical coefficients for a panel of infinite lateral dimensions.

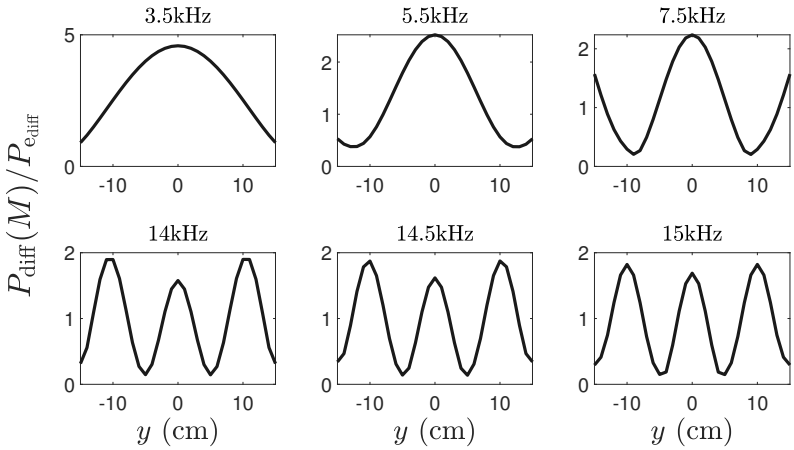

Figure 4.12 – Variations of the diffracted pressure along the y-axis obtained with the analytical model in Appendix D.

On these pressure maps, the infinite pressure p_∞ is almost zero everywhere, which shows that the 3-point method is valid and correctly implemented. Reflected, transmitted and incident pressures are almost identical along the y-axis, which reinforces the assumption of a plane wave condition. However, on both sides of the panel, the diffracted pressure strongly varies along the y-axis. This last observation is consistent with the results given by the analytical model in Figure 4.12. The pattern of the diffracted pressure field then depends on frequency, since for low frequencies the edge-diffracted pressure slowly varies along the y-axis, but as frequency increases, variations become steeper and closer. In addition, the center of the panel ($y = 0$) is always a maximum for the edge-diffracted pressure. This pressure mapping highlights the strong variations of the diffracted pressure along the y-axis and shows that a means of either reducing the edge-diffraction or calculating and removing its contribution is crucial for accurate measurements.

4.3 Experimental Speed of Sound Determination

4.3.1 Measurements

In this section, the longitudinal speed of sound in the polyurethane medium comprising 6% of micro-balloons is experimentally determined. This experimental determination ensures that the material properties used in the optimisation study of Chapter 3 are really those of the material that can be manufactured and not purely theoretical properties. The polyurethane panel comprising of 6% of micro-balloons is of dimensions 900 mm $\times$ 900 mm and of thickness 40.9 mm (on average), as shown in Figure 4.13. The theoretical mass density is 969 kg.m^{-3}. In practice, the measured mass density is 984 kg.m^{-3}.

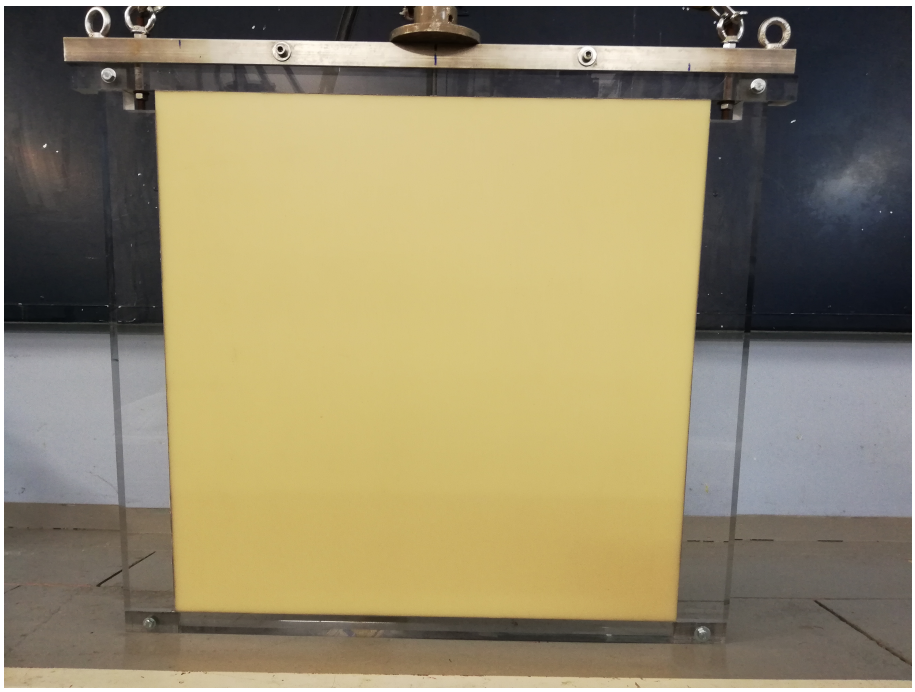

Figure 4.13 – Polyurethane panel comprising 6% of micro-balloons. The panel is hold by a Plexiglas frame.

The reflection and transmission coefficients obtained from measurements in the water tank are first needed. The speed of sound in the panel is then retrieved using these coefficients based on two approaches : (1) the retrieval method of Fokin et al. [45], and (2) a minimisation criterion introduced by Audoly [117]. The 3-point method is used to determine the reflection and transmission coefficients. Three different distances between hydrophone positions along the x-axis are considered corresponding to $\lambda/5$, $\lambda/10$ and $\lambda/15$. The hydrophone spacing of $\lambda/5$ is then applied at several positions along the y-axis to verify the consistency of the measurements. Results for the modulus and unwrapped phase of the reflection and transmission coefficients are shown in Figure 4.14. For all three hydrophone positions, results were consistent.

The case of a panel that has an input impedance lower than that of water is different from the case of an aluminium panel. The diffraction pattern for such panel is indeed not as significant as for a panel with higher impedance [98]. In addition, the amplitude of the diffracted waves is so low that their effects on the reflection and transmission coefficients may be negligible. The 3-point method, with $\theta = 13°$ and $d_X = \lambda/5$, has yielded excellent results and has highlighted the existence of a diffracted signal with low amplitude and very little variation. The coefficients shown in Figure 4.14 are then averaged and used to retrieve the effective speed of sound in the panel.

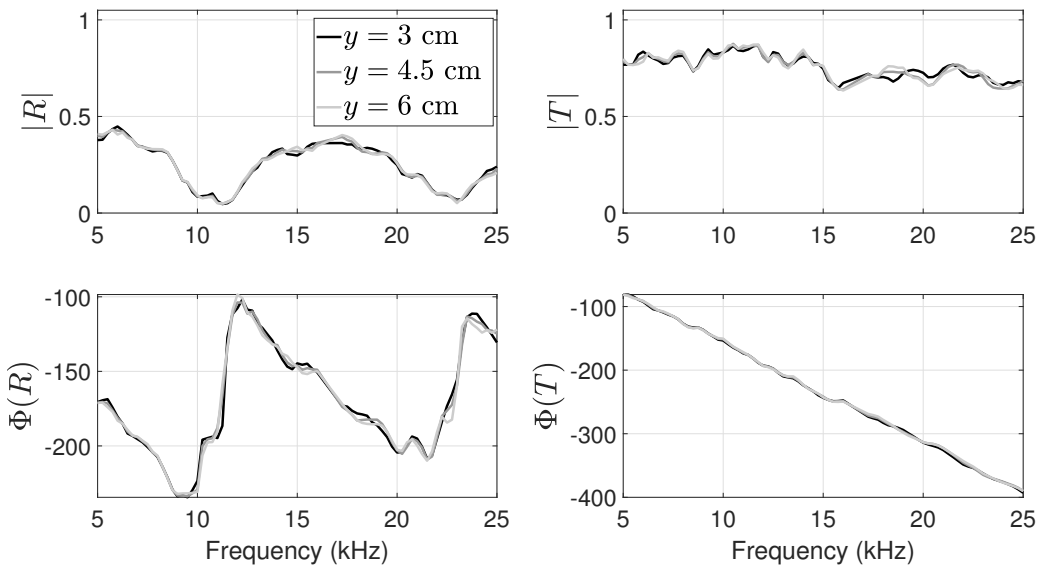

Figure 4.14 – Modulus and unwrapped phase of the reflection and transmission coefficients obtained with the 3-point method at three different positions along the y-axis.

4.3.2 Retrieval Approach 1

Reflection and transmission coefficients of the panel at normal incidence are used to retrieve the complex speed of sound in the panel with the retrieval method of Fokin et al. [45]. This method is based on the transfer matrix method, which can be fully calculated for the medium using the scattering coefficients (Appendix A). From the theoretical expression for the transfer matrix, the effective speed of sound can then be retrieved assuming that the mass density is known. The retrieved effective parameters are given in Figure 4.15. The real part of the speed of sound rises slightly from about 900 m.s^{-1} up to 950 m.s^{-1} at 25 kHz. The loss factor for the effective speed of sound slightly decreases from roughly 10% to 5%.

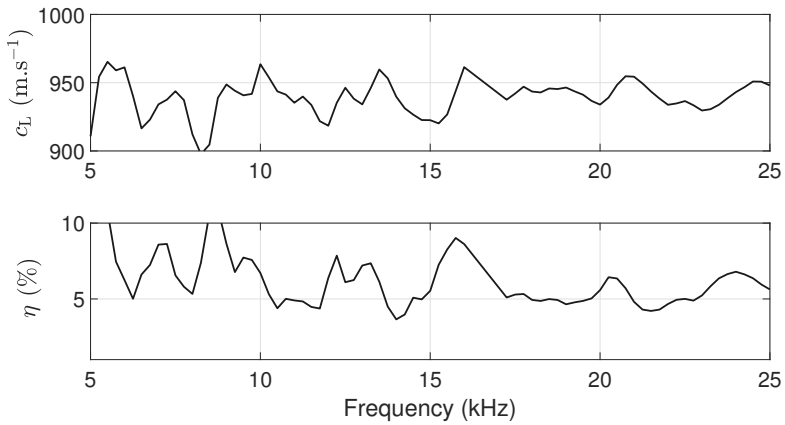

Figure 4.15 – Complex speed of sound $c_L(1+i\eta)$ obtained with the retrieval method of Fokin et al. [45].

4.3.3 Retrieval Approach 2

The unknown values of c_L and η are obtained by numerically minimising over these two parameters the error between the measured values of the coefficients R and T and their calculation using given values of c_L and η. Based on the estimation given by the retrieval approach 1, the two parameters to retrieve are bounded. The range of possible values for the real part of the speed of sound is [800 m.s^{-1} – 1100 m.s^{-1}] and the loss factor taking its values within the range [2% – 12%]. The minimisation criterion C is given by:

$$C(c_L, \eta) = |R_{calc}(c_L, \eta) - R_{meas}| + |T_{calc}(c_L, \eta) - T_{meas}|. \tag{4.9}$$

This criterion should provide a robust solution as it is over-determined [117]. For each frequency, the criterion is calculated in the 2D-space (c_L, η). For example, for the frequency 15 kHz, the criterion map is given in Figure 4.16.

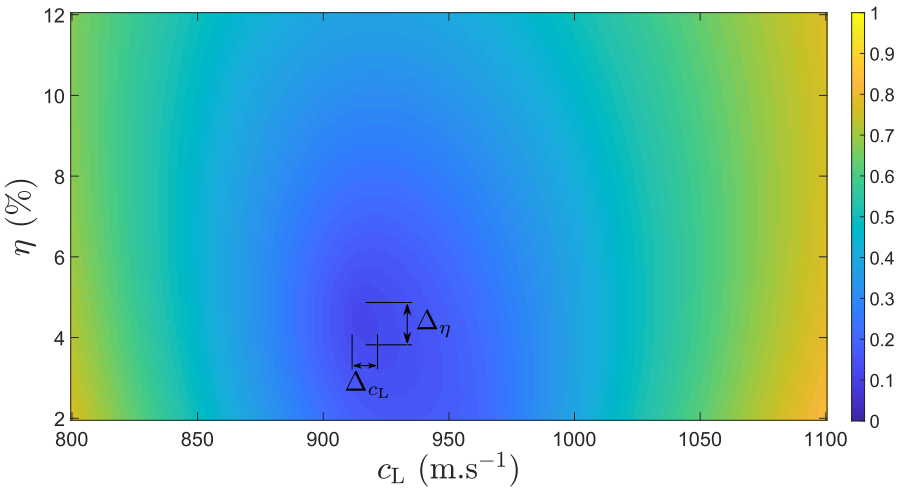

Figure 4.16 – Values of the criterion C for the frequency 15 kHz.

The values of c_{L} and $\eta_{c_{\mathrm{L}}}$ that lead to the global minimum of the criterion are represented by grey dots in Figure 4.17. Moreover, values that are close to this minimum, leading to $C < \epsilon$ with ϵ to be fixed, are also shown by the error bars in Figure 4.17. By considering $\epsilon = 0.13$, these solutions correspond to the darker blue areas and $(\Delta_\eta, \Delta_{c_{\mathrm{L}}})$ in Figure 4.16 for 15 kHz. As such, for each frequency, the set of values that minimise the criterion are visible.

It is observed that for the region between 15 kHz and 17 kHz, there is no solution that satisfies the criterion $C < 0.13$. It is also noted that for frequencies less than 10 kHz, there is greater uncertainty, as shown by the blue bars. Overall, the real part of the speed of sound is growing slightly from 900 ± 10 m.s^{-1} between 5 kHz to 10 kHz to 950 ± 10 m.s^{-1} , whereas the loss factor η is about $5 \pm 0.5\%$. These values are consistent with those obtained using the retrieval method in Figure 4.15. These curves have been fitted to be used in Chapter 3, as shown in Figure 4.18.

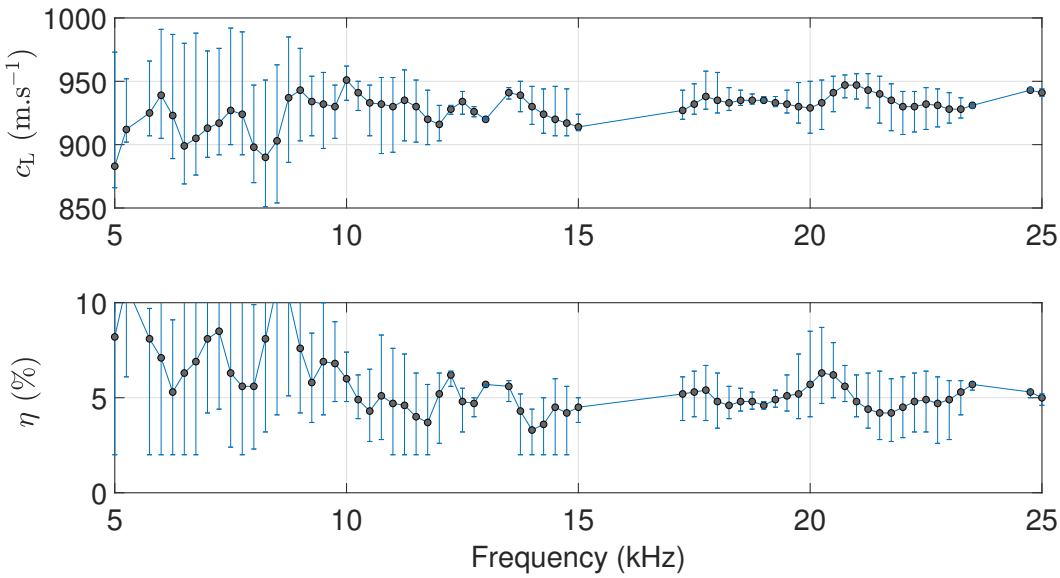

Figure 4.17 – Speed of sound obtained using the minimisation criterion C given in Equation (4.9) for $C < \epsilon$, with $\epsilon = 0.13$. The grey dots are the values of the complex speed of sound that give the global minimum of C whereas the error bars are the sets of solutions that satisfy $C < \epsilon$.

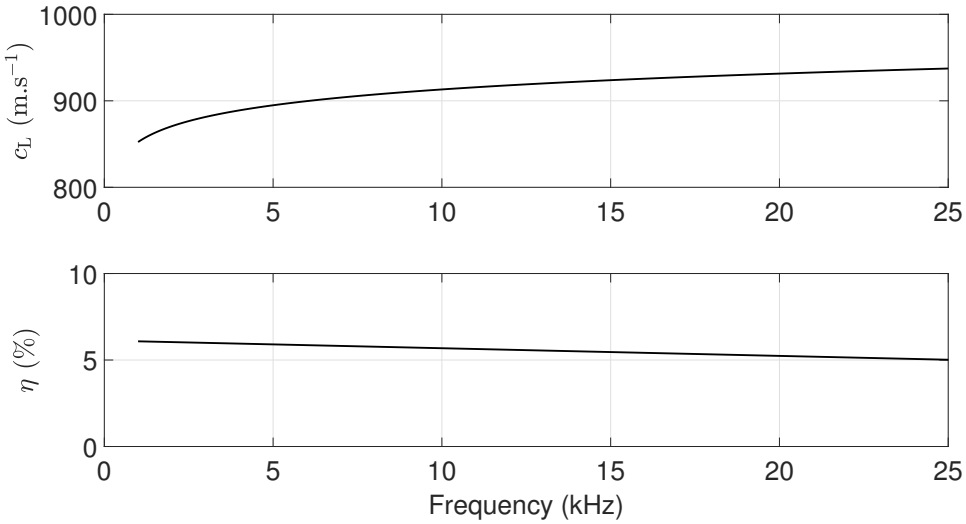

Figure 4.18 – Estimated complex speed of sound in the selected polyurethane matrix comprising 6% of micro-balloons.

4.3.4 Verification

The retrieved complex speed of sound has been fitted, as presented in Figure 4.18. Reflection and transmission coefficients calculated with theses values are given in Figure 4.19 and compared with coefficients obtained experimentally. Close agreement between calculated and experimental values for both the modulus and unwrapped phase can be observed.

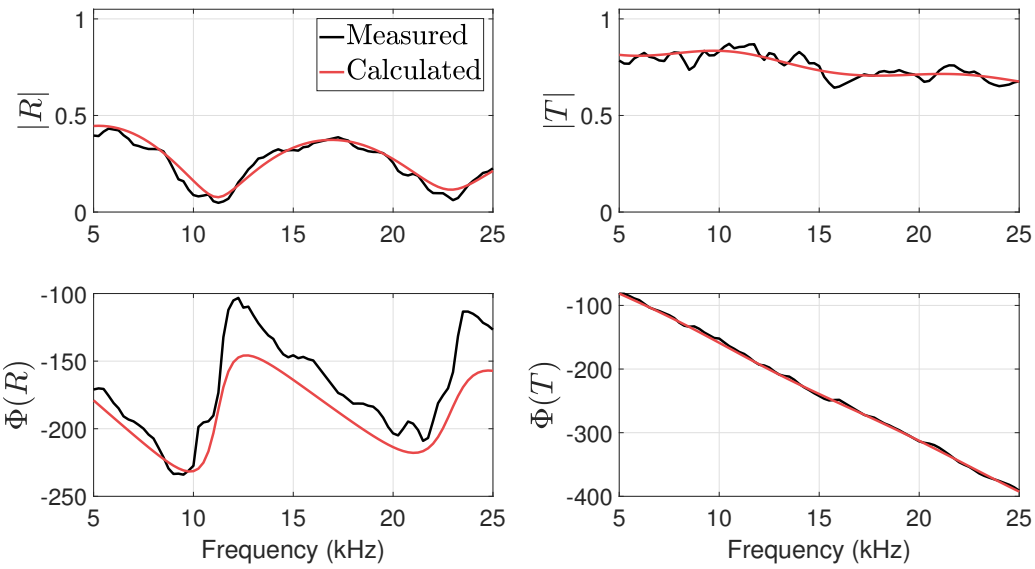

Figure 4.19 – Modulus and unwrapped phase of the reflection and transmission coefficients obtained with the 3-point method (black lines) and calculated with the fit of the retrieved speed of sound in the panel (red lines).

4.4 Multilayered Medium Measurements

4.4.1 Panel and Experimental Set-up

In this section, the selected multilayered medium selected in Chapter 3 (Figure 3.10) is experimentally characterised. Its design is reminded in Figure 4.20 and photographs of the panel are presented in Figure 4.21.

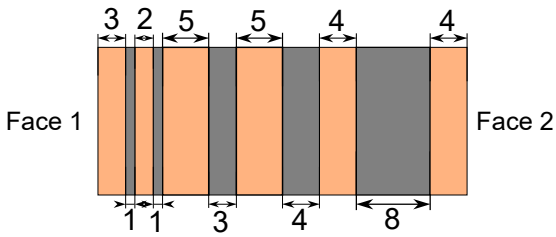

Figure 4.20 – Theoretical layer arrangement and thicknesses (in millimetres) of the manufactured panel. In the anechoic configuration, Face 2 would be on the hull and the incident plane wave arrives on Face 1.

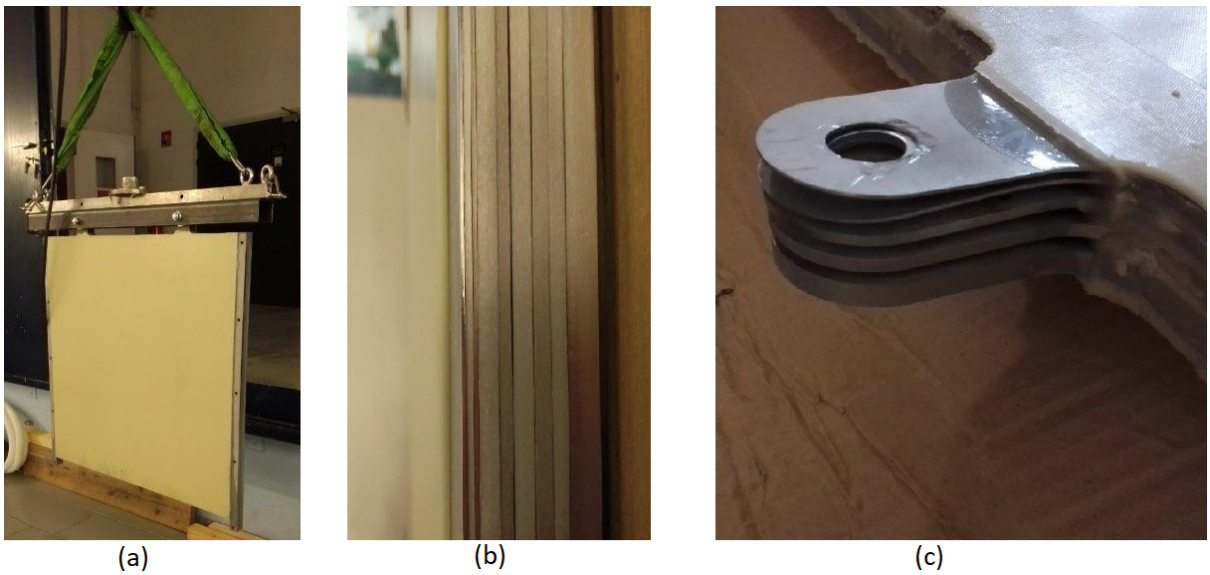

Figure 4.21 – Photo of (a) the panel before being mounted in the water tank, (b) the layer arrangement as per Figure 4.20, and (c) panel holding points that contain all steel layers.

The thickness of each layer has been measured and is consistent with the required design. The main difficulty with this panel was to ensure that the center of mass, which is different from the geometric center since the panel is strongly asymmetric, was correctly aligned with the mounting post. Misalignment can in fact lead to the creation of an unknown angle for the panel which is then not characterised for normal incidence. The theoretical

center of mass was thus calculated in order to align it with the mounting center using specially designed spacers to be placed on either side of the panel holding points (Figure 4.21(c)). However, it is important to note that, despite all the attention paid to the correct placement of the panel, there is still uncertainty since the center of mass calculation was performed on theoretical mass densities and thicknesses of the layers, which cannot be checked independently for this assembled panel.

4.4.2 Measurements

The 3-point method was used to measure the panel. The central position was placed 11 cm away from the face of the panel. A spacing of $\lambda/10$ was defined between the 3 positions of the hydrophone. Both sides of the panel are measured since the multilayered medium is not symmetrical. To do so, the panel was rotated but the acoustic source position remained unchanged.

Pressure magnitudes calculated by the 3-point method are presented in Figure 4.22. This shows that the retrieved incident pressure matches with the pressure obtained by measurements without the panel. In addition, pressure p_∞ is almost zero over the entire frequency range, which is consistent with the theory. These two observations show that the 3-point method is applied under valid conditions. Moreover, it can be seen that from 20 kHz, the transmitted pressure is very low and reaches the same values as the edge-diffracted pressure.

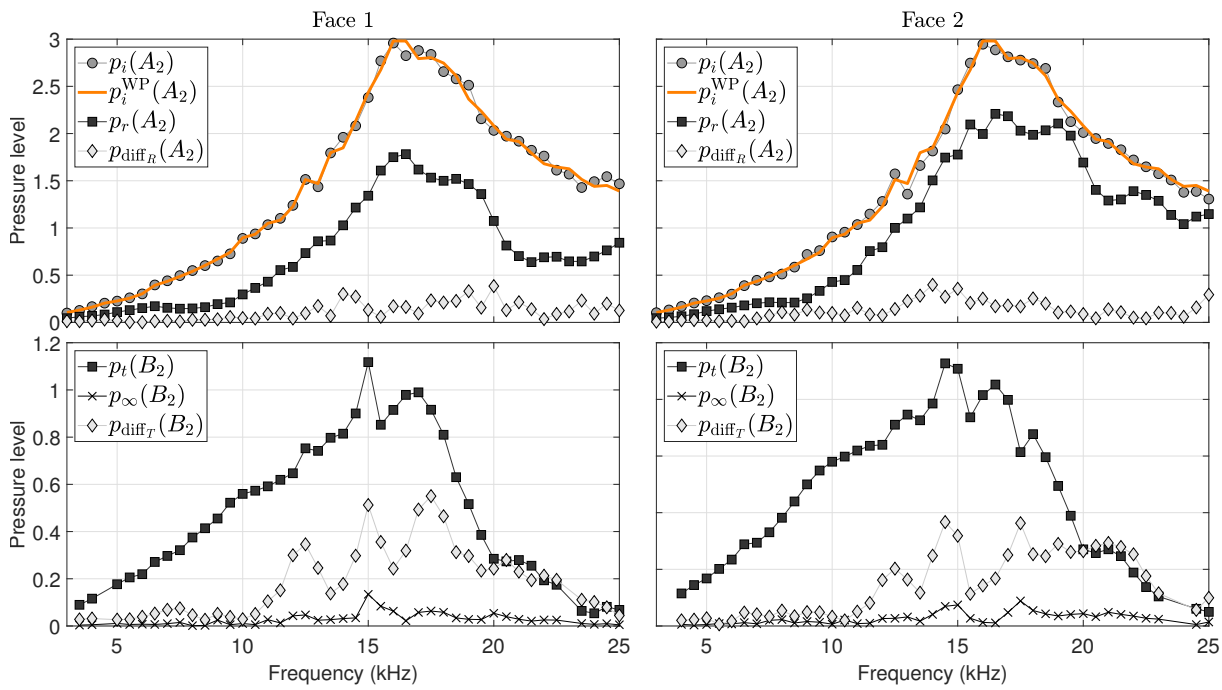

Figure 4.22 – Pressure levels calculated with the 3-point method on the reflection and transmission side, for an incident plane wave on Face 1 (left) and on Face 2 (right). The incident pressure measured without the panel is also given ($p_i^{\mathrm{WP}}(A_2)$).

From these calculated pressures, reflection and transmission coefficients are derived for each side of the panel. They are compared to analytical predictions, as shown in Figure 4.23 and 4.24 for the incoming wave incident on Face 1 and Face 2, respectively.

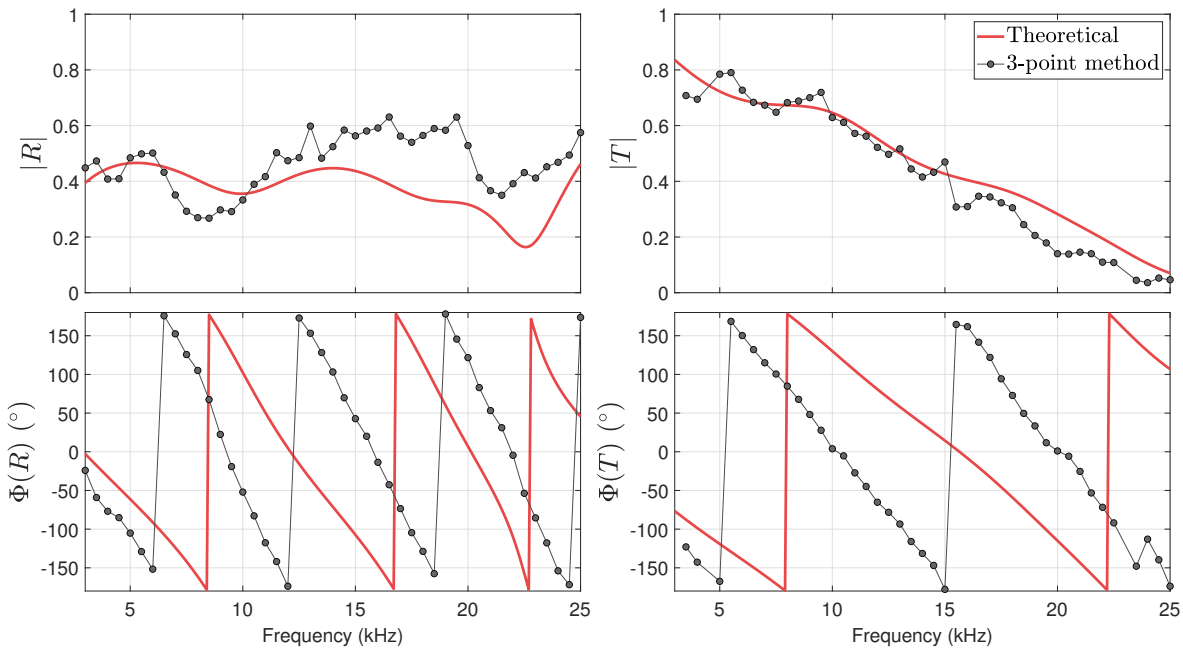

Figure 4.23 – Reflection and transmission coefficients of the multilayered medium obtained by insonification of Face 1.

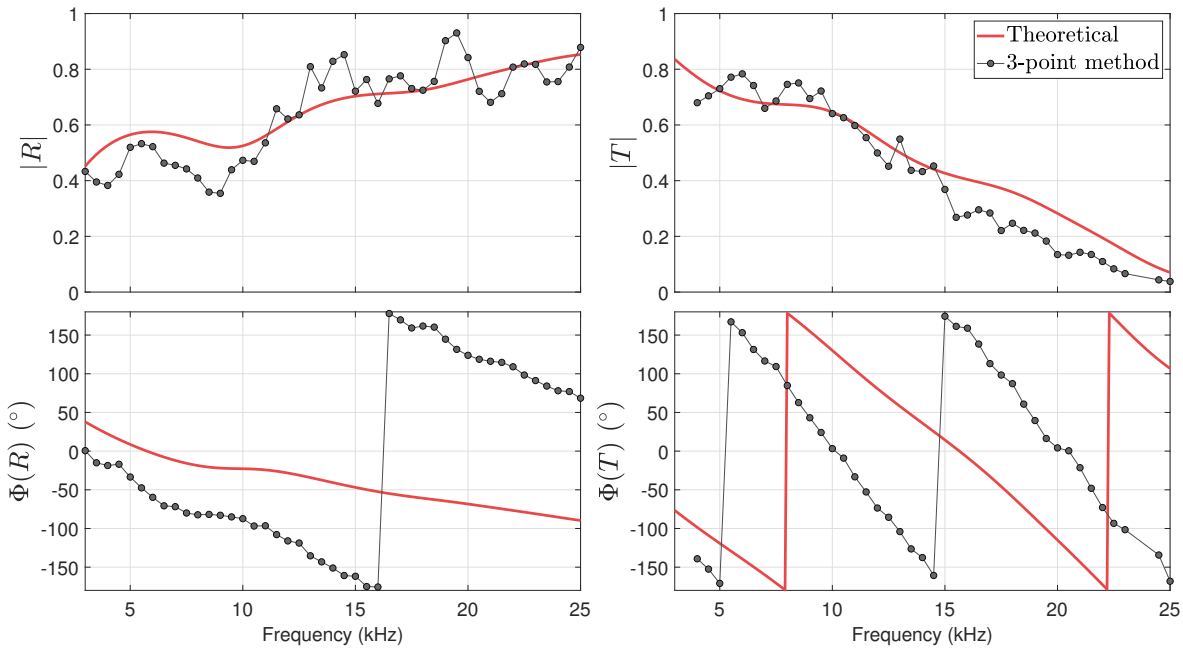

Figure 4.24 – Reflection and transmission coefficients of the multilayered medium obtained by insonification of Face 2.

There is good overall consistency between the experimental and analytical results for the modulus. The transmission coefficients measured on both sides is almost identical and also in agreement with the predictions for the modulus. However, it can be seen for both sides the panel is less reflective at low frequency than what has been predicted. On the contrary, from 10 kHz it becomes slightly more reflective, especially for Face 1. The phases of the two reflection coefficients are notably different from the prediction. This can be explained by significant uncertainty on the exact distance between the hydrophone and the panel. In fact, this distance is considered twice in the calculation of the phase of the reflection coefficient: once to phase-shift the pressure reflected on the face of the panel and once to phase-shift the pressure incident on this same face.

Phase corrections are applied by modifying the hydrophone/panel distances. The 3 corrections are as follows :

- Correction 1 corresponds to the distance corrections determined on the aluminium panel (Figure 4.8). The hydrophone on the reflection side is thus assumed to be placed at $d_{X_2} + 2.2$cm from the panel and the transmission hydrophone is estimated to be at $d_{X_2} + 2.5$cm away from the panel.
- Correction 2 corresponds to the distance corrections determined by attempting to fit the theoretical curves for the insonification of Face 1. The hydrophone on the reflection side is thus assumed to be placed at $d_{X_2} + 1.5$cm from the panel and the transmission hydrophone is estimated to be at $d_{X_2} + 3.3$cm away from the panel.
- Correction 3 corresponds to the distance corrections determined by attempting to fit the theoretical curves for the insonification of Face 2. The hydrophone on the reflection side is thus assumed to be placed at $d_{X_2} + 2.4$cm from the panel and the transmission hydrophone is estimated to be at $d_{X_2} + 2.3$cm away from the panel.

These corrected phases are plotted in Figure 4.25 for the insonification of Face 1 and in Figure 4.26 for the insonification of Face 2. As such, it can be seen that Correction 1, determined on the aluminium panel, is a correction that also applies well for this panel, except for the reflection coefficient obtained by insonification of Face 2.

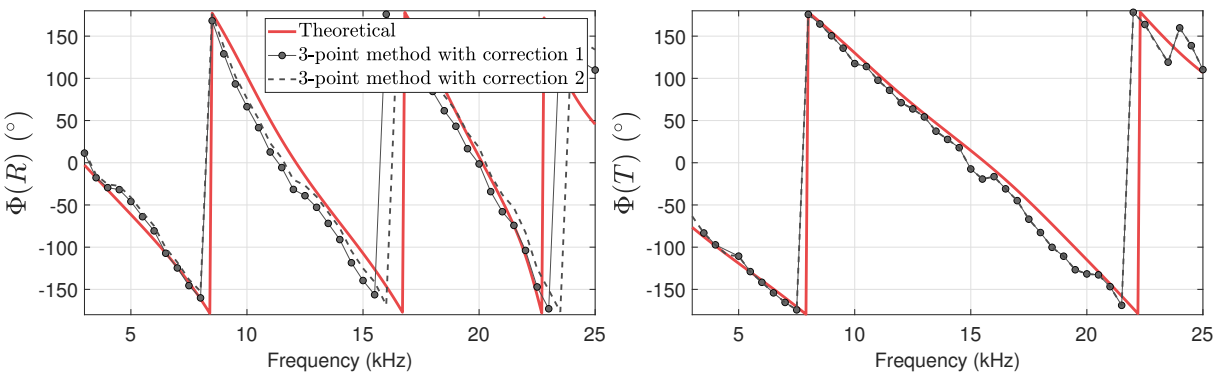

Figure 4.25 – Corrected phases of the reflection and transmission coefficients of the multilayered medium obtained by insonification of Face 1.

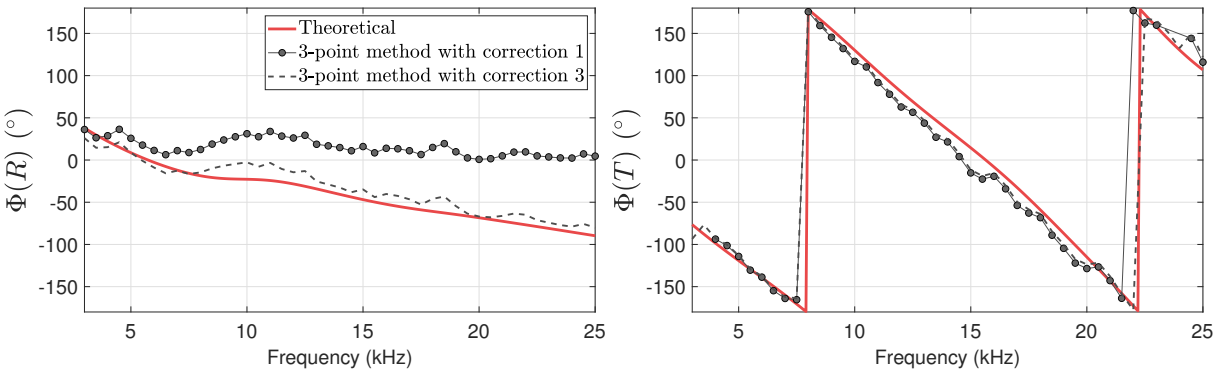

Figure 4.26 – Corrected phases of the reflection and transmission coefficients of the multilayered medium obtained by insonification of Face 2.

4.4.3 Calculation of the Anechoism Coefficient

The anechoism coefficient, defined in Appendix C, can now be derived using the experimental reflection and transmission coefficients. In addition to the calculation using coefficients derived directly from the 3-point method, the anechoism coefficient is also calculated using the coefficients with corrected phases. For the first calculation with phase correction, Correction 1 is applied to all coefficients, as per :

$$C_{A,\text{Correction1}} = R_{\text{Face1,Correction1}} - \frac{T_{\text{Face1,Correction1}} T_{\text{Face2,Correction1}}}{R_{\text{Face2,Correction1}} - 1}. \tag{4.10}$$

For the second calculation, Correction 2 is applied on the coefficients obtained for insonification of Face 1 and Correction 3 for that of Face 2, as given by:

$$C_{A,\text{Mixed Correction}} = R_{\text{Face1,Correction2}} - \frac{T_{\text{Face1,Correction2}} T_{\text{Face2,Correction3}}}{R_{\text{Face2,Correction3}} - 1} \tag{4.11}$$

The resulting fitted anechoism coefficients are given in Figure 4.27 and compared with the theoretical prediction. This shows that the anechoism coefficient obtained experimentally differs from the prediction in a non-negligible way. Since phase corrections are obtained from position corrections, this highlights that it is crucial to know the panel-hydrophone distance exactly if the reflection and transmission coefficients are to be used to calculate the anechoism coefficient, especially at low frequencies. However, the mixed correction seems to provide an anechoism coefficient close to the theoretical value. The slight differences visible for this anechoism coefficient appear to be due to the modulus variations. As mentioned previously, the panel is less reflective than expected for low frequencies and for both sides of the panel, which yields a low anechoism coefficient for this frequency range. On the contrary, the panel becomes more reflective at higher frequencies, thus leading to an higher value of the anechoism coefficient.

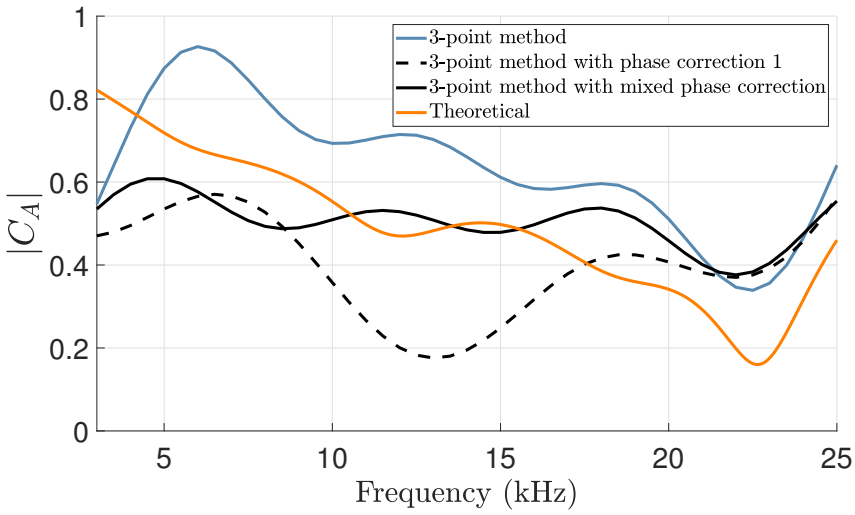

Figure 4.27 – Anechoism coefficient for the multilayered medium obtained theoretically in Chapter 3 and using the measured reflection and transmission coefficients (blue). Coefficients are also calculated considering the phase correction 1 obtained for the aluminium panel and considering mixed phase correction by the use of correction 2 and 3.

To summarise, the multilayered panel optimised in Chapter 3 has been measured in the water tank for both sides, in order to calculate the anechoism coefficient. Modulus of both coefficients, for both sides, are in good agreement with theoretical calculations. Slight differences between the predictions and the experimental modulus can be explained by the use of fitted material properties (obtained from the measurements) in the analytical calculation and by the possible local differences between the theoretical and actual thicknesses and material properties of each layer. However, as for the aluminium panel, phases of the two coefficients are different from the theoretical results since the panel/hydrophone distance is not well known. It is recalled that phase shifts are applied to these experimental coefficients. However, this phase shift requires precise knowledge of the distance between the hydrophone and the panel. As such, the calculation of the anechoism coefficient requires phase corrections to overcome this uncertainty. When the phase of the coefficients are corrected independently for each side and then used together in the calculation of the anechoism coefficient, the agreement between experimental and theoretical anechoism coefficients is better.

4.5 Summary

In this Chapter, the conventional set-up for measurements in open water tank have been described. An experimental method, namely the 3-point method, has also been presented. Using measurements at three different positions, the 3-point method yields estimations of the incident, reflected and transmitted pressures, from which the reflection and transmission coefficients can be derived. The method also provides an estimation of the total contribution of the edge-diffracted waves. The method has been applied to the challenging case of a homogeneous panel made of aluminum, for which edge-diffracted effects usually strongly corrupt the measurements. Experimental reflection and transmission were close to the theoretical calculation. The validity limits of the method have then been studied. It has been shown that it is important to choose the right positions for the hydrophones, so that the assumption on the identical edge-diffracted pressure at the three points is satisfied. A mapping of the different pressures along the y-axis was presented, where the strong variations of the edge-diffracted pressure are clearly visible. The 3-point method has the great advantage of being easy to implement and it does not require any additional device other than the conventional experimental bench for open water tank measurements. This work has been published in [118].

The 3-point method has then been applied to an acoustically soft panel to retrieve its effective speed of sound. This panel is made of polyurethane with the inclusion of 6% of micro-balloons, which is the material used in the multilayered medium. From the scattering coefficients given by the 3-point method, the effective speed of sound has been retrieved using two different approaches, for which results are in agreement.

Finally, the multilayered design selected in Chapter 3 was measured using the 3-point method. Moduli of the reflection and transmission coefficients are consistent with analytical predictions. For Face 1, which is intended to be at the interface with water in an anechoic configuration, the reflection coefficient is rather low over the entire frequency range, while the transmission coefficient is decreasing which is a characteristic of good anechoic media. Differences were however noted on the anechoism coefficient, which proves to be extremely sensitive to the distance between the panel and the hydrophones. Nonetheless, the use of phase corrections seems to overcome this lack of accuracy and yields an anechoism coefficient close to the theoretical prediction.

Part I introduced a homogenisation method for symmetric or asymmetric multilayered media (Chapter 2), which then was used for optimising layer arrangements. This study has shown patterns of performance for the anechoism and hull decoupling coefficients (Chapter 3). The acoustic performance of an optimised multilayered medium was then verified experimentally using the 3-point method. The experimental method was initially validated using an reference aluminum panel and then applied to the polyurethane panel used in the multilayered medium for retrieving its effective speed of sound (Chapter 4). In Part II, the emphasis is on designs with macro-inclusions, for which homogenisation methods, optimisation approaches and experimental performances are presented and are more complex than for their 1D multilayered counterparts.

Part II

DESIGNS WITH MACRO-INCLUSIONS

Chapter 5

Homogenisation for Symmetric Designs

In structures with macro-inclusions, additional physical phenomena may occur compared to one-dimensional periodic finite structures, such as local resonances and boundary effects. It therefore becomes more difficult to apply a simple homogenisation model. In this chapter, the effective properties of acoustic metamaterials are obtained by applying two retrieval methods, referred to as the direct inversion method and the differential method. They employ the scattering coefficients on the reflection and transmission sides of structures immersed in a fluid (in this work, water). As with Chapter 2, a fluid homogenisation model is considered and a transfer matrix approach is used to describe the propagation in the constituent unit cell. A validation case study on a multilayered periodic design is first presented. Two case studies consisting of designs with periodic cylindrical steel or void macro-inclusions in a soft elastic matrix are then examined. Homogenisation issues related to different underlying assumptions in the two retrieval methods are discussed. A hybrid method is also introduced to provide an accurate effective representation of a structure with macro-inclusions.

Contents

5.1 Methodology 107

5.1.1 Fluid Homogenisation Model 107

5.1.2 Direct Inversion Method 107

5.1.3 Differential Method 109

5.2 Implementation 115

5.3 Validation 116

5.4 Case Study: Hard Inclusions 118

5.4.1 Design 118

5.4.2 Effective Parameters 118

5.4.3 Influence of the Number of Unit Cells 123

5.4.4 Scattering Predictions 124

5.5 Case Study: Voided Inclusions 127

5.5.1 Effective Parameters 127

5.5.2 Scattering Predictions 129
5.6 Summary 131

5.1 Methodology

5.1.1 Fluid Homogenisation Model

This chapter is limited to the study of symmetric and periodic structures with macro-inclusions, characterised by a unit cell. Similar to the homogenisation theory for multi-layered structures presented in Chapter 2, the objective is to define the effective medium that would replace the unit cell. A fluid model is selected and is thus characterised by an effective wavenumber k and an effective impedance Z.

The fluid homogenisation model is evidently simplistic when applied to complex periodic media with macro-inclusions. Several homogenisation difficulties will be underlined in this Chapter and are first mentioned here. First of all, only longitudinal waves can propagate in a fluid whereas shear wave propagation occurs in solid media. As structures are studied under normal incidence, this assumption was valid for one-dimensional multilayered structures where only longitudinal modes were excited. However, for structures made of a elastic matrix with macro-inclusions, local resonances may appear and convert longitudinal waves into shear waves, which cannot be described by the present homogenisation model. Shear wave propagation is therefore not accurately modelled but is implicitly taken into account. The fluid model also cannot consider the effects of the near-fields that may be created by media with macro-inclusions, as in practice, fluid media of infinite lateral extent do not produce near-field effects. Aware of the approximations involved by the choice of a fluid model, it is worth emphasising that the retrieval methods are implemented to give approximate predictions of a medium's acoustic performance so that it can be used in an optimisation process. As such, it is not an exact homogenisation model that is sought, but a simple method to get a reasonably accurate representation of the behavior of metamaterials with macro-inclusions.

It is worth remembering that propagation in a fluid medium may be represented by a transfer matrix under the form given by Equation (2.2), recalled below :

$$\mathbf{M} = \begin{bmatrix} \cos(kh) & \mathrm{i}Z\sin(kh) \\ \mathrm{i}Z^{-1}\sin(kh) & \cos(kh) \end{bmatrix}. \tag{5.1}$$

Effective properties k and Z are derived using two retrieval methods, that are techniques based on the scattering response of a structure, such as the reflection and transmission coefficients. These methods are presented in what follows and are referred to as the direct inversion (dir) method and the differential (diff) method.

5.1.2 Direct Inversion Method

The direct inversion method uses the reflection and transmission coefficients of a structure to retrieve its effective parameters, similar to the method proposed by Fokin et al. [45].

The medium is modelled as a segmented structure comprising of periodic repetitions of a constituent unit cell, as shown in Figure 5.1. The segmented medium comprises n unit cells of length L_u. Coefficients R and T, respectively, correspond to the coefficients of the reflected and transmitted pressures calculated at the interfaces between the segmented medium and the surrounding fluid medium. In this method, all unit cells are identical.

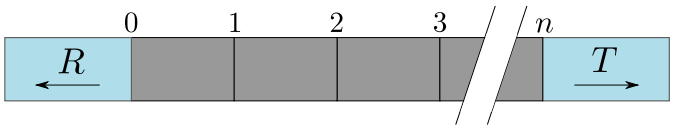

Figure 5.1 – Schematic diagram of a segmented medium comprising n identical unit cells. Reflection and transmission coefficients on the incidence and transmission sides of the medium are also shown.

The direct inversion method follows the same approach as the homogenisation method presented in Chapter 2 for multilayered structures, using the fact that transfer matrices can be expressed and calculated in several ways. One way to obtain the global transfer matrix $\mathbf{M}_n$ of the periodic medium comprising n unit cells is to use its reflection and transmission coefficients in the surrounding fluid of impedance Z_f as follows:

$$\mathbf{M}_n = \frac{1}{2T}\begin{bmatrix} 1 - R^2 + T^2 & ((1+R)^2 - T^2)\, Z_f \\ ((1-R)^2 - T^2)\, Z_f^{-1} & 1 - R^2 + T^2 \end{bmatrix}. \tag{5.2}$$

This expression is derived in Appendix A. Since all unit cells are identical and the homogenisation model is applied to each cell, the global transfer matrix of the segmented medium may also be written as the product of the transfer matrix of each cell. This leads to $\mathbf{M}_n = (\mathbf{M}_u)^n$, where $\mathbf{M}_u$ is the transfer matrix of a constituent unit cell and L_u is its thickness. It is assumed that the transfer matrix $\mathbf{M}_u$ has the same form as the transfer matrix given in Equation (5.1). It is then easy to show that for any transfer matrix under the form given by Equation (5.1), the calculation of $(\mathbf{M}_u)^n$ for any n integer is equivalent to only replacing the thickness L_u by nL_u without changing the wavenumber or the impedance associated with the matrix $\mathbf{M}_u$. Therefore, if the effective parameters may be found for a single unit cell, the same parameters apply for a segmented medium comprising n unit cells. The global transfer matrix expression is thus given by :

$$(\mathbf{M}_u)^n = \begin{bmatrix} \cos(nk_{\text{dir}}L_u) & \mathrm{i}Z_{\text{dir}}\sin(nk_{\text{dir}}L_u) \\ \mathrm{i}Z_{\text{dir}}^{-1}\sin(nk_{\text{dir}}L_u) & \cos(nk_{\text{dir}}L_u) \end{bmatrix}, \tag{5.3}$$

where Z_{dir} is the effective impedance and k_{dir} is the effective wavenumber obtained for the direct inversion method. The global transfer matrix expression given by Equation (5.3) is equal to the global transfer matrix calculated using the scattering response of the medium given by Equation (5.2). The effective parameters are derived from this equality. We herein introduce the notation $\mathbf{M}_{n_{i,j}}$ to express the elements of the global transfer matrix $\mathbf{M}_n$, with $1 \leq i, j \leq 2$. The effective impedance is given by:

$$Z_{\text{dir}} = \pm\sqrt{\frac{\mathbf{M}_{n_{1,2}}}{\mathbf{M}_{n_{2,1}}}}. \tag{5.4}$$

Material passivity condition requires the real part of the effective impedance to be positive (See section 1.4.5). The effective wavenumber is obtained using either $\mathbf{M}_{n_{1,1}}$ or $\mathbf{M}_{n_{2,2}}$, as per:

$$k_{\text{dir}} = \pm\frac{\cos^{-1}(\mathbf{M}_{n_{1,1}})}{nL_u} + \frac{2\pi m}{nL_u}. \tag{5.5}$$

The passive material condition is satisfied when the imaginary part of k_{dir} is negative. Integer m is chosen to ensure continuity of the real part of k_{dir} as a function of frequency (see Section 1.4.5).

5.1.3 Differential Method

The second retrieval method, referred to as the differential method, is an extension of the Bianco and Parodi method [44] and is detailed below. Two versions of the differential method are introduced. In the first version, the transfer matrix of the unit cell is assumed to be of the form given by Equation (5.1), whereas in the second version of the differential method, effective parameters are obtained independently of this transfer matrix form.

Bianco and Parodi Method

The Bianco and Parodi method (BP) is a retrieval method which was originally developed for electromagnetism, in order to derive the propagation constant in a medium of infinite length by examining wave propagation within a section of a finite medium [44]. Figure 5.2 presents the configuration required to apply the Bianco and Parodi method. Two media are considered, differing only by their length, where the second medium is greater in length by Δ_L compared to the first medium. The propagation constant is calculated for this extra length. R_i and T_i $(i = 1, 2)$ respectively correspond to the coefficients of the reflected and transmitted pressures calculated at the interfaces between the two media and the surrounding water.

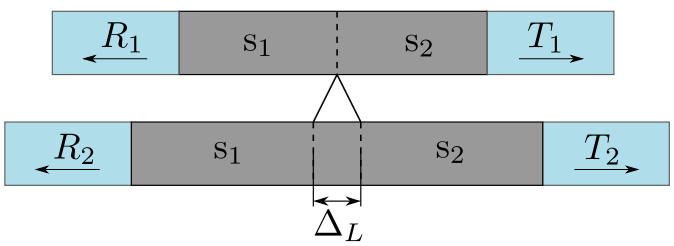

Figure 5.2 – Schematic diagram illustrating the Bianco and Parodi method in which two finite media differ only by length ΔL in the propagation direction. Reflection and transmission coefficients of the two media are defined.

The Bianco and Parodi method does not require the application of a descriptive model to the entire media. The homogenisation model is only applied to the extra portion Δ_L in the second medium, assuming that the medium is long enough to create a region where wave propagation is monomode, thus described by the wavenumber k_{BP} in the medium core. Firstly, the first medium (m1) is virtually segmented in two sections, referred to as section 1 (s_1) and section 2 (s_2), for which the transfer matrices are respectively $\mathbf{M}_{\mathrm{s}_1}$ and $\mathbf{M}_{\mathrm{s}_2}$. The global transfer matrix for the shorter medium is then given by:

$$\mathbf{M}_{\mathrm{m1}} = \mathbf{M}_{\mathrm{s1}}\mathbf{M}_{\mathrm{s2}}. \tag{5.6}$$

The global transfer matrix for the second medium (m2) only differs by the introduction of the section Δ_L in-between the sections 1 and 2, which yields:

$$\mathbf{M}_{\mathrm{m2}} = \mathbf{M}_{\mathrm{s1}}\mathbf{M}_{\Delta_L}\mathbf{M}_{\mathrm{s2}}. \tag{5.7}$$

Equation (5.7) is multiplied by the inverse of the global transfer matrix of the first medium given by Equation (5.6), which leads to:

$$\mathbf{M}_{\mathrm{m2}}(\mathbf{M}_{\mathrm{m1}})^{-1} = \mathbf{M}_{\mathrm{s1}}\mathbf{M}_{\Delta_L}\mathbf{M}_{\mathrm{s2}}(\mathbf{M}_{\mathrm{s2}}^{-1}\mathbf{M}_{\mathrm{s1}}^{-1}) = \mathbf{M}_{\mathrm{s1}}\mathbf{M}_{\Delta_L}\mathbf{M}_{\mathrm{s1}}^{-1}. \tag{5.8}$$

By definition, the matrix $\mathbf{M}_{\mathrm{s1}}\mathbf{M}_{\Delta_L}\mathbf{M}_{\mathrm{s1}}^{-1}$ and $\mathbf{M}_{\Delta_L}$ are similar. As such, these two matrices have the same trace, which is also the same as the product $\mathbf{M}_{\mathrm{m2}}(\mathbf{M}_{\mathrm{m1}})^{-1}$ according to Equation (5.8). Moreover, the transfer matrix $\mathbf{M}_{\Delta_L}$, describing the core of the second medium, is assumed to be under the form of Equation (2.22). Consequently, the effective wavenumber k_{BP} is obtained using:

$$\mathrm{Tr}\left(\mathbf{M}_{\mathrm{m2}}(\mathbf{M}_{\mathrm{m1}})^{-1}\right) = \mathrm{Tr}\left(\mathbf{M}_{\Delta_L}\right) = 2\cos(k_{\mathrm{BP}}\Delta_L). \tag{5.9}$$

The effective wavenumber k_{BP} is thus derived using the trace of the transfer matrix of the unit cell, which is $\mathrm{Tr}\left(\mathbf{M}_{n+1}(\mathbf{M}_n)^{-1}\right) = \mathrm{Tr}\left(\mathbf{M}_u\right) = \mathbf{M}_{u_{1,1}} + \mathbf{M}_{u_{2,2}}$. The effective wavenumber expression is then:

$$k_{\mathrm{BP}} = \pm\frac{\cos^{-1}\left(\frac{\mathrm{Tr}(\mathbf{M}_u)}{2}\right)}{L_u} + \frac{2\pi m}{L_u}. \tag{5.10}$$

The Bianco and Parodi method gives the effective wavenumber in the medium of theoretical infinite length. The method is valid even when the wave coupling process at the inlet/outlet cannot be modelled by a transfer matrix under the form of Equation (5.1), as it is unnecessary to apply a homogenisation model for these sections. The Bianco and Parodi method thus accurately removes physical phenomena that may arise from the finite length of the medium and from the coupling at the interfaces with the surrounding fluid on the incidence and transmission sides of the medium [47]. However, it is worth noting that the Bianco and Parodi method, as well as the following differential method, requires the calculation of the scattering coefficients for two media, unlike the direct inversion method which only needs one medium.

Differential Method

The Bianco and Parodi method is extended here to calculate more effective properties than only the effective wavenumber. This extended method is referred to as the *Differential Method*. The two media are modelled as segmented structures comprising periodic repetitions of a constituent unit cell, as shown in Figure 5.3. The extra portion added to the second segmented medium is one unit cell of length L_u. The shorter segmented medium comprises n unit cells and the longer medium comprises $n+1$ unit cells. Coefficients R_i and T_i $(i = 1, 2)$ respectively correspond to the coefficients of the reflected and transmitted pressures calculated at the interfaces between the segmented media and the surrounding fluid medium. In this extended method, all unit cells are identical.

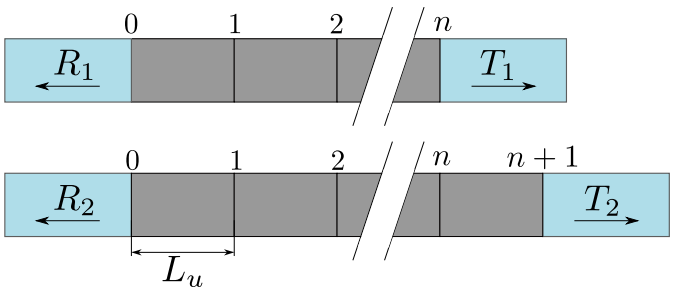

Figure 5.3 – Schematic diagram illustrating the differential method in which two finite segmented media comprising identical unit cells differ only by a single unit cell. Reflection and transmission coefficients of the two segmented media are defined.

Transfer matrices of the two media are expressed and calculated using their scattering coefficients. The global transfer matrix $\mathbf{M}_n$ of the shorter periodic medium comprising n unit cells can be calculated using its refection R_1 and transmission T_1 coefficients as follows:

$$\mathbf{M}_n = \frac{1}{2T_1}\begin{bmatrix} 1 - R_1^2 + T_1^2 & ((1+R_1)^2 - T_1^2)\, Z_f \\ ((1-R_1)^2 - T_1^2)\, Z_f^{-1} & 1 - R_1^2 + T_1^2 \end{bmatrix}. \tag{5.11}$$

Similarly, the global transfer matrix $\mathbf{M}_{n+1}$ of the longer segmented medium can be calculated using its scattering coefficients R_2 and T_2 as given by (Appendix A):

$$\mathbf{M}_{n+1} = \frac{1}{2T_2}\begin{bmatrix} 1 - R_2^2 + T_2^2 & ((1+R_2)^2 - T_2^2)\, Z_f \\ ((1-R_2)^2 - T_2^2)\, Z_f^{-1} & 1 - R_2^2 + T_2^2 \end{bmatrix}. \tag{5.12}$$

Two versions are from now on distinguished.

- **Version 1**

Since all unit cells are identical, the global transfer matrix of a segmented medium may also be written as the product of the transfer matrix of each unit cell. This leads to $\mathbf{M}_n = (\mathbf{M}_u)^n$ for the shorter segmented medium and $\mathbf{M}_{n+1} = (\mathbf{M}_u)^{n+1}$ for the longer

medium, where $\mathbf{M}_u$ is the transfer matrix of a constituent unit cell. The transfer matrix $\mathbf{M}_u$ of a unit cell can be now deduced from the product of the global transfer matrix of the longer segmented medium with the inverse of that of the shorter medium, that is:

$$\mathbf{M}_{n+1}(\mathbf{M}_n)^{-1} = (\mathbf{M}_u)^{n+1-n} = \mathbf{M}_u. \tag{5.13}$$

The left hand side of Equation (5.13) corresponding to the product $\mathbf{M}_{n+1}(\mathbf{M}_n)^{-1}$ can be calculated in terms of the scattering responses of the two segmented media, using Equations (5.11) and (5.12).

The transfer matrix $\mathbf{M}_u$ on the right hand side of Equation (5.13) is assumed to be of the form of Equation (5.1), similar to the direct inversion method. Therefore all unit cells, including the extra unit in the second segmented medium, can be modelled by a transfer matrix in the form of Equation (5.1). This hypothesis was not present in the original Bianco and Parodi retrieval method, where a descriptive model was only applied to the core of the second medium. In this version of the differential method, it is assumed that all the segments (units) can be described by the transfer matrix $\mathbf{M}_u$. As later shown through case studies, this assumption may affect the retrieved parameters particularly if the transfer matrix in the form of Equation (5.1) fails to describe the wave coupling at the medium interfaces. The right hand side of Equation (5.13) is thus expressed as follows:

$$\mathbf{M}_u = \begin{bmatrix} \cos(k_{\text{diff}_1} L_u) & \mathrm{i} Z_{\text{diff}_1} \sin(k_{\text{diff}_1} L_u) \\ \mathrm{i} Z_{\text{diff}_1}^{-1} \sin(k_{\text{diff}_1} L_u) & \cos(k_{\text{diff}_1} L_u) \end{bmatrix}, \tag{5.14}$$

where k_{diff_1} is the longitudinal effective wavenumber and Z_{diff_1} is the effective impedance of the effective unit cell of length L_u. Using Equations (5.11) to (5.14), the effective parameters Z_{diff_1} and k_{diff_1} of the unit cell can be extracted as follows. Elements of the unit cell $\mathbf{M}_u$ are referred to as $\mathbf{M}_{u_{i,j}}$, $1 \leq i, j \leq 2$. The effective impedance is given by:

$$Z_{\text{diff}_1} = \pm \sqrt{\frac{\mathbf{M}_{u_{1,2}}}{\mathbf{M}_{u_{2,1}}}}. \tag{5.15}$$

As for the direct inversion method, the real part of the effective impedance is required to be positive according to the material passivity constraint. The effective wavenumber is obtained using either $\mathbf{M}_{u_{1,1}}$ or $\mathbf{M}_{u_{2,2}}$ as given by:

$$k_{\text{diff}_1} = \pm \frac{\cos^{-1}(\mathbf{M}_{u_{1,1}})}{L_u} + \frac{2\pi m}{L_u}, \tag{5.16}$$

where m is an integer chosen for continuity of the effective wavenumber as a function of frequency. The imaginary part of the wavenumber must be negative with respect to the material passivity constraint.

Since $\mathbf{M}_{u_{2,2}} = \mathbf{M}_{u_{1,1}}$ according to the transfer matrix form of the unit cell given by Equation (5.14), the effective wavenumber from the original Bianco and Parodi method (Equation (5.10)) is supposed to be the same as the wavenumber derived with this version

of the differential method (Equation (5.16)). However, it will be shown later with case studies that $\mathbf{M}_{u_{2,2}}$ may differ from $\mathbf{M}_{u_{1,1}}$ when the transfer matrix in the form of Equation (5.1) fails to describe the unit cell. A second version of the differential method is therefore implemented to overcome this difficulty which disregards the form of the transfer matrix for the constituent unit cell.

- **Version 2**

For the second version of the differential method, the effective wavenumber is obtained in a similar way to the Bianco and Parodi original method. Assuming that wave propagation within the second medium extra portion L_u is monomode and described by the effective wavenumber k_{diff_2}, the fluid homogenisation model is only applied to this core portion L_u which is then described by a transfer matrix in the form given by Equation (5.1), yielding $\text{Tr}\,(\mathbf{M}_u) = 2\cos(k_{\text{diff}_2} L_u)$. The expression for the effective wavenumber can be obtained as:

$$k_{\text{diff}_2} = \pm \frac{\cos^{-1}\left(\frac{\text{Tr}\left(\mathbf{M}_{n+1}(\mathbf{M}_n)^{-1}\right)}{2}\right)}{L_u} + \frac{2\pi m}{L_u}, \tag{5.17}$$

where m is an integer whose value is determined such that the effective wavenumber as a function of frequency is continuous.

For the determination of the effective impedance, Equation (5.13) is considered for which the left hand side is calculated using Equations (5.11) and (5.12). Contrarily to the first version however, the effective impedance is obtained independently of the theoretical expressions for the elements of the transfer matrix $\mathbf{M}_u$. For this purpose, the definition of the transfer matrix of a medium is written as:

$$\begin{cases} p_{\text{left}} = \mathbf{M}_{u_{1,1}} p_{\text{right}} + \mathbf{M}_{u_{1,2}} v_{\text{right}} \\ v_{\text{left}} = \mathbf{M}_{u_{2,1}} p_{\text{right}} + \mathbf{M}_{u_{2,2}} v_{\text{right}} \end{cases}. \tag{5.18}$$

The impedance Z_{right} is defined as the ratio of p_{right} and v_{right} and the impedance Z_{left} is defined as the ratio of p_{left} and v_{left}. Equation (5.18) then becomes:

$$Z_{\text{left}} = \frac{p_{\text{left}}}{v_{\text{left}}} = \frac{\mathbf{M}_{u_{1,1}} Z_{\text{right}} + \mathbf{M}_{u_{1,2}}}{\mathbf{M}_{u_{2,1}} Z_{\text{right}} + \mathbf{M}_{u_{2,2}}}. \tag{5.19}$$

Impedances Z_{left} and Z_{right} are defined locally. Assuming that this definition is valid and using the definition of a fluid, the effective impedance at the inlet is equal to that of the outlet. The impedance Z of the medium is thus defined as $Z = Z_{\text{right}} = Z_{\text{left}}$ and it can be obtained by solving the following quadratic equation:

$$Z^2 \mathbf{M}_{u_{2,1}} + Z(\mathrm{M}_{u_{2,2}} - \mathbf{M}_{u_{1,1}}) - \mathbf{M}_{u_{1,2}} = 0. \tag{5.20}$$

There are then two solutions for $Z = Z_{\text{diff}_2}$, given by:

$$Z_{\text{diff}_2} = \frac{-(\mathbf{M}_{u_{2,2}} - \mathbf{M}_{u_{1,1}}) \pm \sqrt{(\mathbf{M}_{u_{2,2}} - \mathbf{M}_{u_{1,1}})^2 + 4\mathbf{M}_{u_{1,2}}\mathbf{M}_{u_{2,1}}}}{2\mathbf{M}_{u_{2,1}}}. \tag{5.21}$$

It is reminded that elements $\mathbf{M}_{u_{i,j}}$ are calculated using Equation (5.13). However, it is not assumed that their form comply with the element forms given by Equation (5.1) as it was the case in Version 1. Nevertheless, it can be noted that if $\mathbf{M}_{u_{2,2}} = \mathbf{M}_{u_{1,1}}$, then the expression for the effective impedance can be simplified into the expression for the effective impedance in Version 1. Such an equality would also mean that the transfer matrix in the form given by Equation (5.1) for the fluid model accurately represents the unit cell. Consequently, this equality between the transfer matrix elements $\mathbf{M}_{u_{1,1}}$ and $\mathbf{M}_{u_{2,2}}$ can be used as an indicator to identify if the transfer matrix of the fluid homogenisation model fails to describe the unit cell. The difference $\Delta_{\mathbf{M}_u}$ is introduced and defined by:

$$\Delta_{\mathbf{M}_u} = \mathbf{M}_{u_{2,2}} - \mathbf{M}_{u_{1,1}}. \tag{5.22}$$

When this difference is equal to zero, it does not necessarily imply that the transfer matrix of the homogenisation model accurately describes the unit cell. However the reciprocal implication is valid: if this difference is not equal to zero, then the fluid homogenisation model is not suitable for the unit cell, otherwise it would have been possible to describe the unit cell with a transfer matrix in the form of Equation (5.1). In such cases, Version 2 of the differential method would be more suitable as it disregards the constraints of the transfer matrix form, even thought it still considers some hypotheses of the fluid homogenisation model.

In the following case studies, the difference $\Delta_{\mathbf{M}_u}$ is evaluated as a function of frequency in the form of a relative difference $\Delta^{\text{r}}_{\mathbf{M}_u}$, given by:

$$\Delta^{\text{r}}_{\mathbf{M}_u} = \left| \frac{2(\mathbf{M}_{u_{2,2}} - \mathbf{M}_{u_{1,1}})}{(\mathbf{M}_{u_{2,2}} + \mathbf{M}_{u_{1,1}})} \right|. \tag{5.23}$$

5.2 Implementation

The two retrieval methods require the reflection and transmission coefficients of a periodic structure to retrieve the effective properties of a constituent unit cell. Those scattering coefficients may be obtained from an analytical model for simple geometries such as multilayered media, from experimental measurements or from finite element models.

The scattering coefficients are here numerically calculated using the FEM code ATILA [119]. Water is modelled on the incidence and transmission sides of the media, with the fluid speed of sound set as $c_f = 1500$ m/s and fluid density $\rho_f = 1000$ kg/m^3. Each periodic medium is subject to harmonic plane wave excitation at normal incidence from the fluid domain. A periodic boundary condition is applied on the lateral boundaries of the medium to simulate an infinite array of unit cells in the direction transverse to the direction of sound propagation. Reflection and transmission coefficients are calculated from the pressure at the interface between water and the incidence and transmission sides of the media, respectively.
It has to be noted that in practice, for media with macro-inclusions, the scattering coefficients are not directly calculated at the interfaces but are taken further away and then phase-shifted to be brought back at the interfaces. The reason is that the near field of a locally resonant medium is not uniform, unlike one-dimensional multilayered media, as shown in Figure 5.4. This procedure effectively ensures that, in the presence of a non-uniform near-field, the scattering coefficients describe the behaviour of the finite structure in the far field. It should be pointed out that by definition, the fluid homogenisation model used here cannot describe any complex near field at the medium inlet/outlet.

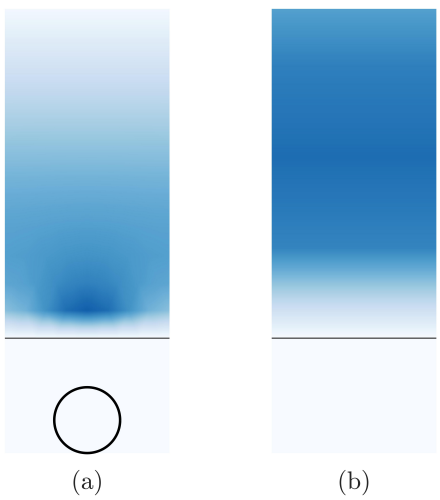

Figure 5.4 – Fluid pressure at the interface with (a) the locally resonant medium and (b) with the multilayered medium.

5.3 Validation

The objective of the current section is to assess the validity of the retrieval methods by comparing the retrieved effective parameters to those obtained with the transfer matrix method of Chapter 2. The multilayered medium examined here corresponds to arrangement version (a) of the periodic cell in Chapter 2. This design is recalled in Figure 5.5. The thickness of silicone and aluminium are selected as $d_\mathrm{s} = 15$ mm and $d_\mathrm{a} = 10$ mm, hence the length of a unit cell becomes $L_u = 40$ mm. The direct inversion method is applied to the multilayered medium comprising $n = 4$ unit cells, as shown in Figure 5.5(b). The differential method is applied for $(n, n+1) = (4, 5)$.

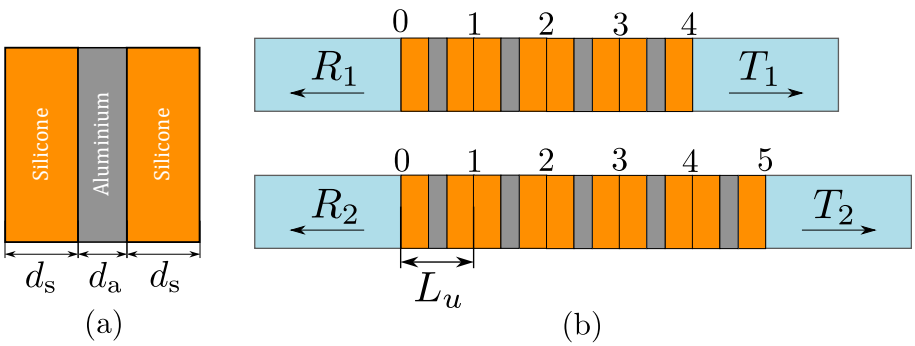

Figure 5.5 – (a) Representation of the symmetric multilayered unit cell comprising layers of silicone and aluminium. (b) Multilayered media comprising 4 and 5 unit cells are also shown for application of the differential method. The direct inversion method is applied to the 4 unit cell medium.

Dispersion curves in terms of the dimensionless (reduced) wavenumber are shown in Figure 5.6, for a frequency range up to 40 kHz. Variations of the effective impedance are presented in Figure 5.7. It can be seen that the direct inversion method, the Bianco and Parodi method and versions 1 and 2 of the differential method give the same wavenumber and the same effective impedance, which is also identical to those calculated with the transfer matrix model presented in Chapter 2. Therefore, both retrieval methods are valid for the description of the propagation in the multilayered medium.

The multilayered structure is not analysed in detail here, as it has already been studied in Chapter 2. As in Chapter 2, the effective properties obtained with the retrieval methods can be used to characterise an effective medium that can accurately predict the reflection and transmission coefficients of a symmetric periodic multilayered medium of arbitrary length. The fluid homogenisation model is thus suitable for the analysis of such structures.

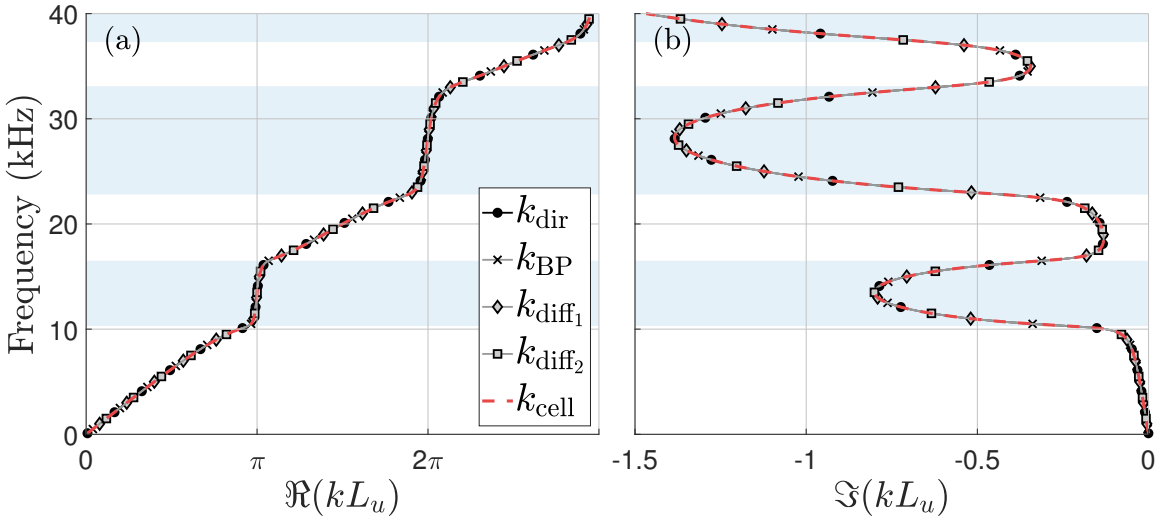

Figure 5.6 – Dispersion curves for the reduced wavenumber obtained with the direct inversion method (k_{dir}), with the Bianco and Parodi method (k_{BP}), with the differential method Version 1 (k_{diff_1}), with the differential method Version 2 (k_{diff_2}) and with the analytical model for multilayered media presented in Chapter 2 (k_{cell}).

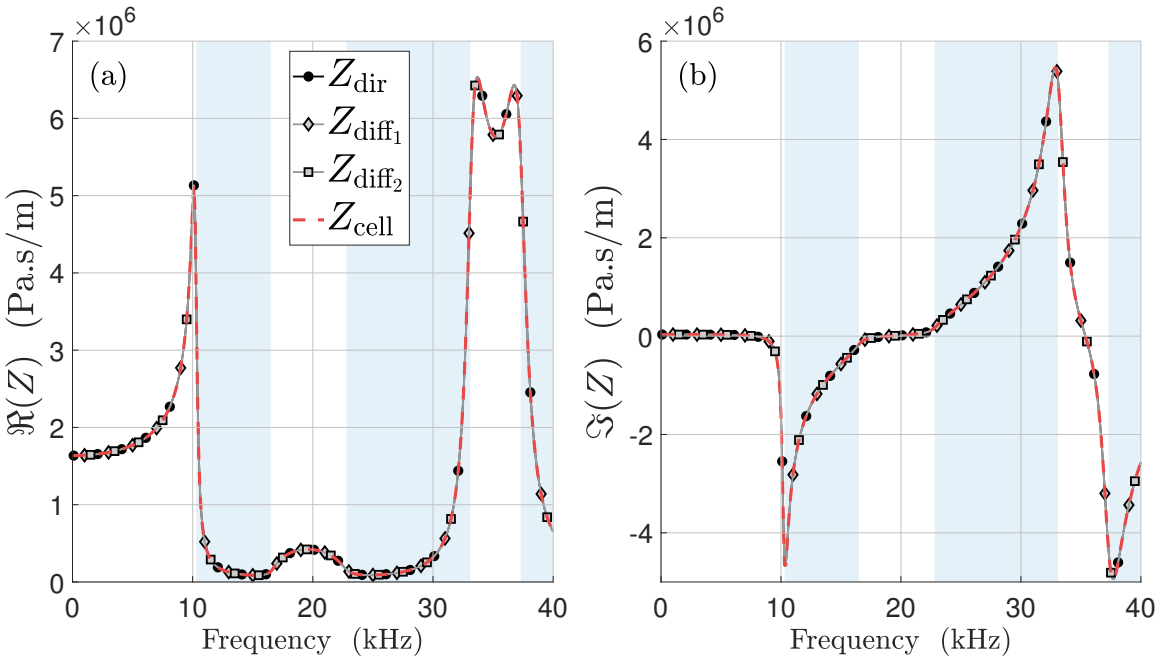

Figure 5.7 – Effective impedance obtained with the direct inversion method (Z_{dir}), with the differential method Version 1 (Z_{diff_1}), with the differential method Version 2 (Z_{diff_2}) and with the analytical model for multilayered media presented in Chapter 2 (Z_{cell}).

5.4 Case Study: Hard Inclusions

5.4.1 Design

In structures with macro-inclusions, additional physical phenomena such as local resonances and boundary effects occur compared to multilayered periodic structures. It therefore becomes more difficult to apply a simple homogenisation model, especially for metamaterials with complex geometry. Several homogenisation difficulties will be identified for the case study of a locally resonant unit cell comprising a cylindrical steel inclusion of diameter $d = 4$ mm in a square polyurethane matrix with a side length of $L_u = 10$ mm, as shown in Figure 5.8(a). Properties of steel and polyurethane are given in Table 5.1.

	ρ (kg.m^{-3})	E (Pa)	ν
Steel	7800	2.15×10^{11}	0.31
Polyurethane	1100	9.9045×10^{7}	0.49333
(loss factors)		12 %	0.17 %

Table 5.1 – Density ρ, Young modulus E and Poisson ratio ν for steel and polyurethane. Loss factors for the polyurethane are expressed as a percentage of the Young modulus and Poisson ratio.

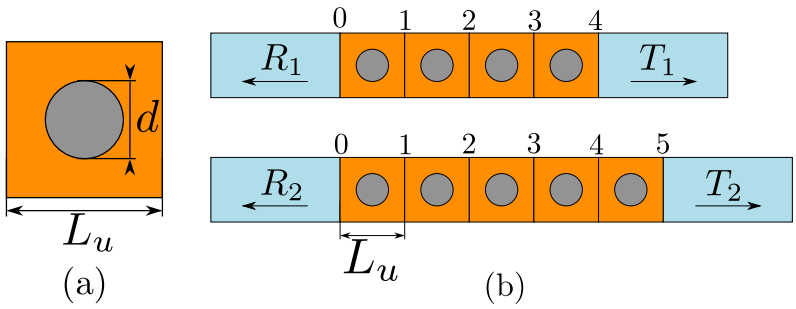

Figure 5.8 – (a) Representation of the locally resonant unit cell. (b) Two segmented media comprising $n = 4$ and $n + 1 = 5$ unit cells. Each cell has length L_u.

5.4.2 Effective Parameters

Dispersion curves in terms of dimensionless wavenumber are plotted in Figure 5.9 up to 30 kHz. Firstly, it can be seen that only the wavenumber from the Bianco and Parodi method (k_{BP}) and the wavenumber from Version 2 of the differential method (k_{diff_2}) are identical, thus validating the fact that the differential method accurately describes propagation in the core of the medium, as does the Bianco and Parodi method. However, the effective wavenumber k_{diff_1} differs significantly, in particular at some frequencies, even

though it should also be the same. To explain this difference, the relative difference between the diagonal elements of the transfer matrix $\mathbf{M}_u$ calculated with the differential method, as per Equation (5.23), is plotted in Figure 5.10.

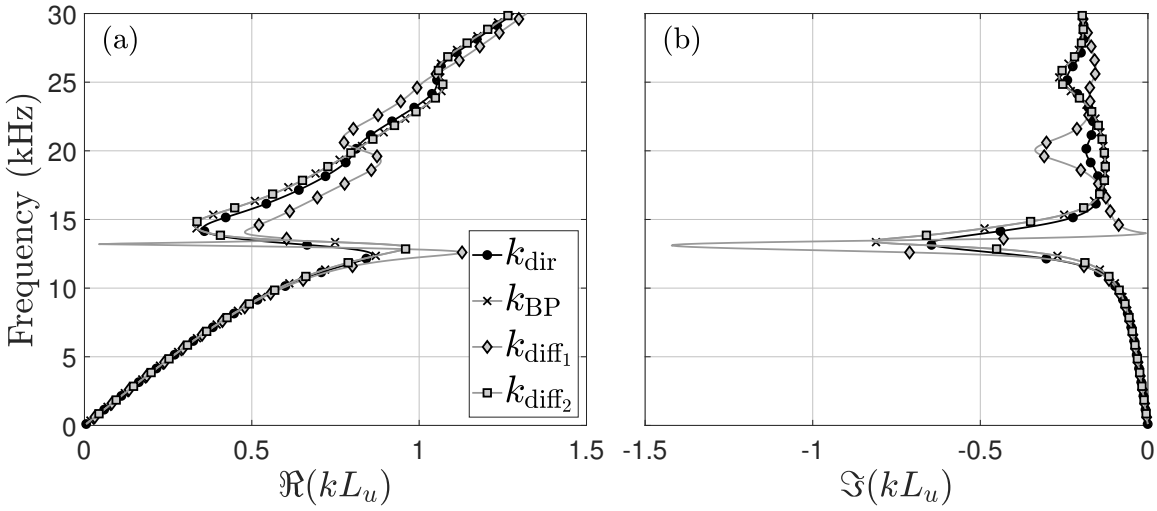

Figure 5.9 – Dispersion curves for the reduced wavenumber obtained with the direct inversion method (k_{dir}), with the Bianco and Parodi method (k_{BP}), with the differential method Version 1 (k_{diff_1}) and with the differential method Version 2 (k_{diff_2}).

This difference reaches a maximum around 13.5 kHz, which exactly corresponds to the frequency where the wavenumber k_{diff_1} differs the most from the others. This significant difference implies that the transfer matrix $\mathbf{M}_u$ of the unit cell does not exist or cannot be in the form of Equation (5.1), as diagonal terms are too different. This explains why Version 1 of the differential method, which is based on the assumption that the transfer matrix $\mathbf{M}_u$ has the form of Equation (5.1) with equal diagonal terms, fails.

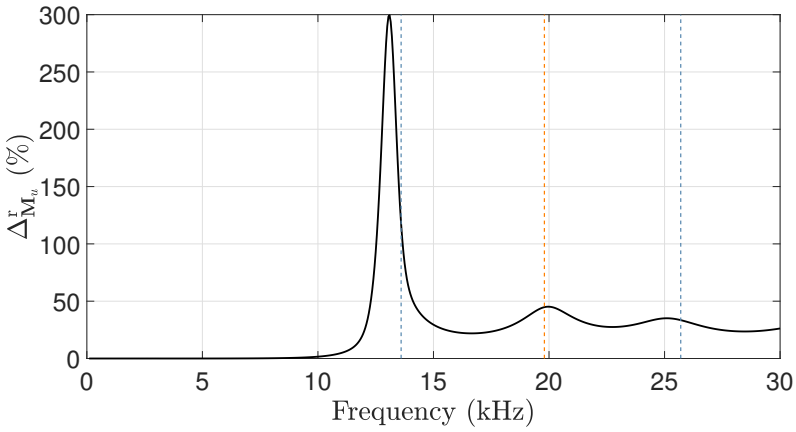

Figure 5.10 – Relative difference between the diagonal elements of the unit transfer matrix calculated with the differential method as per Equation (5.23). The dashed lines highlight the three selected frequencies A, B and C defined in what follows.

Version 1 of the differential method is from now on put aside, since by construction it does not provide a good approximation of the unit cell. Version 2 of the differential method is now referred to as the differential method only. As a reminder, Version 2 gives effective parameters without relying on a transfer matrix form, which is why it still gives good results even though the unit cannot be exactly modelled as a fluid. For the sake of clarity, dispersion curves have also been plotted in Figure 5.11 with only the wavenumber from the direct inversion method and from the differential method (Version 2).

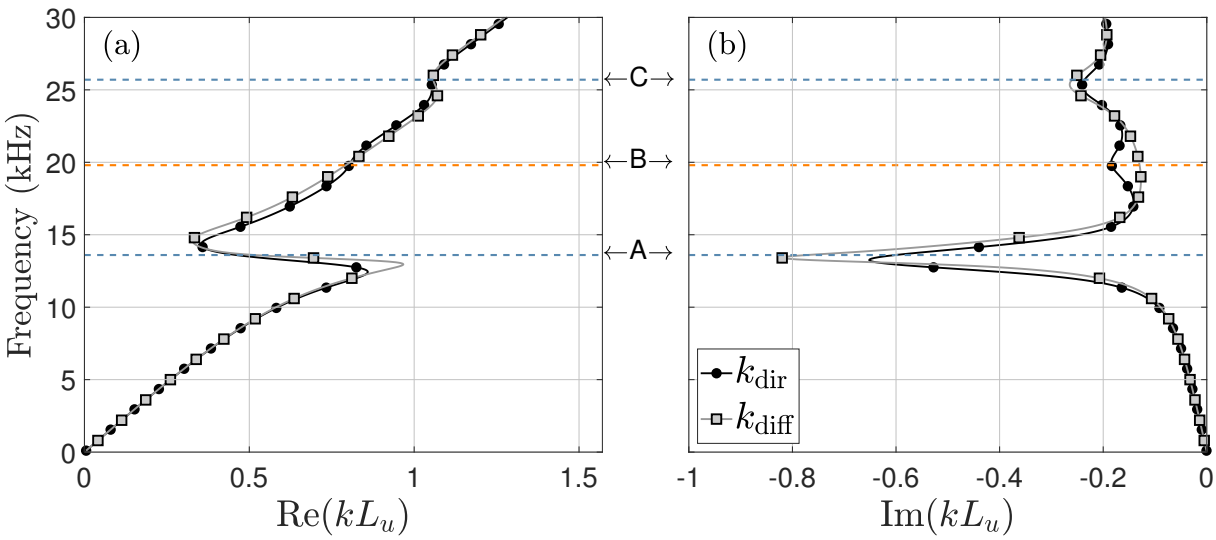

Figure 5.11 – Dispersion curves for the real part (a) and imaginary part (b) of the reduced effective wavenumber for a locally resonant unit cell obtained with the direct inversion method (k_{dir}) and with the differential method (k_{diff}). The dashed lines highlight the three selected frequencies A, B and C.

It can be observed that both retrieval methods lead to the same effective wavenumber up to approximately 10 kHz. Differences appear for frequencies around points A, B and C. These frequencies correspond to resonant modes for which the displacement fields are given in Figure 5.12. Figure 5.12A presents the displacement field in the four-unit medium for frequency A (13.6 kHz). The displacement field exhibits a mass-spring (dipole) resonance where the inclusion represents the rigid mass, translating without undergoing any shape changes, while the host matrix represents the spring that retains the oscillations of the masses. For point C (25.7 kHz), Figure 5.12C shows that the rubber matrix is moving, whereas the steel inclusions are mostly stationary. The waves scattered by the rigid cylinders are trapped in-between the cylinders, leading to resonance of the host rubber. This mode is therefore only existing for the matrix portions which are not at the interfaces in contact with the surrounding water. In Figure 5.11, as the imaginary part of the wavenumber represents the attenuation per distance, the wavenumber derived with the differential method for resonances A and C leads to slightly greater attenuation than the one from the direct inversion method, but the variations remain similar.

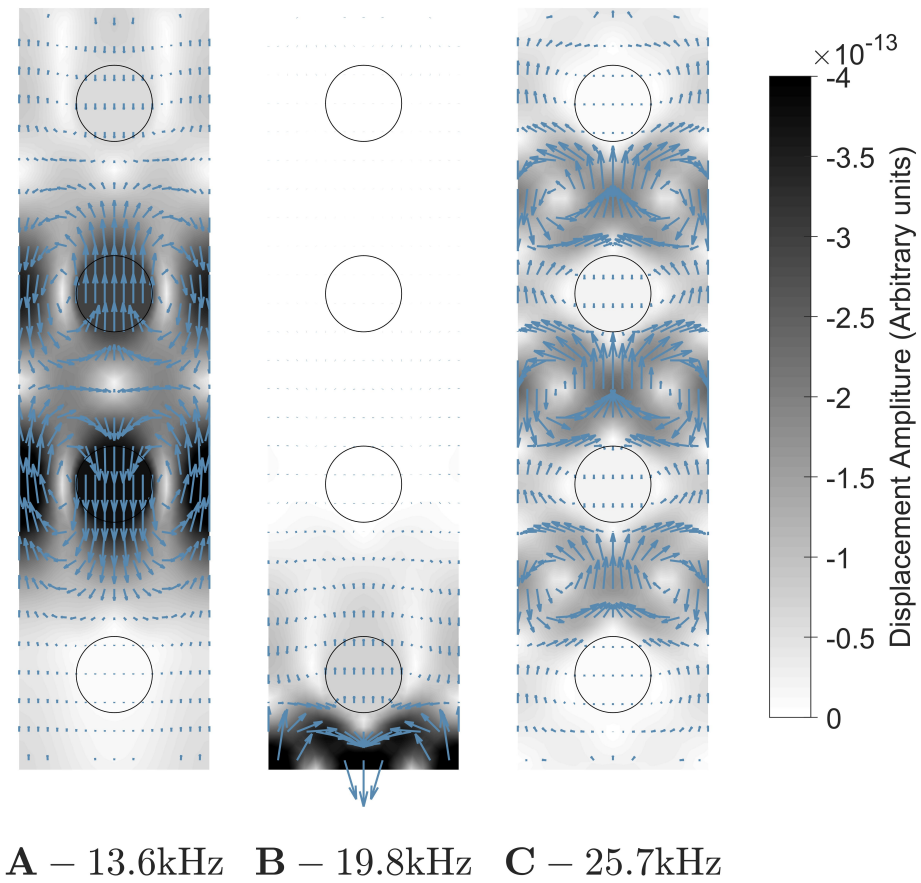

Figure 5.12 – Displacement fields for the four unit medium at given frequencies A, B and C. The arrows indicate the direction of displacement and their length is proportional to the displacement modulus. The shades of grey also reflect the amplitude of the displacement.

Another specific displacement field of the rubber can be observed in Figure 5.12B for frequency B (19.8 kHz), but very localised at the input fluid/medium interface. Point B thus also corresponds to a resonant mode in the matrix which only exists between the interface and the first layer of rigid inclusions. As such, unlike the two other resonances, the boundary interference effects of point B do not vary with the number of unit cells placed after the first unit cell at the interface. In Figure 5.11, the interface mode at point B is associated with an attenuation peak for the direct inversion method. Such attenuation is not apparent using the differential method, which aims to describe the interior of the medium away from the boundary interfaces with the fluid. In contrast, the direct inversion method describes the finite medium including boundary interface effects.

The effective impedance obtained with the direct inversion method and the differential method are plotted in Figure 5.13. It can be seen that the two impedances are fairly similar, except at frequencies around the interface resonance, highlighted by the orange

vertical line. For this resonance, there is a local maximum compared to water impedance, which means the medium is a good reflector for these frequencies. This is consistent with the analysis of the displacement fields in Figure 5.12B corresponding to a coupling between the incident wave and a surface mode only. Nevertheless, it can be noted that the effective impedance from the differential method Z_{diff} is lower than the effective impedance from the direct inversion method Z_{dir}.

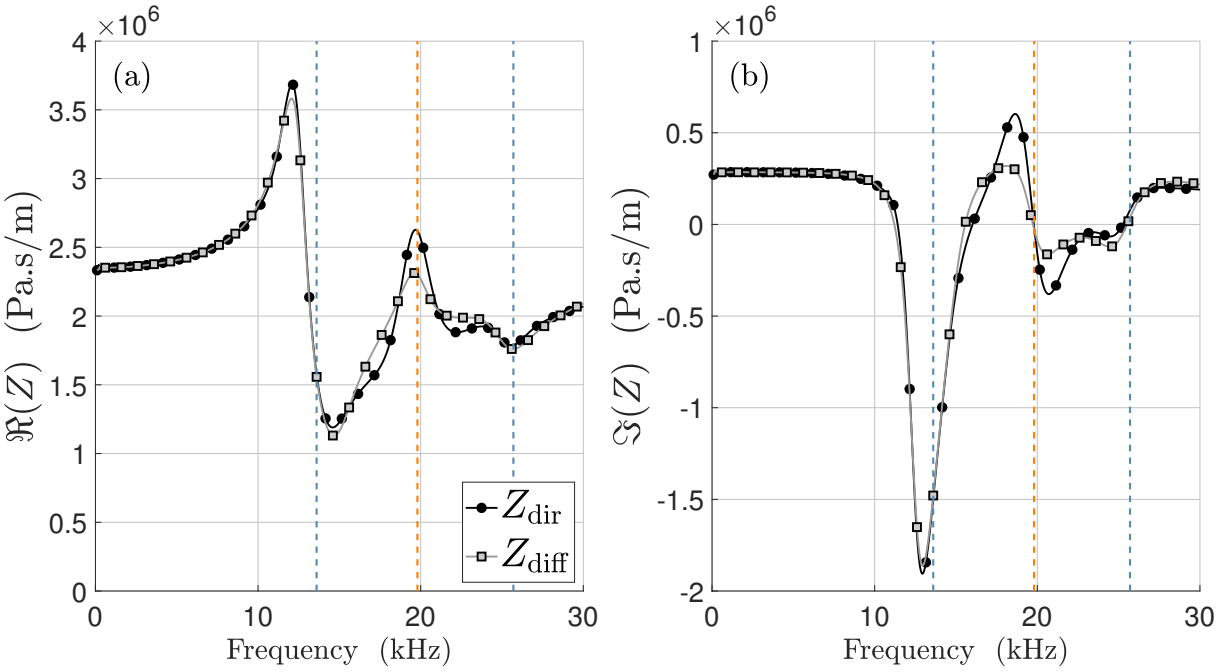

Figure 5.13 – Effective impedance obtained with the direct inversion method (Z_{dir}) and with the differential method (Z_{diff}). The impedance of water is also represented.

The effective properties for the locally resonant medium differ depending on the retrieval method used, which was not the case for the multilayered medium. This is due to the fact that the fluid homogenisation model does not take into consideration complex near field effects and shear wave propagation, as the effective medium is assumed to be a fluid medium in which only longitudinal waves can propagate. This assumption is valid for multilayered structures under normal incidence where only longitudinal modes were excited. However, for structures made of a solid matrix comprising of inclusions, the conversion of longitudinal waves into shear waves due to local resonances cannot be fully described by the present homogenisation model. However, both retrieval methods capture the behaviour of the locally resonant metamaterial with reasonable accuracy. The influence of the number of unit cells used to apply the retrieval methods is examined in the following subsection.

5.4.3 Influence of the Number of Unit Cells

In order to assess the robustness of the two retrieval methods, they are both applied on media of different length. The direct inversion method is applied to four media comprising of designs with $n = 2$, $n = 4$, $n = 8$ and $n = 18$ unit cells. The differential method is applied to the four designs, corresponding to $(2, 3)$, $(4, 5)$, $(8, 9)$ and $(18, 19)$, where the shorter medium is the design used for the direct inversion method, comprising n unit cells. As previously, the wavenumber and effective impedance are calculated for all configurations to visualise the effects of the number of unit cells on the effective parameters.

Figure 5.14 shows the effective wavenumbers obtained by the four applications of the direct inversion method. It can be seen that the effective wavenumbers from the direct inversion method vary depending on the number of units n in the medium. In particular, the attenuation peaks associated to resonances (blue lines) tend to be stronger with increasing n, as indicated by the blue arrows. In contrast, the attenuation peak due to the interface resonance tends to be lower for higher values of n, as indicated by the orange arrow.

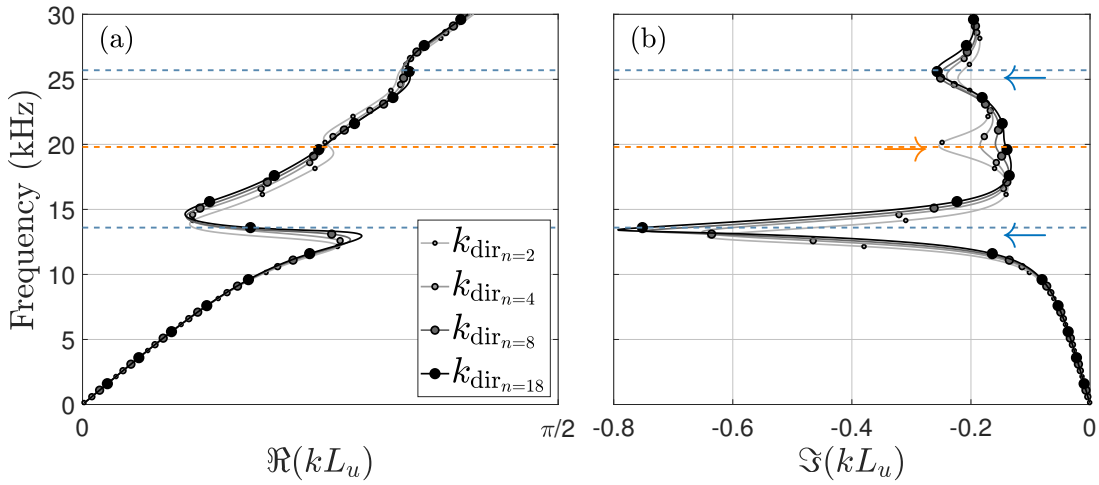

Figure 5.14 – Effective wavenumbers as a function of angular frequency obtained with the direct inversion method for media comprising 2, 4, 8 and 18 unit cells.

For the differential method, in Figure 5.15, there is nearly no difference between the wavenumbers corresponding to the four combinations. As such, the effective wavenumber from the differential method seems independent of the number of unit cells contained in the two segmented media.

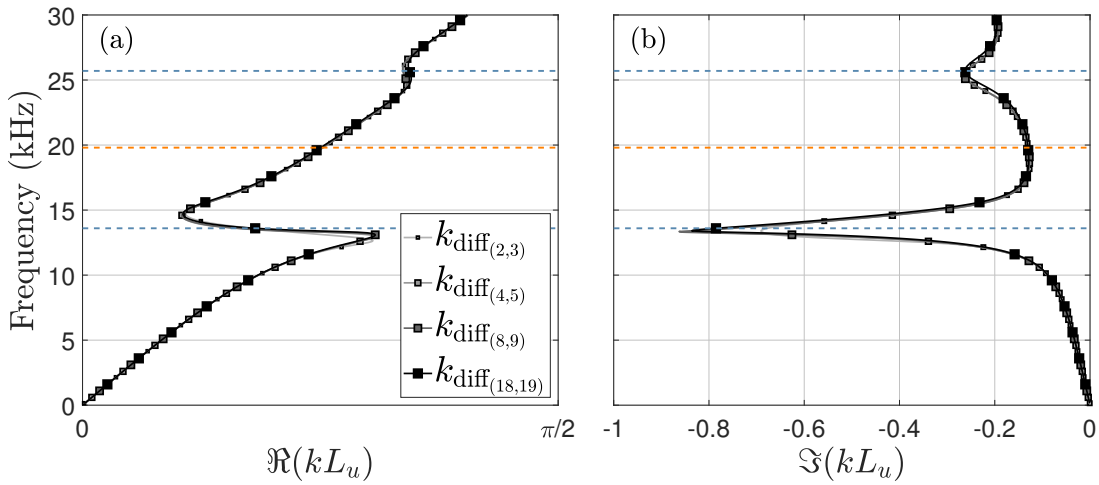

Figure 5.15 – Effective wavenumbers as a function of angular frequency obtained with the differential method for the unit combinations (2,3), (4,5), (8,9) and (18,19).

Similar observations to the effective wavenumber can be made for the variations of the effective impedance. It can therefore be concluded that the effective wavenumber from the direct inversion method is dependent on the number of unit cells n. Further, with increasing number of unit cells, the effective wavenumber converges towards the result obtained using the differential method, corresponding to the effective wavenumber in the medium interior away from boundary interface effects. More specifically, at the interface resonance around 20 kHz, the direct inversion method is strongly influenced by the number of unit cells n whereas the differential method removes the interface effects.

5.4.4 Scattering Predictions

Effective properties from both methods are now used to characterise effective media in order to predict the reflection and transmission coefficients of a segmented metamaterial comprising N unit cells. The length of effective media is thus $L = N \times L_u$. The effective parameters used were obtained for $n = 4$ and are given in Figures 5.11 and 5.13. The scattering coefficients of the effective medium are also compared to coefficients derived from a FE model of the metamaterial comprising N unit cells, as shown in Figure 5.16(a). Figures 5.16(b) and 5.16(c) respectively show the corresponding effective medium characterised by the effective wavenumber and effective impedance obtained using the two retrieval methods. A hybrid effective medium is also introduced in order to take advantages of both methods, by using the effective properties of the direct inversion method at the interfaces and the effective properties from the differential method for the interior of the effective medium. The hybrid medium is therefore made of three domains as shown in Figure 5.16(d).

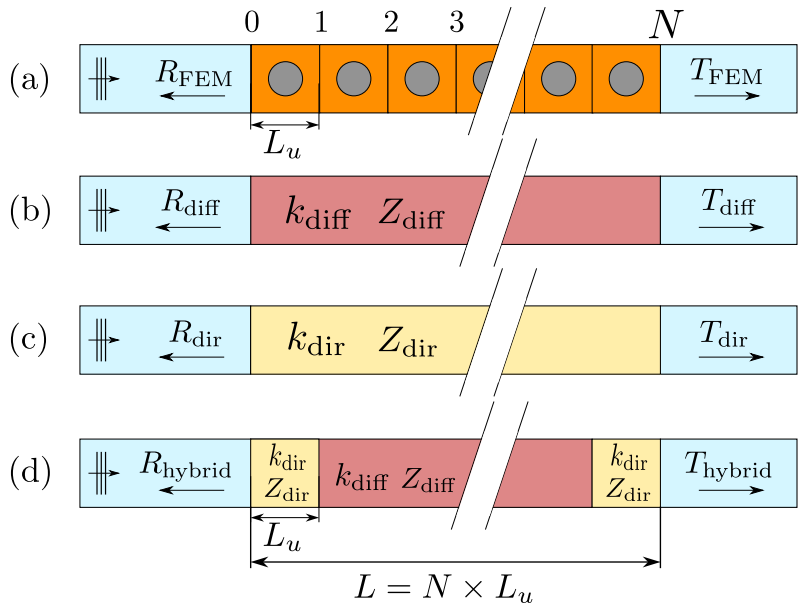

Figure 5.16 – (a) Finite periodic medium of length comprising N unit cells, for which the reflection and transmission coefficients are predicted using an effective medium characterised by the effective wavenumber and impedance obtained using (b) the differential method (diff), (c) the direct inversion method (dir), (d) a hybrid effective medium comprising the direct inversion method at the boundary interfaces and the differential method for the medium away from the interfaces.

Results are presented in Figure 5.17 for $N = 5,\ 9,\ 19$ unit cells. All three effective media represented in Figures 5.16(b) to 5.16(d) accurately predict the reflection and transmission coefficients up to 15 kHz. Above this frequency, the effective parameters from the direct inversion method are strongly dependent on the parameter n, particularly for the interface mode according to Section 5.4.3. As such, using the direct inversion method, the scattering coefficients for a high number N tend to present overestimated interface effects since the effective properties have been obtained for a smaller number n. For the reflection coefficient, the impedance of the first layer plays a major part in the results, as it has been mentioned in Chapter 2 for variant designs of a unit cell. This is because the reflection coefficient is roughly $R \approx (Z_{\text{in}} - Z_f)/(Z_{\text{left}} + Z_f)$, with Z_{in} the effective impedance of the input layer and Z_f the impedance of the fluid. Since $Z_{\text{in}} = Z_{\text{dir}}$ for both effective media represented in Figures 5.16(c) and 5.16(d), the resulting reflection coefficient will be close to that for the medium used to derive Z_{dir}, which here is the $n = 4$-unit medium. Both the direct inversion method and the hybrid method are therefore less suitable for the prediction of the reflection coefficient for various N-layer media than the differential method. For the transmission coefficient, each property characterising the medium is relevant. Accurate predictions are obtained using the differential method, except for the transmission dip around 20 kHz arising from the interface mode. Therefore, the transmission coefficient is better predicted using the hybrid effective medium, as it physically restricts the effective properties of the direct inversion method to the interfaces and the effective properties from the differential method to the core of the effective medium.

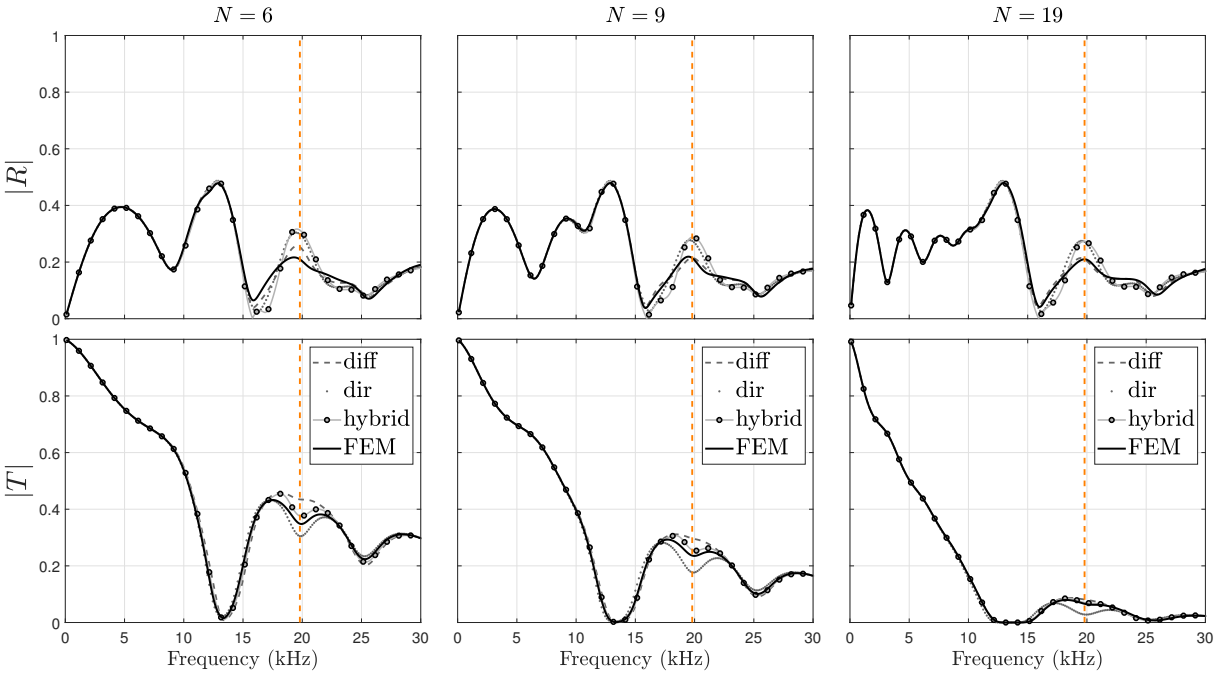

Figure 5.17 – Reflection and transmission coefficients calculated for the effective media characterised by effective parameters of the differential method (dashed lines) or the direct inversion method (dotted lines) that represent a periodic media comprising $N = 5$, $N = 9$ or $N = 19$ unit cells. Scattering coefficients from the hybrid effective medium (circle markers) and from FEM (full lines) are also presented. The dotted orange line highlights the interface resonance frequency.

5.5 Case Study: Voided Inclusions

5.5.1 Effective Parameters

The retrieval methods are herein applied to a different design of a locally resonant unit cell comprising a voided medium, so-called Alberich medium. The design is the same as the previous test case in which rigid steel cylinders are now replaced by voided cylinders of the same diameter. The effective impedances, shown in Figure 5.18, are almost identical and very low for both methods.

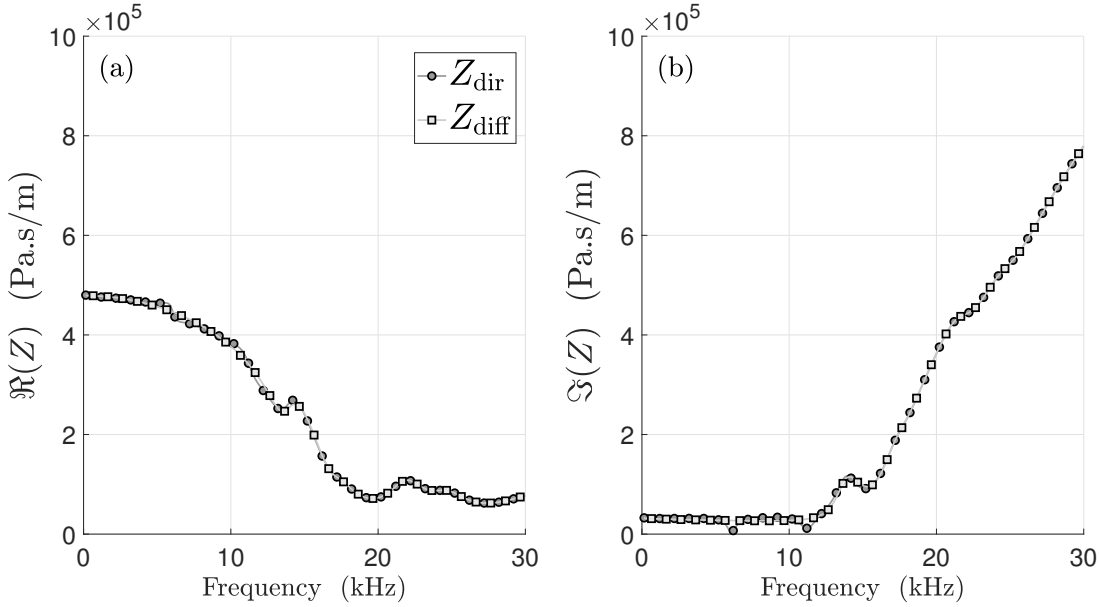

Figure 5.18 – Real and imaginary parts of the effective impedances for the unit cell obtained with the direct inversion method (k_{dir}) and with the differential method (k_{diff}).

The dispersion curves are given in Figure 5.19. We observe that effective wavenumbers differ around 13.8 kHz, which corresponds to a resonant mode in the matrix at the interface similar to the resonant modes observed with the presence of a hard inclusion. The effective wavenumbers using the two retrieval methods significantly differ above 23 kHz. The displacement fields corresponding to point A (23.75 kHz) and B (28.5 kHz) exhibit flexural motion of the matrix layer at the interface, similar to a drum-like up and down motion [33, 120]. This results in significant reflection of the acoustic energy by the first unit cell. As there is very little propagation within the medium beyond the first unit cell, the differential method cannot accurately define the wavenumber in the interior of the medium. The accuracy of the predictions using the effective parameters is studied in what follows.

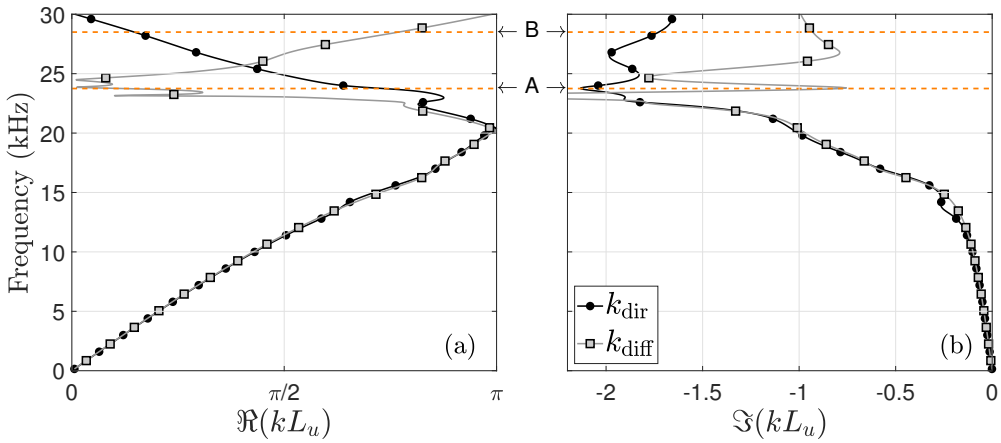

Figure 5.19 – Dispersion curves for the real part (a) and imaginary part (b) of the reduced effective wavenumber for the unit cell obtained with the direct inversion method (k_{dir}) and with the differential method (k_{diff}). Two frequencies, referred to as A and B, are selected and highlighted by the orange dotted lines.

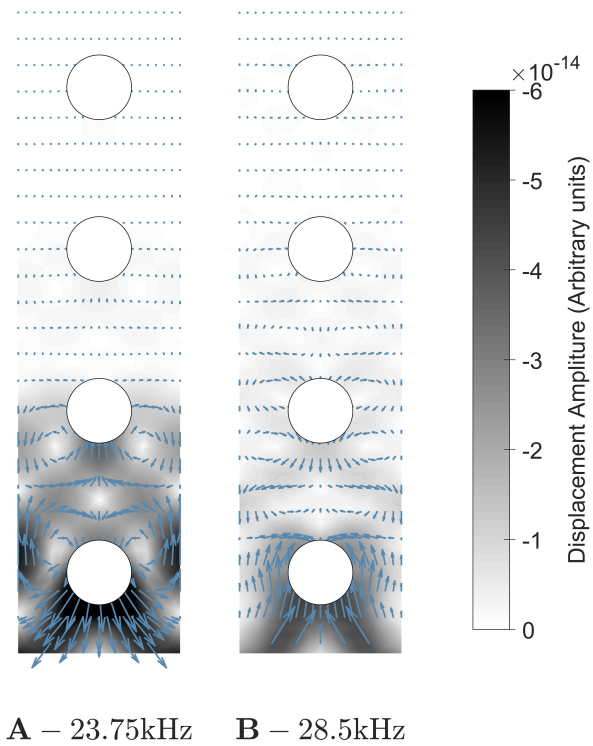

Figure 5.20 – Displacement fields for the four unit cell medium at frequencies corresponding to points A and B in Figure 5.19. The arrows indicate the direction of displacement and their size is proportional to the displacement modulus. The shades of grey also reflect the amplitude of the displacement.

5.5.2 Scattering Predictions

The reflection and transmission coefficients are presented to check the validity of the homogenisation approach for the voided medium design. Results are presented in Figure 5.21 for $N = 5,\ 9,\ 19$ unit cells using the various effective designs shown in Figure 5.16. The reflection coefficients for all effective designs are in close agreement with each other. Since the reflection coefficient is mostly dependent on the medium impedance at the interface on the incident side and since $Z_{\text{dir}} \approx Z_{\text{diff}}$, all effective media give similar results. The accuracy of the predictions then validates the effective impedance given by both retrieval methods.

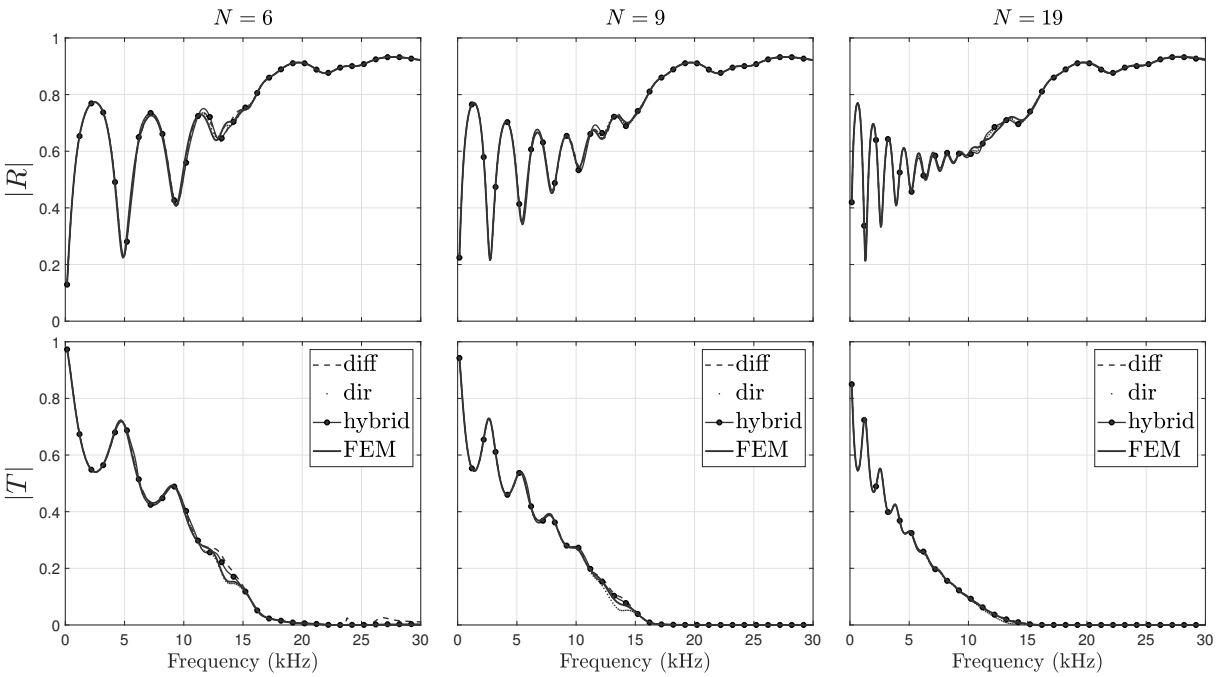

Figure 5.21 – Reflection and transmission coefficients calculated for the effective media characterised by effective parameters of the differential method (dashed lines), the direct inversion method (dotted lines) that represent an Alberich medium comprising $N = 5$, $N = 9$ or $N = 19$ unit cells. Scattering coefficients from the hybrid effective medium (circle markers) and from FEM (full lines) are also presented.

We observe that the interface mode around 13.8 kHz does not lead to a significant dip in the transmission coefficient. The hybrid method nonetheless predicts the local minimum related to the interface resonance with greater accuracy than the differential method, which removes interface effects, and the direct inversion method which accentuates the effects of the interface resonance. At higher frequencies, the transmission coefficient becomes extremely low, which is accurately predicted by the homogenised media. There are however a few discrepancies above 23 kHz for the prediction using the differential method only, for $N = 5$, which do not occur using the hybrid method or the direct inversion method. It thus confirms that when most of the acoustic energy does not

propagate further than the first unit cell, the differential method cannot properly define the effective wavenumber in the interior medium. However, the direct inversion method accurately captures the strong reflection by the first unit cell. As such, the hybrid method provides an accurate prediction as it physically restricts the effective properties of the direct inversion method at the effective medium input.

5.6 Summary

Two retrieval methods have been introduced, corresponding to the direct inversion method and the differential method. The direct inversion method uses the reflection and transmission coefficients of a medium comprising a number of identical unit cells, immersed in a fluid, while the differential method requires two segmented media comprising n and $n+1$ unit cells. Both retrieval methods lead to an effective wavenumber and an effective impedance of a homogeneous fluid medium. The effective wavenumber from the differential method was able to describe the interior of the medium whereas the direct inversion method captures the effects related to the medium's finite size and interfaces with the surrounding fluid media on the incidence and transmission sides. As such, to predict the scattering coefficients, a hybrid effective medium was developed, whereby the first and last layers are defined with the effective properties from the direct inversion method and the core layer is defined by the differential method. Reflection and transmission coefficients have been predicted using effective media characterised by the direct inversion method, by the differential method and by the hybrid medium. The reflection coefficient is accurately predicted by the differential method. The hybrid medium provides accurate predictions of the transmission coefficient as it physically restricts the effective properties of the direct inversion method to the interface and uses the differential method to describe the core of the medium. This work has been published in [121].

Three case studies have been analysed corresponding to a multilayered medium and locally resonant designs with hard or voided cylindrical inclusions. For the multilayered medium, both retrieval methods lead to the same effective parameters, also identical to those obtained with the transfer matrix-based model presented in Chapter 2. However, the two retrieval methods differ for a locally resonant media with either steel or voided cylinders in a viscoelatic matrix. For the design with hard scatterers, variations of the effective parameters have been analysed for each physical phenomena observed, namely, dipole resonance, a trapped mode and an interface mode. The differential method accurately removes the interface effects and gives the effective properties describing the interior of the medium, independent of the number of unit cells initially considered. In contrast, using the direct inversion method, variations in the effective properties at frequencies associated with an interface resonant mode can be observed. Similar observations have been made for the design with voided scatterers. For this design, the differential method cannot provide the effective wavenumber due to very little wave propagation in the medium interior.

The retrieval methods described here may be beneficial to get a better understanding of wave propagation in a metamaterial coating. Moreover, the hybrid method is an efficient tool to predict and optimise the acoustic performance of coating designs that may contain less classical inclusions. In Chapter 7, the retrieval methods will be applied to several metamaterial designs in order to create a database of effective properties associated with various inclusion shapes, sizes and materials. Effective properties will then be used in an optimisation process in order to obtain structures with a good acoustic performance over a wide frequency range. The work in the present chapter is therefore useful to quickly and

easily make a topological optimisation of acoustic coatings for underwater applications using fluid properties.

In general, the goal of these methods is to build homogeneous equivalent media which are a precise approximation of their micro-structured counterparts. Effective media can be used to study metamaterials with complex or arbitrary geometries for which analytical models do not apply. The proposed homogenisation approach may be especially useful in the study of large metamaterial-based systems including structural gradients, such as the ones considered in transformation acoustic designs. Similarly, the proposed homogenisation approach could prove useful in the study of multi-scale metamaterials to alleviate the simulation issues related to the presence of complex geometries at different scales, by allowing the replacement of the smaller structures by equivalent media.

Chapter 6

Homogenisation for Non-symmetric Designs

In this chapter, the direct inversion method and the differential method are extended in order to obtain the effective parameters of finite periodic and asymmetric structures with macro-inclusions. It is assumed that such a structure can be described by an effective Willis fluid similar to the asymmetric multilayered unit cells in Chapter 2. A first case study is presented, consisting of an asymmetric version of the locally resonant medium with hard inclusions studied in Chapter 5. This case study is completed by a parametric study that shows the influence of off-centering the resonant inclusion on the variations of the effective parameters and acoustic performances. A second case study focuses on an asymmetric voided medium in which Willis coupling is not introduced by off-centering the inclusion as in the first case study, but by combining two symmetric layers. The effects on the effective properties and acoustic performance are examined.

Contents

6.1 Methodology 134

6.1.1 Willis Fluid Homogenisation Model 134

6.1.2 Direct Inversion Method 134

6.1.3 Differential Method 136

6.2 Case study: Hard Inclusions 139

6.2.1 Design 139

6.2.2 Homogenisation 140

6.2.3 Parametric Study 143

6.3 Case study: Voided Inclusions 147

6.3.1 Homogenisation 147

6.3.2 Variant Approach 149

6.4 Summary 155

6.1 Methodology

6.1.1 Willis Fluid Homogenisation Model

Similar to the homogenisation theory for one-dimensional multilayered structures presented in Chapter 2, the objective here is to define the effective medium that would replace an asymmetric unit cell. A Willis fluid model is selected to describe the effective medium, thus characterised by an effective wavenumber k, a Wills characteristic impedance Z_W and an asymmetry coefficient W, as previously presented in Chapter 2. Propagation in a Willis fluid can be represented by a transfer matrix of the form:

$$\mathbf{M} = \begin{bmatrix} \cos(kh) - W\sin(kh) & \mathrm{i}Z_W \sin(kh)(1+W^2) \\ \frac{\mathrm{i}\sin(kh)}{Z_W} & \cos(kh) + W\sin(kh) \end{bmatrix}. \tag{6.1}$$

Three effective parameters are thus required (k, Z_W, W), whereas there were only two effective parameters for the symmetric case $(k,\, Z)$. The extensions presented in this Chapter can also be applied to symmetric configurations, since it implies that the asymmetry coefficient W is equal to 0, which reduces the number of undetermined parameters to two.

6.1.2 Direct Inversion Method

As in Chapter 5, the medium is modelled as a segmented structure comprising n repetitions of an identical unit cell of length L_u. Coefficients S are calculated at the interfaces between the segmented medium and the surrounding fluid medium of impedance Z_f. It is worth remembering that S_{11} is different from S_{22} for asymmetric structures. Two calculations are thus required, considering first an incident wave-front towards the x positive and then towards x negative, as shown in Figure 6.1.

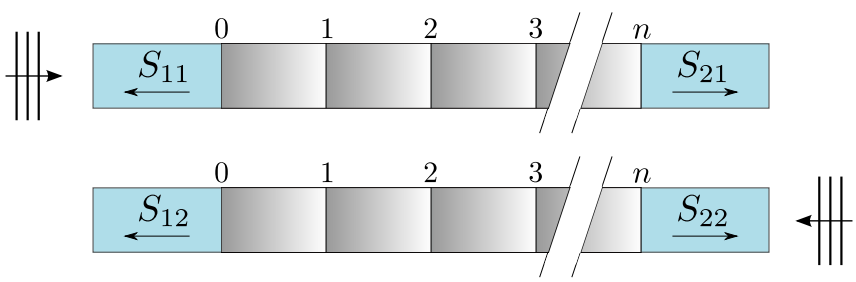

Figure 6.1 – Schematic diagram illustrating the direct inversion method, applied to a segmented medium comprising n identical asymmetric unit cells. Coefficients S of the medium are also shown.

The global transfer matrix $\mathbf{M}_n$ of the periodic medium containing n unit cells can be calculated using its S-parameters:

$$\mathbf{M}_n = \begin{bmatrix} \frac{S_{11}-S_{22}-S_{11}S_{22}+S_{12}S_{21}+1}{2S_{21}} & Z_f\frac{S_{11}+S_{22}+S_{11}S_{22}-S_{12}S_{21}+1}{2S_{21}} \\ \frac{1}{Z_f}\frac{-S_{11}-S_{22}+S_{11}S_{22}-S_{12}S_{21}+1}{2S_{21}} & \frac{-S_{11}+S_{22}-S_{11}S_{22}+S_{12}S_{21}+1}{2S_{21}} \end{bmatrix}. \tag{6.2}$$

This expression is given in Appendix A. The homogenisation model is applied to each unit cell, so the global transfer matrix of the segmented medium may also be written as the product of the transfer matrix of each unit cell. This leads to $\mathbf{M}_n = (\mathbf{M}_u)^n$, where $\mathbf{M}_u$ is the transfer matrix of a constituent unit cell of the form given by Equation (6.1). The calculation of $(\mathbf{M}_u)^n$ for any n integer is equivalent to replacing only the thickness L_u by nL_u without changing the wavenumber or the impedance associated with the matrix $\mathbf{M}_u$. The global transfer matrix expression is thus given by :

$$\mathbf{M}_u^n = \begin{bmatrix} \cos(nk_{\text{dir}}L_u) - W_{\text{dir}}\sin(nk_{\text{dir}}L_u) & \mathrm{i}Z_{\text{dir}}\sin(nk_{\text{dir}}L_u)(1+W_{\text{dir}}^2) \\ \frac{\mathrm{i}\sin(nk_{\text{dir}}L_u)}{Z_{\text{dir}}} & \cos(nk_{\text{dir}}L_u) + W_{\text{dir}}\sin(nk_{\text{dir}}L_u) \end{bmatrix}. \tag{6.3}$$

The global transfer matrix expression given by Equation (6.3) is equal to the global transfer matrix calculated using the scattering response of the medium given by Equation (6.2). The effective parameters are derived from this equality as detailed in what follows. We herein introduce the notation $\mathbf{M}_{n_{i,j}}$ to express the elements of the global transfer matrix $\mathbf{M}_n$, with $1 \leq i, j \leq 2$. The effective wavenumber k_{dir} is first obtained with:

$$k_{\text{dir}} = \frac{\ln(\Lambda_{1,2})}{\mathrm{i}nL_u} + \frac{2\pi m}{nL_u}, \tag{6.4}$$

where m is an integer whose value is determined in such a way that the effective wavenumber as a function of frequency is continuous, and where Λ_1 or Λ_2 are the eigenvalues of the transfer matrix $\mathbf{M}_n$. The material passivity condition imposes the choice of the eigenvalue so that the imaginary part of k_{dir} is negative. The asymmetry coefficient W_{dir} and the Willis characteristic impedance Z_{dir} are then given by:

$$W_{\text{dir}} = \frac{-\mathbf{M}_{n_{1,1}} + \cos(k_{\text{dir}}nL_u)}{\sin(k_{\text{dir}}nL_u)}, \tag{6.5}$$

$$Z_{\text{dir}} = \sqrt{\frac{\mathbf{M}_{n_{1,2}}}{\mathbf{M}_{n_{2,1}}(1+W_{\text{dir}}^2)}}. \tag{6.6}$$

6.1.3 Differential Method

Two media are modelled as segmented structures comprising n and $n+1$ periodic repetitions of an identical constituent unit cell, as shown in Figure 6.2. The extra portion added to the second segmented medium is one unit cell of length L_u.

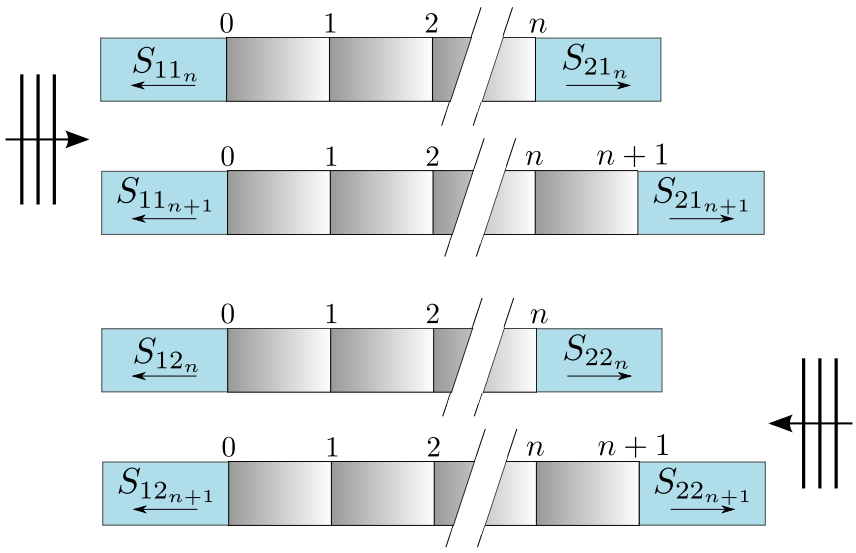

Figure 6.2 – Schematic diagram illustrating the differential method, applied to segmented media comprising n and $n+1$ identical asymmetric unit cells. Coefficients S_n and S_{n+1} of these media are also defined.

The transfer matrices of the two media are expressed and calculated using their S coefficients. The global transfer matrix $\mathbf{M}_n$ of the shorter periodic medium with n unit cells can be calculated as follows:

$$\mathbf{M}_n = \begin{bmatrix} \frac{S_{11_n} - S_{22_n} - S_{11_n}S_{22_n} + S_{12_n}S_{21_n} + 1}{2S_{21_n}} & Z_f \frac{S_{11_n} + S_{22_n} + S_{11_n}S_{22_n} - S_{12_n}S_{21_n} + 1}{2S_{21_n}} \\ \frac{1}{Z_f} \frac{-S_{11_n} - S_{22_n} + S_{11_n}S_{22_n} - S_{12_n}S_{21_n} + 1}{2S_{21_n}} & \frac{-S_{11_n} + S_{22_n} - S_{11_n}S_{22_n} + S_{12_n}S_{21_n} + 1}{2S_{21_n}} \end{bmatrix}. \tag{6.7}$$

The global transfer matrix $\mathbf{M}_{n+1}$ of the longer segmented medium can be calculated using this same equation but replacing n by $n+1$.

As all unit cells are identical, the global transfer matrix of a segmented medium may also be written as the product of the transfer matrix of each unit cell. This leads to $\mathbf{M}_n = (\mathbf{M}_u)^n$ for the shorter segmented medium and $\mathbf{M}_{n+1} = (\mathbf{M}_u)^{n+1}$ for the longer medium, where $\mathbf{M}_u$ is the transfer matrix of a constituent unit cell. The transfer matrix $\mathbf{M}_u$ of a unit cell can now be deduced from the product of the global transfer matrix of the longer segmented medium with the inverse of that of the shorter medium, that is:

$$\mathbf{M}_{n+1}(\mathbf{M}_n)^{-1} = (\mathbf{M}_u)^{n+1-n} = \mathbf{M}_u. \tag{6.8}$$

The left hand side of Equation (6.8) corresponding to the product $\mathbf{M}_{n+1}(\mathbf{M}_n)^{-1}$ can be calculated in terms of the scattering responses of the two segmented media, using Equation (6.7). The transfer matrix $\mathbf{M}_u$ is then used to derived the effective wavenumber k_{diff} as per:

$$k_{\text{diff}} = \frac{\ln(\Lambda_{1,2})}{\mathrm{i}L_u} + \frac{2\pi m}{L_u}, \tag{6.9}$$

where m and Λ are chosen as in the direct inversion method. As for the symmetric case, this expression is independent of the expression of the transfer matrix elements.

The determination of the Willis characteristic impedance and the asymmetry coefficient is less straightforward than the determination of the effective wavenumber. The difficulty here comes from the fact that, unlike the direct inversion method, the effective parameters for the differential method must be obtained without considering the transfer matrix form given by Equation (6.1). This was relatively easy when the unit cell was symmetric since $Z_{\text{left}} = Z_{\text{right}} = Z_{\text{eff}} = Z^+ = -Z^- = Z_W$. Nevertheless, the asymmetry of the unit breaks all these equalities. Therefore, effective impedances for forward propagating waves and for backward propagating waves are first obtained, in dissociated ways, as developed below.

The transfer matrix $\mathbf{M}_u$ calculated as per Equation (6.8) is used to obtain the transfer matrix from which the effective impedance for forward propagating waves is derived, as per Figure 6.3(a). The transfer matrix $\mathbf{M}_u$ derived using Equation (6.8) is thus now referred as $\mathbf{M}_u^+$. A distinction is indeed necessary as it is found that the transfer matrix of the unit changes depending on the orientation of the unit cell. As such, the transfer matrix of the reversed-orientation unit shown in Figure 6.3(b) is also required and is referred to as $\mathbf{M}_u^-$. It is calculated by replacing S_{11} by S_{22} and S_{22} by S_{11} in Equation (6.7), which are then used in Equation (6.8).

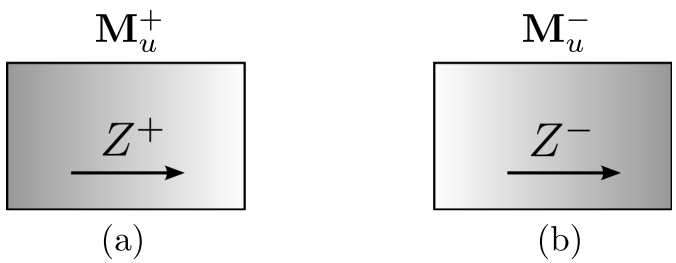

Figure 6.3 – Asymmetric unit cell (a) oriented to derive the effective impedance for forward propagating waves Z^+ and (b) in the reverse orientation to derive Z^-.

The matrix $\mathbf{M}_u^+$ is then used to calculate the effective impedance for forward propagating waves Z^+, while the transfer matrix $\mathbf{M}_u^-$ leads to the effective impedance Z^- for backward propagating waves.

Using $\mathbf{M}^{+}_{u_{i,j}}$ where $1 \leq i,j \leq 2$, the elements of this transfer matrix, the effective impedance for forward propagating waves Z^{+}_{diff} is given by:

$$Z^{+}_{\text{diff}} = \frac{-(\mathbf{M}^{+}_{u_{2,2}} - \mathbf{M}^{+}_{u_{1,1}}) \pm \sqrt{(\mathbf{M}^{+}_{u_{2,2}} - \mathbf{M}^{+}_{u_{1,1}})^2 + 4\mathbf{M}^{+}_{u_{1,2}}\mathbf{M}^{+}_{u_{2,1}}}}{2\mathbf{M}^{+}_{u_{2,1}}}. \tag{6.10}$$

Similarly, the effective impedance for backward propagating waves Z^{-}_{diff} is given by:

$$Z^{-}_{\text{diff}} = \frac{-(\mathbf{M}_{u^{-}_{2,2}} - \mathbf{M}^{-}_{u_{1,1}}) \pm \sqrt{(\mathbf{M}^{-}_{u_{2,2}} - \mathbf{M}^{-}_{u_{1,1}})^2 + 4\mathbf{M}^{-}_{u_{1,2}}\mathbf{M}^{-}_{u_{2,1}}}}{2\mathbf{M}^{-}_{u_{2,1}}}. \tag{6.11}$$

The real part of the effective impedances must be positive to satisfy the material passivity constraint. It is now possible to calculate the Willis characteristic impedance Z_{diff} and the asymmetry coefficient W_{diff} as follows:

$$Z_{\text{diff}} = \frac{Z^{+}_{\text{diff}} + Z^{-}_{\text{diff}}}{2}, \tag{6.12}$$

$$W_{\text{diff}} = \frac{\mathrm{i}(Z^{+}_{\text{diff}} - Z^{-}_{\text{diff}})}{-Z^{-}_{\text{diff}} - Z^{+}_{\text{diff}}}. \tag{6.13}$$

6.2 Case study: Hard Inclusions

6.2.1 Design

Both retrieval methods have been validated by considering the asymmetric multilayered design presented in Chapter 2, for which the retrieved properties are found to be identical to those obtained using the transfer matrix method for the unit cell. A locally resonant unit is now examined, formed by an off-centered cylindrical steel inclusion of 4 mm diameter in a square polyurethane matrix with a side length of 1 cm. Properties of steel and polyurethane are given in Table 5.1 and the design is shown in Figure 6.4.

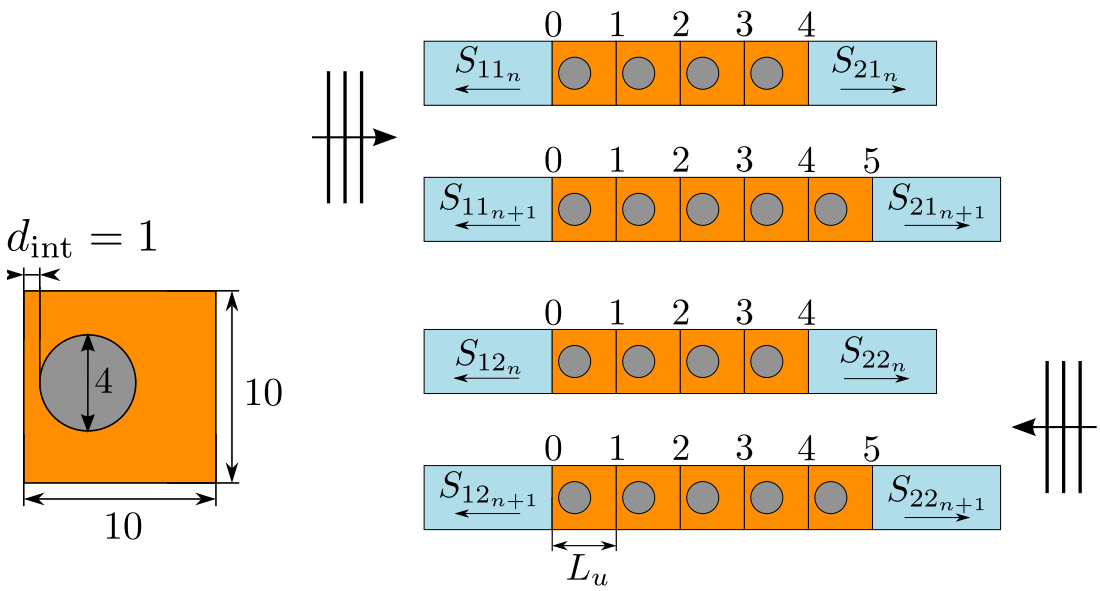

Figure 6.4 – Representation of the asymmetric locally resonant unit cell. Dimensions are in millimetres. The differential method is applied to the segmented media comprising of 4 and 5 unit cells for application of the differential method. The direct inversion method is applied to the first medium, containing 4 unit cells.

6.2.2 Homogenisation

The effective wavenumber for the asymmetric unit cell is shown in Figure 6.5. It is first observed that the differential method leads to the same wavenumber as for the symmetric unit cell considered in Chapter 5. In an infinite periodic medium, the effective wavenumber is indeed independent from the choice of the unit cell, as shown in Chapter 2 with the 4 versions of a multilayered unit cell. Since the differential method provides the wavenumber within the interior of the medium by removing the interface effects, the same wavenumber is obtained for the symmetric unit as for any non-symmetric version of this unit when this method is used.

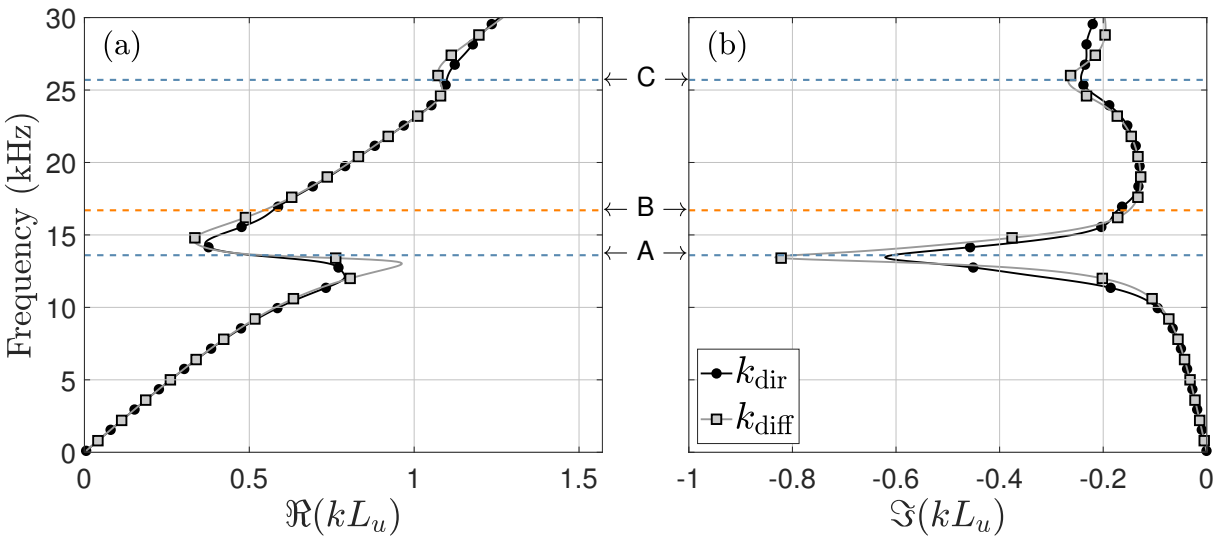

Figure 6.5 – Effective wavenumbers obtained using the direct inversion method and the differential method for the asymmetric unit with macro-inclusions.

On the contrary, the effective wavenumber for the asymmetric unit cell derived using the direct inversion method is different from the one obtained for the symmetric unit. By comparing Figure 5.11 and Figure 6.5, it can be seen that frequencies for resonances A and C remain unchanged, but differences are especially visible for the interface resonance, which is no longer present at about 20 kHz. An interface effect now creates a small attenuation peak at frequency B for the effective wavenumber k_{dir}. This modification of the interface resonance is further studied in the next subsection.

The characteristic Willis impedance is shown in Figure 6.6. Both retrieval methods lead to similar characteristic impedances, also similar to the effective impedance of the symmetric unit.

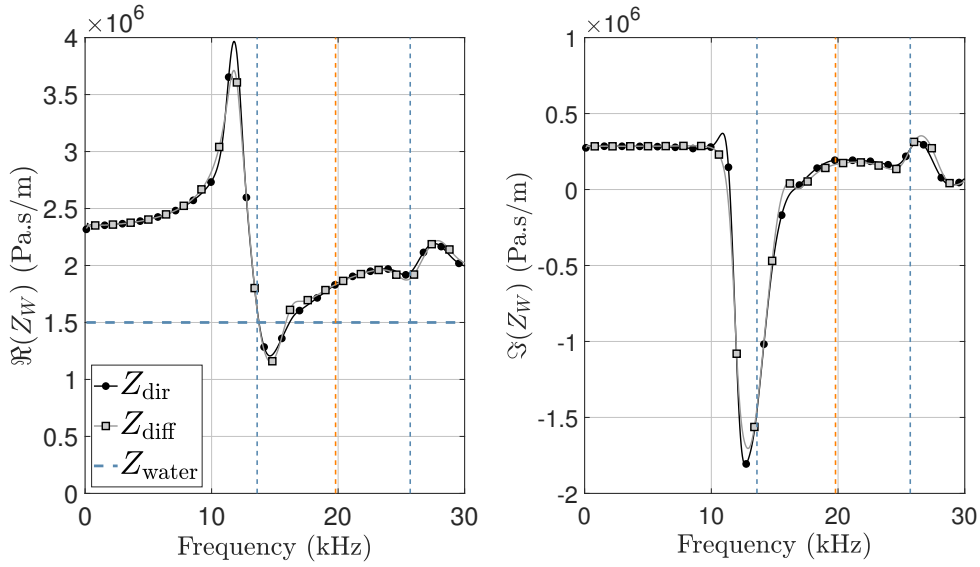

Figure 6.6 – Effective characteristic impedances obtained using the direct inversion method and the differential method for the asymmetric unit with macro-inclusion.

Slight differences between the two retrieval methods are observed amongst the variations of the asymmetry coefficient W, given in Figure 6.7. It is first noted that for the mass-spring resonance corresponding to the first blue dotted line, both methods give almost the same asymmetry coefficient, which is very close to 0, corresponding to the value that W takes for a symmetric medium. This implies that for this resonance, the asymmetry of the unit has very little influence and the behaviour of the asymmetric medium is similar to that of the symmetric medium.

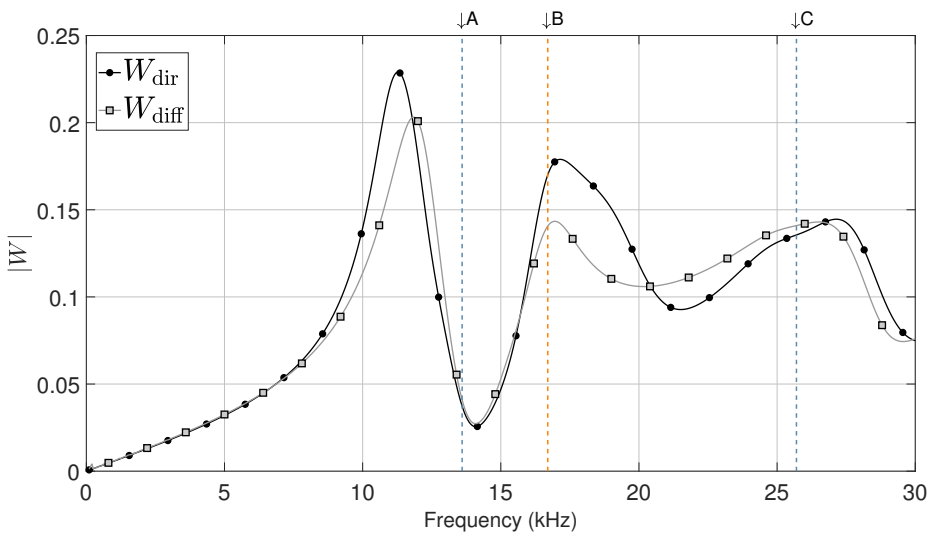

Figure 6.7 – Non-dimensional asymmetry coefficient obtained using the direct inversion method and the differential method for the asymmetric unit with macro-inclusions.

This is also confirmed by the comparison between the scattering coefficients of the asymmetric medium and those of the symmetric medium, respectively shown by the red and green colored dotted lines in Figure 6.8. They are indeed different over the entire frequency range except just after the first resonant frequency, where the asymmetry coefficient of the asymmetric unit is almost null.

In addition, Figure 6.8 leads to the same conclusion as for the symmetric case regarding the accuracy of the predictions, which is that S_{11} is better predicted by the differential method and $T = S_{12} = S_{21}$ by the direct inversion method since the medium is made of only 5 unit cells. Ultimately, the hybrid method best predicts both.

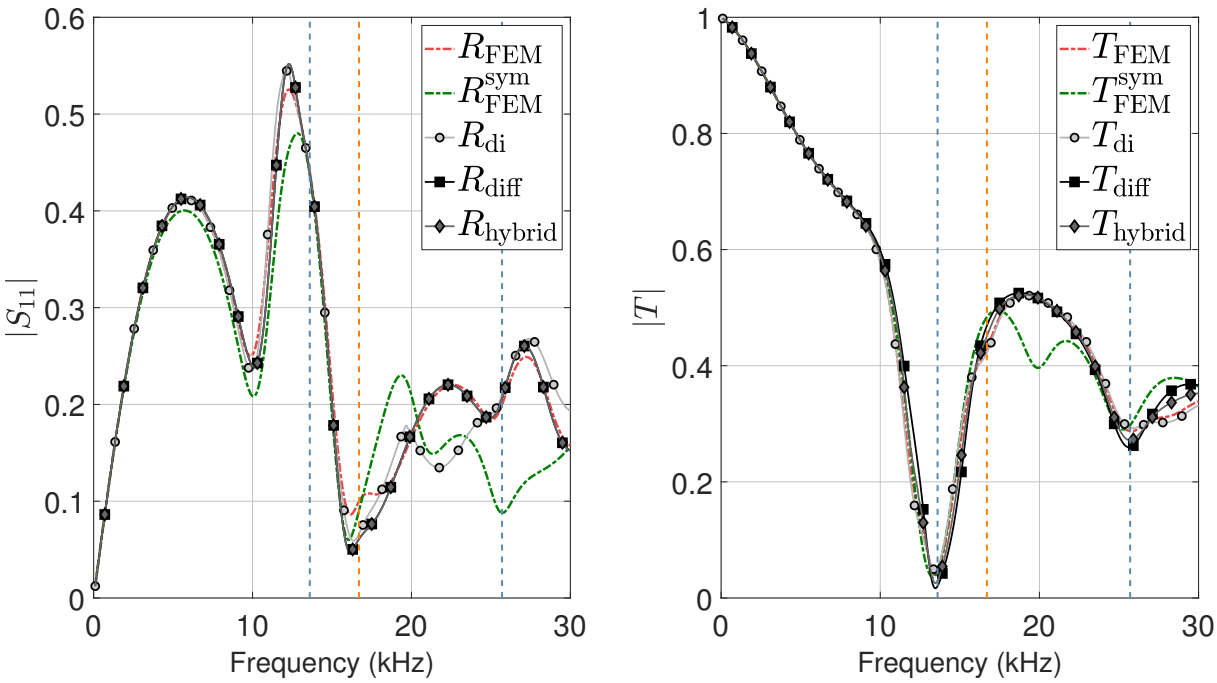

Figure 6.8 – Scattering coefficients for a 5-unit medium, obtained by finite element method (FEM) and effective medium approach with the effective properties from the direct inversion, differential and hybrid method.

Consequently, the extended retrieval methods both lead to the effective properties of the asymmetric unit cell. The effective properties are then used to predict the scattering coefficients as per Chapter 5 and identical conclusions are drawn regarding the accuracy of these predictions using the hybrid method. In comparison with the symmetric version, the major change is related to the interface resonance. The evolution of this resonance depending on the position of the resonant element is investigated in the following subsection.

6.2.3 Parametric Study

A parametric study is conducted in order to assess the influence of the asymmetry on both the acoustic performances and the effective properties. The quantity d_{int}, introduced in Figure 6.4, defines the distance between the resonant inclusion and the input face of the unit cell. It is given different values, which are : 0.5 mm, 1 mm, 1.5 mm, 2 mm, 2.5 mm, 3 mm, 3.5 mm, 4 mm, 4.5 mm, 5 mm and 5.5 mm, as respectively shown in Figures 6.9(a) to 6.9(k).

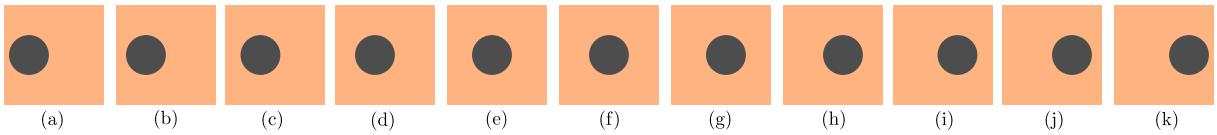

Figure 6.9 – Schematic diagram of the asymmetric inclusions studied, in which the distance interface-inclusion varies.

For these different positions of the inclusions, reflection and transmission coefficients of a 3-unit medium are given in Figure 6.10. With the transmission coefficients, only half of the lines are visible, since the transmission coefficients for an unit cell and its reverse design are identical. For example, the transmission is the same for units (a) and (k), for units (b) and (j), and so on.

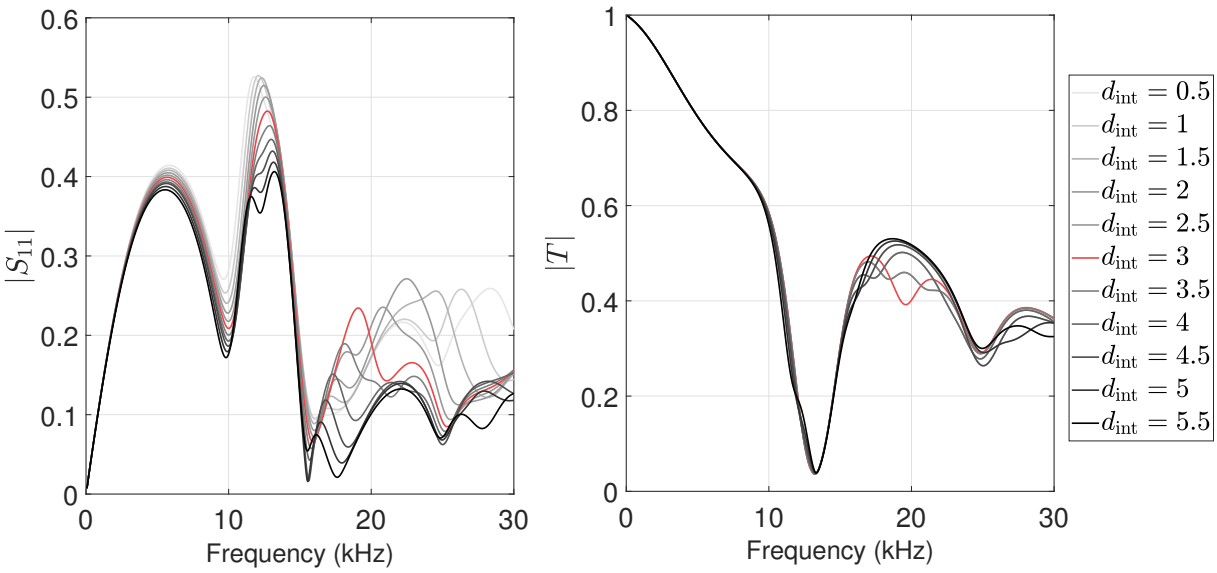

Figure 6.10 – Scattering coefficients S_{11} and $T = S_{12} = S_{21}$ for various distances d_{int} (in millimetres).

It is then observed that the transmission loss from the interface resonance is the greatest for the symmetric unit than for any other configuration. For this same frequency, a local maximum occurs for the absorption coefficient in Figure 6.11. The interface resonance therefore appears to be more beneficial in terms of acoustic performance if the inclusion is centered within the unit. However, for the anechoism coefficient, given in Figure 6.12, the symmetric configuration is not better than any other asymmetric version at the frequency of interface resonance (around 20 kHz).

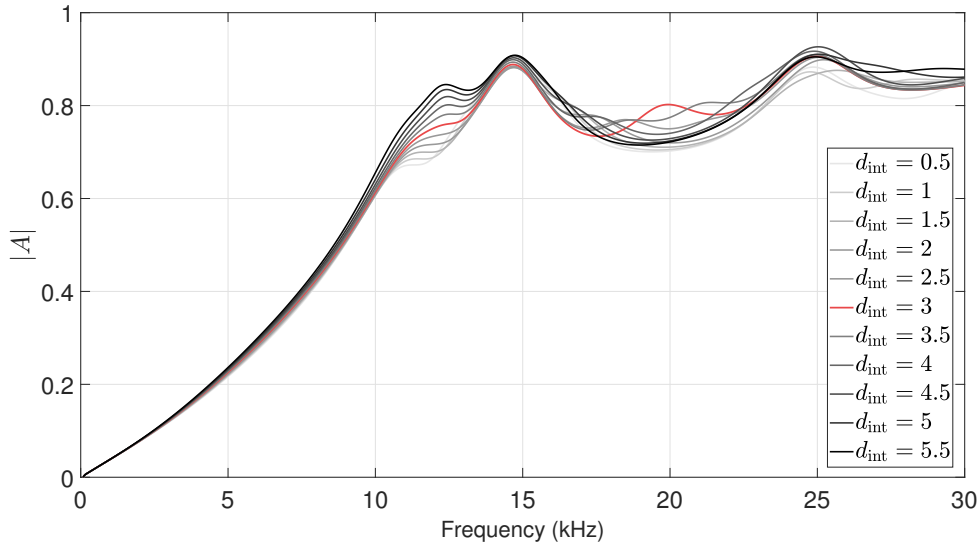

Figure 6.11 – Absorption coefficient $A = 1 - |S_{11}|^2 - |T|^2$ for various distances d_{int} (in millimetres).

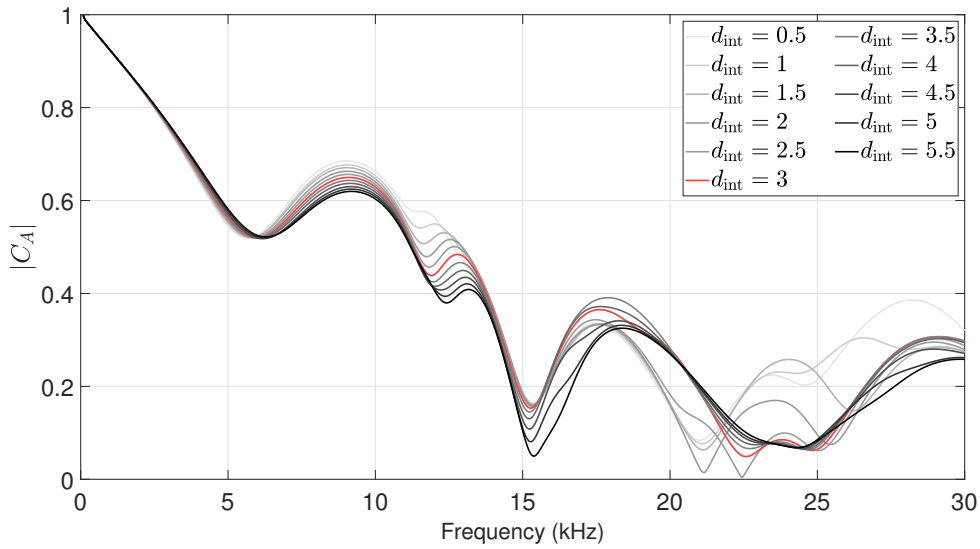

Figure 6.12 – Anechoism coefficient for various distances d_{int} (in millimetres).

For other frequencies, the absorption coefficient is greater for higher values of d_{int}, especially under 15 kHz. For these frequencies, the transmission coefficient is mostly unchanged for the various distances d_{int}, meaning that this gain in performance is related to the reflection coefficient, as shown in Figure 6.10. Moving the hard inclusion away from the interface with water helps to reduce the reflection coefficient. As such, the anechoism coefficient is also better for higher values of d_{int}.

It appears to be beneficial to place the inclusion as far as possible from the medium/water interface, except if the objective is to broaden the frequency range of high absorption. In that case, placing the inclusion at the center of the unit ($d_{\text{int}} = 3$ mm) helps to maximise the interface resonance, which here is well located in-between the dipole resonance A and the matrix resonance C.

The influence of d_{int} on the effective properties, and in particular on the effective density and the effective bulk modulus, is now further investigated. These two parameters are indeed commonly studied given the fact that they may reach negative values that can be linked to resonance phenomena, as mentioned in Chapter 1. Effective density and effective bulk modulus are thus given in Figure 6.13. It should be noted that only half of the lines (units (f) to (k)) are visible, since a unit design and its reverse counterpart have the same effective properties k, Z_W and W, and as such yield identical ρ and κ.

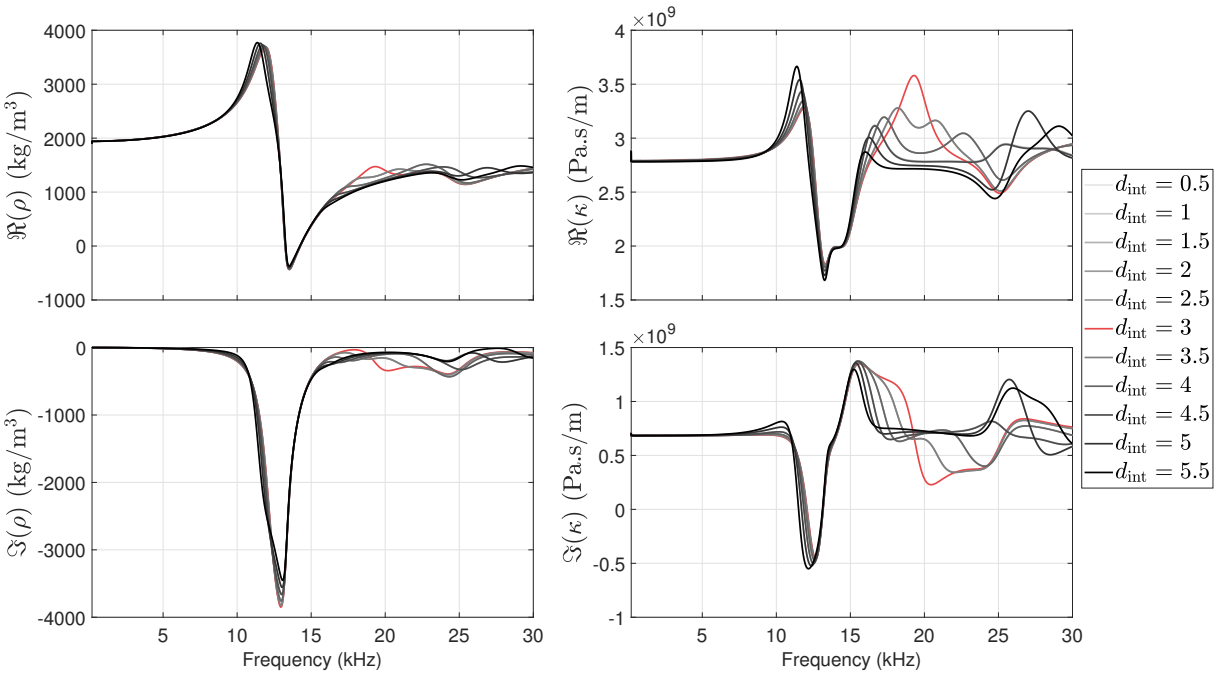

Figure 6.13 – Effective density and bulk modulus of asymmetric unit cells derived with the differential method for various distances d_{int} (in millimetres).

The asymmetry of the unit cell appears to have a very small impact on the effective density, for both its real and imaginary parts, especially under 15 kHz. Upon closer inspection, it can be seen that the differences above 15 kHz are not negligible, but they seem small due to the scale. Nevertheless, there are no significant changes in the overall variations, and the real part of the effective density becomes negative only for the mass-spring (dipole) resonance A. Similarly, the asymmetry does not significantly change the bulk modulus under 15 kHz. However, above 15 kHz, the bulk modulus strongly varies. The values of its real part also remain positive over the entire frequency range independently of the asymmetry of the unit cell.

To summarise this case study, the position of the resonant element is found to impact the acoustic performance. It is preferable to move the hard inclusion away from the interface. It is also found that for this design, the interface resonance has a maximum impact when the inclusion is centred within the unit. It is also observed that when the asymmetry coefficient W is close to 0, the asymmetric medium behaves like its symmetric counterpart. As such, for the dipole resonance around 13.5 kHz, all unit cells are found to have the same effective bulk modulus and effective density, the latter being negative which is characteristic of the dipole resonance in such media.

6.3 Case study: Voided Inclusions

In this section, an asymmetric Alberich-type medium is homogenised. As such media usually perform well as hull decoupling coatings, the acoustic performance is evaluated in terms of transmission coefficient, which is a good indicator of the hull decoupling performance. In Chapter 5, it was observed that the acoustic performance shows very little variation for increasing numbers of unit cells. Alberich coatings are in practice not made of a large number of inclusions in the direction of sound propagation. Here, a single-layer voided medium and a bi-layer voided medium are considered.

6.3.1 Homogenisation

In this subsection, asymmetry is introduced as previously by off-centering the resonant element. The design is presented in Figure 6.14. The host matrix is made out of polyurethane, for which the mass density is 1150 kg.m^{-3}. The longitudinal speed of sound is around 1500 m.s^{-1}, whereas the shear speed of sound strongly varies with frequency between 50 m.s^{-1} and 200 m.s^{-1} with a loss factor of roughly 30%. Medium thickness is $h = 35$ mm and periodicity is defined by $2d = 80$ mm. The medium is studied below the cutoff frequency of the periodical array defined by $f_c = 1489/(2d)$. Inclusions are voided cylinders of radius $r = 10$ mm. Three versions of the units are considered : (a) and (c) are asymmetric, with the inclusion placed at a distance $d_{\text{int}} = 2$ mm from the input and output interfaces, respectively. Unit (a) is the reverse design of unit (c).

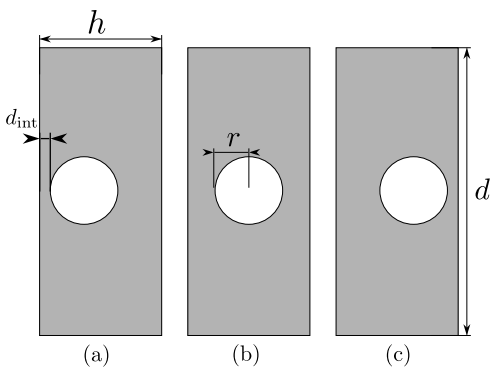

Figure 6.14 – Design and dimensions of the voided medium unit.

Scattering coefficients for these three variant designs are given in Figure 6.15 for one layer immersed in water. The position of the void within the unit slightly changes the reflection coefficient S_{11}. The reflection coefficient is lower when the inclusion is further away from the input interface, as in configuration (c). The transmission coefficient $T = S_{12} = S_{21}$ is mostly unchanged depending on the void position. Therefore, similar to what has been observed for the hard inclusion, the absorption coefficient $A = 1 - |S_{11}|^2 - |T|^2$ is improved for lower frequencies by moving the inclusion away from the input interface.

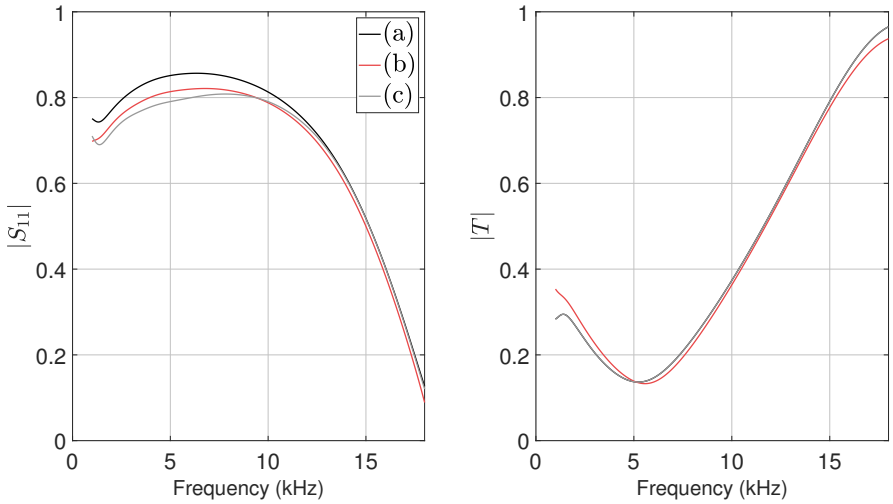

Figure 6.15 – Reflection and transmission coefficients for the units (a), (b) and (c) shown in Figure 6.14.

The effects of the asymmetry on the effective parameters ρ and κ are shown in Figure 6.16. Contrary to what has been observed for the hard inclusion case and the scattering coefficients, the position of the voided inclusion appears to have a strong influence on the effective density ρ. The effective density of units (a) and (c) indeed strongly varies around 12.5 kHz, but remains almost constant for the symmetric version (b).

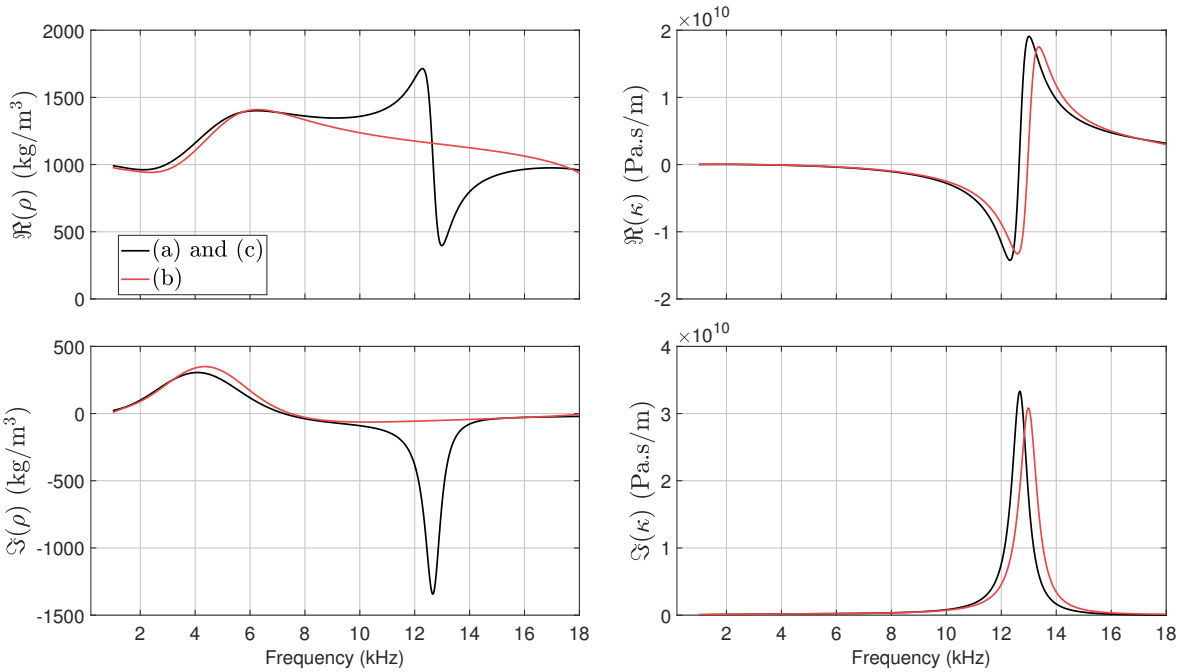

Figure 6.16 – Effective density and bulk modulus for the asymmetric layers presented in Figure 6.14.

All three units lead to similar variation in the effective bulk modulus, which also shows strong variations around 12.5 kHz. It is also observed that the real part of the bulk modulus is negative below this frequency, which is the translation of a monopole resonance of the void. Such voided media for underwater applications are in fact well known for their ability to block acoustic waves by using monopole resonances of the voided inclusions [32].

As for the case study with hard inclusions, it is observed that the Willis asymmetry introduced by moving the resonant inclusion out of the geometric center of a unit does not significantly change the specific metamaterial feature, which here is the negative bulk modulus associated to the monopole resonance. An alternative approach to introducing Willis coupling is presented in the next subsection.

6.3.2 Variant Approach

Another approach to introduce Willis coupling is to create an asymmetric combination of symmetric components having different behaviours. With such an approach, novel properties may be obtained resulting from the interaction between each component. This may result in better broadband performance. A bi-layer unit illustrated in Figure 6.17 is considered. The following dimensions are selected : $h_1 = 22$ mm, $h_2 = 35$ mm, $d_1 = 20$ mm, $d_2 = 40$ mm, $r_1 = 5$ mm and $r_2 = 10$ mm.

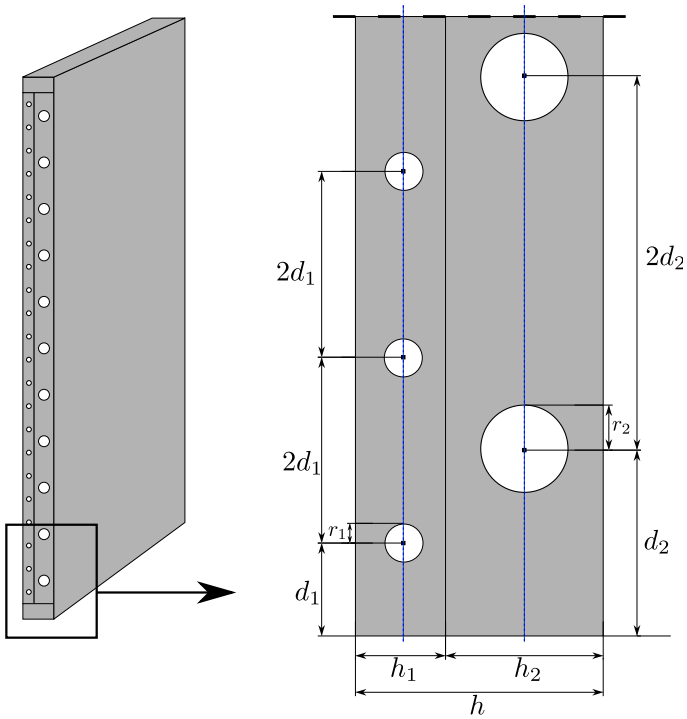

Figure 6.17 – Schematic diagram of the bi-layer Alberich.

Acoustic performance is first studied. The transmission coefficients for the first layer, the second layer and for the bi-layer are shown in Figure 6.18. The onset of the first diffraction orders for the periodical array, defined by $f_c = 1489/(2d_2)$ is highlighted by the orange dotted line. From this frequency, the acoustic response of the panel is no longer specular, so the approach used to calculate the reflection and transmission coefficients needs to be adapted. This aspect will be further studied in Chapter 8.

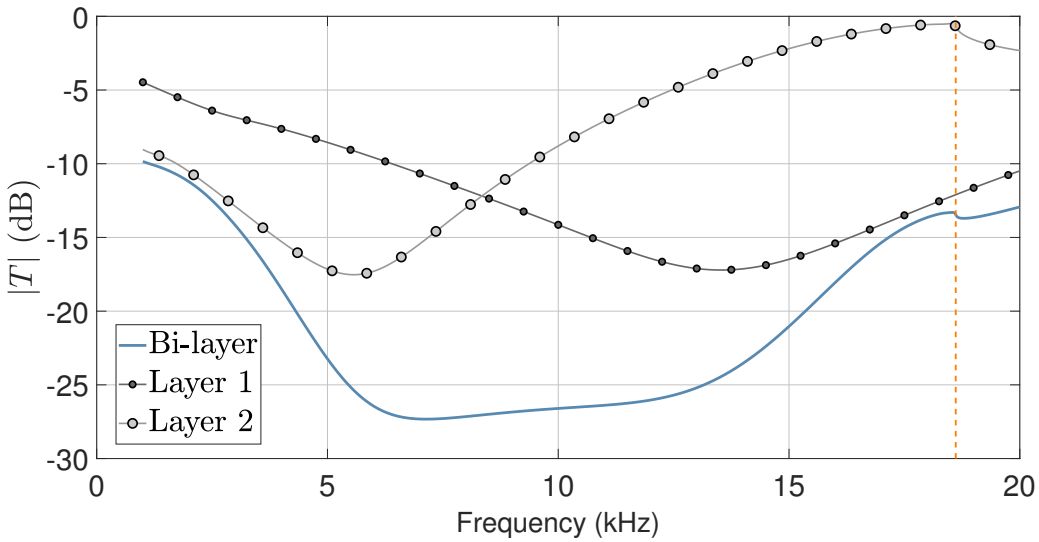

Figure 6.18 – Transmission coefficients for the bi-layer Alberich and for each layer separately.

It is observed that the transmission coefficient of the bi-layer medium remains very low for the entire frequency range of study, attributed to the combination of the two layers, since each layer resonates at a specific frequency. The second layer creates a low transmission peak just above 5 kHz, whereas the first layer of voids leads to a transmission dip just below 15 kHz, creating broadband low transmission.

The effective properties of the medium are now derived. The direct inversion method introduced in previously in the current chapter is applied. Since the unit is a combination of two symmetric layers, another homogenisation approach can be introduced here : each symmetric part is individually homogenised. The transfer matrix method is then used to manipulate the homogenised layers. This option is labeled by Option 2 in Figure 6.19. The first option is the direct homogenisation of the asymmetric medium considering Willis coupling, using the given extended retrieval methods.

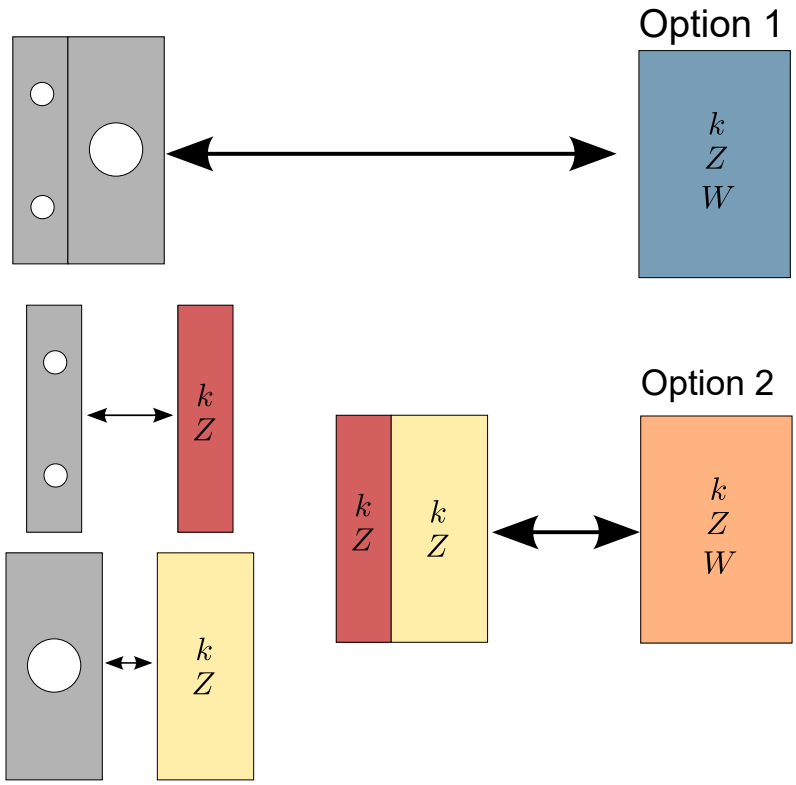

Figure 6.19 – Transmission coefficients for the bi-layer Alberich and for each layer separately.

Both options are applied to investigate whether or not they are equivalent in terms of the final effective medium. The direct inversion is applied to $n = 1$ unit cell, since for such Alberich this method was shown to yield an accurate effective medium (see Chapter 5). For the first option, the bi-layer unit is therefore considered and all four S-parameters are required. For the second option, each layer is modelled individually and only the coefficients R and T are required. A bi-layer unit is then homogenised using the transfer matrix approach of Chapter 3.

The dispersion curves are first obtained and are shown in Figure 6.20. It is observed that both options lead to very similar effective wavenumbers. Moreover, the imaginary parts of the wavenumber of layers 1 and 2 show the attenuation peaks associated with low transmission.

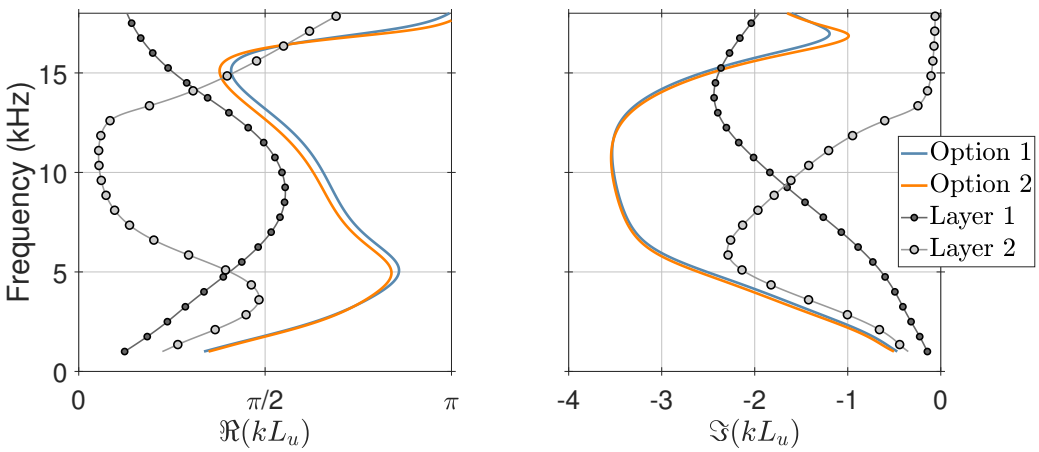

Figure 6.20 – Dispersion curve for the effective bi-layer voided unit derived using the homogenisation Options 1 and 2. The effective wavenumber for each individual unit is also shown.

The Willis impedance and Willis asymmetry parameters are also derived and given in Figure 6.21. There is again very little difference between the two options used to derive the effective properties of the unit cell. It can also be noted that the asymmetry coefficient W becomes very large just after 15 kHz, which will be further discussed in what follows.

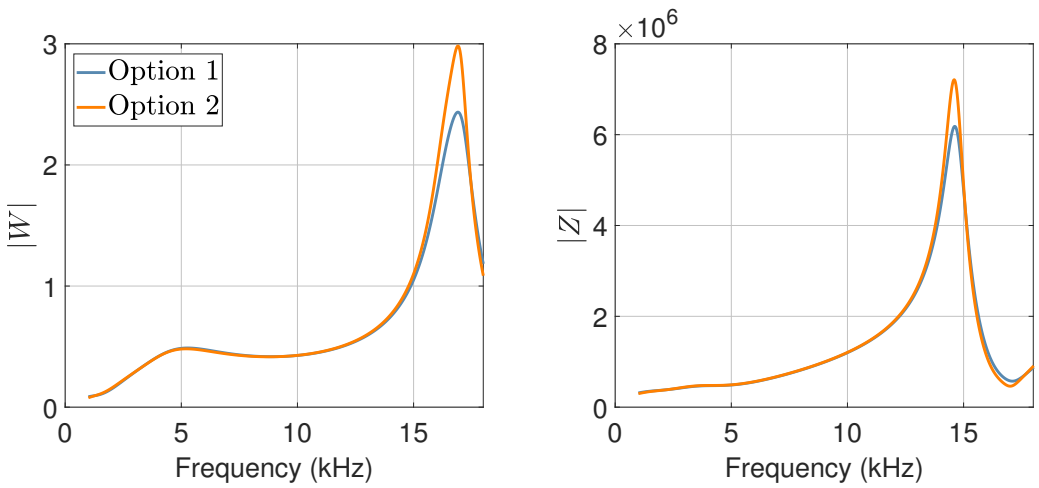

Figure 6.21 – Modulus of the Willis asymmetry coefficient and Willis impedance of the bi-layer voided unit.

There are therefore small differences between the two homogenisation approaches presented herein. It is difficult to assess which one is more suitable or representative of the medium, since differences are negligible here. They may however differ more for other structures where the nature of the 2 layers is different and for which the interface effects captured by the method are significant. In terms of computation time, both approaches are equivalent since they both require two finite element simulations.

Effective density and bulk modulus are now derived for the bi-layer voided medium and are given in Figure 6.22. Independently, both layers lead to negative values for the real part of the effective bulk modulus when their voids create a monopole resonance. The bi-layer unit also provides a bulk modulus that has negative values. The unexpected result to highlight here is the effective density of the bi-layer medium that becomes negative, whereas the effective density of both layers individually remains positive.

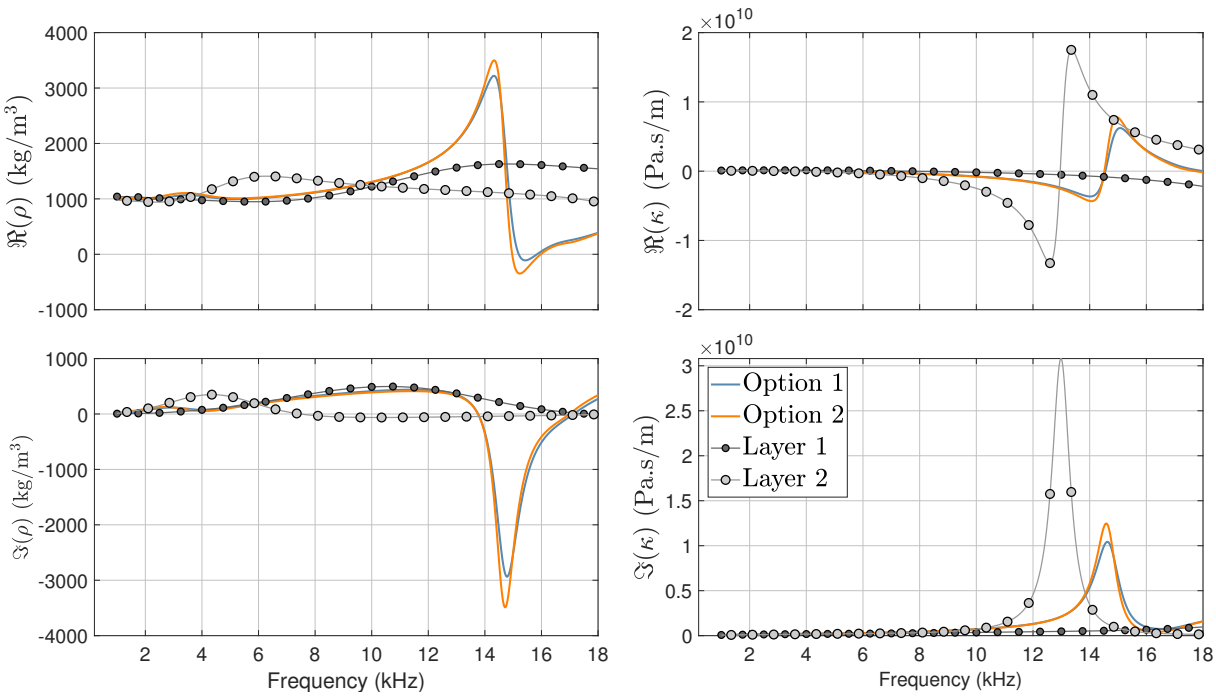

Figure 6.22 – Effective bulk Modulus and mass density for the bi-layer Alberich design.

Such negative values of the effective density may seem surprising for a voided medium, since it is known that the effective density is linked to the translational vibration of an inclusion, whereas the bulk modulus relates the compressibility (bulk oscillations) behaviour of an inclusion. Negative bulk modulus is therefore expected for voided media, but the effective negative density is not expected since there is no mass inclusion. It has been theoretically demonstrated that negative mass density can be obtained for spherical voided inclusions when the motion of the center of mass of the particle is out of phase with an incident directional pressure field [13, 122, 123]. The phase difference between the displacement of the mass center, located at 32.83 mm from the input interface, and

the incident field is plotted in Figure 6.23. In this figure, frequencies where the effective density is negative are highlighted by the blue shaded area (Option 1) and by the orange shaded area (Option 2). It is noted that these areas exactly correspond to a phase opposition between the phase of the incident signal and the phase of the center of mass displacement. They also exactly correspond to the maximum of the asymmetry coefficient W. This study case may be one of the first evidence of a design with 2D macro-inclusions that exhibits negative density appears when the displacement of the center of mass is in phase opposition with the incident field.

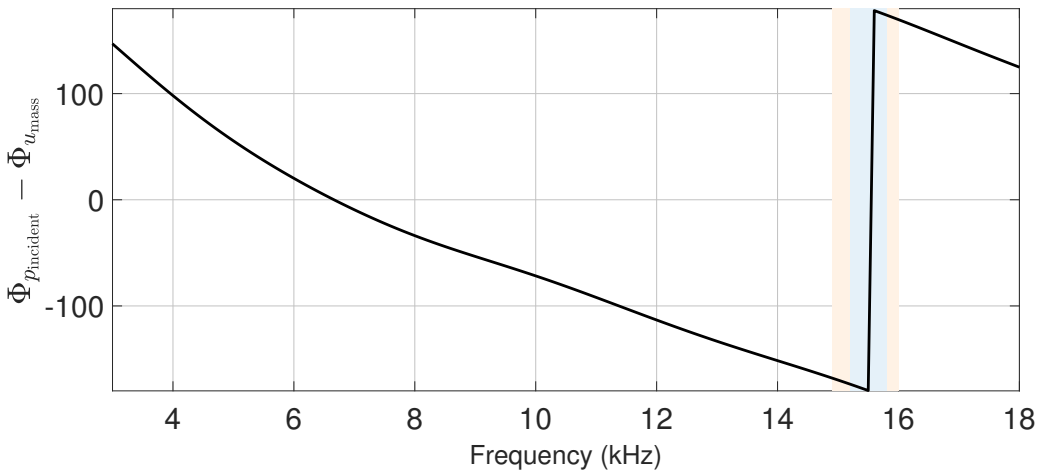

Figure 6.23 – Phase difference (in degree) between the displacement of the center of mass and the incident field.

To summarise this case study, Willis coupling has been introduced by combining two symmetric layers. It has been shown that this method of introducing asymmetry considerably helps to improve the broadband performance compared to off-centering the resonant element. Moreover, negative values for both the effective density and effective bulk modulus have been obtained. The origin of the negative mass density, which is uncommon for such voided media, is explained. The bi-layer Alberich design analysed in this section is selected for fabrication, and its characterisation will be presented in Chapter 8.

6.4 Summary

In this Chapter, the direct inversion method and the differential method were extended to consider asymmetric media. These methods were then employed for two case studies, in which the introduction of Willis coupling through the asymmetry is investigated, including the impact on the acoustic performance and on the effective properties.

The first case study is used as an example of application of the retrieval methods, in which a locally resonant medium containing an off-centred hard inclusion is homogeneised. It was found that the acoustic performance is slightly improved by moving the hard inclusion away from the input interface. However, the position of the inclusion does not particularly affect the effective parameters, including the effective density at the frequency of dipole resonance where it reaches negative values. It was found that this absence of difference between the unit versions at this dipole frequency is also linked to low values of the asymmetry coefficient W.

For the second case study, an asymmetric voided medium is considered. The asymmetry was introduced so that the acoustic performance was improved over a broadband frequency range. The asymmetry coefficient for this asymmetric unit was also found to be maximised when the effective density of the unit was negative, attributed to a phase opposition between the center of mass displacement and the incident field. Consequently, these two case studies are examples of the application of the extended retrieval methods. Further, these case studies show how the introduction of Willis coupling may affect both the acoustic performance and the effective properties.

Chapter 7

Optimisation

In this chapter, a topological-like optimisation of metamaterials with macro-inclusions is conducted. Media to be optimised are made of several units with inclusions of different shape and size. In order for the optimisation process to be computationally efficient, each unit is represented by its effective unit counterpart that has been obtained with the retrieval methods presented in Chapter 5. For this purpose, a database of effective properties associated with unit cell designs is created. The influence of the inclusion shape and inclusion size on the effective properties are also investigated. The database is then used as input for an optimisation process, based on the layer optimisation approach presented in Chapter 3 for multilayered media, with the goal of minimising the anechoism coefficient at low frequencies. The work in the current chapter is therefore useful to make a topological-like optimisation of acoustic coatings for underwater applications using fluid properties.

Contents

7.1 Optimisation Approach 158

7.2 Database 160

7.2.1 Presentation 160

7.2.2 Influence of the Inclusion Shape 161

7.2.3 Influence of the Inclusion Size 164

7.3 Results for Anechoism 167

7.3.1 Approach Validation 167

7.3.2 Low Frequencies 169

7.4 Performance Levels 174

7.5 Summary 175

7.1 Optimisation Approach

The optimisation approach for two dimensional designs is detailed in what follows and is illustrated by Figure 7.1. Both the direct inversion method and the differential method are applied to different periodic designs in order to get the effective properties of the constituent unit cells. The direct inversion method is applied to $n = 3$ unit cells. Since it has been shown in Chapter 5 that the differential method is almost independent to the parameter n, the method is applied to $(n, n+1) = (2, 3)$ unit cells. As a result, a database is created with short computation times.

This database comprises a range of effective wavenumbers and effective impedances associated with an inclusion design. For the sake of simplicity, only symmetric unit cells are considered. This database of effective properties is used to optimise the layer arrangement of a segmented medium. With this optimisation approach, the optimisation tools for multilayered media optimisation are used for structures with two-dimensional macro-inclusions through the use of effective media. That is, for a given number of unit cells (characterising the minimal layer thickness and the total medium thickness), each layer is affected with a set of effective properties (wavenumber and impedance) from the database. As for the optimisation for multilayered media, the objective functions are then calculated and the layer arrangement is optimised until the genetic algorithm gives a set of best solutions.

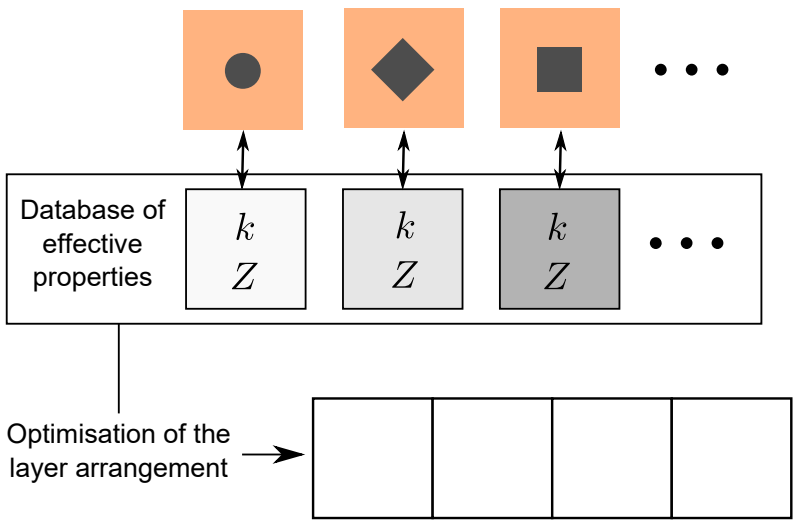

Figure 7.1 – Diagram of the optimisation approach, which uses a database of effective properties derived with the retrieval methods for various inclusion shapes.

For the optimisation of the anechoism coefficient, the same objective functions used in Chapter 3 are used : the first objective function is the root mean square of the anechoism coefficient, which aims at reducing its overall value, while the second objective function is the normalised standard deviation to this value of the root mean square, which aims at avoiding high peaks.

In order to calculate the anechoism coefficient, the scattering coefficients of the multi-layered medium of effective layers are calculated. Nevertheless, the segmented media obtained are more likely to be asymmetric. It is thus crucial to calculate the anechoism coefficient using all S-parameters, as per (Appendix C):

$$C_A = S_{11} - \frac{S_{21}^2}{S_{22} - 1} \tag{7.1}$$

7.2 Database

7.2.1 Presentation

The database of unit cells is presented in Figure 7.2 and contains 14 possibilities for the unit cell. Two of them are homogeneous, made of either polyurethane or steel, whereas the others comprise a polyurethane matrix containing a steel inclusion. Material properties are given in Chapter 5.

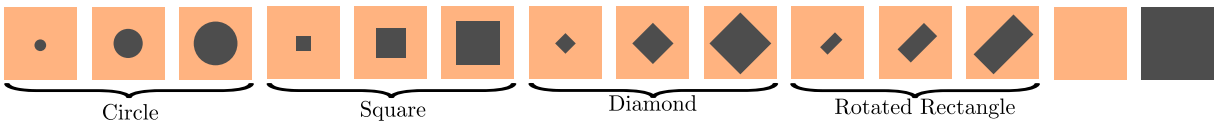

Figure 7.2 – Schematic diagram of the unit cells composing the database. Inclusions are not drawn to scale.

Figure 7.3 introduces the dimensions of (a) the circle inclusion, (b) the square inclusion, (c) the diamond inclusion, (d) the rotated rectangular inclusion and (e) the unit cell. These dimensions are then given in Table 7.1 considering three different surface areas for each one of the inclusion shapes. These surface areas are $\mathcal{A} = 4$ mm^2, $\mathcal{A} = 16$ mm^2 and $\mathcal{A} = 25$ mm^2. The inclusions are centered within a 1 cm^2 polyurethane unit, with $L_u = 10$ mm. Using this database, the influence of the inclusion shape for a same surface area as well as the influence of the inclusion size for a given shape can be studied.

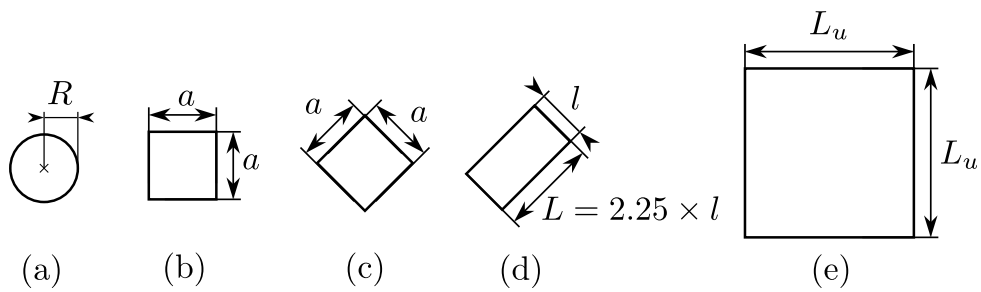

Figure 7.3 – Dimensions for the four inclusions, consisting of (a) a circle, (b) a square, (c) a diamond and (d) a rotated rectangle. The dimensions of the unit cell are also shown (e).

Surface area	R (mm)	a (mm)	L (mm)
$\mathcal{A} = 4$ mm^2	1.284	2	3
$\mathcal{A} = 16$ mm^2	2.257	4	6
$\mathcal{A} = 25$ mm^2	2.821	5	7.5

Table 7.1 – Dimensions defining the size of the inclusion depending on their surface area $\mathcal{A}$.

7.2.2 Influence of the Inclusion Shape

The influence of the inclusion shape on the variations of the effective properties is investigated. For this purpose, the four inclusions of surface area $\mathcal{A} = 16$ mm^2 are considered.

The effective wavenumber for each of these units is obtained using both the direct inversion method and the differential method, respectively given in Figure 7.4 and Figure 7.5. It is observed that even if these different inclusions have the same surface area, their effective wavenumber differs depending on the shape, for both inversion methods.

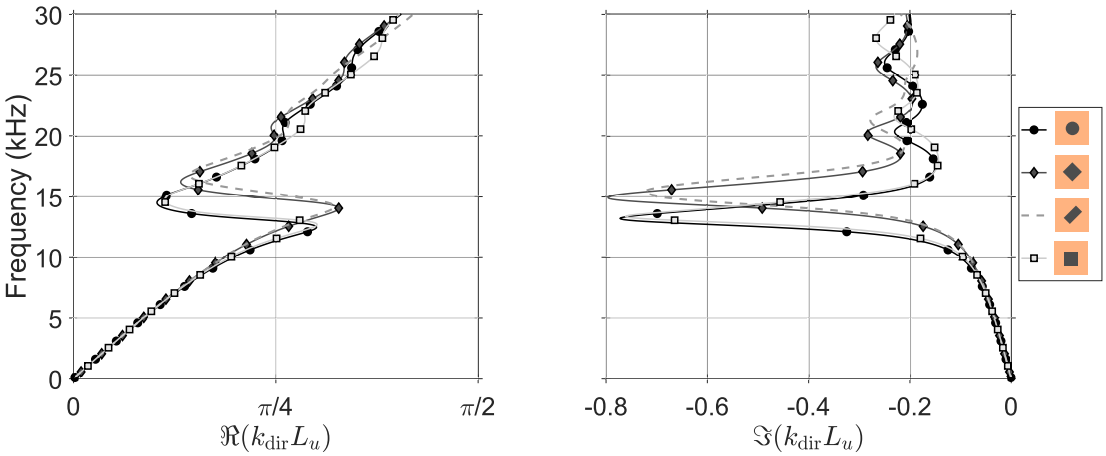

Figure 7.4 – Dispersion curves obtained using the direct inversion method for the four different units of surface area $\mathcal{A} = 16$ mm^2.

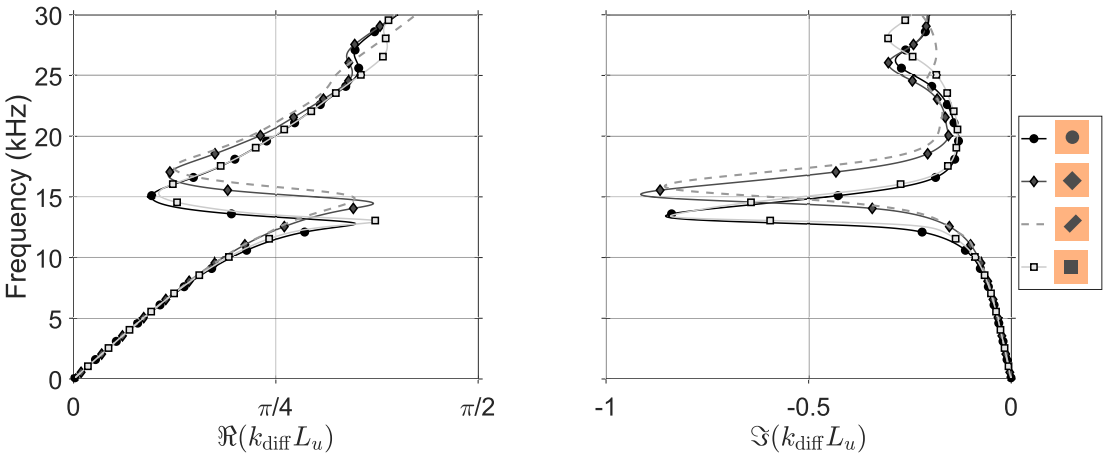

Figure 7.5 – Dispersion curves obtained using the differential method for the four different units of surface area $\mathcal{A} = 16$ mm^2.

In Figure 7.5, it appears that the effective wavenumbers for the square and the circle inclusions are very similar up to 20 kHz, which includes the mass-spring resonance. The same observation is made for the effective wavenumber for the diamond and rotated rectangular inclusions. Moreover, the mass-spring resonance for these last two inclusion shapes appears at higher frequencies than for the square and circle inclusions.

The variations for the second resonance, corresponding to the matrix resonance around 25 kHz, are studied using the effective wavenumber obtained using the differential method such that there is no confusion with the interface resonance since the differential method erases the interface effects. It is observed that the rotated rectangular inclusions correspond to a matrix resonance that appears at lower frequencies than the other shape, but also corresponds to a low wave attenuation as shown by the small amplitude peak just under 25 kHz. The wavenumber for the diamond inclusions and the circle inclusions are similar and lead to a matrix resonance at roughly 26 kHz. The matrix resonance for the square inclusion appears at higher frequencies, almost at the end of the frequency range of study.

As such, the effective wavenumber for two inclusions may have similar variations for one type of resonance, but quite different variations for another type of resonance. Each inclusion shape thus leads to its own variations for the wavenumber although the surface area is the same.

The frequency of the interface resonance, around 20 kHz, also differs depending on the inclusion shape, as visible in Figure 7.4. The diamond, the circle, the rotated rectangular and the square inclusions respectively correspond to an interface resonance at the frequencies 20.2 kHz, 20.3 kHz, 21.3 kHz and 21.6 kHz.

Therefore, the change of inclusion shape does not modify the general behaviour of the medium since it is still possible to observe the mass-spring resonance, the interface resonance as well as the matrix resonance. However, these phenomena are shifted in frequency depending on the shape. Moreover, it appears that the attenuation per distance, represented by the amplitude of the imaginary part of the wavenumber, may also be slightly modified depending on the inclusion shape. The same observations as for the effective wavenumber can be made for the effective impedance obtained with the differential method, shown in Figure 7.6.

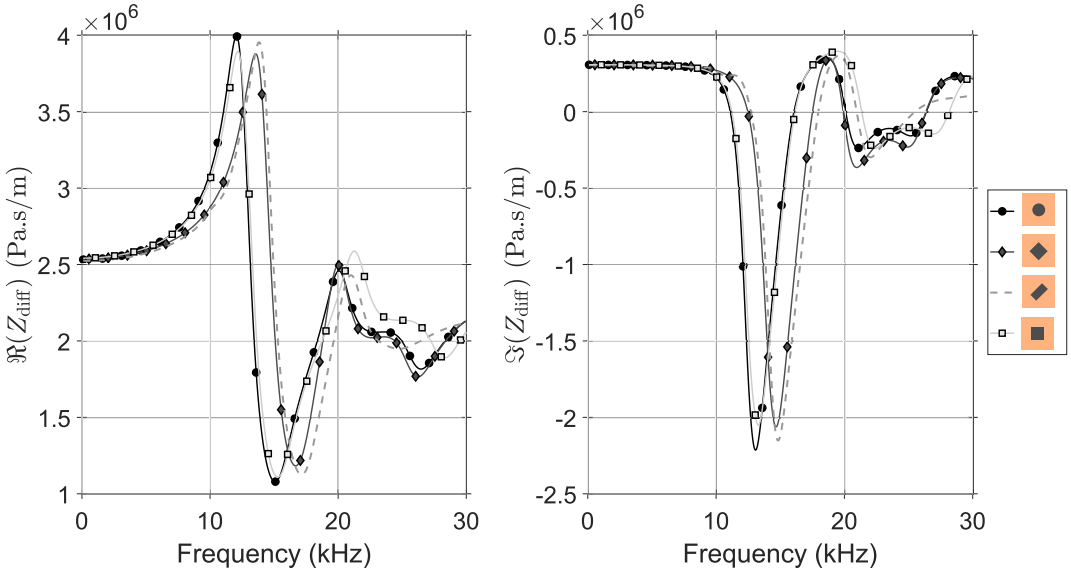

Figure 7.6 – Effective impedance obtained using the differential method for the four different units of surface area $\mathcal{A} = 16$ mm^2.

The scattering response of these units, obtained from FEM, is now compared in Figure 7.7 for media comprising $n = 3$ unit cells. The reflection and transmission coefficients differ accordingly to what has been observed with the effective wavenumbers. Additionally, the absorption coefficient, defined as $A = 1 - |R|^2 - |T|^2$, shows that with all these inclusions, high absorption peaks are nicely spread between 11 kHz and 30 kHz. As such, using multiple inclusion shapes is of interest to spread the dissipating physical phenomena, resulting in a better broadband performance.

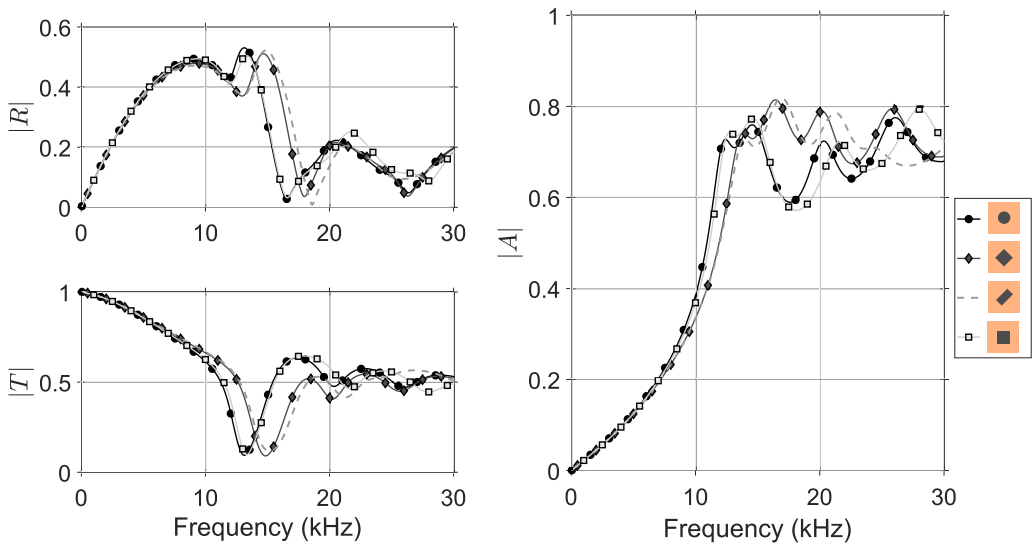

Figure 7.7 – Reflection (R), transmission (T) and absorption coefficients ($A = 1 - |R|^2 - |T|^2$) for four 3-unit media, each one made of repetitions of one of the four different units of surface area $\mathcal{A} = 16$ mm^2.

7.2.3 Influence of the Inclusion Size

The influence of the inclusion's surface area is further investigated in this section. The diamond inclusion in Figure 7.3(c) is selected for the three surface areas of 4 mm^2, 16 mm^2 and 25 mm^2. The dispersion curves are given in Figure 7.8 for the differential method, and in Figure 7.9 for the direct inversion method. In these two figures, the differences are significant amongst the curves for the 3 surface areas in both amplitude and frequency of resonances. It is therefore observed that a small inclusion leads to small amplitude variations at resonance frequencies, and that these resonances occur at low frequencies. A large inclusion leads to significant amplitude variation of the effective wavenumber and resonance phenomena that are shifted to higher frequencies.

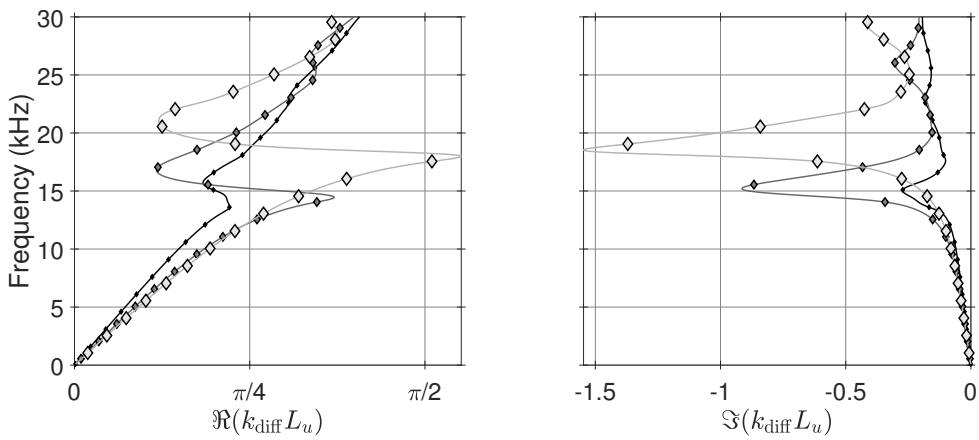

Figure 7.8 – Dispersion curves obtained using the differential method for the diamond inclusion of surface area $\mathcal{A} = 4$ mm^2 (small markers), $\mathcal{A} = 16$ mm^2 (medium markers) and $\mathcal{A} = 25$ mm^2 (large markers).

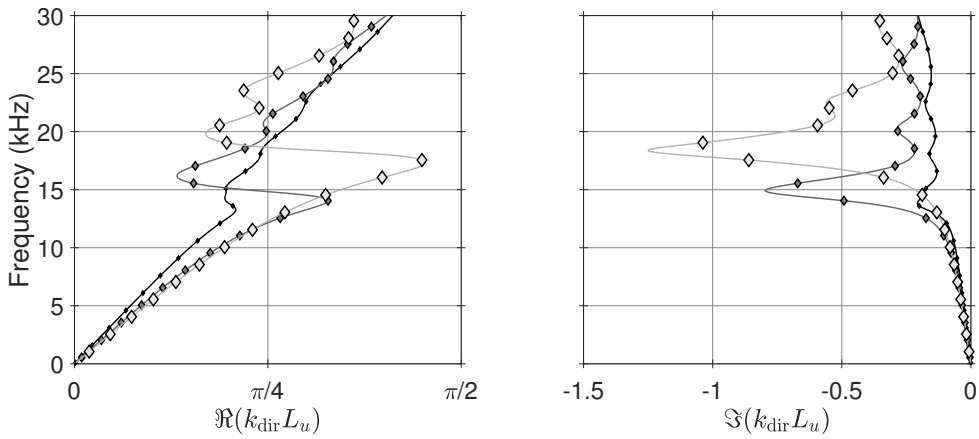

Figure 7.9 – Dispersion curves obtained using the direct inversion method for the diamond inclusion of surface areas $\mathcal{A} = 4$ mm^2 (small markers), $\mathcal{A} = 16$ mm^2 (medium markers) and $\mathcal{A} = 25$ mm^2 (large markers).

For the effective wavenumber in Figure 7.9 obtained using the direct inversion method it is also observed that the interface resonance shifts to higher frequencies with increasing surface area.

The effective impedance is also strongly affected by the inclusion surface area, especially for such heavy inclusions made of steel, as shown in Figure 7.10. Contrary to the wavenumber, differences between inclusions are herein especially significant at low frequencies. Such significant differences in the impedances are of interest as it has been shown in Chapter 3 that strong variation in impedance may be beneficial to improve anechoism performance.

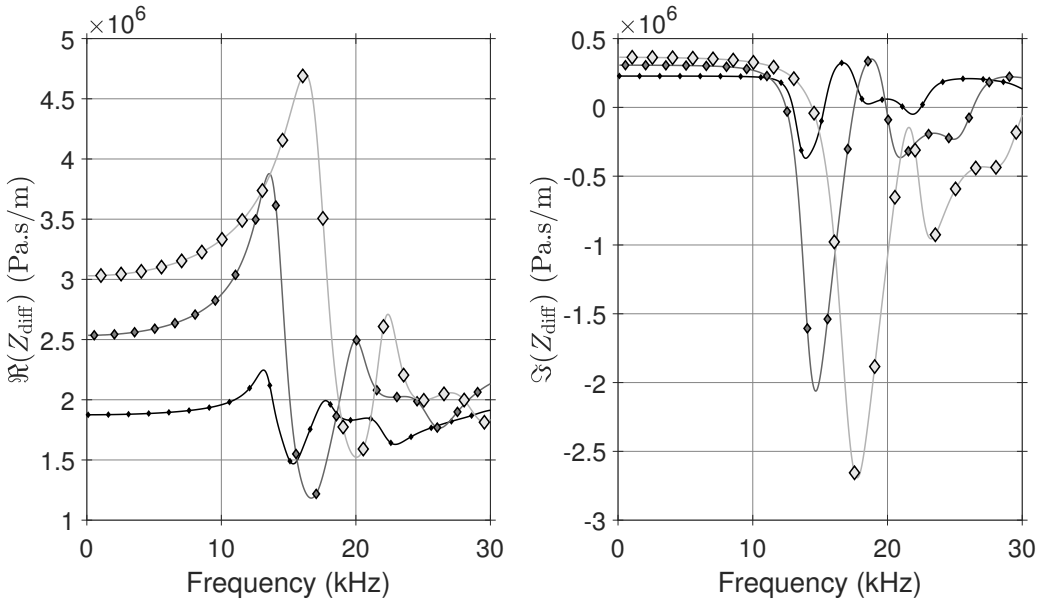

Figure 7.10 – Effective impedance obtained using the differential method for the diamond inclusion of surface areas $\mathcal{A} = 4$ mm^2 (small markers), $\mathcal{A} = 16$ mm^2 (medium markers) and $\mathcal{A} = 25$ mm^2 (large markers).

The influence of the size of the inclusion on the scattering coefficients is shown in Figure 7.11. It is observed that the reflection coefficient may significantly differ from one inclusion size to another, especially at low frequencies as per the effective impedance. The absorption coefficient $A = 1 - |R|^2 - |T|^2$ reaches maximal values for the largest inclusion at resonant frequencies. The medium size inclusion seems nevertheless to provide the most interesting absorption coefficient since it remains relatively high from 13 kHz.

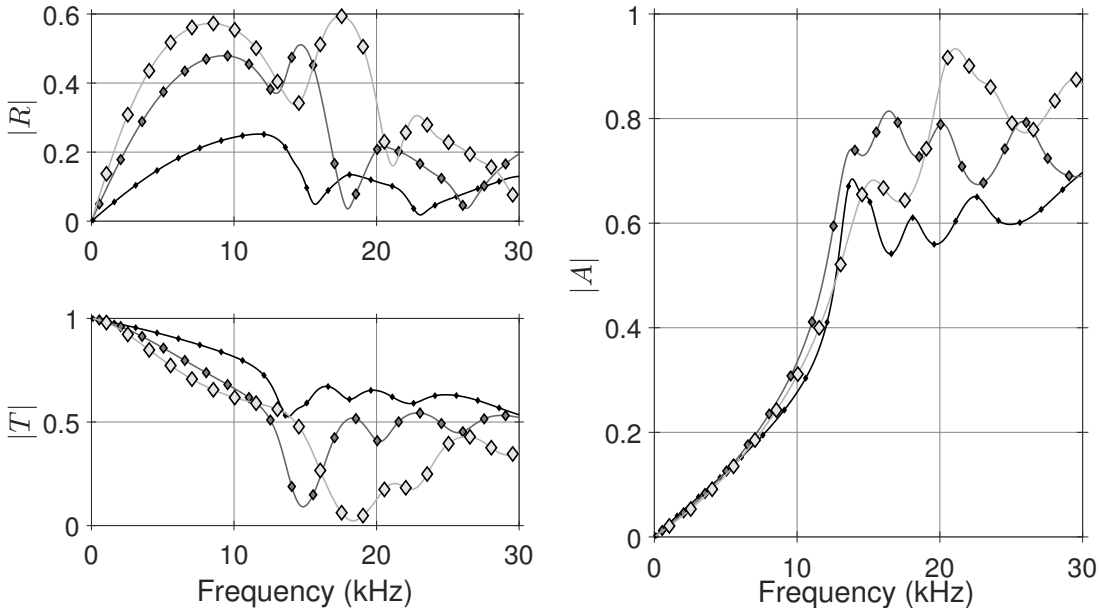

Figure 7.11 – Reflection, transmission and absorption coefficients for three 3-unit media, each one made of repetitions of units comprising diamond inclusions of surface area $\mathcal{A} = 4$ mm^2 (small markers), $\mathcal{A} = 16$ mm^2 (medium markers) and $\mathcal{A} = 16$ mm^2 (large markers).

7.3 Results for Anechoism

7.3.1 Approach Validation

The optimisation is now conducted for a broadband frequency range [200 Hz – 30000 Hz]. The aim of this first optimisation is simply to check the validity and accuracy of the approach that uses effective properties obtained using the hybrid prediction method in such an optimisation scheme. The layer arrangement is optimised for a 10-unit medium, considering the database of Figure 7.2 without the homogeneous steel unit.

The Pareto front is plotted for all generations in Figure 7.12. For the last generation, the 10 leftmost arrangements, having the lowest $|C_A|$, as well as the 10 rightmost arrangements, with the minimum σ_{C_A}, are also represented.

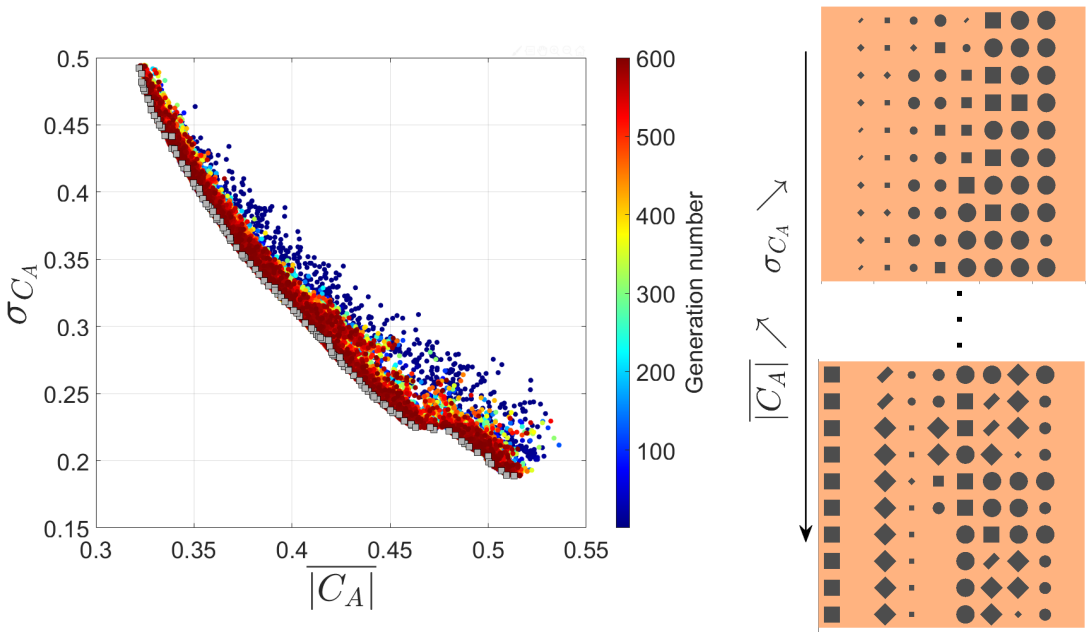

Figure 7.12 – Scores of the Pareto front for all generations (left) and layer arrangements for the 10 first and last solutions of the Pareto front (right), from the lowest $|C_A|$ to the highest, considering the left hand-side as the incidence side and the right hand-side as the hull side.

The first arrangement of the Pareto front for which $\overline{|C_A|}$ is minimum, as well as the last arrangement with the minimum σ_{C_A}, are selected to assess the validity of the optimisation approach. Their scattering coefficients obtained using the effective medium approach (full lines) are compared to those obtained using a finite element model (dashed lines) in Figures 7.13 and 7.14.

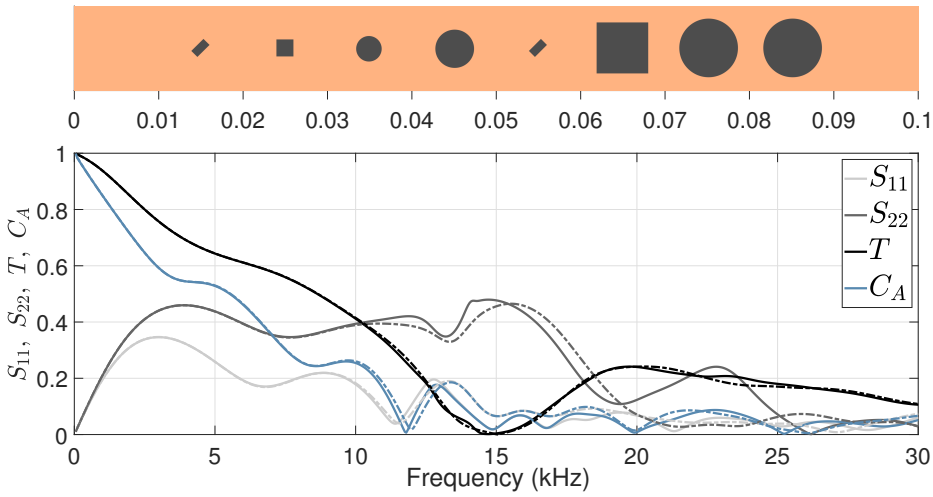

Figure 7.13 – Scattering coefficients, S_{11}, S_{22} and $T = S_{12} = S_{21}$, as well as the anechoism coefficient C_A for the first arrangement of the Pareto front, obtained using the effective medium approach (full lines) and finite element simulation (dashed-dotted lines).

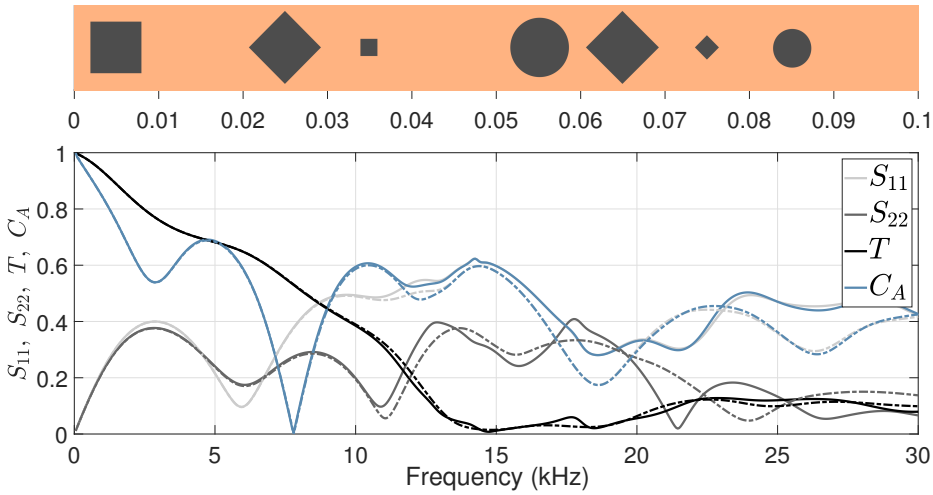

Figure 7.14 – Scattering coefficients, S_{11}, S_{22} and $T = S_{12} = S_{21}$, as well as the anechoism coefficient C_A for the last arrangement of the Pareto front, obtained using the effective medium approach (full lines) and finite element simulation (dashed-dotted lines).

For these two cases, the predictions are very accurate up to 10 kHz. They then start differing from the finite element model between 10 and 20 kHz. Above 20 kHz, the difference between predictions and the FEM may become significant, especially for the S_{11} and S_{22} parameters. Predictions of anechoism coefficients are nevertheless relatively accurate as these differences seem to compensate amongst S_{11}, S_{22} and $T = S_{12} = S_{21}$. The optimisation approach is therefore judged satisfactory and suitable to predict the anechoism coefficient of such complex media with macro-inclusions.

7.3.2 Low Frequencies

The optimisation process is now conducted aiming to lower the anechoism coefficient for the subwavelength domain, for a frequency range up to 10 kHz. Optimisation parameters are given in Table 7.2.

Optimisation Parameter	Value
Total thickness	L = 0.1 m
Unit thickness	$l = 0.01$ m
Number of layers	$n_l = 10$
Population size	$N = 400$
Proportion of children created by Crossover	$C_{\%} = 80\%$
Proportion of children created by Mutation	$100 - C_{\%} = 20\%$
Mutation probability	$m = 0.02$
First rank ratio	$r_1 = 0.35$
Maximum number of Generations	$G_{\max} = 1000$

Table 7.2 – Parameters to optimise the layer arrangement of a medium to lower the anechoism coefficient up to 10 kHz.

Figure 7.15 presents the evolution of the Pareto front for all generations as well as the 30 leftmost layer arrangements of the last generation. It is observed that all the arrangements have their last unit cell free of inclusion, and all comprise a small inclusion in their first unit cell. Heavy steel layers close to the back end of the medium also seems to be a pattern that stands out for low anechoism in the selected frequency range.

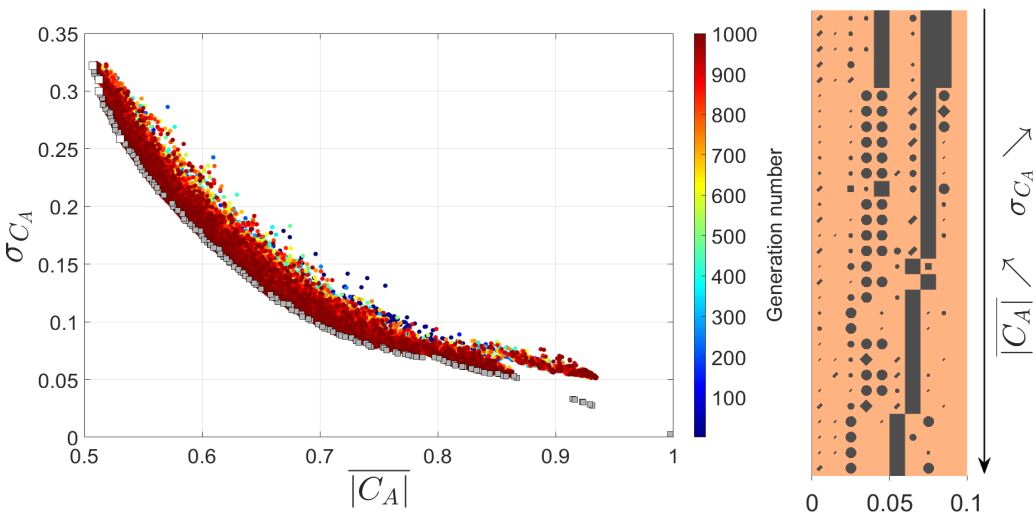

Figure 7.15 – Scores of the Pareto front along generations (left) and 30 first layer arrangements of the Pareto front (right), from the lowest $|C_A|$ to the highest, considering the left hand-side as the incidence side and the right hand-side as the hull side. White squares highlight the scores of four selected arrangements.

Four arrangements are selected for comparison. Their scores are highlighted by the white squares in Figure 7.15. The anechoism coefficient for these selections is shown in Figure 7.16.

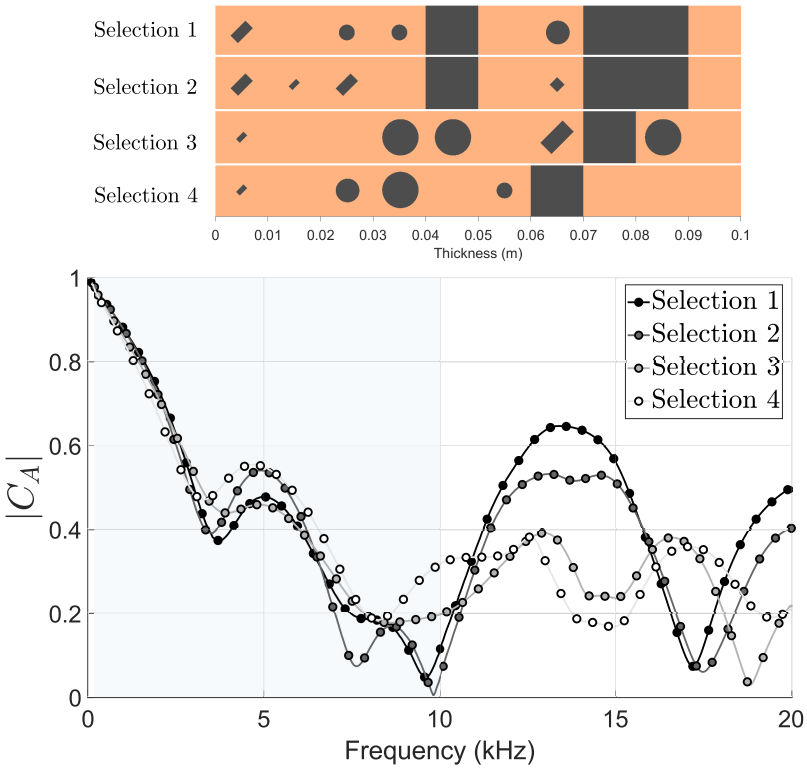

Figure 7.16 – Layer arrangements and anechoism coefficients of four selected configurations chosen for their low anechoism coefficient under 10 kHz.

For these four selections, it is observed that the anechoism coefficient remains low only in the frequency range of optimisation, and then increases above 10 kHz, especially for Selections 1 and 2.

The first arrangement is further studied for a frequency range up to 10 kHz. The scattering coefficients obtained using the effective medium approach are given in Figure 7.17 and compared to those obtained using FEM. Predictions and FEM results are very close to each other. It is also observed that the optimised arrangement improves the anechoic performance from 2 kHz compared to the matrix alone, as shown by the difference between the blue and orange lines in Figure 7.17 (right). Nevertheless, since the performance is optimised below 10 kHz, the origin for this improved performance is not a resonance effect. According to the results in sections 7.2.2 and 7.2.3, the only main difference between the units of the database is the effective impedance within this frequency range.

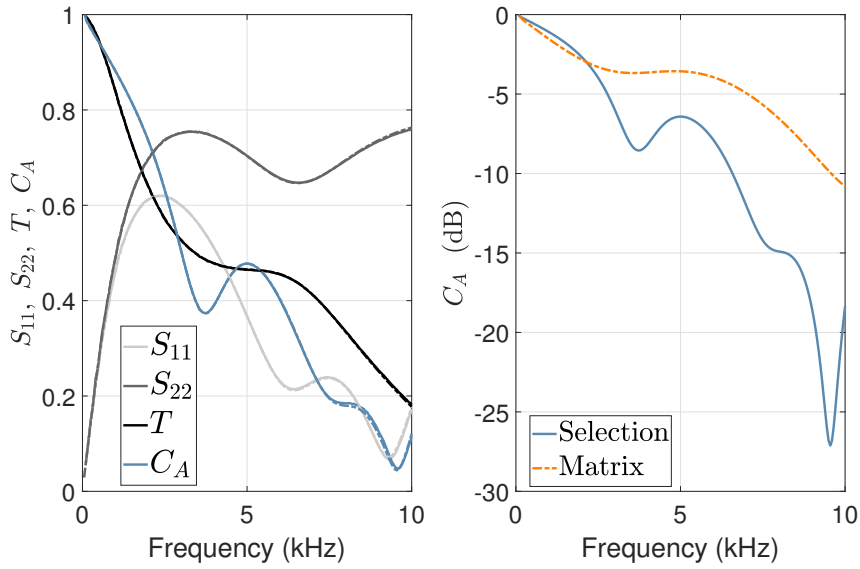

Figure 7.17 – (Right) Scattering coefficients, S_{11}, S_{22} and T, as well as the anechoism coefficient C_A for the first arrangement of the Pareto front, obtained using the effective medium approach (full lines) and finite element simulation (dashed lines). (Left) Anechoism coefficient, in decibels, of the optimised medium and of the matrix free of inclusions.

The effective impedance along the medium is thus calculated and is given in Figure 7.18 at 9.8 kHz, which is the frequency where the anechoism coefficient is a minimum. It is obtained by using the effective impedance of each unit. Similar variations to what has been observed in Chapter 3 are again found: effective impedance tends to remain constant around the impedance of water so that a wave entering the medium does not encounter major reflection. It shows a high peak close to the back end of the medium (on the right-hand side), followed by a drop at the end of the medium.

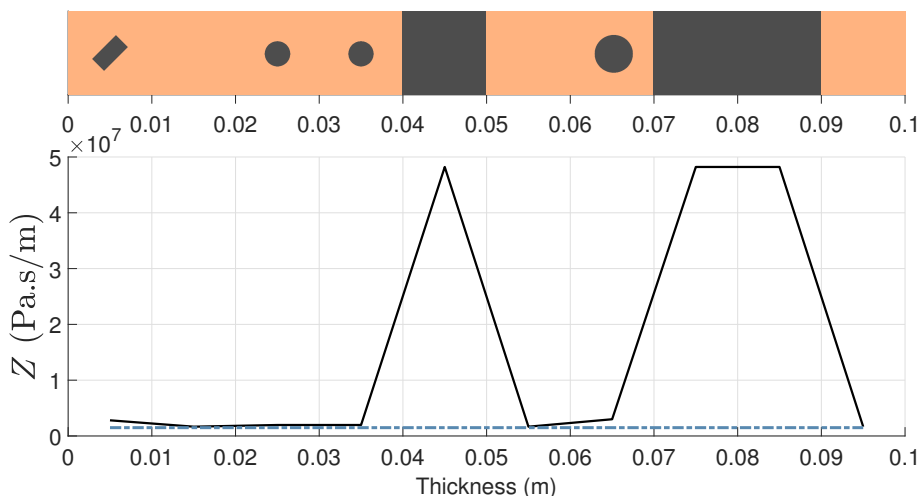

Figure 7.18 – Effective impedance for each unit at a frequency of 9.8 kHz.

This result therefore reinforces that such an impedance pattern leads to low anechoism, as it has been concluded for multilayered media, even though the gradual feature is less visible here. Resonances phenomena associated with the presence of inclusions are then not necessary to improve anechoic performance on the subwavelength domain. As such, it is interesting to verify if better performance could be obtained without inclusions, considering a multilayered medium only. The same optimisation algorithm has been run for multilayered media, considering the same material properties and total length as for the media-counterparts with macro-inclusions (which are different than those used in Chapter 3). The Pareto front is given in Figure 7.19.

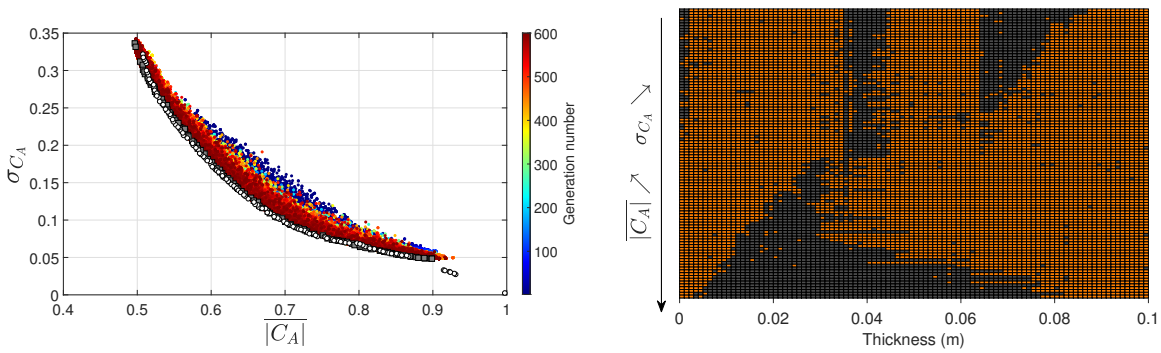

Figure 7.19 – Scores for all generations for the optimisation of the multilayer (1D) arrangement (colored dots). The Pareto front for the last generation is represented by the grey squares. Layer arrangements are also presented on the right hand-side. The white circles show the Pareto front obtained previously when optimising the arrangement of units with macro-inclusions, shown in Figure 7.15.

It can be seen that the difference between the Pareto front for multilayered media (grey squares) and the Pareto front for media with macro-inclusions (white dots) is not significant. The former provides slightly better solutions for $\overline{|C_A|}$, whereas the latter gives solutions of lower σ_{C_A}. It is also observed that the arrangements are similar : thick layers of steel are found where homogeneous steel units are located in the arrangements with macro-inclusions, and thinner layers of steel are found at similar locations as small inclusions. One of the multilayered media has a score very close to that of the selected medium with macro-inclusions. They are both compared in Figure 7.20.

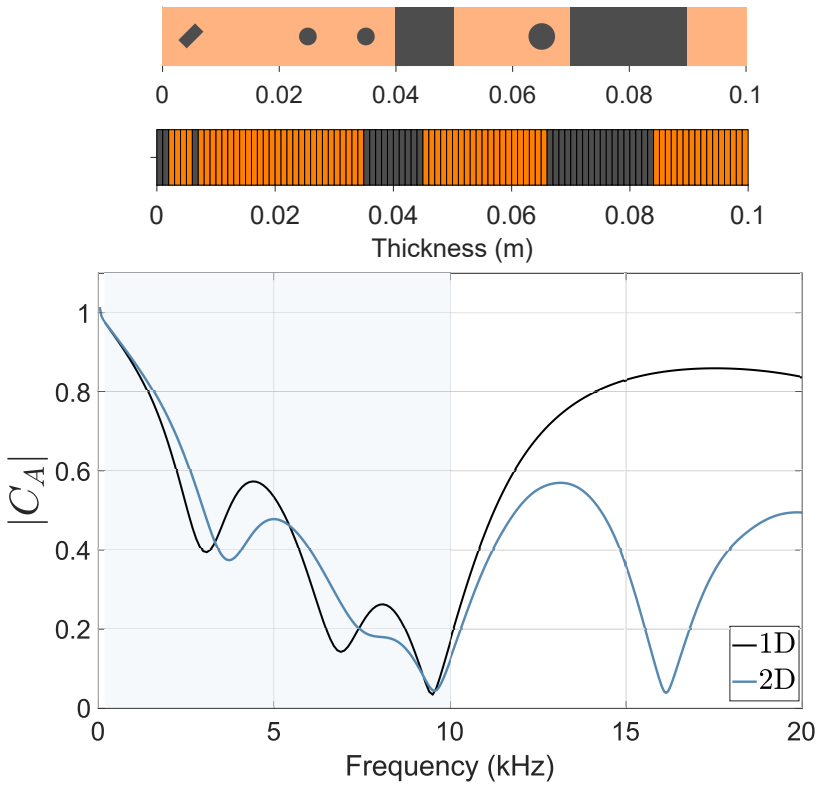

Figure 7.20 – Comparison of the design and anechoism coefficient of two solutions having the same scores.

It is observed that the multilayered solution leads to the same - even slightly better - anechoism coefficient as the solution with macro-inclusions under 10 kHz. However, the difference is significant at higher frequencies, where the solution with 2D-macro-inclusions provides a much lower anechoism coefficient, even though this solution was the one with the worse performance at higher frequencies according to Figure 7.16.

Therefore, inclusions and their resonances are not essential to optimise the anechoism coefficient at low frequencies, or within a relatively narrow frequency range. However, they may help generate strong and sudden variations of the effective impedance at the resonance frequencies, as shown in Figure 7.10, which may help lower the anechoism coefficient for these resonance frequencies. They are also crucial to broaden the frequency range of performance using their various resonances that can be tuned to be nicely spread in the frequency range of study. Consequently, an efficient approach for an anechoic coating of broadband performance may be to combine uniform layers and macro-inclusions, whereas steel layers lower the anechoism coefficient at low frequencies and inclusions help to dissipate the energy at higher frequencies through their resonances. This optimisation approach could also be improved by adding multilayered unit cells to the database, with various steel thicknesses.

7.4 Performance Levels

The layer arrangement is now optimised for both the anechoism and the hull decoupling coefficient, using the objective functions defined in Chapter 3, Section 3.4.

The Pareto front along generations is given in Figure 7.21, which also shows a selection of 35 solutions. It appears that with the parameters given in the optimisation (materials, frequency range, medium thickness), a better anechoic performance than hull decoupling performance is obtained, since $\sigma^L_{C_A}$ is mostly lower than $\sigma^L_{C_D}$. It is observed that the portion of polyurethane on the hull side is increased compared to the optimisation for the anechoism coefficient alone. Inclusions are then moved to the water/medium interface as the hull decoupling performance improves. As such, results here are similar to those obtained with the optimisation for multilayered media, that is, better hull decoupling performance is obtained with media close to a simple bi-layer, with the softer absorbing material being in contact with the hull. It is also worth highlighting that the "steps" in the Pareto front are linked to the position of the unit cell made of steel.

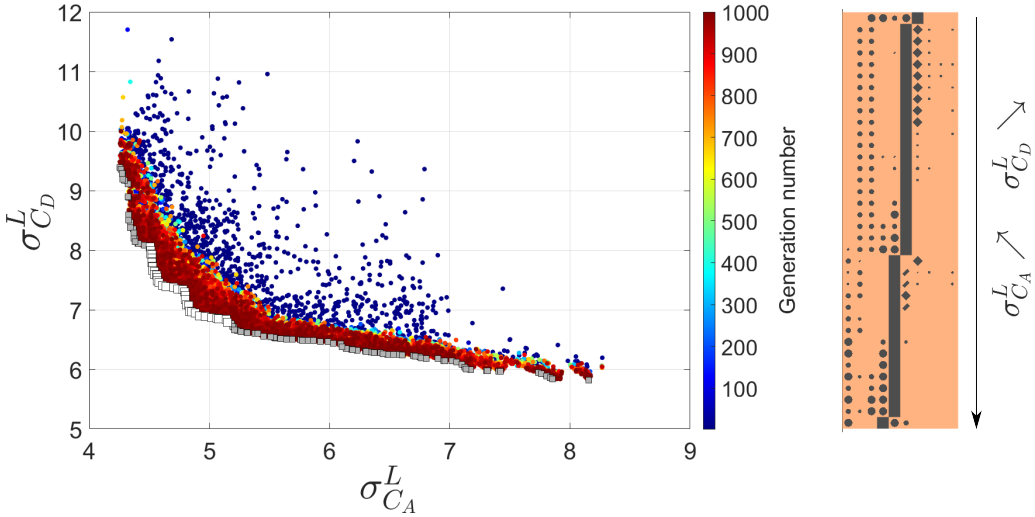

Figure 7.21 – Scores of the Pareto front along generations (left) and selection of 35 layer arrangements of the Pareto front (right), from the lowest $\sigma^L_{C_A}$ to the highest, considering the left hand-side as the incidence side and the right hand-side as the hull side.

7.5 Summary

In this section, a new approach for optimising structures with macro-inclusions has been introduced. It uses the effective properties of different polyurethane units comprising inclusions of different sizes and shapes. The influence of the shape and size of the inclusion on the variations of the effective properties was investigated. The database was then used to optimise a 10 cm-thick media for subwavelength anechoic performance. Similar to what was found for multilayered media, an impedance pattern leading to a low coefficient of anechoism arose. This pattern transcribes the fact that, in the optimised medium, acoustic waves propagate in the medium and are trapped in the damped layer at the end of the medium, resulting in a strong dissipation of energy. This study has also shown that the design of an anechoic coating need not be limited to multilayered media or media with macro-inclusions, as the combination of the two (ie. media with macro-inclusions and uniform layers) can greatly help improve the broadband acoustic performance.

Such an optimisation approach has also proved to be very satisfactory in terms of prediction accuracy and calculation time. In a short time, a complex optimisation problem of 1.3786×10^{11} potential solutions was treated analytically. In addition, this new optimisation concept can be used, adapted and applied to thousands of other problems, for example by considering other criteria of acoustic performance (reflection, transmission, absorption, effective properties, etc.), other materials, other shapes, other total unit lengths and thicknesses, other frequency ranges, and so on. As such, this optimisation tool is easily adaptable.

Chapter 8

Experiments

In this Chapter, the bi-layer Alberich panel designed in Chapter 6 is measured in the acoustic water tank presented in Chapter 4. Since the panel contains periodically embedded void inclusions, the experimental characterisation becomes more complex. The grating diffraction phenomenon is first presented to highlight these difficulties. The 3-point method, presented in Chapter 4, as well as an extension of the method are then applied to measure the acoustic response of the panel. The scattering coefficients of the voided medium are also compared to those obtained using a FE model.

Contents

8.1 Experimental Characterisation of Diffraction Gratings 178

8.1.1 Grating Diffraction Phenomenon 178

8.1.2 Challenges 180

8.2 Measurements of the Alberich 181

8.2.1 Presentation of the panel 181

8.2.2 Below the Cut-off Frequency 181

8.2.3 Above the Cut-off Frequency 187

8.3 Summary 197

8.1 Experimental Characterisation of Diffraction Gratings

For the homogenisation and optimisation of periodic metamaterials with macro-inclusions, the diffraction grating phenomenon was ignored since its influence can easily be neglected for the frequency range of study and the numerical method used. However, the measurement of the Alberich panel poses new challenges due to its periodic arrangement of macroscopic inclusions. In order to apply the 3-point method under valid conditions, the phenomenon of diffraction induced by gratings, which are periodically structured media, is first described. The implications, in terms of the additional challenges for the experimental characterisation, are then discussed.

8.1.1 Grating Diffraction Phenomenon

For an acoustic panel containing a diffraction grating, the scattered field consists of a superposition of an infinite number of diffracted waves. This phenomenon is also well known in optics, using optical diffraction gratings. Each diffracted wave is associated with a diffracted mode number n, where n is an integer. In the case of plane wave excitation of a panel at normal incidence, the 0th-order corresponds to the specular reflection (transmission). As such, it has the same propagation direction as the incident plane wave while the other modes $|n| > 0$ propagate in other directions, as illustrated in Figure 8.1.

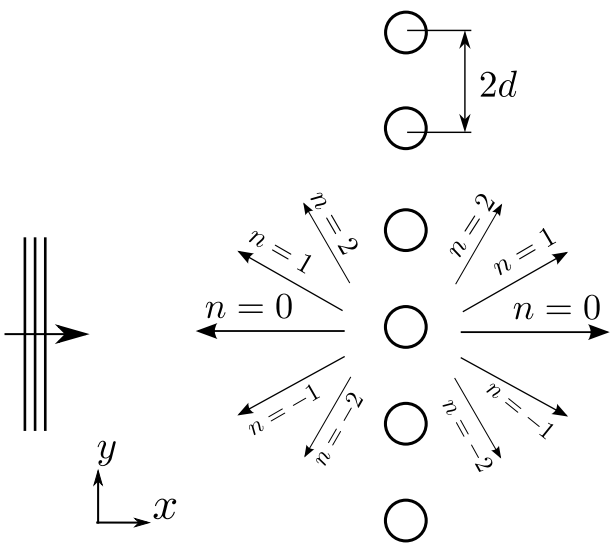

Figure 8.1 – Schematic diagram illustrating the scattered field from a grating. Only the 0th, 1st and 2nd orders on both the reflection and transmission sides are shown.

In what follows, the reflected and transmitted pressures of a panel containing a periodic array are expressed based on [1,116] but using the coordinate system presented in Chapter 4 for the water tank. The incident plane wave is therefore travelling in the direction x, while the panel is in an (y, z)-plane. For the theoretical approach, the inclusions are considered to be infinite along the z-axis and the grating is periodic in the y-direction from $-\infty$ to $+\infty$. Figure 8.2 introduces the projections of the n mode propagation vector in this coordinate system.

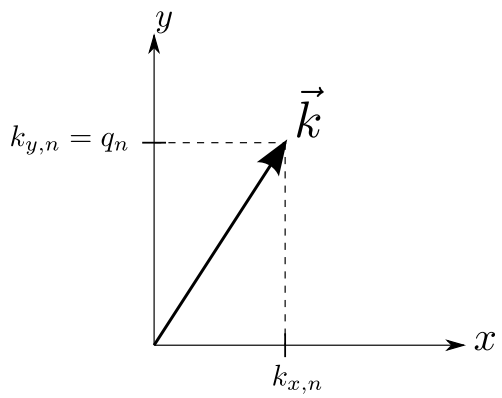

Figure 8.2 – Projections of the n mode propagation vector in the (x,y)-plane.

The reflected and transmitted pressures, denoted respectively by $p_{\mathrm{r}}(x, y)$ and $p_{\mathrm{t}}(x, y)$, are written as an infinite series of waves diffracted by the grating of periodicity $2d$, which yields:

$$p_{\mathrm{r}}(x, y) = \sum_{n=-\infty}^{+\infty} c_{r,n} e^{-\mathrm{i}q_n y} e^{\mathrm{i}k_{x,n} x} \tag{8.1}$$

$$p_{\mathrm{t}}(x, y) = \sum_{n=-\infty}^{+\infty} c_{t,n} e^{-\mathrm{i}q_n y} e^{-\mathrm{i}k_{x,n} x} \tag{8.2}$$

where q_n and $k_{x,n}$ are given as follows:

$$q_n = \frac{n\pi}{d}, \tag{8.3}$$

$$k_{x,n}^2 = k^2 - q_n^2, \tag{8.4}$$

where k is the wavenumber in water and n is the mode number (or mode order) of the diffracted wave whose contribution coefficient is $c_{r,n}$ or $c_{t,n}$. When $k_{x,n}^2 < 0$, the corresponding diffracted wave propagates parallel to the y-axis and decays exponentially along the x-axis. In this case, it only contributes to the near-field and it is referred to as an evanescent wave.

On the contrary, if $k_{x,n}^2 > 0$, the diffracted wave propagates away from the panel in the x-direction. The cut-off frequency f_c for diffracted wave n is therefore given by:

$$f_\mathrm{c}(n) = \frac{c_\mathrm{w} n}{2d}, \tag{8.5}$$

where c_w is the speed of sound in water.

Consequently, there is a cut-off frequency for each diffracted mode n for which a diffracted wave converts from a evanescent wave to a propagating wave. The diffracted waves that do not propagate along the x-axis decay exponentially with distance to the plane which contains the centers of the inclusions. For example, for a frequency f such that $f < c_\mathrm{w}/(2d)$, only the 0th mode exists in the far-field since all the other diffracted waves are evanescent. As the frequency increases, a greater number of diffracted waves convert to propagating waves.

8.1.2 Challenges

In the past, the grating diffraction phenomenon appearing in Alberich-type panels has been studied analytically [1, 116, 124, 125]. Additionally, Ivansson [126] highlighted some of the array diffraction features through experiments. For an Alberich-type coating comprising spherical cavities of 2 mm diameter periodically spaced every 10 mm, ultrasonic pulse measurements showed that above the first cut-off frequency (of 148kHz), the specular reflected wave is closely followed by diffracted waves of higher modes. The author also presented a pulse computation for an Alberich coating below the first cut-off frequency, showing that evanescent waves that exponentially decay in the normal direction are no longer discernible 1 meter away from the panel but are non negligible at the interface [127]. This phenomenon has also been mentioned in the study of materials other than Alberich-type designs, but results above the first cut-off frequency are usually not investigated [128, 129].

Therefore, the experimental characterisation of a metamaterial with a periodic arrangement of macroscopic inclusions such as the Alberich coating is not common in the literature since lattice-diffracted non-specular waves make the experimental study of such media even more complex than for a homogeneous panel. Difficulties in panel measurements highlighted in Chapter 4, such as panel edge-diffraction, are still present and these challenges are increased by the presence of diffracted waves traveling in directions other than the incident plane wave and further, may or may not be evanescent depending on the frequency. Therefore, in what follows, the applicability and robustness of the 3-point method for measurements of the Alberich panel is studied. The physical phenomena that occurs below and above the first cut-off frequency are studied separately.

8.2 Measurements of the Alberich

8.2.1 Presentation of the panel

The panel is shown in Figure 8.3. Its lateral dimensions are 980 × 980 mm and is maintained by a Plexiglas frame. Due to the important concentration of air in the panel, a weight has been placed at the bottom to prevent it from floating.

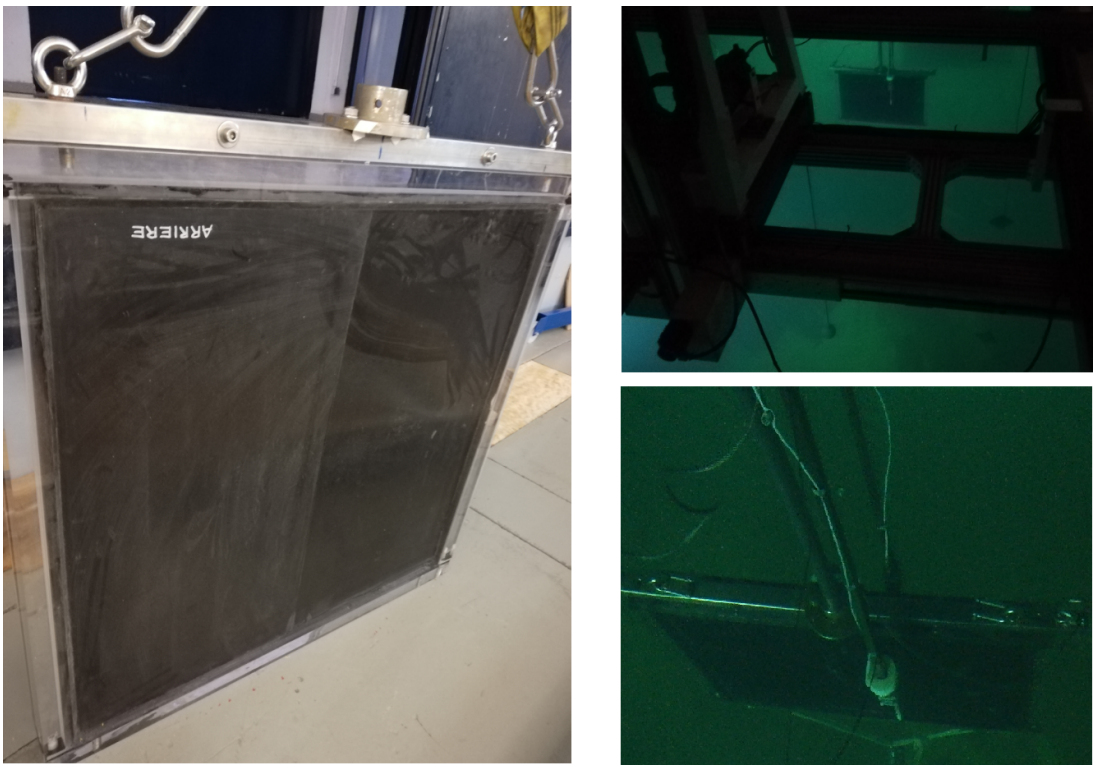

Figure 8.3 – Photography of the Alberich panel before immersion (left) and during the experiments (right).

8.2.2 Below the Cut-off Frequency

Applicability

The panel design presented in Figure 8.4 is used. The 3-point method set-up is also shown. For this panel, the first cut-off frequency for the grating is $f_c = \frac{c_w}{2d} = 18.75$ kHz. Below the first cut-off frequency, only the 0th-order mode propagates. The main challenge here is to ensure that the evanescent field does not pollute measurements near the panel, where the hydrophones are placed. For the 3-point method, the hydrophones must be placed sufficiently close to the panel so that the edge-diffracted pressure can be assumed to be the same at the 3 positions.

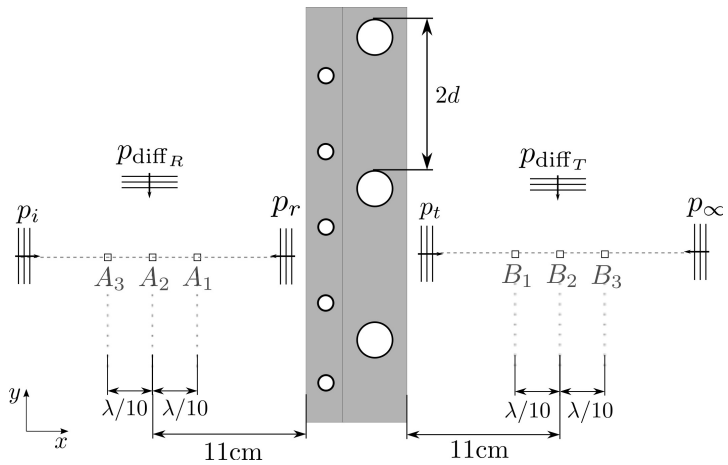

Figure 8.4 – Alberich panel measured with the 3-point method below the first cut-off frequency.

In order to verify if the experimental method can be correctly applied to measure the Alberich grating, the near-field evanescence is analysed. Using Equation (8.4), the term $e^{\mathrm{i}k_{x,n}x}$ is evaluated, since it weights the contribution coefficients c_n of the diffracted mode n. For the panel studied here, only the $n = \pm 1$ modes are considered since there are no other cut-off frequencies included in the measurement frequency range up to 25 kHz for the water tank used. In Figure 8.5, the position x at which $e^{\mathrm{i}k_{x,\pm 1}x}$ becomes equal to 0.01, 0.05 and 0.1 are plotted for each frequency. Theses curves show that at the corresponding position x, the amplitude of the evanescent diffracted wave ± 1 has decreased by 99%, 95% or 90%. In addition, the 3 positions of the hydrophone on the reflection side are plotted for each frequency, considering a central position X_2 at 11cm from the interface and a spacing of $\lambda/10$ between the 3 positions.

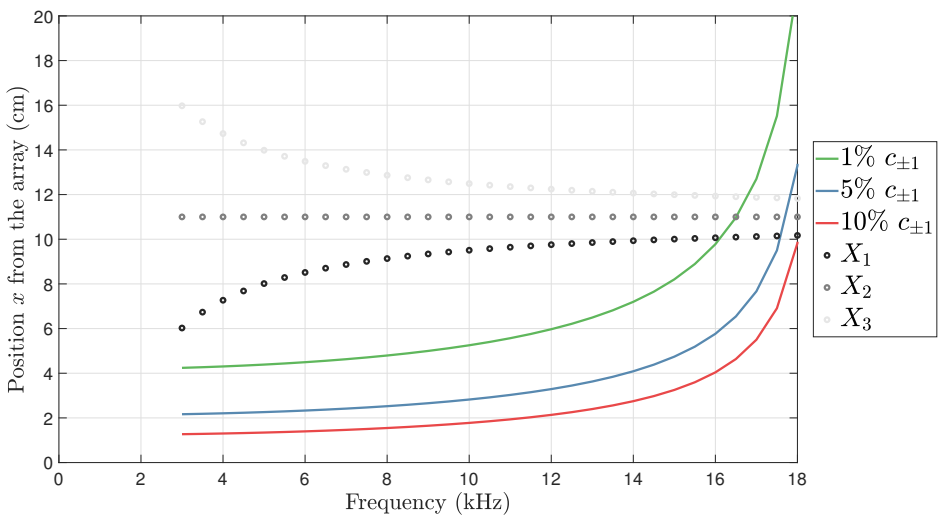

Figure 8.5 – Distances at which the amplitude of the evanescent diffracted waves $n = \pm 1$ from the large inclusion array is less than 1%, 5% and 10% of its initial amplitude. The positions of the hydrophones for the 3-point method set-up are also shown.

Below 15 kHz, the diffracted modes ± 1 should not disturb the 3-point method measurements since their amplitude should be reduced by at least 99% of their initial amplitude. It can nevertheless be observed that the evanescent feature of the diffracted waves decreases as the cut-off frequency approaches. Between 15 kHz and the first cut-off frequency, some discrepancies may consequently appear due to a potential contribution of the diffracted modes ± 1.

Results

Hydrophone positions along the x-axis defined previously ($X_2 = 11$cm, $X_1 = X_2 - \lambda/10$ and $X_3 = X_2 + \lambda/10$) are considered hereafter. Along the y-axis, 16 positions regularly spaced by 5 mm are considered, so fully covering one unit cell of period $2d = 8$ cm. The total pressures recorded at the three positions on each side of the panel are shown in Figures 8.6 and 8.7 respectively for the incident side and transmission side.

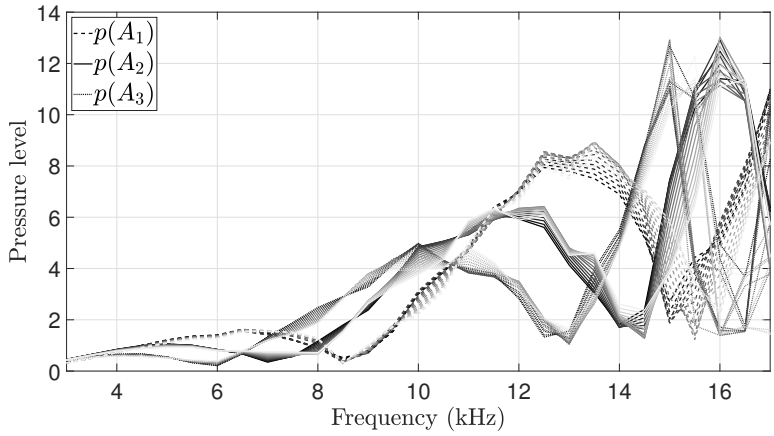

Figure 8.6 – Pressure amplitudes measured at the 3 positions A_1, A_2 and A_3 for the reflection side. The graduation of grey represents the y-positions along the unit cell.

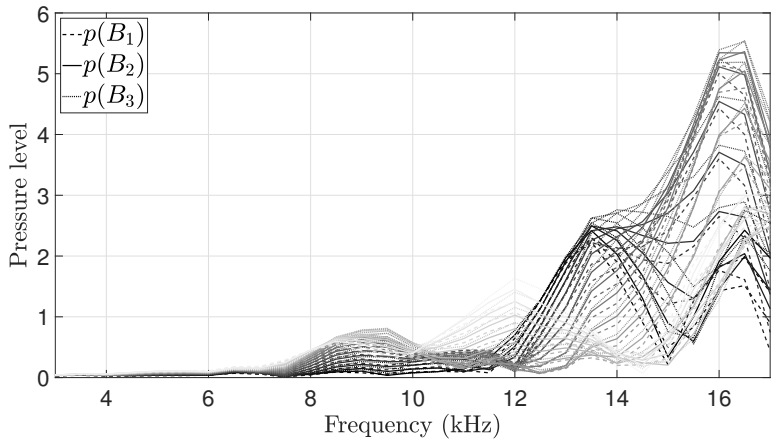

Figure 8.7 – Pressure amplitudes measured at the 3 positions B_1, B_2 and B_3 for the transmission side. The graduation of grey represents the y-positions along the unit cell.

In both figures, it can be observed that the measured pressures are slightly different depending on the position along the y-axis, due to the contribution of the edge-diffracted pressure. For higher frequencies, the evanescent field may also contribute slightly to the measured pressures as shown in Figure 8.5.

It is crucial here to draw attention to the fact that the acoustic source resonates around 16 kHz which sometimes leads to an overload of the received signal, thus invalidating the measurement. Usually, the power of the source is reduced to avoid such an overload. However, a strong acoustic emission was required here in order to be able to detect a signal on the transmission side that stood out from the noise, since the transmission through the panel is extremely low (as expected for such panels). Therefore, results from 15 kHz should be taken with caution.

On the reflection side, the total pressures measured are used to derive the incident pressure p_i, the reflected pressure p_r and the edge-diffracted pressure on the reflection side p_{diff_R}. These calculated pressures are shown in Figure 8.8. The incident pressure is compared to that obtained by measurements without the panel, referred to as p_i^{WP}. This incident pressure p_i^{WP} is maximum at the resonance frequency of the acoustic source. It can be seen that the calculated incident pressure p_i is consistent with p_i^{WP} up to 15 kHz, thus validating the estimation of the incident pressure using the 3-point method. However, there is a significant difference around 16 kHz, which invalidates the results from 15 kHz for the reflection side. It is nonetheless difficult to identify whether this divergence originates from the overload of the received signal due to the source resonance or from the higher contribution of the evanescent diffracted waves close to the cut-off frequency.

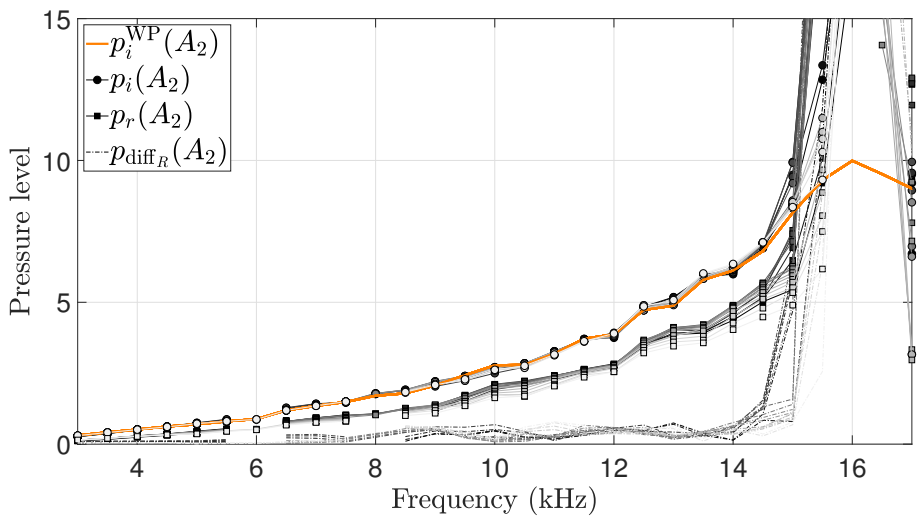

Figure 8.8 – Incident pressure p_i, reflected pressure p_r and edge-diffracted pressure p_{diff_R} at the central position A_2 on the reflection side. The incident pressure measured without the panel (p_i^{WP}) is also plotted. The graduation of grey represents the y-positions along the unit cell.

On the transmission side, the 3-point method leads to the transmitted pressure p_t and the edge-diffracted pressure p_{diff_T}. Pressure p_∞ coming from infinity and travelling towards the negative x is also obtained for the transmission side. These pressures are plotted in Figure 8.9, where it can be seen that the infinite pressure is almost null, thus validating that the 3-point method is correctly applied. The transmitted pressure p_t is also significantly low. It can finally be noticed that the edge-diffracted pressure varies significantly as a function of the y-position and most often appears as the main component of the pressure field behind the panel.

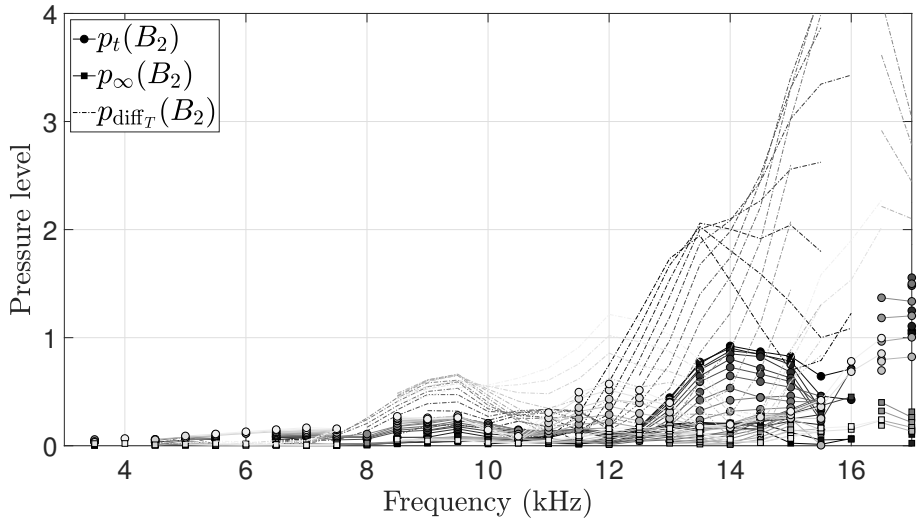

Figure 8.9 – Transmitted pressure p_t, infinite pressure p_∞ and edge-diffracted pressure p_{diff_T} at the central position B_2 on the transmission side. The graduation of grey represents the y-position along the unit cell.

Finally, since the 3-point method eliminates edge-diffraction contributions, the experimental coefficients could, in practice, be directly compared to those of an infinite panel. Reflection and transmission coefficients are thus calculated using the pressures from the 3-point method given in Figures 8.8 and 8.9. They are derived for each y-position independently. Coefficients are also averaged along the unit cell by considering all y-positions. The numerically obtained reflection and transmission coefficients for a medium of infinite lateral dimensions (shown in Chapter 6) are also shown for comparison in Figure 8.10. Additionally, a raw calculation of the coefficient is performed, using the total pressure measured at the central position X_2 and the incident pressure measured without a panel p_i^{WP}, according to :

$$R = \frac{p(A_2) - p_i^{\mathrm{WP}}}{p_i^{\mathrm{WP}}}, \tag{8.6}$$

$$T = \frac{p(B_2)}{p_i^{\mathrm{WP}}}. \tag{8.7}$$

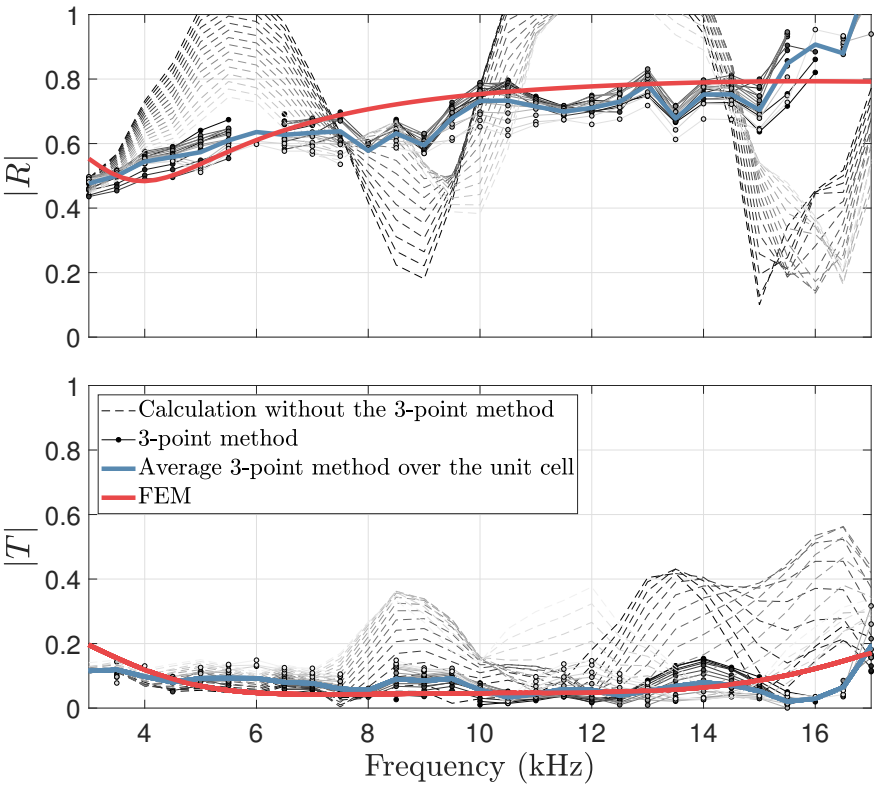

Figure 8.10 – Magnitude of the reflection and transmission coefficients obtained with the 3-point method and without as per Equations (8.6) and (8.7). The color graduation of grey represents the y-position along the unit cell. Numerical results for a panel of infinite lateral dimensions are also shown.

It is first noted that the coefficients of the calculation without the 3-point method are significantly different from the numerical results. Even by averaging these coefficients over the unit cell, the acoustic response obtained would be very different from the numerical prediction. On the contrary, the coefficients derived from the 3-point method are consistent with the predictions. There are some slight discrepancies which may be attributed to the fact that the panel is not infinite. Consequently, the 3-point method leads to reflection and transmission coefficients which correspond well to those calculated numerically for an infinite panel up to 15 kHz. This again underlines the importance of removing the contribution of the edge-diffracted pressure.

To summarise, the 3-point method provides accurate and robust measurements of the Alberich medium without being influenced by the evanescent field created by the grating. Nevertheless, it must be ensured that the distance between the grating and the hydrophone is large enough but also not too large so that the assumption on the edge-diffracted pressure can be applied. This can be achieved by using criteria established in Chapter 4 for homogeneous panels. However, between 15 kHz and the first cut-off frequency, there are significant discrepancies, which may be due to the resonance of the acoustic source or to the evanescent field of higher amplitude close to the cut-off frequency.

8.2.3 Above the Cut-off Frequency

Direct Calculation

Above the first cut-off frequency, the acoustic response is no longer specular and diffracted waves convert from evanescent to propagating. Since the reflected and transmitted pressures are written as an infinite sum of waves diffracted by the grating (Equations (8.1) and (8.2)), the approach used to calculated the reflection and transmission coefficients is different. Formulas given in [1, 116] are used and rewritten in what follows using the notations of the manuscript. The contribution coefficient $c_{r,n}$ (or $c_{t,n}$) of each diffracted mode is obtained by using the reflected (or transmitted) pressure measured or calculated along a linear mesh covering a complete constituent unit. Formulas are the same for both the reflected and transmitted sides, so the notation c_n is used in what follows. As presented in Figure 8.11, the linear mesh corresponds to the definition of M regularly spaced points, labeled y_m. Reflected or transmitted pressure p_m is measured/calculated on each of these points.

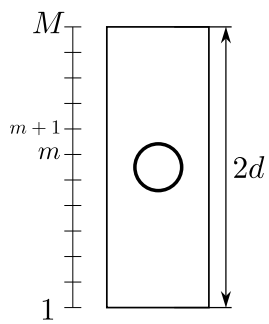

Figure 8.11 – Segmented line where the pressure is measured/calculated along a full period of the array.

The expression of the contribution coefficient for the 0th mode is first given by :

$$c_0 = \sum_{m=1}^{M} \frac{c_{0,m}}{2d}, \tag{8.8}$$

where c_0^m is an elementary contribution calculated on each segment $[y_m, y_{m+1}]$ using the pressures p_m and p_{m+1} measured/calculated at these points as per:

$$c_{0,m} = \frac{y_{m+1} - y_m}{2}(p_{m+1} + p_m). \tag{8.9}$$

The contribution coefficient of the nth mode for $n \neq 0$ is:

$$c_n = \sum_{m=1}^{M} \frac{c_{n,m}}{2d}, \tag{8.10}$$

where c_n^m is the elementary contribution obtained using the pressures p_m and p_{m+1} measured/calculated at the points y_m and y_{m+1} as per:

$$c_{n,m} = \alpha_{(n,m)} p_m + \alpha_{(n,m+1)} p_{m+1}. \tag{8.11}$$

The expression for the coefficients $\alpha_{(n,m)}$ and $\alpha_{(n,m+1)}$ are:

$$\begin{cases} \alpha_{(n,m)} = e^{-\mathrm{i}q_n y_m}\left(\frac{1}{\mathrm{i}q_n} - \frac{1}{(\mathrm{i}q_n)^2}\frac{e^{-\mathrm{i}q_n(y_{m+1}-y_m)}-1}{-y_{m+1}+y_m}\right) \\ \alpha_{(n,m+1)} = e^{-\mathrm{i}q_n y_{m+1}}\left(\frac{1}{-\mathrm{i}q_n} - \frac{1}{(\mathrm{i}q_n)^2}\frac{1-e^{\mathrm{i}q_n(y_{m+1}-y_m)}}{y_{m+1}-y_m}\right) \end{cases} \tag{8.12}$$

Thus, the use of measurements/calculations on a meshed line covering a complete unit cell should, in theory, lead to the reflected and transmitted pressures of the grating diffracted modes 0, +1 and −1 for the Alberich panel. This approach is used in a FEM calculation to obtain the reflection and transmission coefficients for orders 0 and ±1. It is also used to perform a raw calculation of the coefficients using the pressures measured along an elementary cell. Such a calculation therefore does not take into account an eventual contribution of the panel's edge-diffraction and it can thus be seen as an equivalent to the results "without the 3-point method" presented in the preceding section below the cut-off frequency. These coefficients will be compared later in this Chapter. An extension of the 3-point method is first proposed to calculate both the grating diffracted modes and the edge-diffracted pressure.

The 5-point method

Above the first cut-off frequency, diffracted modes ±1 are no longer evanescent and begin to propagate. Diffracted modes ±2 are still present but remain evanescent up to 37.5 kHz. For measurements, this means that the associated pressures, p_{-1} and p_{+1}, must be calculated in addition to the other unknowns of the 3-point method. It is therefore necessary to add two unknowns, resulting in two additional inputs which are measurement points. Since the 3-point method is applied in several positions y_m along the y-axis to cover a complete unit cell, a fourth and a fifth point, X_4 and X_5, are chosen and correspond to the central point at the previous and next y positions where the 3-point method is applied, so $X_4 = X_2(y_{m-1})$ and $X_5 = X_2(y_{m+1})$. This adaptation is illustrated in Figure 8.12. It should be noted that the elementary cell is not represented as centered since, in practice, it may not be possible to know where the hydrophones are located in relation to the position of inclusion. However, if the inclusions were centered with respect to the measurement line, the 5-point method could be reduced to the 4-point method since $p_{-1} = p_{+1}$.

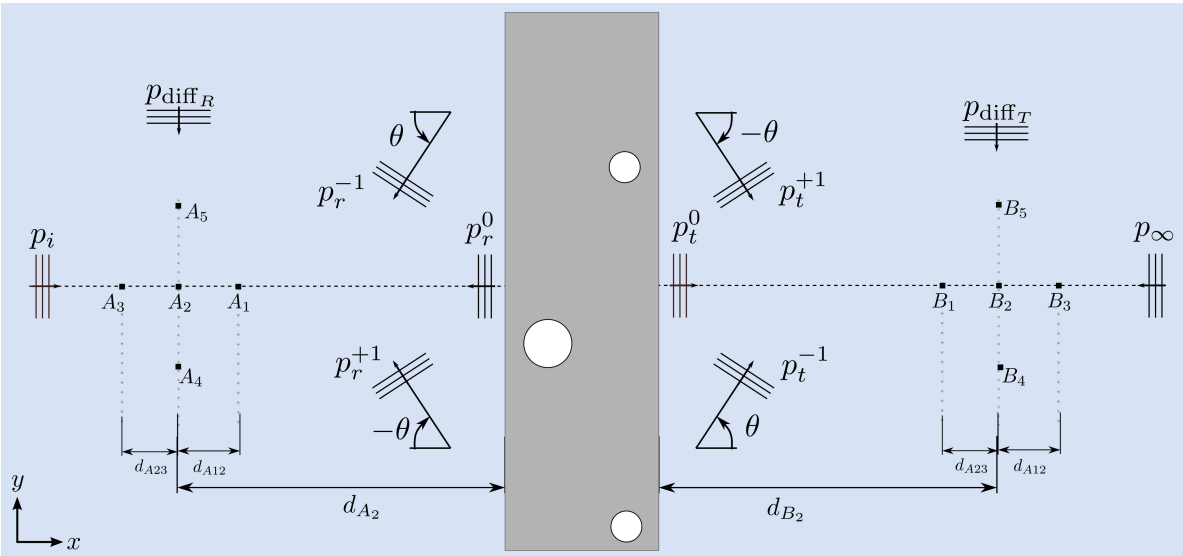

Figure 8.12 – Experimental set-up specific to the application of the 5-point method along one unit cell. Pressure contributions and geometric parameters are also presented.

The 5-point method is first introduced for the reflection side. Five points A_1, A_2, A_3, A_4 and A_5 are considered. The central position A_2 is a reference, and the distances $d_{A12} = A_1A_2$, $d_{A23} = A_2A_3$, $d_{A24} = A_2A_4$ and $d_{A25} = A_2A_5$ are defined. At each point, the total pressure p can be expressed as a function of the contributions of the incident pressure p_i and the reflected pressure of the 0th mode p_r^0 at the central position, the edge-diffracted pressure on the reflection side p_{diff_R} as well as the pressure of the diffracted modes ± 1, p_r^{-1} and p_r^{+1}.

The system of equations to implement a five-point method can now be written by adding two unknowns to the 3-point method system as follows:

$$\begin{cases} p(A_1) = p_i(A_2)e^{-\mathrm{i}kd_{A12}} + p_r^0(A_2)e^{\mathrm{i}kd_{A12}} + p_{\mathrm{diff}_R}(A_1) + p_r^{+1}(A_2)e^{\mathrm{i}kd_{A12}\cos(\theta)} + p_r^{-1}(A_2)e^{\mathrm{i}kd_{A12}\cos(\theta)} \\ p(A_2) = p_i(A_2) + p_r^0(A_2) + p_{\mathrm{diff}_R}(A_2) + p_r^{+1}(A_2) + p_r^{-1}(A_2) \\ p(A_3) = p_i(A_2)e^{\mathrm{i}kd_{A23}} + p_r^0(A_2)e^{-\mathrm{i}kd_{A23}} + p_{\mathrm{diff}_R}(A_3) + p_r^{+1}(A_2)e^{-\mathrm{i}kd_{A23}\cos(\theta)} + p_r^{-1}(A_2)e^{-\mathrm{i}kd_{A23}\cos(\theta)} \\ p(A_4) = p_i(A_4) + p_r^0(A_4) + p_{\mathrm{diff}_R}(A_4) + p_r^{+1}(A_2)e^{-\mathrm{i}kd_{A24}\sin(\theta)} + p_r^{-1}(A_2)e^{\mathrm{i}kd_{A24}\sin(\theta)} \\ p(A_5) = p_i(A_5) + p_r^0(A_5) + p_{\mathrm{diff}_R}(A_5) + p_r^{+1}(A_2)e^{\mathrm{i}kd_{A25}\sin(\theta)} + p_r^{-1}(A_2)e^{-\mathrm{i}kd_{A25}\sin(\theta)} \end{cases} . \tag{8.13}$$

Since the incident wave travels along the x-axis and it is a plane wave, $p_i(A_2) = p_i(A_4) = p_i(A_5)$. The same observation applies for the specular reflection p_r^0. It is also assumed that the 5 positions are close enough so that $p_{\mathrm{diff}_R}(A_1) = p_{\mathrm{diff}_R}(A_2) = p_{\mathrm{diff}_R}(A_3) = p_{\mathrm{diff}_R}(A_4) = p_{\mathrm{diff}_R}(A_5)$. Equation (8.13) can thus be simplified and written in a matrix form as follows:

$$\begin{pmatrix} p(A_1) \\ p(A_2) \\ p(A_3) \\ p(A_4) \\ p(A_5) \end{pmatrix} = \begin{bmatrix} e^{-\mathrm{i}kd_{A12}} & e^{\mathrm{i}kd_{A12}} & 1 & e^{\mathrm{i}kd_{A12}\cos(\theta)} & e^{\mathrm{i}kd_{A12}\cos(\theta)} \\ 1 & 1 & 1 & 1 & 1 \\ e^{\mathrm{i}kd_{A23}} & e^{-\mathrm{i}kd_{A23}} & 1 & e^{\mathrm{i}kd_{A23}\cos(\theta)} & e^{\mathrm{i}kd_{A23}\cos(\theta)} \\ 1 & 1 & 1 & e^{-\mathrm{i}kd_{A24}\sin(\theta)} & e^{\mathrm{i}kd_{A24}\sin(\theta)} \\ 1 & 1 & 1 & e^{\mathrm{i}kd_{A25}\sin(\theta)} & e^{-\mathrm{i}kd_{A25}\sin(\theta)} \end{bmatrix} \begin{pmatrix} p_i(A_2) \\ p_r^0(A_2) \\ p_{\mathrm{diff}_R}(A_2) \\ p_r^{+1}(A_2) \\ p_r^{-1}(A_2) \end{pmatrix}. \quad (8.14)$$

By inverting Equation (8.14), the pressures $p_i(A_2)$, $p_r^0(A_2)$, $p_r^{+1}(A_2)$, $p_r^{-1}(A_2)$ and $p_{\mathrm{diff}_R}(A_2)$ are obtained.

On the transmission side, the same approach is adopted, considering the five points B_1, B_2, B_3, B_4 and B_5 and the distances $d_{B12} = B_1B_2$, $d_{B23} = B_2B_3$, $d_{B24} = B_2B_4$ and $d_{B25} = B_2B_5$, where position B_2 is taken as the reference. Assuming that the edge-diffracted pressure is the same at the five positions, the total pressures at these points are expressed by:

$$\begin{cases} p(B_1) = p_t^0(B_2)e^{\mathrm{i}kd_{B12}} + p_\infty(B_2)e^{-\mathrm{i}kd_{B12}} + p_{\mathrm{diff}_T}(B_2) + p_t^{+1}(B_2)e^{\mathrm{i}kd_{B12}\cos(\theta)} + p_t^{-1}(B_2)e^{\mathrm{i}kd_{B12}\cos(\theta)} \\ p(B_2) = p_t^0(B_2) + p_\infty(B_2) + p_{\mathrm{diff}_T}(B_2) + p_t^{+1}(B_2) + p_t^{-1}(B_2) \\ p(B_3) = p_t^0(B_2)e^{-\mathrm{i}kd_{B23}} + p_\infty(B_2)e^{\mathrm{i}kd_{B23}} + p_{\mathrm{diff}_T}(B_2) + p_t^{+1}(B_2)e^{-\mathrm{i}kd_{B23}\cos(\theta)} + p_t^{-1}(B_2)e^{-\mathrm{i}kd_{B23}\cos(\theta)} \\ p(B_4) = p_t^0(B_4) + p_\infty(B_4) + p_{\mathrm{diff}_T}(B_2) + p_t^{+1}(B_2)e^{-\mathrm{i}kd_{B24}\sin(\theta)} + p_t^{-1}(B_2)e^{-\mathrm{i}kd_{B24}\sin(\theta)} \\ p(B_5) = p_t^0(B_5) + p_\infty(B_5) + p_{\mathrm{diff}_T}(B_2) + p_t^{-1}(B_2)e^{-\mathrm{i}kd_{B25}\sin(\theta)} + p_t^{-1}(B_2)e^{\mathrm{i}kd_{B25}\sin(\theta)} \end{cases}. \quad (8.15)$$

Since the infinite pressure is theoretically a non-existing wave travelling along the x-axis and is a plane wave, $p_\infty(B_2) = p_\infty(B_4) = p_\infty(B_5)$. The same observation applies for the specular transmission p_t^0. The contributions of the transmitted, infinite and edge-diffracted pressures are then be calculated by solving the following system of equations:

$$\begin{pmatrix} p(B_1) \\ p(B_2) \\ p(B_3) \\ p(B_4) \\ p(B_5) \end{pmatrix} = \begin{bmatrix} e^{\mathrm{i}kd_{B12}} & e^{-\mathrm{i}kd_{B12}} & 1 & e^{\mathrm{i}kd_{B12}\cos(\theta)} & e^{\mathrm{i}kd_{B12}\cos(\theta)} \\ 1 & 1 & 1 & 1 & 1 \\ e^{-\mathrm{i}kd_{B23}} & e^{\mathrm{i}kd_{B23}} & 1 & e^{-\mathrm{i}kd_{B23}\cos(\theta)} & e^{-\mathrm{i}kd_{B23}\cos(\theta)} \\ 1 & 1 & 1 & e^{-\mathrm{i}kd_{B24}\sin(\theta)} & e^{\mathrm{i}kd_{B24}\sin(\theta)} \\ 1 & 1 & 1 & e^{\mathrm{i}kd_{B25}\sin(\theta)} & e^{-\mathrm{i}kd_{B25}\sin(\theta)} \end{bmatrix} \begin{pmatrix} p_t^0(B_2) \\ p_\infty(B_2) \\ p_{\mathrm{diff}_T}(B_2) \\ p_t^{+1}(B_2) \\ p_t^{-1}(B_2) \end{pmatrix}. \quad (8.16)$$

Numerical Results

In order to verify the equations implemented in the 5-point method, a finite element model is carried out in which the pressures are recorded at the same positions as for the measurements, as illustrated in Figure 8.13. The FEM model includes only one unit cell of the bi-layer Alberich. Periodic Bloch-Floquet conditions are applied on the lateral sides. In the finite element model, the total pressures are calculated at 16 lateral positions covering one spatial period of the medium, 11 cm away from its interface with water. For such a numerical model with theoretically infinite lateral dimensions, there is no edge-diffracted pressure.

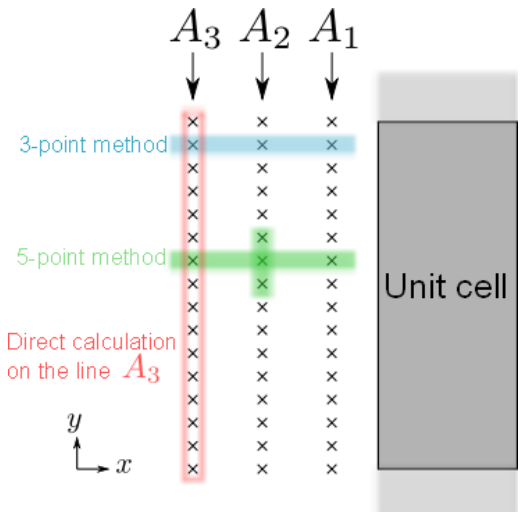

Figure 8.13 – Set of measurements points on the reflection side.

The calculated pressures obtained by the numerical implementation of the 5-point method are shown in Figure 8.14. It is worth noting that the method is applied to each y_m position, but in the figure the curves for each of these positions are superimposed. This shows that the 5-point method seems to be adequate to characterise the panel independently of the position along the periodic panel. It can be seen that the retrieved incident pressure is equal to unity, which corresponds to the amplitude of the incident plane wave used in the finite element model. Also, the pressure $p_\infty(B_2)$ is zero as one would expect.

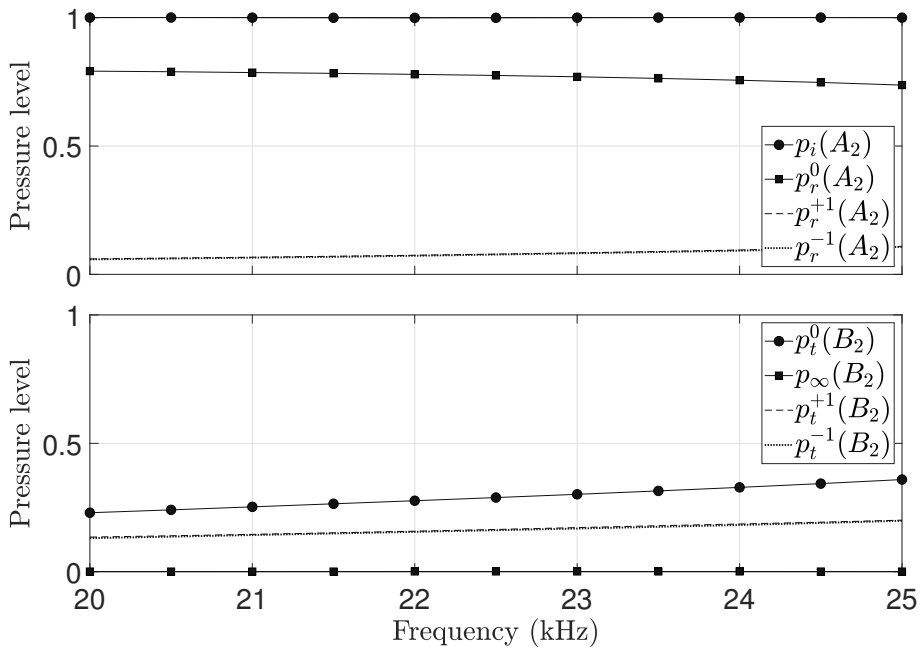

Figure 8.14 – Retrieved pressures by applying the 5-point method with a finite element model of the unit cell.

To verify the amplitudes of the reflected and transmitted pressures given by the 5-point method, a direct calculation using Equations (8.8) to (8.12) is also applied to the finite element model. From the total pressure obtained from the FEM calculation, Equations (8.8) to (8.12) are used to calculate the contribution of the 0th mode and the $\pm 1^{\text{st}}$ modes. By also calculating the incident pressure in the numerical model, it is possible to derive the reflection and transmission coefficients from the 0th mode using p^0/p_i and from the $\pm 1^{\text{st}}$ modes with $p^{\pm 1}/p_i$. Reflection and transmission coefficients for the 0th and $\pm 1^{\text{st}}$ modes are given in Figure 8.15. This shows that the direct calculation and the 5-point method lead to the same scattering coefficients, thus validating the approach implemented in the 5-point method.

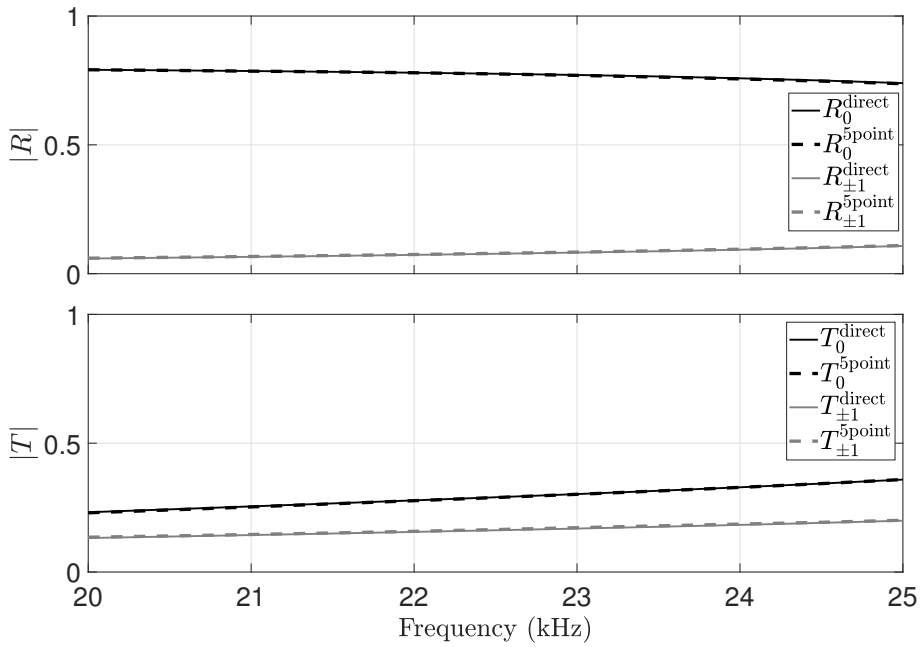

Figure 8.15 – Reflection and transmission coefficients for the specular response and the $\pm 1^{\text{st}}$ order obtained using a direct calculation as per section 8.2.3 and the 5-point method as per section 8.2.3, both using the total pressures calculated with a finite element model of a the constituent unit cell.

Experimental Results

The 5-point method is now applied on measured pressures. Contrary to the previous results based on the finite element model, the measured pressures are now influenced by the edge-diffracted pressure. The total pressures recorded at the three positions on each side of the panel are plotted in Figures 8.16 and 8.17 for the incident side and transmission side, respectively. It can be seen that the pressure levels are very low on the transmission side in comparison with the reflection side.

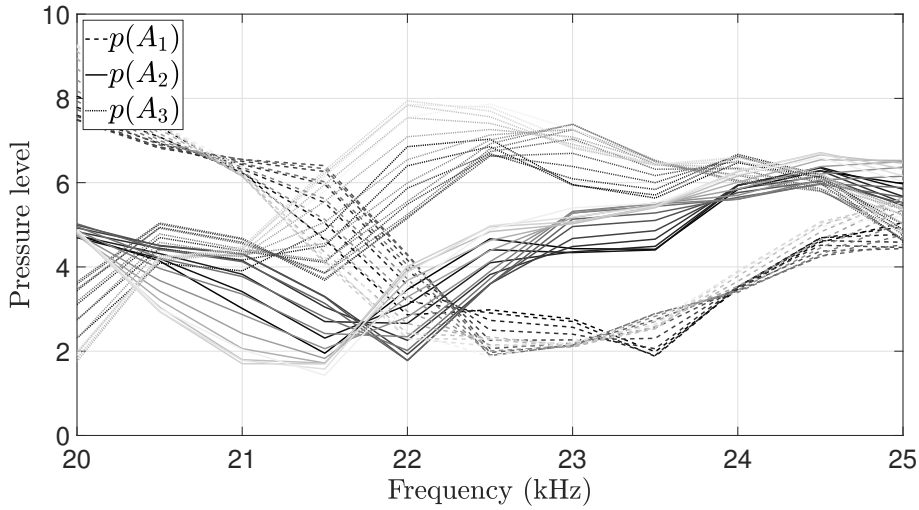

Figure 8.16 – Pressure amplitudes measured at the 3 positions A_1, A_2 and A_3 on the reflection side. The graduation of grey represents the y-positions along the unit cell.

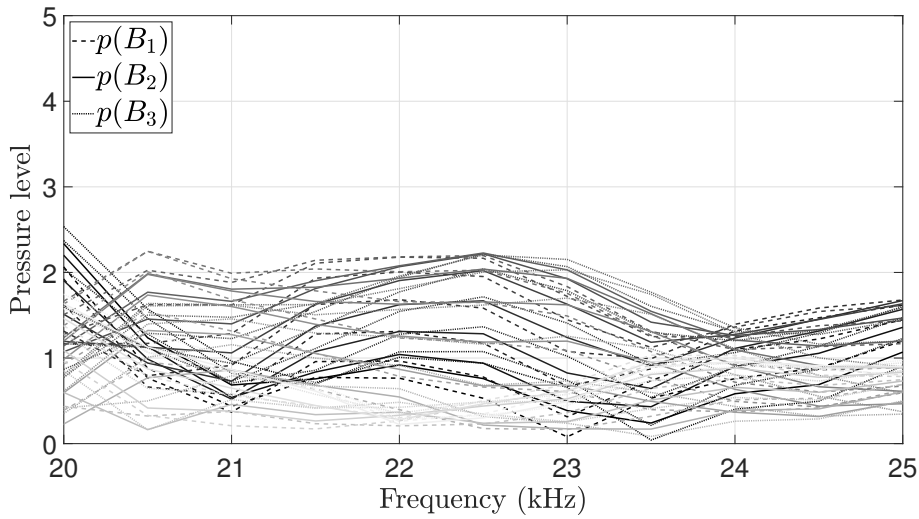

Figure 8.17 – Pressure amplitudes measured at the 3 positions B_1, B_2 and B_3 on the transmission side. The graduation of grey represents the y-positions along the unit cell.

The calculated pressures on the incident and transmission sides are shown in Figures 8.18 and 8.19, respectively. It is first observed that the incident pressure obtained with the 5-point method is consistent with the one measured without a panel. It is also seen that the 0th mode is predominant on the reflection side over the $\pm 1^{\text{st}}$ modes. Moreover, discrepancies are visible along the y-axis for all these calculated pressures where theoretically only the edge-diffracted pressure should vary from one y-position to another. It can also be noted that at such "high frequencies" (in the context of coatings for underwater acoustics), the results may be more sensitive to the material properties and geometry irregularities. These discrepancies may therefore be representative of the panel and its local irregularities. On the transmission side, the infinite pressure is almost

null for the whole frequency range, as it is expected when the simplifying assumptions of the method are acceptable. Therefore, the results seems overall consistent and might, as for the reflection side, be influenced by local irregularities having more impact since the wavelength is getting smaller.

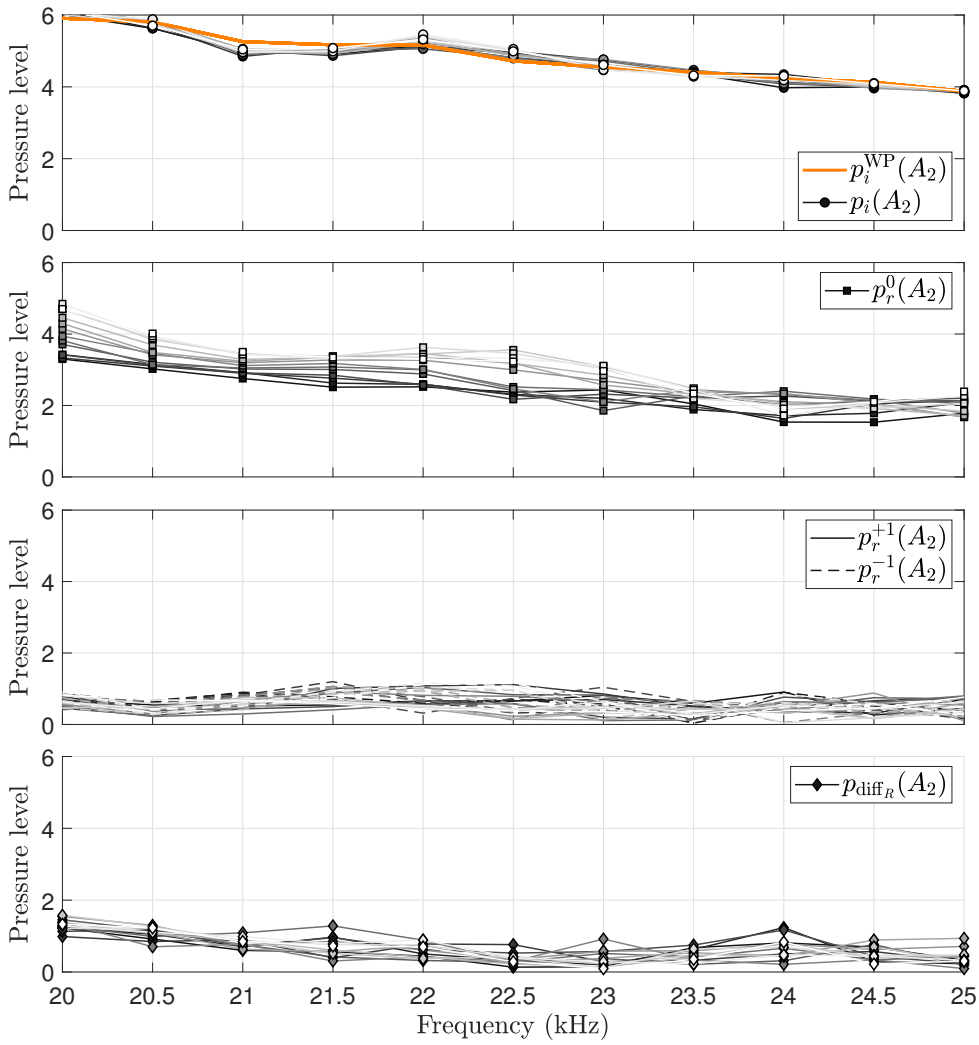

Figure 8.18 – Incident pressure (p_i), reflected pressure of the 0th mode (p_r^0) and of the diffracted modes ± 1 ($p_r^{\pm 1}$) and edge-diffracted pressure (p_{diff_R}) at the central position A_2 on the reflection side. The incident pressure measured without the panel (p_i^{WP}) is also plotted. The graduation of grey represents the y-positions along the unit cell.

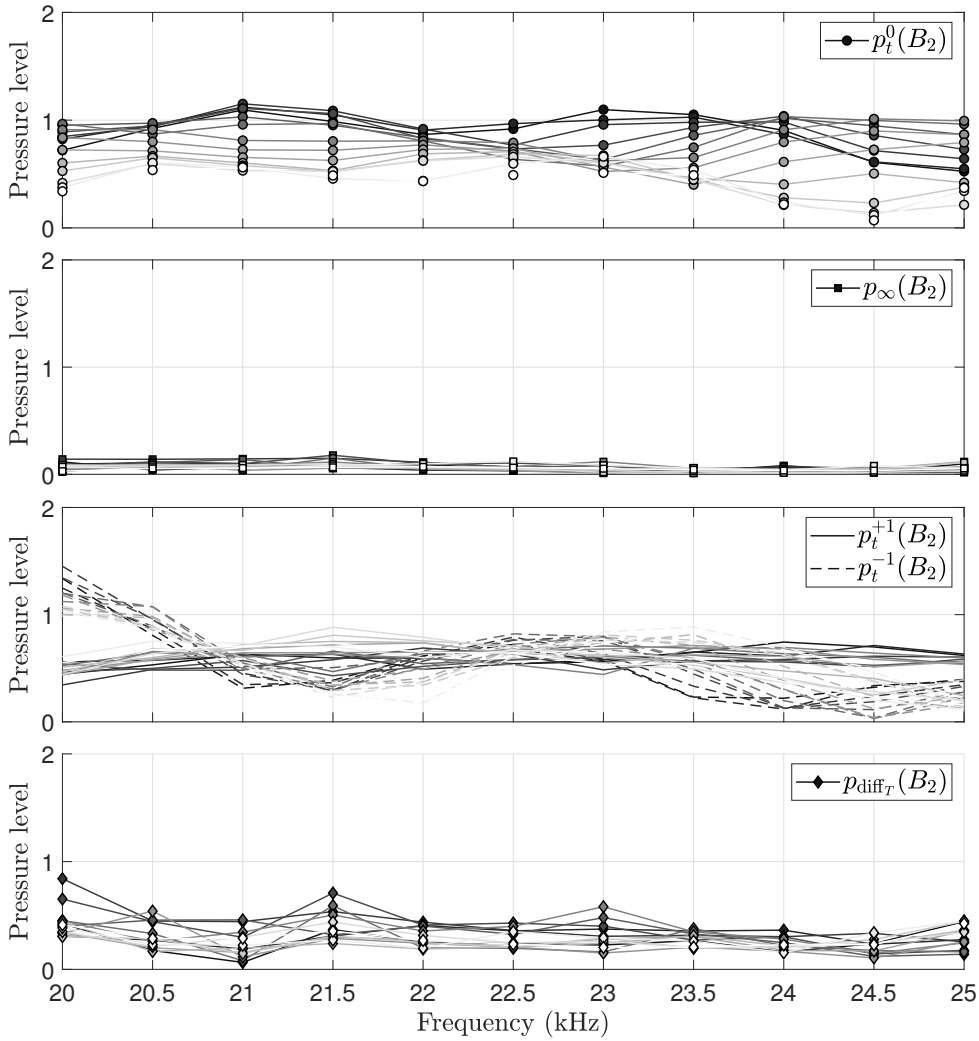

Figure 8.19 – Transmitted pressure for the 0th mode (p_t^0) and for the diffracted modes ± 1 ($p_r^{\pm 1}$), the infinite pressure (p_∞) and the edge-diffracted pressure (p_{diff_T}) at the central position B_2 on the transmission side. The graduation of grey represents the y-positions along the unit cell.

The reflection and transmission coefficients are now derived from these calculated pressures and compared to numerical results presented in Figure 8.15. In addition to the coefficients obtained by the 5-point method and those calculated with the FEM model, a direct calculation from measurements using Equations (8.8) to (8.12) is made. The latter therefore ignores the existence of the edge-diffracted pressures and only requires, as for the FE model, the total pressure over a linear mesh covering the unit cell and the incident pressure obtained separately. Using the measurements made, this direct calculation can be applied 3 times : on the lines of A_1, A_2 and A_3 for the reflection side and on the lines of B_1, B_1 and B_3 for the transmission side. All results are compared in Figure 8.20. Coefficients R_{+1} and R_{-1} are averaged under the label $R_{\pm 1}$ in the figure (the same is done for the transmission coefficients).

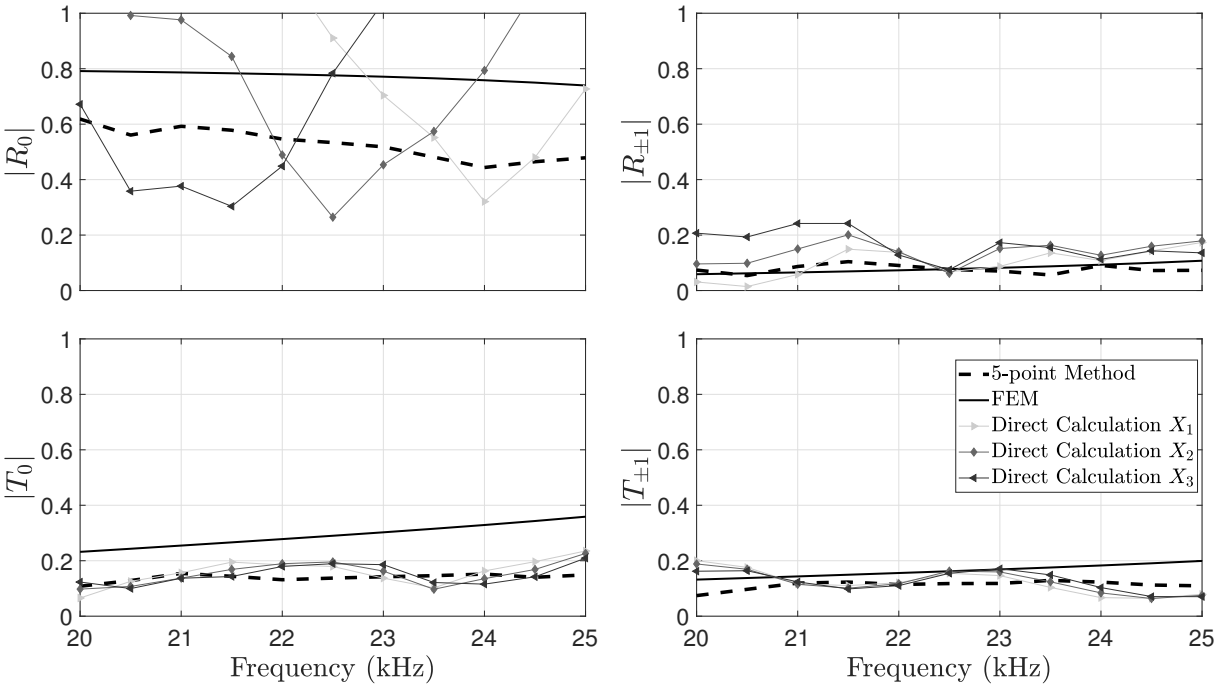

Figure 8.20 – Magnitudes of the reflection coefficient (top) and the transmission coefficient (bottom) obtained numerically for a panel of infinite lateral dimensions and measured with the 5-point method. For each side, three direct calculations are also performed as per Equations (8.8) to (8.12) using the total pressures measured on each y-line, thus not taking into account the edge-diffracted pressure.

For the reflection coefficient, it is first observed that the result of the 5-point method for the 0th mode is lower to the one calculated numerically, whereas they are identical for the ± 1 modes. The level difference for R_0 is non negligible and is attributed to the fact that the panel is not infinitely periodic. Further, the panel material properties and geometries may slightly differ from those in the FE model. The same observations apply for the transmission coefficients.

The coefficients R_0 from the direct calculations over the 3 y-lines are significantly different from both other results. This can be explained by the fact that the edge-diffracted pressure is not taken into account in these calculation and, even if its amplitude is quite low (Figure 8.18), it contributes to the pressure field. The direct calculation is based on the exact knowledge of the reflected and transmitted fields. It is therefore not applicable in the presence of non-modeled acoustic sources, such as the edge-diffraction phenomenon. This shows that the 5-point method is more suitable for measurements of an Alberich-type coating since it takes into account the main contributions, which are edge-diffraction and the first modes diffracted by the diffraction grating .

8.3 Summary

The Alberich panel containing a grating of voided cylinders has been characterised experimentally. The post-processing of the experimental data has been divided into two different approaches: below the first cut-off frequency and above the first cut-off frequency. Below the first cut-off frequency, the 3-point method is applied as for a homogeneous panel. A preliminary analysis was carried out to ensure that the hydrophones were located far enough from the panel so that the evanescent waves were no longer discernible. Results were consistent with predictions, except around the first cut-off frequency, where the source resonance and the ± 1 modes invalidated the results. Above the cut-off frequency, the ± 1 modes are no longer evanescent and must be calculated to fully characterise the panel. For this purpose, the 5-point method was implemented and led to consistent results. Nevertheless, the frequency range above the cut-off frequency is such that geometric irregularities and local uncertainties in material properties further influence the results, thus leading to differences with the finite element model of exact geometric and material properties. In addition, the panel is not infinitely periodic as in the FE model. Finally, it was shown by the significant divergence of the direct calculations from the FE predictions that it is crucial to take into account the edge-diffracted pressure as in the 3- and 5-point methods. Therefore, both the 3- and 5-point methods appear as a robust and unique way to characterise panels embedded with periodic inclusions above the first cut-off frequency.

Chapter 9

Conclusion and Perspectives

Contents

9.1 Thesis Summary **200**

9.2 Perspectives for Future Work **203**

9.1 Thesis Summary

This thesis studied the concept of metamaterials for underwater applications, from theoretical analysis to experimental characterisation. For this purpose, methods were developed to homogenise a range of metamaterial designs. Further, this thesis presented ways to optimise complex structures with low computation cost. This thesis also studied experimental methods to obtain the acoustic performance of metamaterials.

In the first chapter of the manuscript, the concept of hull coatings used for the discretion or stealth of submerged vehicles was introduced. Metamaterials are seen as good candidates for subwavelength coatings with good acoustic performances at low frequencies. A literature review has been conducted to present the concept of metamaterials and some methods to study them. A non exhaustive state of the art of metamaterial designs optimised for underwater applications was presented, followed by a review of measurement techniques.

In Part I of this thesis, tools for the study and design of multilayered media were introduced. Chapter 2 describes a homogenisation method based on transfer matrices. Either a fluid homogenisation model or a Willis fluid homogenisation model was adopted depending on the symmetry of the layer arrangement. The effective medium was found to be an exact representation of a multilayered medium studied under normal incidence.

The homogenisation theory was then used to optimise multilayered media in Chapter 3. The optimisation approach is computationally efficient and it was validated on a case study. Objective functions aiming to reduce the anechoism coefficient for a wide frequency range have then been defined. It was found that the best performing multilayered media show an impedance adaptation pattern. For the hull decoupling coefficient, it was found that simple bi-layer media give the best results. The optimisation approach was then applied for performance levels of both the anechoism and hull decoupling coefficients, which confirmed the observations made for the separate optimisations of each coefficient. Following the optimisation studies, a multilayered arrangement was selected for fabrication.

In Chapter 4, a measurement method in an open water tank, namely the 3-point method, has been introduced. The main advantage of this method is that it determines the contribution of the edge-diffracted waves. The method has been validated on an aluminium panel and the validity limits of the method have been studied. The method was then applied to a polyurethane panel containing micro-balloons in order to retrieve the effective speed of sound in the medium. Two approaches were used, for which results are comparable. Finally, the multilayered medium presented in Chapter 3 has been measured and it was found that moduli of the reflection and transmission coefficients are consistent with analytical predictions. Significant differences were however noted on the anechoism

coefficient, which proves to be extremely sensitive to the distance between the panel and the hydrophones. By applying phase shifts, it was found that the anechoism coefficient converged to the predicted value.

In Part II, metamaterials with macro-inclusions were homogenised, optimised and measured. The homogenisation of such designs was achieved using two retrieval methods, the direct inversion method and the differential method. These two retrieval methods were presented in Chapter 5. Both retrieval methods lead to an effective wavenumber and an effective impedance of a homogeneous fluid medium. The effective wavenumber from the differential method was able to describe the interior of the medium whereas the direct inversion method captured the effects related to the medium's finite size and interfaces with the surrounding fluid media on the incidence and transmission sides. Three case studies were examined corresponding to a 1D multilayered medium and 2D locally resonant designs with hard or voided cylindrical inclusions. Through these case studies, applicability and limitations of the methods have been discussed. It was found that the proposed hybrid medium provides accurate predictions of the transmission coefficient as it physically restricts the effective properties of the direct inversion method to the interface and uses the differential method to describe the core of the medium.

Chapter 6 presented extensions of both retrieval methods in order to obtain the effective properties of asymmetric unit cells with inclusions. These methods were then employed for two case studies, in which the introduction of Willis coupling through asymmetry was investigated. The impact of asymmetry on the acoustic performance and on the effective properties was examined. In the first case study, off-centred hard inclusions were considered and the influence of the inclusion position was investigated. For the second case study, an asymmetric voided medium was analysed. The asymmetry coefficient was found to be at its maximum when the effective density of the unit cell was negative. This physical mechanism was attributed to an anti-phase difference between the center of mass displacement and the incident field.

In Chapter 7, the retrieval methods for symmetric media were applied to several metamaterial designs in order to create a database of effective properties associated with various inclusion shapes, sizes and materials. Effective properties were then used in an optimisation process in order to obtain structures with a low anechoism coefficient over a wide frequency range. This work is therefore useful to make a topological-like optimisation of acoustic coatings for underwater applications using fluid properties. For the example illustrating this new approach for optimising structures with macro-inclusions, the same impedance pattern leading to a low coefficient of anechoism as in Chapter 3 was found. This study also showed that it is worth not limiting the design of an anechoic coating to multilayered solutions or designs with inclusions, as the combination of the two, by alternating homogeneous layers with layers comprising macro-inclusions, can greatly help improve the broadband acoustic performance.

In Chapter 8, the bi-layer Alberich panel designed in Chapter 6 was measured in the

acoustic water tank presented in Chapter 4. Since the panel contains periodically embedded void inclusions, the experimental characterisation becomes more complex because of the grating diffraction phenomenon. The experimental characterisation of the panel was divided into two different approaches: below the first cut-off frequency and above the first cut-off frequency. Below the first cut-off frequency, the 3-point method was found to be robust up to 15 kHz, after which the source resonance and the ± 1 modes invalidated the results. Above the cut-off frequency, the ± 1 modes were no longer evanescent and needed to be calculated to fully characterise the panel. For this purpose, an extension of the 3-point method was implemented and results were consistent with numerical predictions. In particular, it was highlighted that it is crucial to take into account edge diffraction, which makes the 5-point method suitable for measurements of such Alberich coating designs. Therefore, the 3-point method and its extension to the 5-point method were shown to be robust and unique approaches to characterise panels embedded with periodic inclusions.

9.2 Perspectives for Future Work

As the experiments of this thesis have shown, it is sometimes difficult to accurately know the dynamic properties of polyurethane. Moreover, the manufacturing processes can introduce uncertainties to both the material and geometric properties of acoustic coatings. Studying the influence of these uncertainties on the acoustic performance could help explain some experimental results.

It would also be interesting to look at different solutions to accurately measure the distance between the hydrophone and the panel in the water tank, since it was shown that the anechoism coefficient is very sensitive to this distance. A laser solution could be implemented. Ultrasound patches may be placed on the panel to determine the panel/hydrophone distance.

The optimisation approach for metamaterials with resonant inclusions could be used with a larger database, in which effective media could be obtained quickly with analytical models for simple geometries (using models by Sharma et al. for instance [32], [70]) or with the retrieval methods for complex geometries. The retrieval methods implemented in this thesis as well as the optimisation approach can also be applied to coatings containing three-dimensional inclusions of different shapes, such as spheres, elliptical and conical shapes. Further, the analytical and semi-analytical models presented in this thesis could also be extended to consider oblique incidence.

The homogenisation methods for metamaterials with inclusions could be modified to predict the vibro-acoustic behavior of a submerged hull in order to assess the noise radiated by a cylindrical hull coated with a metamaterial. Indeed, since the homogenisation models provide effective properties of a fluid, the coating could be integrated using a fluid-loaded shell.

Usually the radiated noise of a submerged vehicle is assessed using large-scale models of uncoated hulls. The difference between the desired performances and these predictions then leads to the definition of anechoic or hull decoupling performances that a coating must satisfy. Assuming that coatings can be modeled easily by fluid effective media in large scale models, a future study could be to derive a metamaterial design from a given set of effective fluid properties. For this purpose, it is interesting to investigate the link between effective fluid properties and acoustic performance. This last point was the subject of a preliminary study which includes performance mapping in the effective property space, the first elements of which are presented in Appendix E.

Appendix A

Transfer Matrix

A.1 Definition

Transfer matrix $\mathbf{M}$ for one-dimensional acoustic wave propagation through a layer relates acoustic pressure p and normal particle velocity v of the fluid on either side of the medium, as follows:

$$\begin{pmatrix} p_{\text{left}} \\ v_{\text{left}} \end{pmatrix} = \mathbf{M} \begin{pmatrix} p_{\text{right}} \\ v_{\text{right}} \end{pmatrix}. \tag{A.1}$$

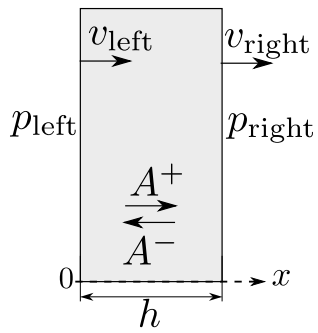

Figure A.1 – Pressures and particles velocities on the left and right sides of a medium in which the acoustic field is decomposed into forward and backward propagating waves.

In the field of Acoustics, physical quantities (p,v) are commonly used, rather than (p,u), u being the displacement. Nevertheless, the transition from the quantity u to v is possible with a derivative, equivalent to multiplying by $\mathrm{i}\omega$ for harmonic problems.

A.2 Expression with S-parameters

Elements of the transfer matrix can be expressed using S-parameters. S-parameters and two-port network notions are widely used in electrical and microwave engineering. These

notions can also be suitable for acoustic analyses using an analogy between the physical quantities involved. The scattering parameters (or S-parameters) of a two-port network are herein introduced and linked to the elements of the transfer matrix (also called the $ABCD$-matrix), based on notations shown in Figure A.2. For the sake of simplicity, S-parameters are herein always defined with the surrounding fluid impedance Z_f as the reference impedance for all ports.

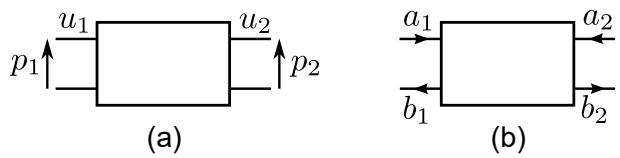

Figure A.2 – Two-port network with (a) pressure/flow notations and (b) power waves notations.

The transfer matrix elements A, B, C and D are defined as [130]:

$$\begin{pmatrix} p_1 \\ u_1 \end{pmatrix} = \begin{bmatrix} A & B \\ C & D \end{bmatrix} \begin{pmatrix} p_2 \\ u_2 \end{pmatrix}. \tag{A.2}$$

The relationship between the reflected, incident power waves and the S-parameter matrix is given by:

$$\begin{pmatrix} b_1 \\ b_2 \end{pmatrix} = \begin{bmatrix} S_{11} & S_{12} \\ S_{21} & S_{22} \end{bmatrix} \begin{pmatrix} a_1 \\ b_2 \end{pmatrix}, \tag{A.3}$$

where S_{11} is the reflection coefficient on the left-hand side and S_{21} the transmission coefficient and where S_{12} is the transmission coefficient for an excitation on the right-hand side for which the reflection coefficient is S_{22}, as per the expressions:

$$S_{11} = \left(\frac{b_1}{a_1}\right)_{a_2=0}, \tag{A.4}$$

$$S_{12} = \left(\frac{b_1}{a_2}\right)_{a_1=0}, \tag{A.5}$$

$$S_{21} = \left(\frac{b_2}{a_1}\right)_{a_2=0}, \tag{A.6}$$

$$S_{22} = \left(\frac{b_2}{a_2}\right)_{a_1=0}. \tag{A.7}$$

Note : *As one may not be familiar with S-parameters, equivalents in terms of the usual reflection coefficient and transmission coefficient notations are given. R and T are the*

coefficients for an incident wave arriving on one face of the medium. When the medium is reversed, R_b and T_b are the coefficients for the same incident wave arriving on the other (backward) face. As such, S-parameters are : $S_{11} = R$, $S_{12} = T_b$, $S_{21} = T$ and $S_{22} = R_b$.

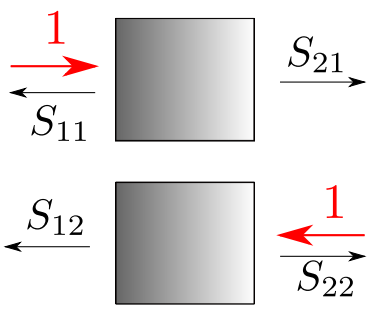

Figure A.3 – S-parameters depending on the incident side, represented by the red arrow.

The transfer matrix and S-parameters are linked together by:

$$\begin{pmatrix} 1+S_{11} \\ \frac{1-S_{11}}{Z_f} \end{pmatrix} = \begin{bmatrix} A & B \\ C & D \end{bmatrix} \begin{pmatrix} S_{21} \\ \frac{S_{21}}{Z_f} \end{pmatrix}, \tag{A.8}$$

$$\begin{pmatrix} S_{12} \\ \frac{-S_{12}}{Z_f} \end{pmatrix} = \begin{bmatrix} A & B \\ C & D \end{bmatrix} \begin{pmatrix} 1+S_{22} \\ \frac{-1+S_{22}}{Z_f} \end{pmatrix}. \tag{A.9}$$

By combining the two previous equations, elements of the $ABCD$-matrix are expressed with the S-parameters as given by:

$$A = \frac{S_{11} - S_{22} - S_{11}S_{22} + S_{12}S_{21} + 1}{2S_{21}}, \tag{A.10}$$

$$B = Z_f \frac{S_{11} + S_{22} + S_{11}S_{22} - S_{12}S_{21} + 1}{2S_{21}}, \tag{A.11}$$

$$C = \frac{1}{Z_f} \frac{-S_{11} - S_{22} + S_{11}S_{22} - S_{12}S_{21} + 1}{2S_{21}}, \tag{A.12}$$

$$D = \frac{-S_{11} + S_{22} - S_{11}S_{22} + S_{12}S_{21} + 1}{2S_{21}}. \tag{A.13}$$

For a symmetric medium, scattering coefficients are identical whether the acoustic wave is incident on a face or on the other, which means that $S_{11} = S_{22} = R$. Reciprocity implies that $S_{21} = S_{12} = T$. Elements of the transfer matrix can thus be simplified as follows:

$$A = \frac{-R^2 + T^2 + 1}{2T}, \tag{A.14}$$

$$B = Z_f \frac{(R+1)^2 - T^2}{2T}, \tag{A.15}$$

$$C = \frac{1}{Z_f} \frac{(R-1)^2 - T^2}{2T}, \tag{A.16}$$

$$D = \frac{-R^2 + T^2 + 1}{2T}. \tag{A.17}$$

A.3 Expression with Material Properties

Considering the time convention $e^{\mathrm{i}\omega t}$, expressions of the transfer matrix elements are found by decomposing the acoustic field into forward and backward-propagating waves, as shown in Figure A.1. Pressures and particle velocities on both sides of the medium of length h are written at $x = 0$ and $x = h$ as:

$$\begin{cases} p_{\text{left}} = A^+ + A^- \\ v_{\text{left}} = \frac{A^+}{Z^+} + \frac{A^-}{Z^-} \\ p_{\text{right}} = A^+ e^{-\mathrm{i}k^+ h} + A^- e^{-\mathrm{i}k^- h} \\ v_{\text{right}} = \frac{A^+ e^{-\mathrm{i}k^+ h}}{Z^+} + \frac{A^- e^{-\mathrm{i}k^- h}}{Z^-} \end{cases}, \tag{A.18}$$

where k^+ and k^- are the wavenumbers for forward and backward-propagating waves respectively and where Z^+ and Z^- are the impedances for forward and backward-propagating waves respectively.

Wave amplitudes A^+ and A^- are extracted from system (A.18) using the first two lines, which leads to:

$$\begin{cases} A^+ = \frac{1}{Z^+ - Z^-}(p_{\text{left}} Z^+ - v_{\text{left}} Z^+ Z^-) \\ A^- = \frac{1}{Z^+ - Z^-}(-p_{\text{left}} Z^- + v_{\text{left}} Z^+ Z^-) \end{cases}. \tag{A.19}$$

Those expressions for wave amplitudes A^+ and A^- are next injected in the last two lines of system (A.18) so that p_{right} and v_{right} are expressed as a function of p_{left} and v_{left}. These two lines can be rewritten in a matrix form as follows:

$$\begin{pmatrix} p_{\text{right}} \\ v_{\text{right}} \end{pmatrix} = \frac{1}{Z^+ - Z^-} \begin{bmatrix} Z^+ e^{-\mathrm{i}k^+ h} - Z^- e^{-\mathrm{i}k^- h} & Z^+ Z^- (e^{-\mathrm{i}k^- h} - e^{-\mathrm{i}k^+ h}) \\ e^{-\mathrm{i}k^+ h} - e^{-\mathrm{i}k^- h} & Z^+ e^{-\mathrm{i}k^- h} - Z^- e^{-\mathrm{i}k^+ h} \end{bmatrix} \begin{pmatrix} p_{\text{left}} \\ v_{\text{left}} \end{pmatrix}. \tag{A.20}$$

This system can be reversed to obtain the transfer matrix expression according to Equation (A.1), which finally leads to:

$$\mathbf{M} = \frac{1}{Z^+ - Z^-} \begin{bmatrix} Z^+ e^{\mathrm{i}k^+ h} - Z^- e^{\mathrm{i}k^- h} & Z^+ Z^- (e^{\mathrm{i}k^- h} - e^{\mathrm{i}k^+ h}) \\ e^{\mathrm{i}k^+ h} - e^{\mathrm{i}k^- h} & Z^+ e^{\mathrm{i}k^- h} - Z^- e^{\mathrm{i}k^+ h} \end{bmatrix}. \tag{A.21}$$

For a fluid medium, the material properties are meant to be the same whether the acoustic wave is forward or backward propagating. However, the distinction is voluntarily kept to in order to apply to an asymmetric fluid-like medium, which is one of the homogenisation models considered in the manuscript. However, even if the medium is asymmetric, it will always be reciprocal (ie $S_{12} = S_{21}$) and consequently $k^+ = -k^- = k$. This equality can be proved using the $ABCD$ transfer matrix expressed with Equations (A.10) to (A.13), for which the determinant is equal to 1 when $S_{12} = S_{21}$ as well as using the fact that the determinant of the transfer matrix form given by Equation (A.21) is also equal to 1 if and only if $k^+ = -k^-$. Hence, there is no need to keep the distinction between k^+ and k^-. The transfer matrix for an asymmetric fluid-like medium is then given by:

$$\mathbf{M} = \frac{1}{Z^+ - Z^-} \begin{bmatrix} Z^+ e^{\mathrm{i}kh} - Z^- e^{-\mathrm{i}kh} & Z^+ Z^- (e^{-\mathrm{i}kh} - e^{\mathrm{i}kh}) \\ e^{\mathrm{i}kh} - e^{-\mathrm{i}kh} & Z^+ e^{-\mathrm{i}kh} - Z^- e^{\mathrm{i}kh} \end{bmatrix}. \tag{A.22}$$

Moreover, if the medium is symmetric, then $Z^- = -Z^+ = -Z$. The transfer matrix expression of Equation (A.21) can then be simplified as follows:

$$\mathbf{M} = \begin{bmatrix} \cos(kh) & \mathrm{i}Z\sin(kh) \\ \mathrm{i}Z^{-1}\sin(kh) & \cos(kh) \end{bmatrix}. \tag{A.23}$$

A.4 Expression for Determination of Willis-parameters

For Willis-type systems, the effective properties may depend on the direction of wave propagation. For example, the effective impedance Z^+, mentioned in the previous section, is the effective impedance of a medium for forward-propagating waves. In the publication of Muhlestein et al. [40], the effective impedances Z^+ and Z^- are referred to as specific impedances for a Willis-type system. Considering the time convention $e^{\mathrm{i}\omega t}$, the specific acoustic impedances in the $\pm$ directions may be written as:

$$Z^{\pm} = Z_W(\pm 1 + \mathrm{i}W), \tag{A.24}$$

where $W = \omega\psi/Z_W$ the complex asymmetry coefficient, where ψ is the Willis-coupling coefficient and where Z_W is the complex characteristic impedance. Therefore, the transfer matrix expression given by Equation (A.22) can be changed considering the parameters Z_W and W instead of the specific impedances $Z^{\pm}$. For this purpose, pressures and particle velocities on both sides of the medium of length h are written at $x = 0$ and $x = h$ as:

$$\begin{cases} p_{\text{left}} = A^+ + A^- \\ v_{\text{left}} = \frac{A^+}{Z_W(1+\mathrm{i}W)} + \frac{A^-}{Z_W(-1+\mathrm{i}W)} \\ p_{\text{right}} = A^+ e^{-\mathrm{i}kh} + A^- e^{\mathrm{i}kh} \\ v_{\text{right}} = \frac{A^+ e^{-\mathrm{i}kh}}{Z_W(1+\mathrm{i}W)} + \frac{A^- e^{\mathrm{i}kh}}{Z_W(-1+\mathrm{i}W)} \end{cases}. \tag{A.25}$$

Wave amplitudes A^+ and A^- are extracted from system (A.25) using the first two lines, which leads to:

$$\begin{cases} A^+ = \frac{1}{2}\left[p_{\text{left}}(1+\mathrm{i}W) + v_{\text{left}}Z_W(1+W^2)\right] \\ A^- = \frac{1}{2}\left[p_{\text{left}}(1-\mathrm{i}W) - v_{\text{left}}Z_W(1+W^2)\right] \end{cases} . \tag{A.26}$$

The last two equations are then injected into the last two lines of the system (A.25) to obtain expressions of p_{right} and v_{right} according to p_{left} and v_{left}, as given by:

$$\begin{pmatrix} p_{\text{right}} \\ v_{\text{right}} \end{pmatrix} = \begin{bmatrix} \cos(kh) + W\sin(kh) & -\mathrm{i}Z_W\sin(kh)(1+W^2) \\ \frac{-\mathrm{i}\sin(kh)}{Z_W} & \cos(kh) - W\sin(kh) \end{bmatrix} \begin{pmatrix} p_{\text{left}} \\ v_{\text{left}} \end{pmatrix} . \tag{A.27}$$

The latter system can be reversed to obtain the transfer matrix expression according to Equation (A.1), which finally leads to:

$$\mathbf{M} = \begin{bmatrix} \cos(kh) - W\sin(kh) & \mathrm{i}Z_W\sin(kh)(1+W^2) \\ \frac{\mathrm{i}\sin(kh)}{Z_W} & \cos(kh) + W\sin(kh) \end{bmatrix} . \tag{A.28}$$

Appendix B

Effective Wavenumber

B.1 Expression

Wave propagation in an infinite periodic structure can be studied by using the constitutive unit cell and periodic boundary conditions. The unit cell is defined as the smallest pattern that leads to the infinite structure when it is endlessly repeated. Its transfer matrix for longitudinal modes $\mathbf{M}_u$ is defined by:

$$\begin{pmatrix} p_{\text{left}} \\ v_{\text{left}} \end{pmatrix} = \mathbf{M}_u \begin{pmatrix} p_{\text{right}} \\ v_{\text{right}} \end{pmatrix}. \tag{B.1}$$

The longitudinal effective wavenumber k is derived by applying the Bloch-Floquet relation on the unit cell of length L_u. Such condition can be written as:

$$\begin{pmatrix} p_{\text{left}} \\ v_{\text{left}} \end{pmatrix} = e^{-\mathrm{i}kL_u} \begin{pmatrix} p_{\text{right}} \\ v_{\text{right}} \end{pmatrix}. \tag{B.2}$$

Equation B.2 is subtracted to Equation B.1, which yields:

$$[\mathbf{M}_u - e^{-\mathrm{i}kL_u}\mathbf{I}] \begin{pmatrix} p_{\text{right}} \\ v_{\text{right}} \end{pmatrix} = 0. \tag{B.3}$$

Solving Equation (B.3) comes down to the calculation of the eigenvalues $\lambda^{\pm}$ of the transfer matrix $\mathbf{M}_u$. The effective wavenumber is thus given by:

$$k = \frac{\ln(\lambda^{\pm})}{\mathrm{i}L_u} + \frac{2\pi m}{L_u}. \tag{B.4}$$

where m is an integer whose value is determined in such way that the effective wavenumber as a function of frequency is continuous. Moreover, for a forward propagating wave, eigenvalue λ is chosen so that the imaginary part of k is negative in order to comply with the material passivity requirement considering the phasor convention $e^{\mathrm{i}(\omega t - kx)}$. In fact, the decomposition into real and imaginary parts of the wavenumber, respectively k' and k'' for a forward propagating wave leads to:

$$e^{-\mathrm{i}kL_u} = e^{-\mathrm{i}(k^{'}+\mathrm{i}k^{''})L_u} = e^{k^{''}L_u}e^{-\mathrm{i}k^{'}L_u}. \tag{B.5}$$

The modification of the wave amplitude, under the effect of losses, is represented in the term $e^{k^{''}L_u}$. This term is required to be inferior to unity if the material is passive. Thus, the imaginary part of wavenumber has to be negative.

Other Expression

Eigenvalues of the transfer matrix $\mathbf{M}_u$ are given by:

$$\lambda^{\pm} = \frac{1}{2}(\mathrm{Tr}(\mathbf{M}_u) \pm \sqrt{\mathrm{Tr}(\mathbf{M}_u)^2 - 4\mathrm{Det}(\mathbf{M}_u)}). \tag{B.6}$$

Thus, $\lambda^+ + \lambda^- = \mathrm{Tr}(\mathbf{M}_u)$. However, $\lambda^+ + \lambda^-$ can also be expressed with the wavenumber k using Bloch-Floquet conditions, yielding:

$$\lambda^+ + \lambda^- = e^{\mathrm{i}kL_u} + e^{-\mathrm{i}kL_u} = 2\cos kL_u. \tag{B.7}$$

Consequently, $\cos kL_u = \mathrm{Tr}(\mathbf{M}_u)/2$.

B.2 Representation

At normal incidence, the wavenumber k derived for a unit cell of thickness h can be represented as a function of frequency f, which is commonly referred to as the dispersion curve. An example of such graphical representation is given in Figure B.1 for the reduced wavenumber kh. Band gaps are frequency ranges where the acoustic waves do not propagate in the given direction, assuming the periodic medium to be infinite. Band gaps are obtained when there is no mode with k and ω real.

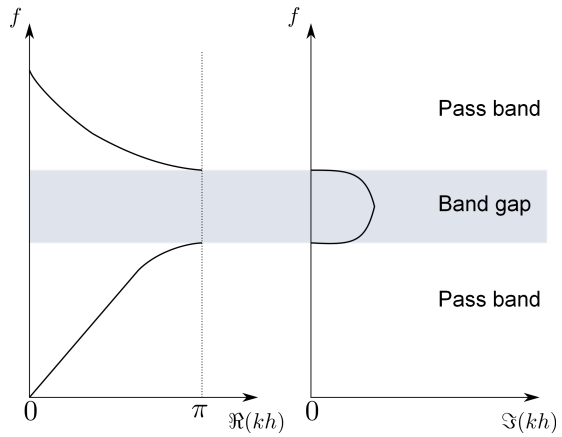

Figure B.1 – Example of dispersion curve on the irreducible Brillouin zone for a normal incidence angle.

Systems studied in this manuscript are not in fact strictly periodic, as periodicity suggests an infinite repetition of a unit cell, whereas a finite number of repetitions of a pattern are herein considered. Misuses of language are thus voluntarily used for three notions taken from the terminology of periodic systems: (1) systems are qualified as *periodic* to refer to finite repetitions of a pattern, (2) the repeated pattern is referred to as the *unit cell* or the constituent unit, and (3) the representation of the wavenumber k as a function of frequency f is referred to as a *dispersion curve*.

Appendix C

Acoustic Performance

C.1 S-parameters

Scattering coefficients defined for a plane wave normally incident in the fluid of impedance Z_f on a panel of finite thickness and infinite lateral extent can be calculated using its total transfer matrix. According to the two-port network presented in Figure A.2, the S-parameters in the fluid of impedance Z_f are linked to the $ABCD$-matrix as per Equations A.8 and A.9.
Consequently, expressions for the S-parameters are now given by:

$$S_{11} = \frac{B + Z_\mathrm{f}(A - D) - Z_\mathrm{f}^2 C}{\Delta}, \tag{C.1}$$

$$S_{21} = S_{12} = \frac{2Z_\mathrm{f}}{\Delta}, \tag{C.2}$$

$$S_{22} = \frac{B - Z_\mathrm{f}(A - D) - Z_\mathrm{f}^2 C}{\Delta}, \tag{C.3}$$

where Δ is:

$$\Delta = B + Z_\mathrm{f}(A + D) + Z_\mathrm{f}^2 C. \tag{C.4}$$

C.2 Anechoism Coefficient

The anechoism coefficient aims to evaluate the energy reflected by a medium of finite thickness and infinite lateral extent when it is fixed to a rigid surface, as shown in Figure C.1.

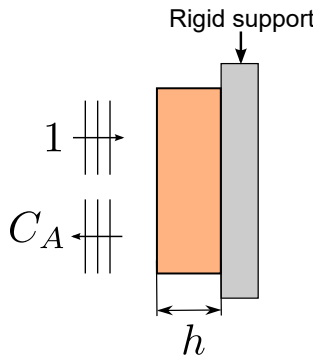

Figure C.1 – Configuration used to calculate the anechoism coefficient of a medium fixed on a rigid surface.

To express the anechoism coefficient C_A, the following boundary conditions are thus introduced :

$$\begin{cases} p_{\text{left}} = C_A + 1 \\ v_{\text{left}} = \frac{1-C_A}{Z_{\text{f}}} \\ v_{\text{right}} = 0 \end{cases} . \tag{C.5}$$

Considering these boundary conditions, the transfer matrix definition is given by:

$$\begin{pmatrix} 1 + C_A \\ \frac{1-C_A}{Z_{\text{f}}} \end{pmatrix} = \begin{pmatrix} A & B \\ C & D \end{pmatrix} \begin{pmatrix} p_{\text{right}} \\ 0 \end{pmatrix}, \tag{C.6}$$

where A, B, C and D are the elements of the transfer matrix. The anechoism coefficient C_A can then be obtained by expressing the $ABCD$-elements in terms of S-parameters as per Appendix A, which yields:

$$C_A = S_{11} - \frac{S_{21}S_{12}}{S_{22} - 1}. \tag{C.7}$$

If the medium is symmetric, then $S_{11} = S_{22} = R$ and $S_{12} = S_{21} = T$, which simplifies the anechoism coefficient expression into:

$$C_A = R - \frac{T^2}{R - 1}. \tag{C.8}$$

C.3 Hull Decoupling Coefficient

The determination of the hull decoupling coefficient C_D requires the consideration of a vibrating support of prescribed particle velocity v_0, as shown in Figure C.2.

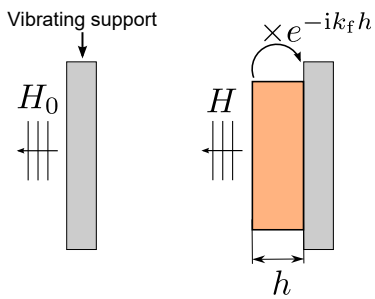

Figure C.2 – Configuration used to calculate the hull decoupling coefficient, showing the radiation from the vibrating support with and without the decoupling material.

It is assumed that without the material, this support radiates into the fluid a plane wave of complex amplitude H_0 in the plane of the vibrating surface. When the support is coated with the material of thickness h, then the plane wave complex amplitude calculated in the same reference plane becomes H. The hull decoupling coefficient in the reference plane is then defined by $C_D = He^{-\mathrm{i}k_\mathrm{f}h}/H_0$.

To express the hull decoupling coefficient C_D, the following boundary conditions are thus introduced :

$$\begin{cases} p_{\text{left}} = H \\ v_{\text{left}} = \frac{-H}{Z_\mathrm{f}} \\ v_{\text{right}} = v_0 = \frac{-H_0}{Z_\mathrm{f}} \end{cases} . \tag{C.9}$$

Considering these boundary conditions, the transfer matrix definition is given by:

$$\begin{pmatrix} H \\ \frac{-H}{Z_\mathrm{f}} \end{pmatrix} = \begin{pmatrix} A & B \\ C & D \end{pmatrix} \begin{pmatrix} p_{\text{right}} \\ \frac{-H_0}{Z_\mathrm{f}} \end{pmatrix} . \tag{C.10}$$

where A, B, C and D are the elements of the transfer matrix. The hull decoupling coefficient C_D can then be obtained by expressing the $ABCD$-elements in terms of S-parameters as per Appendix A, which yields:

$$C_D = \frac{He^{-\mathrm{i}k_\mathrm{f}h}}{H_0} = \frac{S_{12}}{-S_{22}+1} e^{-\mathrm{i}k_\mathrm{f}h}. \tag{C.11}$$

The hull decoupling coefficient can thus be obtained without the use of a vibrating support and by only measuring the reflection and transmission coefficients R and T:

$$C_D = \frac{T}{-R+1} e^{-\mathrm{i}k_\mathrm{f}h}. \tag{C.12}$$

Appendix D

Panel Edge-diffraction

A simple analytical model is presented here to express the diffracted pressure at one point. A square flat panel of side $2a$ is considered and represented in Figure D.1, where the point of coordinates (0,0,0) corresponds to the center 0 of the panel .

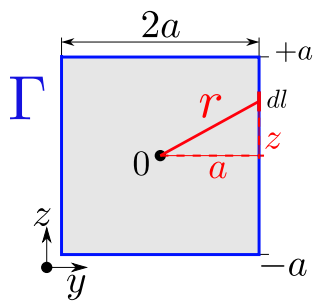

Figure D.1 – Schematic diagram of a square panel of side $2a$.

It is considered that each edge portion of the square behaves as a point source for edge-diffracted waves. It is assumed that each of these portions produces the same response to a plane wave excitation, so that the elementary pressure of edge-diffracted waves, called $P_{\mathrm{e_{diff}}}$, is identical along edges of the square. With these simplifying considerations, the total contribution of the edge-diffracted pressure at point 0, referred to as $P_{\mathrm{diff}}(0)$, can be expressed using the elementary edge-diffracted pressure $P_{\mathrm{e_{diff}}}$ and a source term that is summed over the square edges:

$$P_{\mathrm{diff}}(0) = P_{\mathrm{e_{diff}}} \int_{\Gamma} \frac{e^{-\mathrm{i}kr}}{r} dl, \tag{D.1}$$

where r is the distance between point 0 and a point on the edge. Distance r is expressed as $r = \sqrt{a^2 + y^2}$ for horizontal edges or $r = \sqrt{a^2 + z^2}$ for vertical edges. As the panel is square, Equation D.1 is simplified into:

$$P_{\mathrm{diff}}(0) = 4P_{\mathrm{e_{diff}}} \int_{-a}^{a} \frac{e^{-\mathrm{i}k\sqrt{a^2+l^2}}}{\sqrt{a^2 + l^2}} dl. \tag{D.2}$$

Edge diffracted pressure $P_{\text{diff}}(M)$ at a point M away from the panel face, of coordinates (x_M,y_M,z_M), can then be expressed using the same approach, with projections of the distance r in the 3D space.

Appendix E

Performance Maps and Frequency Paths

For the scientific community interested in metamaterials, a topic of interest is the search for designs presenting single or double negative values for the effective properties. Effective properties can also be used to simplify an optimisation process by using homogenised media instead of finite element models of a complex structure, as in Chapter 7. However, there are very few studies on the link between effective properties and acoustic performance. It is of course known, and it has also been exhibited in the preceding chapters, that a dipole resonance can result in a negative effective density and that a negative bulk modulus appears during a monopolar resonance. But what is the link between the values of these effective properties and how much the structure will absorb, dissipate or transmit the acoustic energy? For example, is it better to use metamaterials with effective density or negative bulk modulus to improve anechoism?

This appendix presents a general study on the relation between the effective properties and the anechoic performances of a structure. The aim of this appendix is not to cover the full extent of such a study, but simply to open up the subject for possible future studies or discussions. In the first section, a visual concept is introduced to investigate this link for the coefficient of anechoism. A multilayered structure is then defined in the second section, for which the effective properties are used to follow a frequency path.

E.1 Mapping Approach

E.1.1 Presentation

The link between absorption and effective properties has already been investigated by the scientific community. For example, the concept of double-negative [131], or double-zero [132] effective parameters has been exploited for the absorption of sound waves. Duan et al. [133] have theoretically studied perfect absorption of elastic waves with either (1) imaginary large mass density and a free space boundary, or (2) imaginary small bulk modulus and hard wall boundary. Total absorption could also be realised by an acoustic coherent perfect absorber (CPA) in which the scattered waves at the resonant frequency can be cancelled through interference with another coherent incident acoustic wave with a suitable phase and amplitude [134, 135]. These links between effective properties and absorption performance are very specific to a given design, set-up and are rather frequency-localised.

In this section, a general approach is proposed to visually study the link between the anechoism coefficient and the effective properties of a structure. These effective properties are the properties of a fluid. Such a fluid equivalent model may be accurate for the description of a multilayered medium under normal incidence, as in Chapter 2. These effective properties could also be used for the approximate representation of a metamaterials with macro-inclusions above the homogenisation limit, as in Chapter 5. It is worth noting that the performance mapping approach introduced here can also be applied to other performance coefficients, such as the hull decoupling coefficient or the absorption coefficient. For the anechoism coefficient, a visual approach is particularly useful as it is mathematically difficult to guess how the effective properties should vary to improve anechoic performance. For a symmetric medium, the anechoism coefficient is given by:

$$C_A = R - \frac{T^2}{R-1}, \tag{E.1}$$

where R and T are respectively the reflection and transmission coefficients. These coefficients are themselves expressed using the elements A, B, C and D from the transfer matrix, as per Appendix C. Finally, the elements of the transfer matrix of the medium are expressed using its effective properties, as in Appendix A. The expression of the anechoism coefficient as a function of the effective properties is therefore quite convoluted, especially since the effective properties are complex numbers. A performance mapping approach is thus introduced in order to visually exhibit the link between effective properties and anechoism performance.

Building the anechoism map is however not simple, since the anechoism coefficient C_A is a complex-valued function $\mathbf{F}$ of 6 real variables :

$$C_A = \mathbf{F}(\Re(\rho), \Re(\kappa), \Im(\rho), \Im(\kappa), f, L), \tag{E.2}$$

where $\Re(\rho)$ and $\Im(\rho)$ are respectively the real and imaginary parts of the effective density,

$\Re(\kappa)$ and $\Im(\kappa)$ are respectively the real and imaginary parts of the effective bulk modulus, f is the frequency and L is the length of the medium. At first, frequency f and medium length L are fixed. These two parameters can also be expressed in terms of a reduced wavenumber in water, $k_{\mathrm{w}}L = \omega L/1500$, where 1500 m.s^{-1} is the usual value for the speed of sound in water, commonly used in underwater acoustics.

For these given parameters, the mapping approach to be developed needs to show the anechoism coefficient according to the four other variables, which means that a 4D-space has to be represented in 2D using projections. Additionally, it is worth noting that the anechoism coefficient C_A can also be expressed as a complex-valued function with only 4 real variables $(\Re(z), \Im(z), \Re(kL), \Im(kL))$, where z is the reduced impedance and kL is the reduced wavenumber.

Two types of representation are introduced. The first representation is presented in Figure E.1. The main performance map (on the left) is a representation in the space of the real parts, where the x-axis corresponds to the real part of the bulk modulus $\Re(\kappa)$ and the y-axis corresponds to the real part of the density $\Re(\rho)$. For a given value of $\Re(\kappa)$ and $\Re(\rho)$, the anechoism coefficient is calculated for all values of the imaginary parts $\Im(\kappa)$ and $\Im(\rho)$. This leads to a performance map of $|C_A|$ in the $\Im$-coordinate system ($\Im(\kappa)$,$\Im(\rho)$), shown on the right hand side in Figure E.1, where the color of each pixel corresponds to the value of $|C_A|$. Within this $|C_A|$-map in the $\Im$-coordinate system, the minimum value of the anechoism coefficient is spotted and reported in the main $|C_A|$-map in the $\Re$-coordinate system ($\Re(\kappa)$,$\Re(\rho)$). Therefore, the main map shows the minimal values of the anechoism coefficient calculated for all $\Im(\kappa)$ and $\Im(\rho)$.

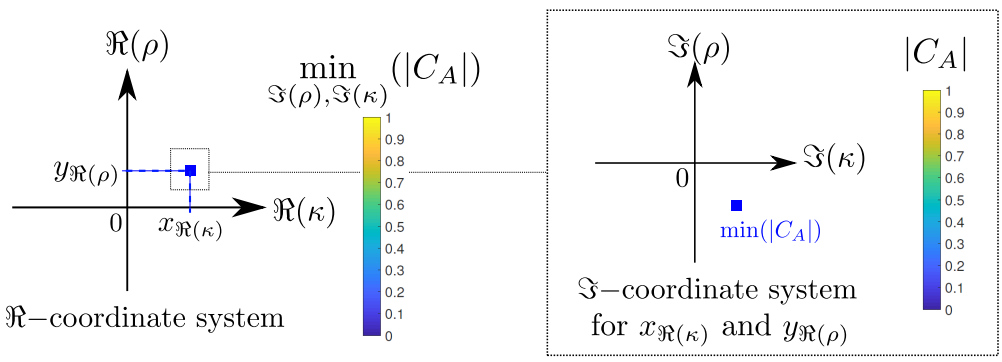

Figure E.1 – Representation 1 of the performance map for a given frequency and medium length.

A second type of representation is introduced, as illustrated in Figure E.2. The main map is identical to that of Representation 1: in the $\Re$-coordinate system ($\Re(\kappa)$,$\Re(\rho)$), the minimal values of $|C_A|$ for all $\Im(\kappa)$ and $\Im(\rho)$ are shown. The same coordinate system is then kept in two other secondary maps, where values of $\Im(\kappa)$ and $\Im(\rho)$ are given by the colorbar. Each pixel gives the values of $\Im(\kappa)$ and $\Im(\rho)$ that lead to the minima of $|C_A|$ in the main map.

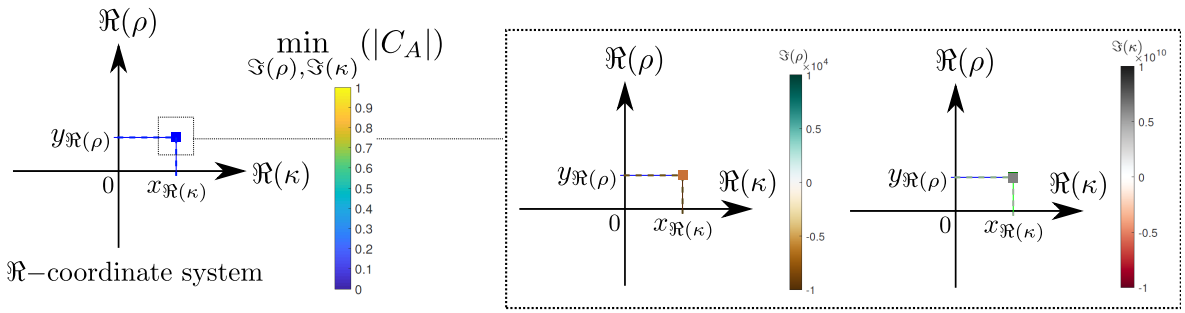

Figure E.2 – Representation 2 of the performance map for a given frequency and medium length.

In each map, four quadrants are identified and referred to as Quadrants 1 to 4 as per Figure E.3.

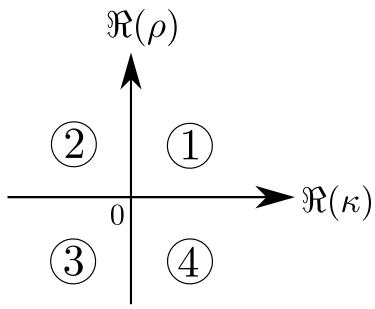

Figure E.3 – Definition of Quadrants 1 to 4.

A condition is added in order to satisfy the passivity constraint, based on Section 1.4.5: if the imaginary part of the wavenumber is positive or if the real part of the impedance is negative, then passivity constraint is not satisfied.

E.1.2 Analysis

Pre-Analysis

The mapping approach is applied for the frequency $f = 5$ kHz and a medium length $L = 6$ cm surrounded by water. This corresponds to $k_{\mathrm{w}}L = 1.25$. The main map is first pre-analysed to define areas that are then further investigated. The definition of the bounds of the map was based on the values of the effective density ρ_e and effective bulk modulus κ_e obtained in Chapters 2 and 5. The ranges for the real part of the effective density and bulk modulus are $[-10000 \quad 10000]$ kg.m^{-3} and $[-10 \quad 10] \times 10^9$ Pa, respectively. Ranges for the imaginary parts $\Im(\rho)$ and $\Im(\kappa)$ are the same as for their real part counterparts. These bounds may seem extreme, but such values can be reached by the effective properties at dipole resonance frequencies for example (see Chapter 5). Duan et al. [133] have also reported that perfect absorption can be obtained for large values of $\Im(\rho)$.

The performance map as per Representation 2 (Figure E.2) is given in Figure E.4. A few observations are made: (1) There seems to be a central symmetry around the coordinate system origin, (2) in the main map (on the left hand side) branches with low $|C_A|$ stand out in Quadrants 1 and 3 and are associated to strong discontinuities of the imaginary parts, and (3) low $|C_A|$ values are obtained in Quadrants 2 and 4 for very low values of $\Re(\kappa)$ and/or $\Re(\rho)$. These three observations are further investigated in what follows.

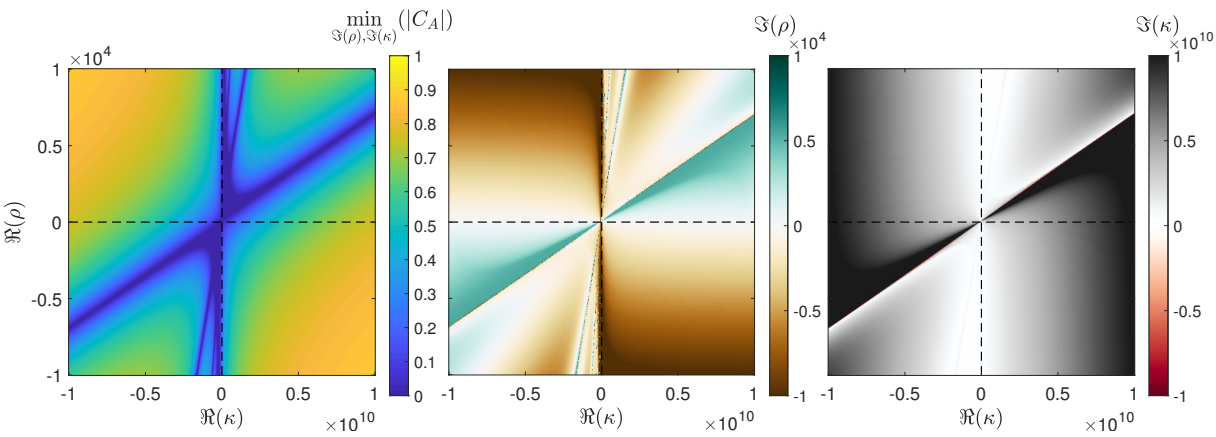

Figure E.4 – Anechoism performance mapping based on Representation Type 2, showing $|C_A|$-maps in the $(\Re(\rho), \Re(\kappa))$ coordinate system and values of $\Im(\rho)$ and $\Im(\kappa)$ that led to these $|C_A|$, for the frequency $f = 5$ kHz and the medium length $L = 6$ cm.

Central Symmetry

In all 3 maps of Figure E.4, it is observed that Quadrant 3, corresponding to $(\Re(\kappa) < 0$, $\Re(\rho) < 0)$, is the central symmetric about the coordinate system origin of Quadrant 1 $(\Re(\kappa) > 0$, $\Re(\rho) > 0)$. The same observation is made for Quadrants 2 and 4. Further investigation remains to be done to demonstrate if (ρ,κ) leads to the same anechoism

coefficient as $(-\rho,-\kappa)$. A way to do so could be to write the anechoism coefficient in terms of the effective wavenumber $k_e^2 = \omega^2\rho/\kappa$ and the effective impedance $Z_e = \sqrt{\rho\kappa}$. Figure E.5 is used to obtain an expression of the anechoism coefficient based on the partial reflection at an interface and on the transmission coefficient through one layer of medium of thickness L, respectively r and t, which themselves are expressed using k_e and Z_e, as per:

$$r = \frac{z-1}{z+1}, \tag{E.3}$$

$$t = e^{-\mathrm{i}k_e L}, \tag{E.4}$$

with $z = Z_e/Z_\mathrm{w}$ the normalised impedance.

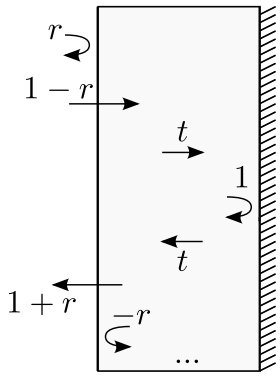

Figure E.5 – Multiple reflections and transmission through a layer in an anechoic configuration.

In an anechoic configuration, that is to say for a medium applied on a rigid backing, the anechoism coefficient corresponds to the total reflection coefficient R, resulting from the multiple reflections within the medium. The expression of the total reflected wave is obtained using Figure E.5 and is given by:

$$C_A = R = r + (1-r)t(1)t(1+r) + (1-r)t(1)t(-r)t(1)t(1+r) + ... \tag{E.5}$$

This last equation can be also written as:

$$C_A = r + (1-r)(1+r)t^2 \sum_{n=0}^{\infty} (-rt^2)^n, \tag{E.6}$$

in which there is a geometric series for $|-rt^2| < 1$ converging toward $1/(1+rt^2)$. The final expression of the anechoism coefficient is thus given by:

$$C_A = \frac{r+t^2}{1+rt^2}. \tag{E.7}$$

This last Equation as well as Equations (E.3) and (E.4) can be used to show that the anechoism coefficient is the same for (ρ,κ) as for ($-\rho$,$-\kappa$), which leads to the central symmetry.

Quadrant 1

In Quadrant 1 ($\Re(\kappa) > 0$, $\Re(\rho) > 0$), several blue branches stand out, corresponding to very low values of $|C_A|$. One branch is very close to the diagonal of the map, while the other blue branches are condensed close to the $\Re(\kappa) = 0$ axis.

Maps have been drawn in Figure E.6 for other values of $k_{\mathrm{w}}L$, around 2 and 3.5, to observe how these branches evolve. They differ greatly as a function of this parameter, therefore as a function of the frequency and of the thickness. Their variations for different $k_{\mathrm{w}}L$ can be explained by the fact that these low $|C_A|$ are related to the resonances of the slab and therefore depend on the thickness and the frequency.

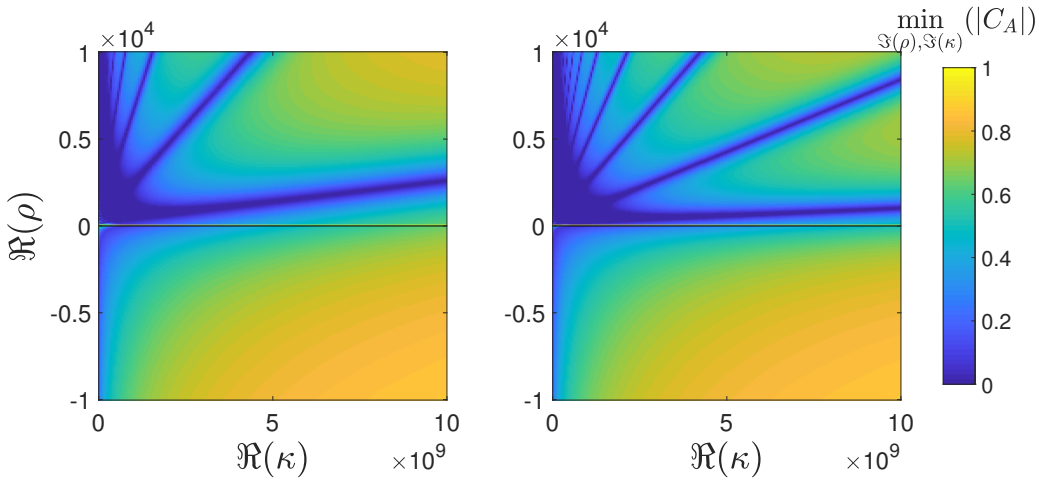

Figure E.6 – $|C_A|$-map for $k_{\mathrm{w}}L = 2.09$ (left) and $k_{\mathrm{w}}L = 3.44$ (right).

The origins and conditions of these low $|C_A|$-branches are discussed in more details here. Since they seem to be related to specific values of the wavenumber, the anechoism coefficient expression in terms of the effective wavenumber k_e and the effective impedance Z_e given in Equation (E.7) is used in order to determine the conditions on these parameters which make it possible to obtain exactly $|C_A| = 0$.

The only non-trivial solution that can exactly cancel the anechoism coefficient is $r = -t^2$. In terms of effective wavenumber and effective impedance, this equality becomes:

$$\frac{z-1}{z+1} = -e^{-2\mathrm{i}k_e L}. \tag{E.8}$$

The reduced wavenumber is thus given by:

$$k_e L = -\frac{1}{2\mathrm{i}} \log(|\frac{1-z}{1+z}|) - \frac{1}{2}\arg(\frac{1-z}{1+z}) - m\pi, \tag{E.9}$$

where m is an integer, since the complex logarithm is multi-branched function.

Type 2 Representation is now used for the wavenumber and effective impedance to visually evaluate Equation (E.9). In Figure E.7, minima of $|C_A|$ have been plotted in the ($\Re(kL/pi)$,$\Re(z)$)-plan. The horizontal grey line shows the impedance of water, corresponding to a real normalised impedance $\Re(z) = 1$. In the $|C_A|$ map, the branches of low anechoism can be seen. There is a clear distinction between the areas with higher and lower impedances than that of water.

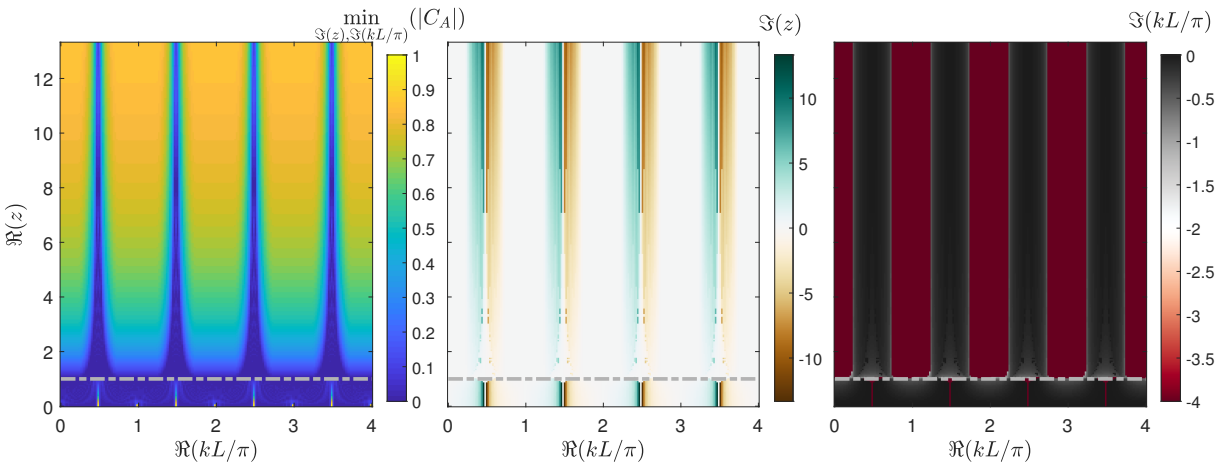

Figure E.7 – Type 2 Representation for the $|C_A|$-map in the ($\Re(kL/pi)$, $\Re(z)$) coordinate system where the grey dashed lines show the impedance of water.

For $\Re(Z_e) > Z_\mathrm{w}$, so for $\Re(z) > 1$, the only areas where $\min(|C_A|)$ seems null are when $\Re(kL/\pi)$ is a multiple of 0.5. In the middle and right hand-side maps, it can be seen that these lines are obtained for $\Im(z) = 0$ and $\Im(kL/\pi) \approx 0$. For $\Re(z) < 1$, the zeros of the anechoism coefficient seem centred around areas where $\Re(kL/\pi)$ is an integer. It is moreover observed that they are also associated to $\Im(z) = 0$ and $\Im(kL/\pi) \approx 0$. Using the fact that $\Im(z) = 0$ and $\Im(kL/\pi) = 0$, Equation (E.9) which gives the zeros of the anechoism coefficient is re-written as:

$$k_e L = \begin{cases} -\frac{(2m+1)}{2}\pi, \text{ if } z > 1 \\ -m\pi, \text{ if } z < 1 \end{cases}, \tag{E.10}$$

with z a real value. This equation is consistent with the location of the blue branches of low $|C_A|$. Perfect anechoism can therefore be obtained for the effective wavenumber satisfying Equation (E.10), obtained for $\Im(z) = 0$ and $\Im(kL/\pi) = 0$. This Equation actually corresponds to the fundamental and harmonic modes for wave propagation in a

open/closed tube. These low $|C_A|$-branches are thus obtained thanks to coherent modes resulting from the slab resonances.

The coherent perfect anechoism is in practice feasible but it cannot achieve a broadband performance. It seems however that very low values of the anechoism coefficient can be obtained close to these branches. According to Figure E.7, it appears that for both $z > 1$ and $z < 1$, the conditions that exactly cancel the anechoism coefficient on the branches, which are $\Im(z) \approx 0$ and $\Im(kL/\pi) \approx 0$, are also the conditions that minimise it around the branches.

Equation (E.10) can now be used to derive the expression of the zeros for the anechoism coefficient in terms of effective properties κ and ρ. Using $\rho = k_e^2/(\omega^2 L^2)\kappa$, the zeros of $|C_A|$ are obtained for:

$$\rho = \begin{cases} \frac{(1+2m)^2}{16f^2L^2}\kappa, & \text{if } z > 1 \\ \frac{m^2}{4f^2L^2}\kappa, & \text{if } z < 1 \end{cases} . \tag{E.11}$$

This equation is verified on the main map in Figure E.8. The distinction between areas for $z < 1$ and $z > 1$ is also highlighted by the grey dotted line. The red lines are plotted according to Equation (E.11) for $m = 0$, $m = 1$ and $m = 2$. They perfectly match with the low $|C_A|$ branches, which confirms that the perfect anechoism of these branches results from slab resonances. The areas $z < 1$ and $z > 1$ are now treated separately to study the imaginary parts of the effective properties. By introducing damping parameters as $\eta_\rho = \Im(\rho)/\Re(\rho)$ and $\eta_\kappa = \Im(\kappa)/\Re(\kappa)$ and by using Equation (E.11), it is expected that $\eta_\kappa = \eta_\rho$. Therefore, at the slab resonance, z is purely real but this does not mean that the damping is zero, since it results in fact from an equilibrium between the losses.

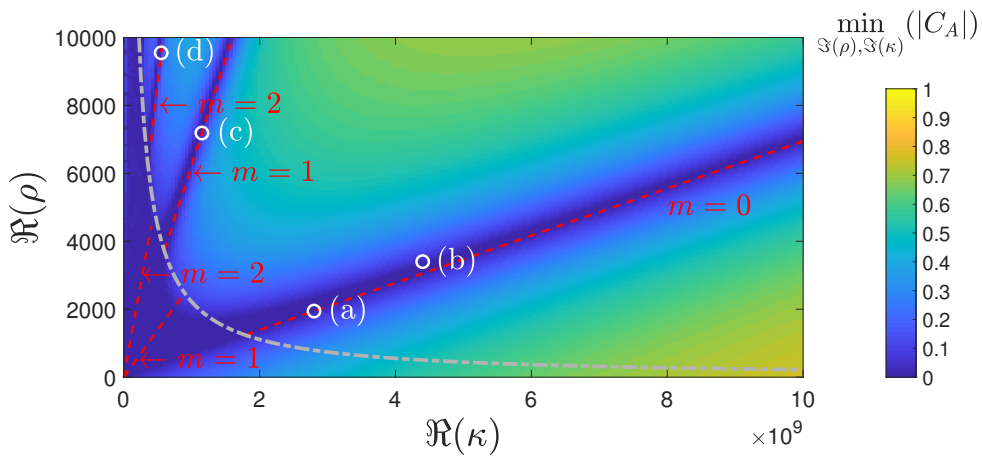

Figure E.8 – $|C_A|$-map in the $(\Re(\rho), \Re(\kappa))$ coordinate system highlighting four couples $(\Re(\kappa), \Re(\rho))$ by white circles. The grey line shows the delimitation between areas $z < 1$ and $z > 1$. The red lines are plotted according to Equation (E.11) for $m = 0$, $m = 1$ and $m = 2$.

$\Re(z) > 1$

In Figure E.8, four points are selected in the area $z > 1$. Point (a) is located exactly on the branch $m = 0$ whereas point (b) is slightly off the branch. Points (c) and (d) are then chosen on branches $m = 1$ and $m = 2$, respectively. For this selection, the $|C_A|$-maps in the ($\Im(\rho)$, $\Im(\kappa)$) coordinate system are given in Figure E.9. It can be seen that these four maps show some similarity: the minimum of $|C_A|$ is located on a straight "isoline" for the low values of $|C_A|$. These "isolines" have the same slope as their counterpart in the $\Re$-coordinate system of Figure E.8, which is given by Equation (E.11). According to Equation (E.11), it is expected that the isoline cuts the system origin for points (a), (c) and (d), which are exactly on the dotted lines in Figure E.8. Nevertheless, for point (a), a shift of the isoline is observed. This may be explained by the fact that perfect anechoism is not exactly obtained for $\Re(kL/\pi) = 0$ as seen in Figure E.7.

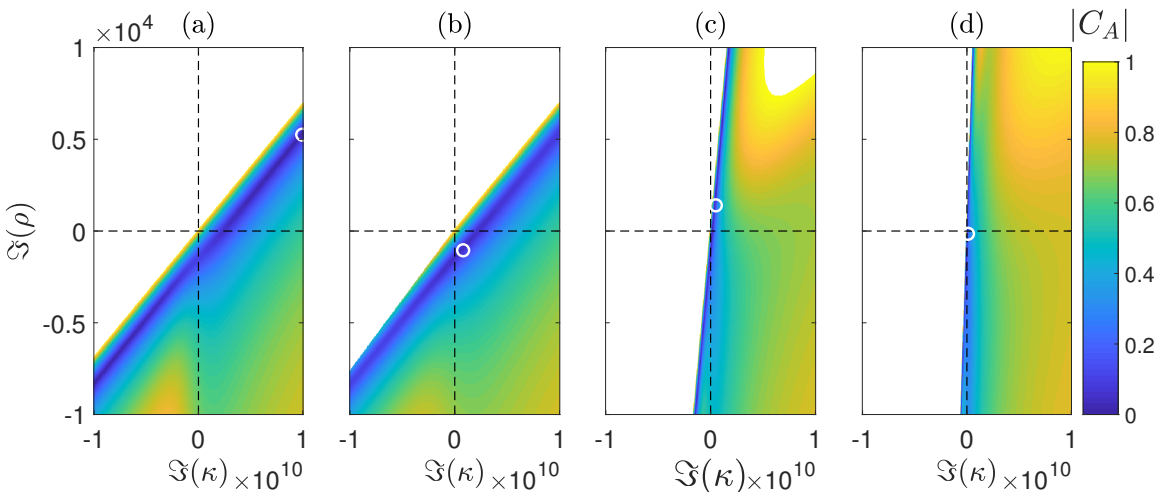

Figure E.9 – Representation Type 1, showing $|C_A|$-maps in the ($\Im(\rho)$, $\Im(\kappa)$) coordinate system for the four couples ($\Re(\kappa)$, $\Re(\rho)$) represented in Figure E.8 by the white circles and highlighted here as well. The white areas break the passivity constraint.

Additionally, it is observed that maps for (a) and (b) are extremely similar. This shows that it is not necessary to be exactly on a branch to obtain low anechoism. It seems however better to be around the branch corresponding to $m = 0$ than the others as their are fewer options for low $|C_A|$ in the maps for (c) and (d). It can also be noticed that the position on these isolines seems quite random. Type 2 representation is used in Figure E.10 to visualise the values of $\Im(\rho)$ and $\Im(\kappa)$, which confirms that on the branches, and only precisely on the branches, numerical errors are present due to the discontinuity so that there is no consistency for the values of the imaginary parts.

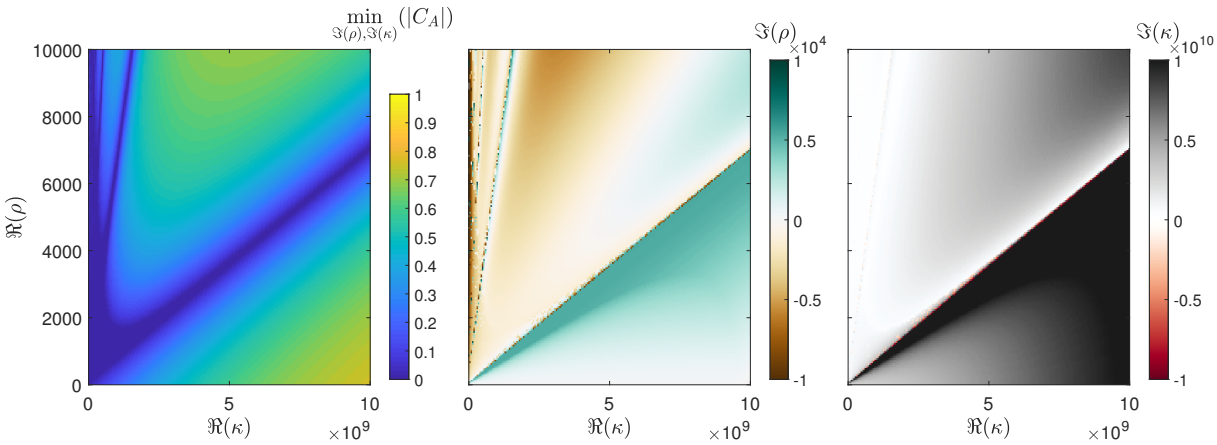

Figure E.10 – Type 2 representation for the Quadrant 1, showing $|C_A|$-maps in the $(\Re(\rho), \Re(\kappa))$ coordinate system and the values of $\Im(\rho)$ and $\Im(\kappa)$ that led to these $|C_A|$.

Maps in Figure E.10 also show that, around the discontinuity lines associated with the branches, the optimal anechoism performance is obtained for extremely high or nearly null values of both $\Im(\rho)$ and $\Im(\kappa)$, as for point (b) in Figure E.9.

$\underline{\Re(z) < 1}$

The area $z < 1$ is now further studied. For the sake of clarity, Figure E.11 is introduced as a zoom in Figure E.8 of the area $z < 1$. In this map, points (a) and (c) are localised exactly on the branches $m = 1$ and $m = 2$, respectively, whereas points (b) and (d) are randomly placed off the branches. The $|C_A|$-maps in the imaginary coordinate system for these four points are given in Figure E.12.

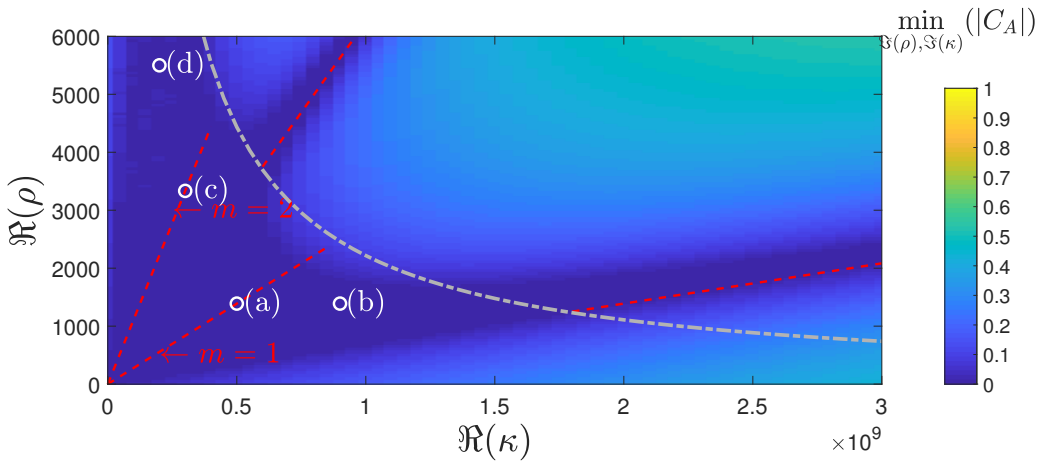

Figure E.11 – $|C_A|$-map in the $(\Re(\rho), \Re(\kappa))$ coordinate system highlighting four couples $(\Re(\kappa), \Re(\rho))$ by white circles. The grey line shows the delimitation between areas $z < 1$ and $z > 1$. The red lines are plotted according to Equation (E.11) for $m = 1$ and $m = 2$.

It is observed that maps (a) and (b) are very similar. The same observation is made for

maps (c) and (d). It therefore appears that being exactly on the branch in Figure E.11 is not necessary to obtain very low anechoism. It is also observed that low anechoism areas are obtained for low values of $\Im(\kappa)$, which are in fact of the same order of magnitude as $\Re(\kappa)$.

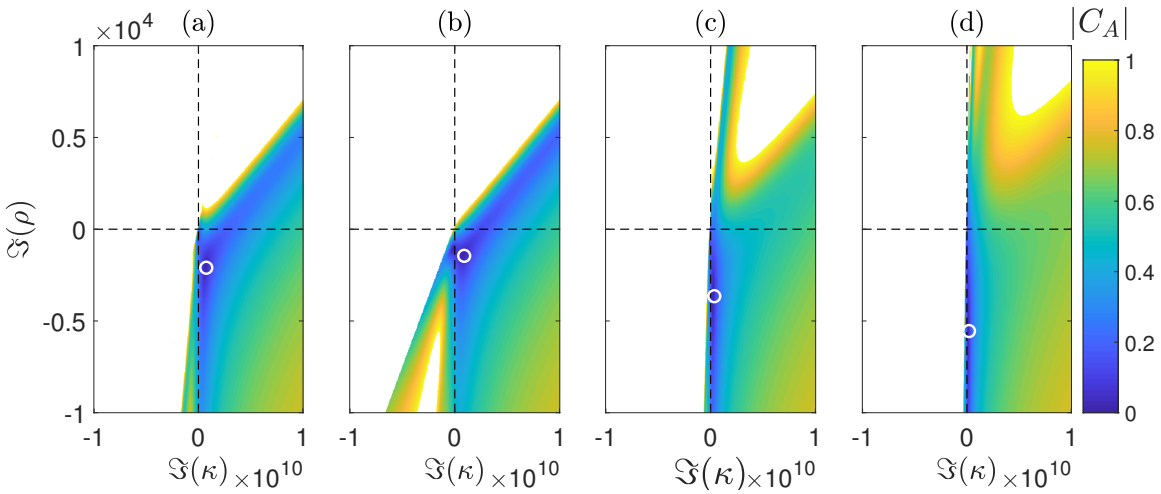

Figure E.12 – Type 1 representation, showing $|C_A|$-maps in the $(\Im(\rho), \Im(\kappa))$ coordinate system for the four couples $(\Re(\kappa), \Re(\rho))$ represented in Figure E.11 by the white circles and highlighted here as well. The white areas break the passivity constraint.

To summarise, perfect anechoism can be obtained in Quadrant 1 as the result of a coherent mode at a slab resonance. The mapping approach helped the derivation of Equation (E.11), that gives the link between ρ and κ when $|C_A| = 0$. Around the branches defined by Equation (E.11), it is possible to obtain really low values of the anechoism coefficient. The imaginary parts of the effective properties then seems to play an important role. It also appears that the areas of low $|C_A|$, around the branches, are larger if $z < 1$. If effective properties are such that $z > 1$, having a low anechoism may be more difficult since Figure E.6 showed that these branches are strongly dependent on both the frequency and the medium thickness. To obtain broadband performance in this quadrant, the dispersion on the properties of waves in a medium would need to be tuned to follow the branches. The notion of dispersion here refers to the dispersion that occurs when pure plane waves of different wavelengths have different propagation velocities. However, by increasing the thickness or the frequency or both, it is visually clear that areas of low $|C_A|$ are more likely to be reached. Quadrant 4 ($\Re(\rho) < 0$, $\Re(\kappa) > 0$) is now further studied as it appears that low real parts of ρ, κ or both is a condition that can yield low anechoism coefficient independently of the frequency, as visible in Figure E.6. It may therefore be advantageous to restrict the dispersion on the waves' properties to this zone of Quadrant 4 to create a low broadband anechoism.

Quadrant 4

In the quadrant ($\Re(\kappa)>0$, $\Re(\rho) < 0$), low values of $|C_A|$ can be obtained, as shown in Figure E.13. Low values are concentrated close to the $\Re(\kappa) = 0$ axis, so for very low values of $\Re(\kappa)$. The anechoism coefficient seems to be also low for extremely low values of $|\Re(\rho)|$, as well as for values of $\Re(\kappa)$ and $\Re(\rho)$ close to 0.

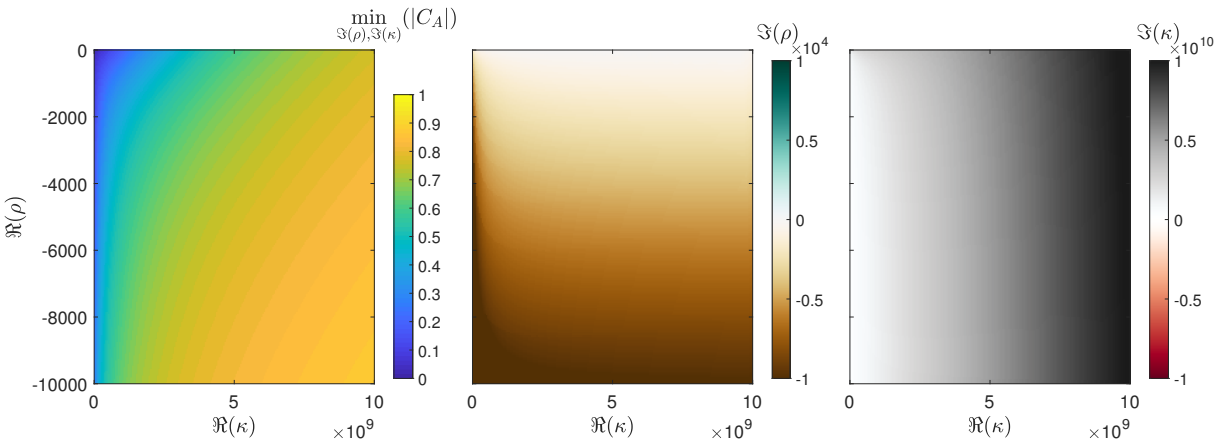

Figure E.13 – Type 2 representation of the Quadrant 4, showing $|C_A|$-maps in the ($\Re(\rho)$, $\Re(\kappa)$) coordinate system and the values of $\Im(\rho)$ and $\Im(\kappa)$ that led to these $|C_A|$.

In terms of values of the imaginary parts, a peculiar observation can be made using middle and right-hand side maps in Figure E.13: the values of $\Im(\kappa)$ and $\Im(\rho)$ follow the evolution of the real part counterparts. In fact, in the middle map showing $\Im(\rho)$, there is a vertical color gradient from the top at $\Re(\rho) = 0$ to the bottom at $\Re(\rho) = -10000$. This color gradient represents the values of $\Im(\rho)$, also going from 0 to -10000. As such, the value of the imaginary part matches the value of the real part. The same observation is made on the right hand-side map for κ, but with a horizontal gradient color. As such, in the Quadrant 4, the lowest values of the anechoism coefficient are obtained for $\Re(\kappa) \approx \Im(\kappa)$ and $\Re(\rho) \approx \Im(\rho)$.

In order to understand why minimal values of the anechoism coefficient seem to be obtained when the imaginary and real parts of ρ and κ are equal, the effective properties are written as:

$$\begin{cases} \rho = \rho_{\Re}(1+\mathrm{i}) \\ \kappa = \kappa_{\Re}(1+\mathrm{i}) \end{cases}, \tag{E.12}$$

with $\rho_{\Re} = \Re(\rho) = \Im(\rho)$ and $\kappa_{\Re} = \Re(\kappa) = \Im(\kappa)$. These expressions are used to express the wavenumber $k = \omega\sqrt{\rho/\kappa}$, which yields:

$$k = \omega\sqrt{\frac{\rho_{\Re}}{\kappa_{\Re}}}. \tag{E.13}$$

Since $\rho_{\Re} < 0$ and $\kappa_{\Re} > 0$, the wavenumber is shown to be purely imaginary, which means that waves do not propagate and are purely evanescent.

Consequently, minima of the anechoism coefficient are obtained for $\Re(\rho) = \Im(\rho)$ and $\Re(\kappa) = \Im(\kappa)$, as seen in Figure E.13. This condition results in the existence of evanescent waves only and the absence of propagating waves. Having imaginary parts almost as high as the real parts means that there is significant damping. Such values may be obtained only for effective properties of complex structures, at frequencies of dipole or matrix resonance for instance, as shown in Chapter 6. However, the values where the anechoism coefficient is actually really low correspond to the lowest values of both ρ and κ. A design strategy may be to combine coherent absorption branches in Quadrant 1 with low $\Re$-values and high damping in Quadrant 4. The latter can be obtained with resonances : dipole resonance for $\Re(\rho) < 0$ and monopole resonance for $\Re(\kappa) < 0$. Spreading these effects over the frequency range of interest using the dispersion would help in having a broadband low anechoism coefficient.

Summary

Some of the main observations are summarised here. In Quadrant 1 and for $|z| > 1$, it has been shown that $|C_A| = 0$ can only be obtained at slab resonances, satisfying Equation (E.9). For $|z| < 1$, very low values of the anechoism coefficient can be obtain even away from the branches. Around these branches, it is possible to obtain a low anechoism coefficient for either extreme values or near-zero values of the imaginary parts $\Im(\kappa)$ and $\Im(\rho)$. Using effective parameters, such values may be reached through local resonance of inclusions.

Quadrant 4 has then be studied. This Quadrant seems promising since there is a small area of low $|C_A|$ which seems to remain at this location independently of the frequency and medium thickness. This area is mainly concentrated near the $\Re(\kappa) = 0$ axis.

Consequently, to obtain a broadband performance, it would be interesting to tune the dispersion in order to be either next to a branch or below $|z| < 1$ in Quadrant 1 or close to the $\Re(\kappa) = 0$ axis in Quadrant 4. In both cases, it has been observed that the values of the imaginary parts have a significant impact. In the following section, two multilayered media are homogenised and their effective properties are derived. They are then used to create a "frequency path", so that one can follow the evolution of the anechoic performance based on the maps.

E.2 Frequency Path

E.2.1 Introduction

In this section, performance maps are generated for several frequencies in order to follow the "frequency path" of a multilayered structure. The notion of frequency path is explained/illustrated later in this section. Two case studies are conducted, described below :

1. A layer arrangement is defined aiming to maximise the number of frequencies for which the effective properties remain in Quadrant 4 ($\Re(\kappa) > 0$, $\Re(\rho) < 0$) since it has been observed that this area can always provide low values of the anechoism coefficient independently of the reduced frequency. The objective of this approach is thus to determine if, by containing the dispersion on the waves' properties in the medium to this area, it is possible to obtain broadband low anechoism.

2. The second layer arrangement is defined so that the anechoism coefficient is minimised over the entire frequency range, as per Chapter 3. As such, it would be possible to observe the behaviour of performance-driven dispersion within the maps.

In both case studies, it is the layer arrangement of a **unit cell** of thickness L_u that is defined. The transfer matrix of the unit cell is first calculated, from which effective properties and scattering coefficients are derived as per Chapter 2. The same materials as in Chapter 3 are considered, that is to say a polyurethane containing 6% of micro-balloons as well as stainless steel. The thickness of the unit is $L_u = 16$ mm and the minimal layer thickness is $l = 2$ mm. There are thus $2^8 = 256$ possible designs for the unit cell. Even though the performance mapping can be applied to asymmetric media by adding extra parameters, a symmetric unit is herein selected for the sake of simplicity. This reduces the number of possible designs to $2^4 = 16$.

E.2.2 Quadrant Driven Design

In this section, a multilayered medium is selected based on its effective properties so that they remain in the quadrant ($\Re(\kappa)>0$, $\Re(\rho) < 0$) for a large number of frequencies within the frequency range of interest which is [3 kHz - 20 kHz]. As a reminder, the objective here is to contain the dispersion in this area, which seems unchanged with frequency, in order to obtain broadband low anechoism.

The layer arrangement shown in Figure E.14 is selected. Amongst all possible symmetric units, it corresponds to the largest range of frequencies with negative values of $\Re(\rho)$.

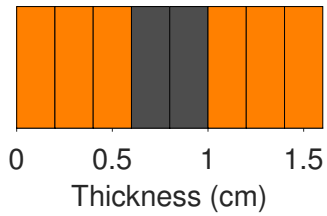

Figure E.14 – Layer arrangement for the selected unit cell.

For the selected unit cell, the effective bulk modulus and effective density are given in Figure E.15. It is observed that the effective density becomes negative around 16.5 kHz.

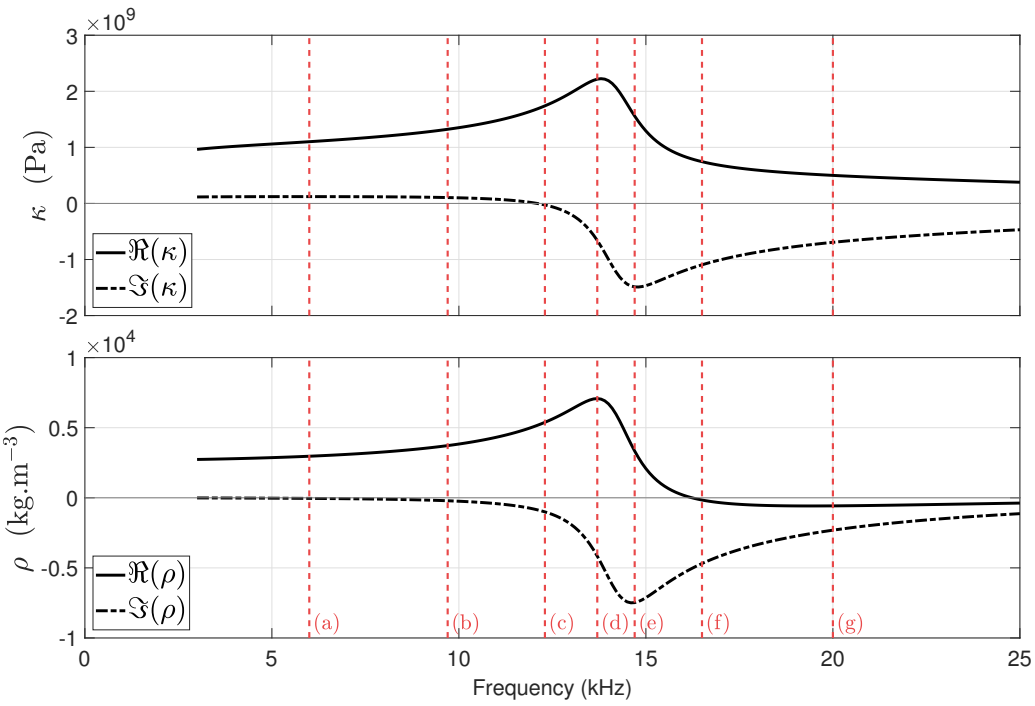

Figure E.15 – Effective bulk modulus and effective mass density for the selected unit cell. Seven frequencies are selected and highlighted by the red dotted lines.

Several frequencies, referred to as frequencies (a) to (g), have been selected and are shown by the red vertical lines. They are used to follow the frequency path for a multilayered medium comprising 3 of unit cells. The length of the effective medium is therefore $L = 3 \times L_u = 4.8$ cm. Scattering coefficients for this medium are given in Figure E.16.

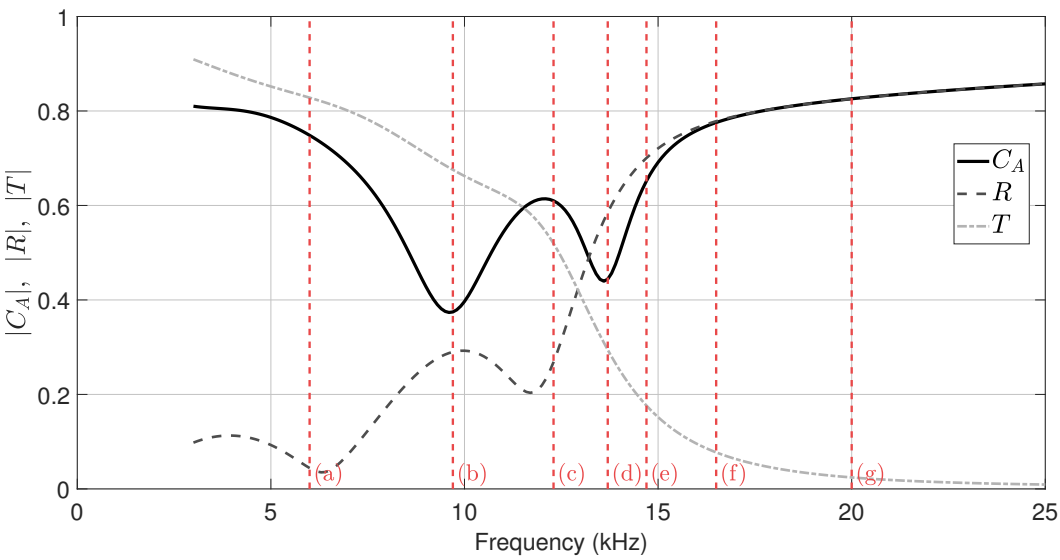

Figure E.16 – Anechoism, reflection and transmission coefficients for a 3-unit medium.

For each of the frequencies previously selected, the ($\Re(\kappa)$, $\Re(\rho)$)-map is plotted. The effective properties obtained for the unit cell are then spotted on the $\Re$-map. For this given set of values for ($\Re(\kappa)$ and $\Re(\rho)$), the $\Im$-map is generated, in which the values of ($\Im(\kappa)$ and $\Im(\rho)$) obtained for the unit cell are highlighted, along with the value of the anechoism coefficient. With this approach, applied for successive frequencies, the frequency path of a design is created and is given in Figure E.17 for (a) 6 kHz, (b) 9.7 kHz, (c) 12.3 kHz, (d) 13.7 kHz, (e) 14.7 kHz, (f) 16.5 kHz and (g) 20 kHz.

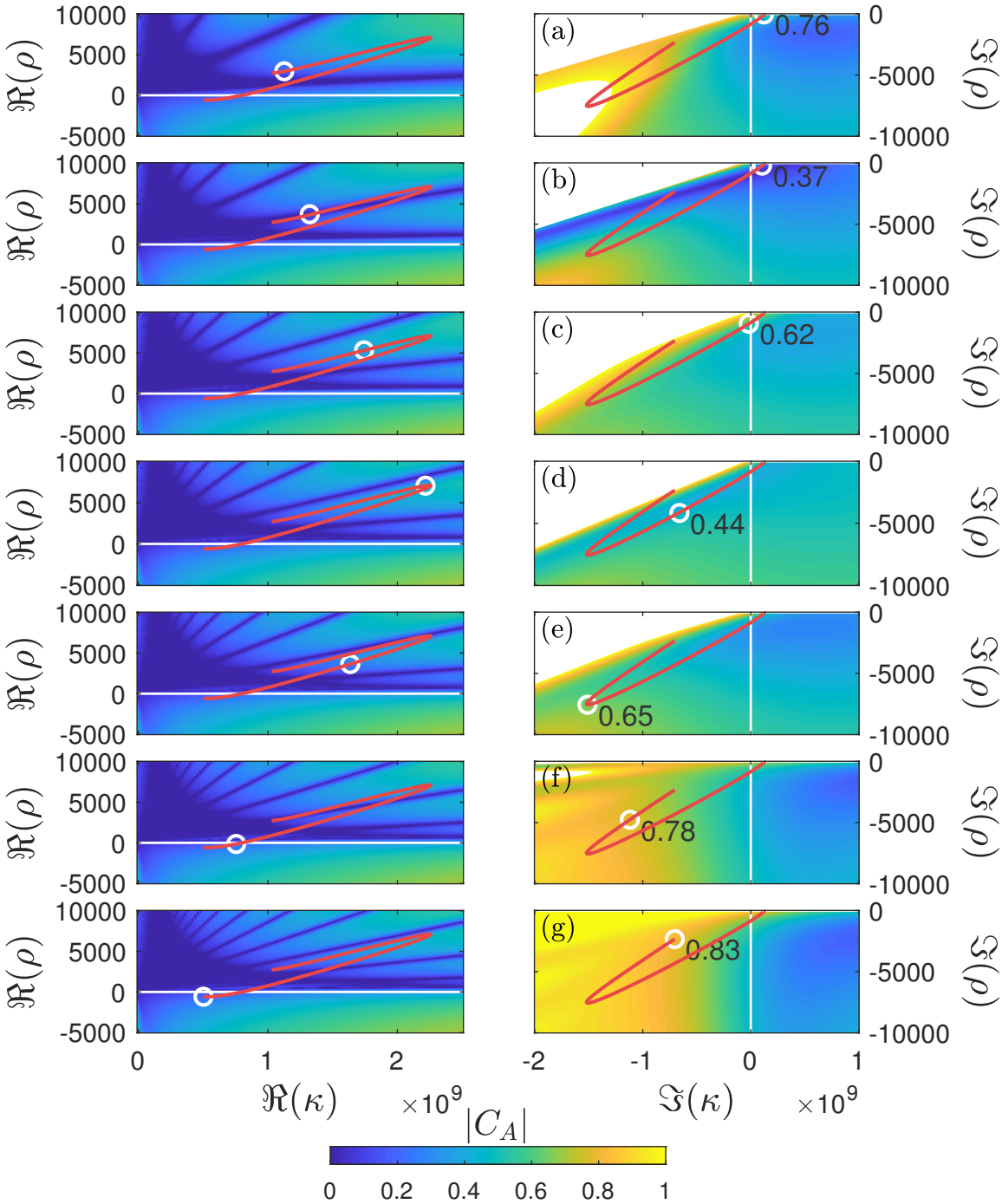

Figure E.17 – Frequency paths for a medium of length $L = 3 \times L_u = 4.8$ cm at the frequencies (a) 6 kHz, (b) 9.7 kHz, (c) 12.3 kHz, (d) 13.7 kHz, (e) 14.7 kHz, (f) 16.5 kHz and (g) 20 kHz. On the $\Re$-maps (left hand side), the white circle shows the values of $\Re(\kappa)$ and $\Re(\rho)$ obtained for the unit cell in Figure E.14. The red line represents the complete path. In the $\Im$-map obtained for these values (right hand side), the white circle shows the values of $\Im(\kappa)$ and $\Im(\rho)$ obtained for the unit cell and the value of the anechoism coefficient.

The frequency path is analysed along with the variations of the anechoism coefficient for a 3-unit multilayered medium of length $L = 3 \times L_u = 4.8$ cm, given in Figure E.16. Comparisons are made according to the overall variations of the anechoism coefficient, that is to say that the results are not compared to the performance of another anechoic medium.

At frequency (a) 6 kHz, values of the effective properties in Figure E.15 are still close to the quasi-static values obtained for very low frequencies. In Figure E.17, those values of the effective properties are located in Quadrant 1 ($\Re(\kappa)>0$, $\Re(\rho) > 0$) where the anechoism coefficient can reach very low values around branches. At this frequency, the real parts of ρ and κ are located relatively close to one of the branches. As such, with high values of the imaginary parts, it could be possible to obtain relatively low values of the anechoism coefficient (around 0.4). However, the anechoism coefficient here is quite high, equal to 0.76, since the imaginary parts are both nearly null. This result is confirmed by the scattering response of the 3-unit multilayered medium in Figure E.16.

At frequency (b) 9.7 kHz, effective parameters start differing slightly from the quasi-static values at low frequencies. This frequency has been selected because it corresponds to the minimum of the anechoism coefficient of the 3-unit medium in Figure E.16. For this low value of C_A, the performance maps for (b) show that the real parts ρ and κ are located on a branch of slab resonance. In the corresponding $\Im$-map, it is observed that the isoline of perfect anechoism is almost reached, thus leading to $C_A = 0.37$.

In Figure E.15, $\Im(\kappa)$ changes sign at the frequency (c) 12.3 kHz and the real parts are still located in Quadrant 1, but relatively far from branches. The situation is slightly similar to the frequency (a), where a high coefficient is obtained because imaginary parts are close to 0. It can nonetheless be observed that, in the $\Im$-maps, the coefficient possible values are higher for (c) than for (a) due to the fact that (c) is further away to a branch in Quadrant 1.

At frequency (d) 13.7 kHz, both $\Re(\rho)$ and $\Re(\kappa)$ reach their maximal value in Figure E.15. In the performance maps of Figure E.17, these values are located close to a branch in Quadrant 1. Additionally, the values of $\Im(\rho)$ and $\Im(\kappa)$ are well located within in the $\Im$-map. As such, at this frequency, a relatively low value of the anechoism coefficient is obtained, as also shown in Figure E.16. Consequently, by comparing frequencies (b) and (d), it appears that, in terms of anechoic performance, being out of a branch with suitable imaginary parts may be as beneficial as being on a slab resonance branch with unsuitable imaginary parts.

In Figure E.15, both the $\Im(\rho)$ and $\Im(\kappa)$ reach their minimal value at the frequency (e) 14.7 kHz. In the $\Re$-map of Figure E.17, the real parts are still located in Quadrant 1 in between two branches. Low $|C_A|$ could therefore be obtained as for frequency (d), but the values of the imaginary parts lead in the area where the anechoism coefficient is high. It would have been preferable to have $\Im(\kappa) > 0$.

At frequency (f) 16.5 kHz in Figure E.15, $\Re(\rho)$ becomes negative. In the real map in Figure E.17(f), the frequency path now goes into Quadrant 4 ($\Re(\kappa)>0$, $\Re(\rho) < 0$). In the $\Re$-map, it is observed that very low values of the anechoism coefficient can be reached and the objective was initially to remain in this area for a large frequency range. However, the values for $\Im(\kappa)$ and $\Im(\rho)$ for the unit cell at this frequency are located in the area where $|C_A|$ is relatively high, which is confirmed by Figure E.16. For lowering the anechoism coefficient, $\Im(\kappa) > 0$ or lower values of $\Im(\kappa)$ would have been necessary as for frequency (e).

For frequency (g) 20 kHz, a interesting location is reached in Quadrant 4 of the $\Re$-map, but, as previously, the imaginary parts are such that the anechoism coefficient remains very high. It can nonetheless be noted that for frequencies (f) and (g), the $\Im$-maps tend to be split into two spaces: very low anechoism for $\Im(\kappa) > 0$ and very high anechoism for $\Im(\kappa) < 0$.

Consequently, it was observed that the imaginary parts of the effective properties play a significant role in the acoustic performance. Even though a specific metamaterial feature (being a negative effective density) is obtained, it is not associated here to a good anechoism coefficient. A better anechoism performance may therefore be obtained with a better control of the dispersion and more particularly of the imaginary parts of the effective properties. In what follows, a design is chosen for its broadband anechoism performance in order to observe the "natural" evolution of the dispersion for a performance driven design.

E.2.3 Performance Driven Design

In this section, a multilayered medium is selected based on its broadband anechoism performance on the frequency range [3 kHz - 20 kHz]. The same criteria as in Chapter 3 are used to chose amongst the 16 possible symmetric units. Scores are given in Figure E.18.

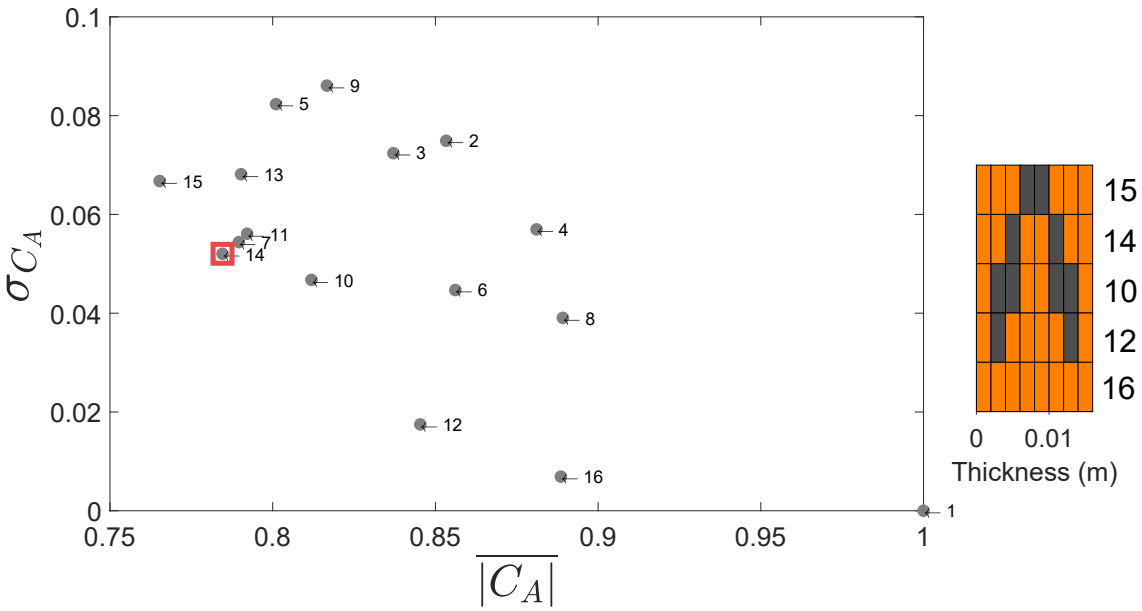

Figure E.18 – Scores of the 16 possible designs and layer arrangements of configurations in the Pareto front.

Configuration 15 is the one studied previously. Very low values of the anechoism coefficient are indeed reached, but the standard deviation is high. Configurations 12 and 16 are excluded as the anechoism coefficient remains too high. It can be seen that the unit of Configuration 10 actually consists of 2 identical symmetric units of length $L_u/2$. The effective properties thus remain almost constant since all periodic effects are shifted to higher frequencies. Configuration 14 is therefore selected. The layer arrangement is shown in Figure E.19.

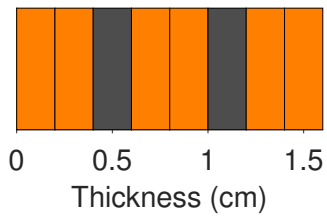

Figure E.19 – Layer arrangement for the selected unit cell.

For the selected unit cell, the anechoism coefficient for a 3-unit medium is given in Figure E.20 and the effective bulk modulus and effective density are given in Figure E.21.

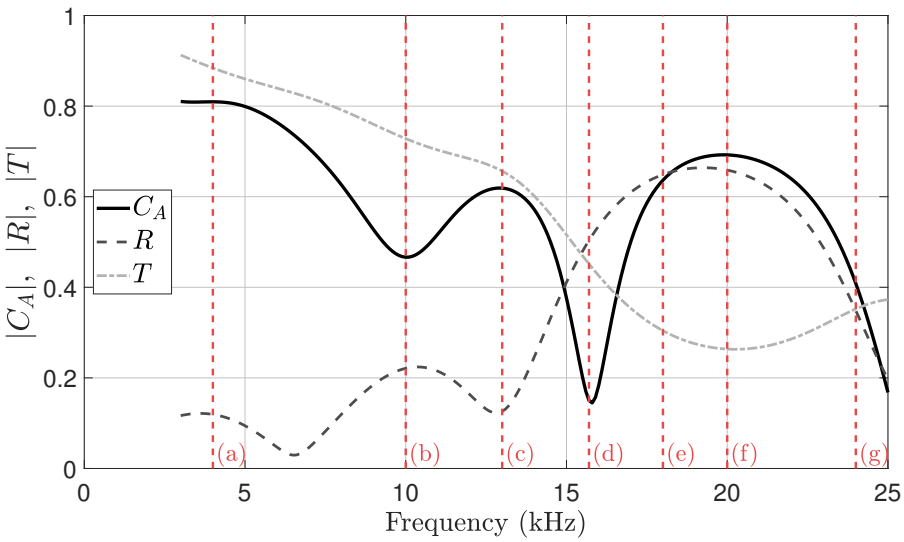

Figure E.20 – Anechoism, reflection and transmission coefficients for a 3-unit medium.

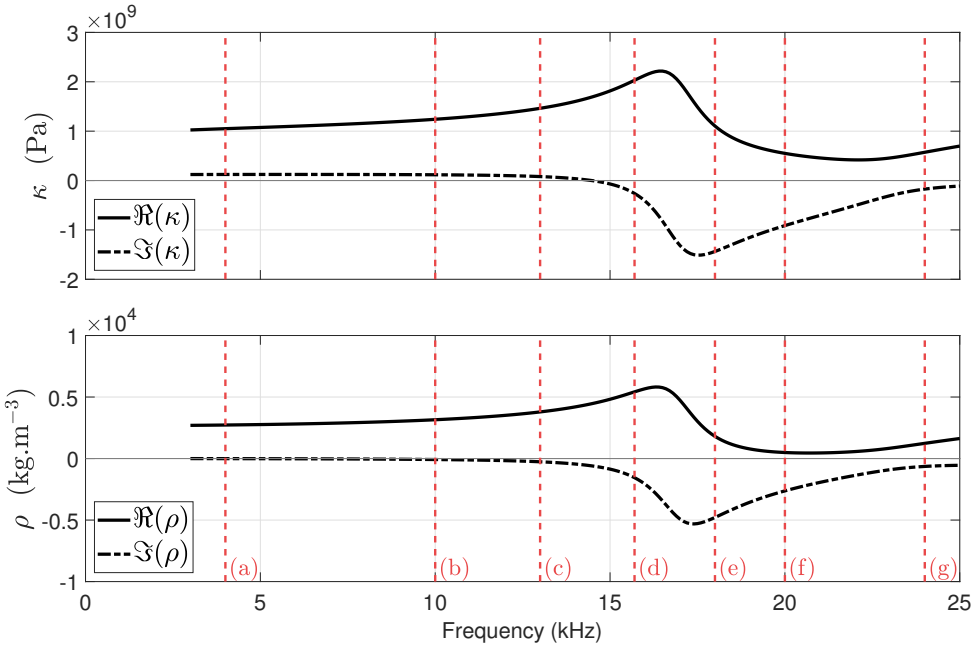

Figure E.21 – Effective bulk modulus and effective mass density for the selected unit cell. Seven frequencies are selected and highlighted by the red dotted lines.

It is observed the real parts of both effective properties remain positive. It is also seen that the anechoism coefficient remains under 0.7 from 6 kHz. New frequencies are selected, referred to as frequency (a) to (g), corresponding to peculiar point in the anechoism coefficient variations. They are used to follow the frequency path for a multilayered medium comprising of 3 unit cells, presented in Figure E.22.

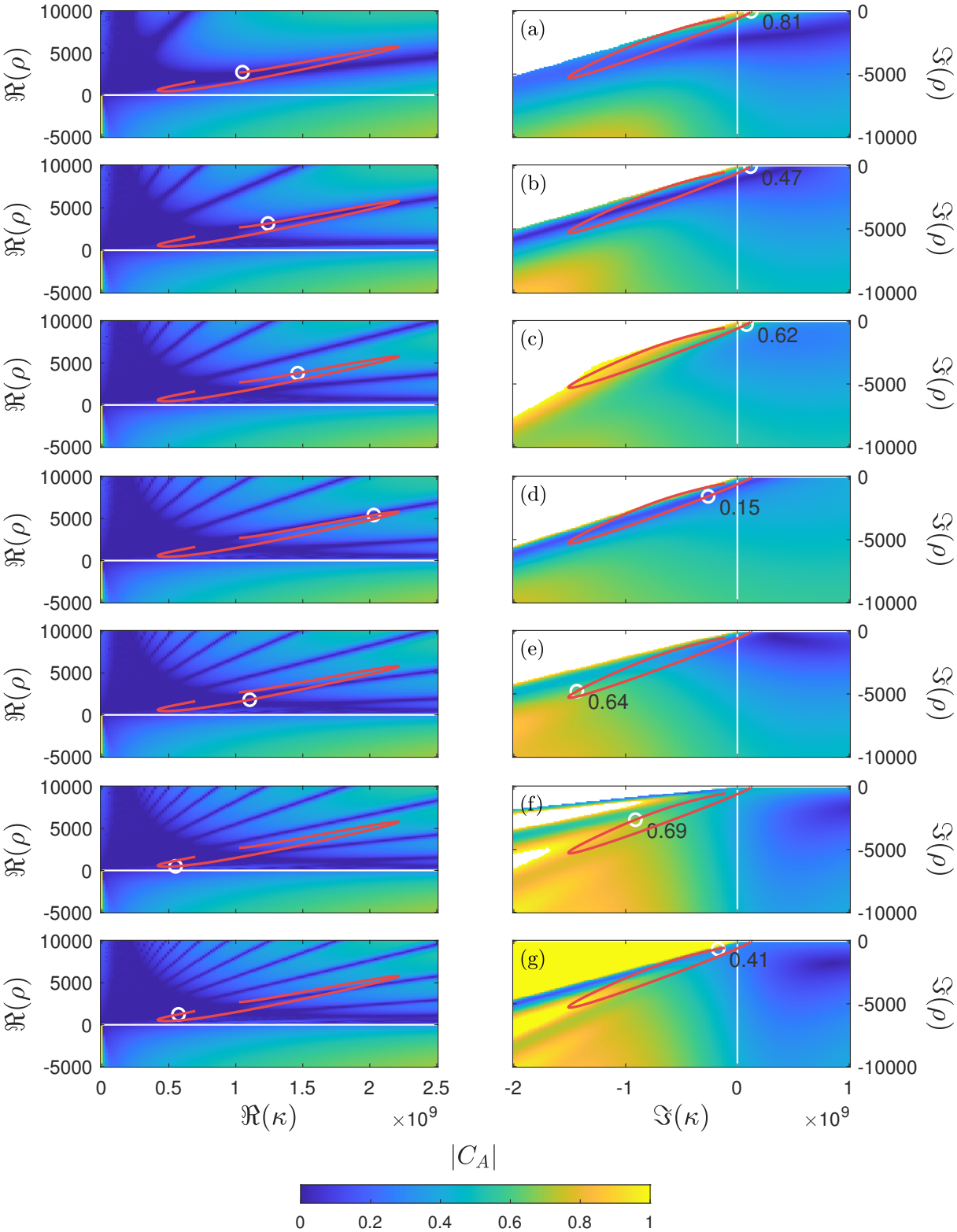

Figure E.22 – Frequency path for a medium of length $L = 3 \times L_u = 4.8$ cm at the frequencies (a) 4 kHz, (b) 10 kHz, (c) 13 kHz, (d) 15.7 kHz, (e) 18 kHz, (f) 20 kHz and (g) 24 kHz. On the $\Re$-maps (left hand side), the white circle shows the values of $\Re(\kappa)$ and $\Re(\rho)$ obtained for the unit cell in Figure E.19. The red line represents the complete path. In the $\Im$-map obtained for these values (right hand side), the white circle shows the values of $\Im(\kappa)$ and $\Im(\rho)$ obtained for the unit cell and the value of the anechoism coefficient.

For frequencies (a) to (d), the real parts of the effective properties are in Quadrant 1 in the area where $z > 1$. Amongst these frequencies, (a), (b) and (d) are located on a slab resonance branch. For frequencies (b) and (d), the imaginary parts at these frequencies are also well located, close to the isoline of null $|C_A|$. As a result, a very low anechoism coefficient is obtained for these two frequencies, especially for the frequency (d) with $|C_A| = 0.15$. For the frequency (c), the real part is slightly off the branches and very low values for the imaginary parts are obtained. The anechoism coefficient is relatively good, but could be improved with higher values of the imaginary parts $\Im(\kappa)$.

At frequency (e) to (g), the area $z < 1$ is reached, where extremely low values of the anechoism coefficient could be obtained. For both (e) and (f), it can be seen however that $|C_A|$ is quite high here since the imaginary parts are not suitable. Similarly to the design previously studied, it would be beneficial here to have $\Im(\kappa) > 0$. In fact, it is observed that very low values of $|C_A|$ are obtained at 24 kHz (frequency (g)) in the the area $z < 1$ thanks to values of $\Im(\kappa)$ going towards positive values.

To summarise, low values of the anechoism coefficients have been obtained as a result of slab resonances associated with the branches. Once on the branch, it does not seem to be difficult to obtain the imaginary parts that lead to a good anechoism coefficient. Slightly off the branches, it was observed that it is beneficial to aim for positive values of $\Im(\kappa)$ or alternatively for near-zero values of $\Im(\kappa)$.

This confirms what has been observed for the 2D optimisation (Chapter 7), that is that multilayered media can lead to low anechoism in a given frequency range, but fail to provide a broadband performance since they do not provide local resonances that could help tuning the imaginary parts. Multilayered media are therefore found to provide low anechoism coefficient due to slab resonances, thus depending on the length of the medium. The fact that $\Re(\rho) < 0$ is therefore not an indicator that the anechoism coefficient is low, but simply signifies that the center of mass displacement is in phase opposition to the incident fields (Chapter 6), which for multilayered media seems to only happen when a heavy layer is located in-between two damped layers.

Although the presented results are not always intuitive, this concept of performance maps and frequency path helped understanding the feature that lead to low anechoism and it gave keys on how to tune the dispersion on waves' properties to achieve the desired goal.

Bibliography

[1] A.-C. Hladky-Hennion. *Application de la méthode des éléments finis à la modelisation de structures périodiques utilisées en acoustique. (An application of the finite element method to the modeling of periodic structures used in acoustics.)*. PhD thesis, University of Lille, 1990.

[2] G. Ma and P. Sheng. Acoustic metamaterials: From local resonances to broad horizons. *Science Advances*, **2**(2), 1501595, 2016.

[3] J. J. Yang, M. Huang, G. H. Cai, R. S. Xie, and J. Yang. Design of acoustic metamaterial devices based on inverse method. *Journal of Vibration and Acoustics*, **135**(5), 051024, 2013.

[4] L. Joseph and R. Craster. Reflection from a semi-infinite stack of layers using homogenization. *Wave Motion*, **54**, 145–156, 2015.

[5] Y. Wu, Y. Lai, and Z.-Q. Zhang. Effective medium theory for elastic metamaterials in two dimensions. *Physical Review B*, **76**(20), 205313, 2007.

[6] C. Croënne, E. Lee, H. Hu, and J. Page. Band gaps in phononic crystals: Generation mechanisms and interaction effects. *AIP Advances*, **1**(4), 041401, 2011.

[7] T. Brunet, J. Leng, and O. Mondain-Monval. Soft acoustic metamaterials. *Science*, **342**(6156), 323–324, 2013.

[8] N. Fang, D. Xi, J. Xu, M. Ambati, W. Srituravanich, C. Sun, and X. Zhang. Ultrasonic metamaterials with negative modulus. *Nature Materials*, **5**(6), 452–456, 2006.

[9] S. H. Lee, C. M. Park, Y. M. Seo, Z. G. Wang, and C. K. Kim. Composite acoustic medium with simultaneously negative density and modulus. *Physical Review Letters*, **104**(5), 054301, 2010.

[10] V. M. Graciá-Chocano, R. Graciá-Salgado, D. Torrent, F. Cervera, and J. Sánchez-Dehesa. Quasi-two-dimensional acoustic metamaterial with negative bulk modulus. *Physical Review B*, **85**(18), 184102, 2012.

[11] X. Jing, Y. Meng, and X. Sun. Soft resonator of omnidirectional resonance for acoustic metamaterials with a negative bulk modulus. *Scientific Reports*, **5**, 16110, 2015.

[12] L. Lu, T. Yamamoto, M. Otomori, T. Yamada, K. Izui, and S. Nishiwaki. Topology optimization of an acoustic metamaterial with negative bulk modulus using local resonance. *Finite Elements in Analysis and Design*, **72**, 1–12, 2013.

[13] J. Li and C. T. Chan. Double-negative acoustic metamaterial. *Physical Review E*, **70**(5), 055602, 2004.

[14] X. Zhou, X. Liu, and G. Hu. Elastic metamaterials with local resonances: An overview. *Theoretical and Applied Mechanics Letters*, **2**(4), 041001, 2012.

[15] Z. Liu, X. Zhang, Y. Mao, Y. Y. Zhu, Z. Yang, C. T. Chan, and P. Sheng. Locally resonant sonic materials. *Science*, **289**(5485), 1734–1736, 2000.

[16] Z. Yang, J. Mei, M. Yang, N. H. Chan, and P. Sheng. Membrane-type acoustic metamaterial with negative dynamic mass. *Physical Review Letters*, **101**(20), 204301, 2008.

[17] S. Yao, X. Zhou, and G. Hu. Experimental study on negative effective mass in a 1D mass-spring system. *New Journal of Physics*, **10**, 043020, 2008.

[18] R. Graciá-Salgado, V. M. García-Chocano, D. Torrent, and J. Sánchez-Dehesa. Negative mass density and ρ-near-zero quasi-two-dimensional metamaterials: design and applications. *Physical Review B*, **88**(22), 224305, 2013.

[19] L. Fok and X. Zhang. Negative acoustic index metamaterial. *Physical Review B*, **83**(21), 214304, 2011.

[20] X. N. Liu, G. K. Hu, G. L. Huang, and C. T. Sun. An elastic metamaterial with simultaneously negative mass density and bulk modulus. *Applied Physics Letters*, **98**(25), 251907, 2011.

[21] G. Zhou, J. H. Wua, K. Lu, X. Tian, W. Huang, and K. Zhu. Broadband low-frequency membrane-type acoustic metamaterials with multi-state anti-resonances. *Applied Acoustics*, **159**, 107078, 2020.

[22] H. Zou, P. Li, and P. Peng. An ultra-thin acoustic metasurface with multiply resonant units. *Physics Letters A*, page 126151, 2019.

[23] Y. Lai, Y. Wu, P. Sheng, and Z.-Q. Zhang. Hybrid elastic solids. *Nature Materials*, **10**(8), 620–624, 2011.

[24] S. M. Rytov. Acoustical properties of a thinly laminated medium. *Soviet Physics Acoustics*, **2**, 68–80, 1956.

[25] P. Langlet. *Finite element analysis if the propagation of acoustic waves in periodic materials*. PhD thesis, Valenciennes University, 1993.

[26] W. Lu, C. guang Xu, S. Zhang, B. qiang Xu, and W. Cao. Low-frequency gibbs-type oscillation in finite solid–fluid sonic crystals and its application in sub-wavelength wave isolation for waterborne sound. *Journal of Physics D: Applied Physics*, **52**, 505114 – 505122, 2019.

[27] M. Yang, Z. Yang, and P. Sheng. Full-band exact homogenization of one-dimensional elastic metamaterials. Proceedings of the 21st International Congress on Acoustics (ICA 2013), Montreal, Canada, 2-7 June 2013.

[28] W. Xu, T. Yang, and W. Wang. Double-negative dynamic properties in onedimensional multi-phase metamaterial based on the symmetrical equivalent layer. *Waves in Random and Complex Media*, **23**(3), 258–266, 2013.

[29] B. H. Song and J. S. Bolton. A transfer-matrix approach for estimating the characteristic impedance and wave numbers of limp and rigid porous materials. *Journal of the Acoustical Society of America*, **107**(3), 1131–1152, 2000.

[30] G. Wang, D. Yu, J. Wen, Y. Liu, and X. Wen. One-dimensional phononic crystals with locally resonant structures. *Physics Letters A*, **327**(5), 512–521, 2004.

[31] Y. Zhao and P. Wei. The band gap of 1D viscoelastic phononic crystal. *Computational Materials Science*, **46**(3), 603–606, 2009.

[32] G. S. Sharma, A. Skvortsov, I. MacGillivray, and N. Kessissoglou. Sound transmission through a periodically voided soft elastic medium submerged in water. *Wave Motion*, **70**, 101–112, 2017.

[33] A.-C. Hladky-Hennion and J.-N. Decarpigny. Analysis of the scattering of a plane acoustic wave by a doubly periodic structure using the finite element method: Application to Alberich anechoic coatings. *Journal of the Acoustical Society of America*, **90**(6), 3356–3367, 1991.

[34] G. S. Sharma, A. Skvortsov, I. MacGillivray, and N. Kessissoglou. Sound scattering by a bubble metasurface. *Physical Review B*, **102**(21), 214308, 2020.

[35] L. Quan, Y. Ra'di, D. L. Sounas, and A. Alù. Maximum willis coupling in acoustic scatterers. *Physical Review Letters*, **120**(25), 254301, 2018.

[36] X. Su and A. N. Norris. Retrieval method for the bianisotropic polarizability tensor of willis acoustic scatterers. *Physical Review B*, **98**, 174305, 2018.

[37] M. B. Muhlestein. *Willis Coupling in Acoustic and Elastic Metamaterials.* PhD thesis, University of Texas (Austin), 2016.

[38] M. Muhlestein and M. R. Haberman. Analysis of one-dimensional wave phenomena in willis materials. In *Procedings of 173rd Meeting of Acoustical Society of America and 8th Forum Acusticum*, Boston, Massachusetts, 25-29 June 2017.

[39] A. V. Amirkhizi. Homogenization of layered media based on scattering response and field integration. *Mechanics of Materials*, **114**, 17–87, 2017.

[40] M. B. Muhlestein, C. F. Sieck, P. S. Wilson, and M. R. Haberman. Experimental evidence of willis coupling in a one-dimensional effective material element. *Nature Communications*, **8**, 15625, 2017.

[41] C. F. Sieck, A. Alù, and M. R. Haberman. Origins of willis coupling and acoustic bianisotropy in acoustic metamaterials through source-driven homogenization. *Physical Review B*, **96**, 104303, 2017.

[42] A. Merkel, V. Romero-García, J.-P. Groby, J. Li, and J. Christensen. Unidirectional zero sonic reection in passive $\mathcal{PT}$-symmetric willis media. *Physical Review B*, **98**(20), 201102, 2018.

[43] F. Ma, M. Huang, Y. Xu, and J. H. Wu. Bi-layer plate-type acoustic metamaterials with willis coupling. *Journal of Applied Physics*, **123**, 035104, 2018.

[44] B. Bianco and M. Parodi. Determination of the propagation constant of uniform microstrip lines. *Alta Frequenza*, **45**, 107–110, 1976.

[45] V. Fokin, M. Ambati, C. Sun, and X. Zhang. Method for retrieving effective properties of locally resonant acoustic metamaterials. *Physical Review B*, **76**(14), 144302, 2007.

[46] R. Zhu, G. L. Huang, and G. K. Hu. Effective dynamic properties and multi-resonant design of acoustic metamaterials. *Journal of Vibration and Acoustics*, **134**(3), 031006, 2012.

[47] C. Croënne, A.-C. Hladky-Hennion, J. Vasseur, and B. Dubus. Effective parameter retrieval of phononic crystal slabs. In *Proceedings of IEEE International Ultrasonics Symposium*, San Diego, USA, 11-14 October 2010.

[48] P. Méresse, C. Audoly, C. Croënne, and A.-C. Hladky-Hennion. Acoustic coatings for maritime systems applications using resonant phenomena. *Comptes Rendus Mecanique*, **343**(12), 645–655, 2015.

[49] C.-L. Ding and X.-P. Zhao. Multi-band and broadband acoustic metamaterial with resonant structures. *Journal of Physics D: Applied Physics*, 2011.

[50] H. Chen, S. Zhai, C. Ding, C. Luo, and X. Zhao. Acoustic metamaterial with negative mass density in water. *Journal of Applied Physics*, **118**(9), 094901, 2015.

[51] F. Aghighi, J. Morris, and A. V. Amirkhizi. Low-frequency micro-structured mechanical metamaterials. *Mechanics of Materials*, **130**, 65–75, 2018.

[52] J. H. Park, H. J. Lee, and Y. Y. Kim. *Journal of Applied Physics*, **119**(3), 034901, 2016.

[53] Y. Bi, H. Jia, W. Lu, P. Ji, and J. Yang. Design and demonstration of an underwater acoustic carpet cloak. *Scientific Reports*, **7**, 705–714, 2017.

[54] Y. Chen and G. Hu. Broadband and high-transmission metasurface for converting underwater cylindrical waves to plane waves. *Physica Review Applied*, **12**(4), 044046, 2019.

[55] H. Bai, Z. Zhan, J. Liu, and Z. Ren. From local structure to overall performance: An overview on the design of an acoustic coating. *Materials*, **12**, 2509, 2019.

[56] M. Hinders, B. Rhodes, and T. Fang. Particle-loaded composites for acoustic anechoic coatings. *Journal of Sound and Vibration*, **185**(2), 219–246, 1995.

[57] H. Zhao, Y. Liu, J. Wen, D. Yu, and X. Wen. Tri-component phononic crystals for underwater anechoic coatings. *Physics Letters A*, **367**(3), 224–232, 2007.

[58] A. A. E. Ouahabi, V. V. Krylov, and D. O'Boy. Gradient metamaterial layers as impedance matching devices for efficient sound absorption. In *10th European Congress and Exposition on Noise Control Engineering (EuroNoise 2015)*, 31 May - 3 June, 2015, Maastricht, Netherlands.

[59] Y. Feng, J. Qiao, and L. Li. Acoustic behavior of composites with gradient impedance. *Materials and Design*, **193**, 108870, 2020.

[60] C. J. Naify, T. P. Martin, C. N. Layman, M. Nicholas, A. L. Thangawng, D. C. Calvo, and G. J. Orris. Underwater acoustic omnidirectional absorber. *Applied Physics Letters*, **104**(7), 073505, 2014.

[61] G. Lepert, C. Aristégui, O. Poncelet, T. Brunet, C. Audoly, and P. Parneix. Determination of the effective mechanical properties of inclusionary materials using bulk elastic waves. In *Proceedings of 12th Anglo-French Physical Acoustics Conference (AFPAC2013)*, 16-18 January, 2013, Frejus, France.

[62] T. Brunet, A. Merlin, B. Mascaro, K. Zimny, J. Leng, O. Poncelet, C. Aristégui, and O. Mondain-Monval. Soft 3d acoustic metamaterial with negative index. *Nature Materials*, **14**(4), 384–388, 2014.

[63] S. Beretti. Réponse acoustique d'élastomères micro-inclusionnaires soumis à la pression d'immersion. In *Proceedings of 10ème Congrès Français d'Acoustique*, 12-16 April, 2010, Lyon, France.

[64] H. Meyer. Sound absorption and sound absorbers in water. Department of the Navy, Bureau of Ships, Washington, D.C., 1950.

[65] P. Langlet, A.-C. Hladky-Hennion, and J.-N. Decarpigny. Analysis of the propagation of plane acoustic waves in passive periodic materials using the finite element method. *Journal of the Acoustical Society of America*, **98**(5), 2792–2800, 1995.

[66] G. Gaunaurd. One-dimensional model for acoustic absorption in a viscoelastic medium containing short cylindrical cavities. *Journal of the Acoustical Society of America*, **62**(2), 298–307, 1977.

[67] R. Lane. Absorption mechanisms for waterborne sound in Alberich anechoic layers. *Ultrasonics*, **19**(1), 28–30, 1981.

[68] V. Leroy, A. Strybulevych, M. Lanoy, F. Lemoult, A. Tourin, and J. H. Page. Super-absorption of acoustic waves with bubble meta-screens. *Physical Review B*, **91**(2), 020301, 2015.

[69] M. Thieury, V. Leroy, J. Dassé, and A. Tourin. Phenomenological law for the acoustic reflection by an array of cylindrical cavities in a soft elastic medium. *Journal of Applied Physics*, **128**(13), 135106, 2020.

[70] G. S. Sharma, A. Skvortsov, I. MacGillivray, and N. Kessissoglou. Acoustic performance of gratings of cylindrical voids in a soft elastic medium with a steel backing. *Journal of the Acoustical Society of America*, **141**(6), 4694–4704, 2017.

[71] S. M. Ivansson. Numerical design of alberich anechoic coatings with superellipsoidal cavities of mixed sizes. *Journal of the Acoustical Society of America*, **124**(4), 1974–1984, 2008.

[72] S. M. Ivansson. Anechoic coatings obtained from two- and three-dimensional monopole resonance diffraction gratings. *Journal of the Acoustical Society of America*, **131**(4), 2622–2637, 2012.

[73] Z. Liu and M. Sheng. Study on characteristics of sound absorption of underwater visco-elastic coated compound structures. *Modern Applied Science*, **3**(1), 32–41, 2008.

[74] J. Zhong, H. Zhao, H. Yang, J. Yin, and J. Wen. On the accuracy and optimization application of an axisymmetric simplified model for underwater sound absorption of anechoic coatings. *Applied Acoustics*, **145**, 104–111, 2019.

[75] Z. Zhang, L. Li, Y. Huang, and Q. Huang. Sound absorption performance of underwater anechoic coating in plane wave normal incidence condition. *Materials Science and Engineering*, **552**(1), 012001, 2019.

[76] N. Gao and K. Lu. An underwater metamaterial for broadband acoustic absorption at low frequency. *Applied Acoustics*, **169**, 107500, 2020.

[77] Z. Wang, Y. Huang, X. Zhang, L. Li, M. Chen, and D. Fang. Broadband underwater sound absorbing structure with gradient cavity shaped polyurethane composite array supported by carbon fiber honeycomb. *Journal of Sound and Vibration*, **479**, 115375, 2020.

[78] H. Zhao, J. Wen, H. Yang, L. Lv, and X. Wen. Backing effects on the underwater acoustic absorption of a viscoelastic slab with locally resonant scatterers. *Applied Acoustics*, **76**, 48–51, 2014.

[79] R.-B. Yang and A. K. Mal. Multiple scattering of elastic waves in a fiber-reinforced composite. *Journal of the Mechanics and Physics of Solids*, **42**(12), 1945–1968, 1994.

[80] G. S. Sharma, A. Skvortsov, I. MacGillivray, and N. Kessissoglou. Acoustic performance of periodic steel cylinders embedded in a viscoelastic medium. *Journal of Sound and Vibration*, **443**, 652–665, 2019.

[81] Y. Gu, H. Zhong, B. Bao, Q. Wang, and J. Wu. Experimental investigation of underwater locally multi-resonant metamaterials under high hydrostatic pressure for low frequency sound absorption. *Applied Acoustics*, **172**, 107605, 2021.

[82] J. Wen, H. Zhao, L. Lv, B. Yuan, G. Wang, and X. Wen. Effects of locally resonant modes on underwater sound absorption in viscoelastic materials. *Journal of the Acoustical Society of America*, **130**(3), 1201–1208, 2011.

[83] P. Méresse. *Matériaux absorbants à structure périodique et inclusions résonantes pour l'acoustique sous-marine (Absorbing materials with periodic arrangements and resonant inclusions for underwater acoustics).* PhD thesis, University of Lille 1, 2015.

[84] K. Shi, G. Jin, R. Liu, T. Ye, and Y. Xue. Underwater sound absorption performance of acoustic metamaterials with multilayered locally resonant scatterers. *Results in Physics*, **12**, 132–142, 2019.

[85] J. Zhong, J. Wen, H. Zhao, J. Yin, and H. Yang. Effect of core position of locally resonant scatterers on acoustic absorption. In *Proceedings of the 21st International Congress on Sound and Vibration*, Beijing, China, 13-17 July, 2014.

[86] J. Duan, S. Li, X. Wu, C. Wang, and Y. Ma. A new eccentric resonance matching layer with anti-reflection characteristics for underwater acoustic scattering suppression. *Physica Scripta*, **96**, 035001, 2021.

[87] H. Meng, J. Wen, H. Zhao, and X. Wen. Optimization of locally resonant acoustic metamaterials on underwater sound absorption characteristics. *Journal of Sound and Vibration*, **331**(20), 4406–4416, 2012.

[88] G. S. Sharma, A. Skvortsov, I. MacGillivray, and N. Kessissoglou. Sound absorption by rubber coatings with periodic voids and hard inclusions. *Applied Acoustics*, **143**, 200–210, 2019.

[89] G. Jin, K. Shi, T. Ye, J. Zhou, and Y. Yin. Sound absorption behaviors of metamaterials with periodic multi-resonators and voids in water. *Applied Acoustics*, **166**, 107351, 2020.

[90] A. Krushynska, V. Kouznetsova, and M. Geers. Visco-elastice effects on wave dispersion in three-phase acoustic metamaterials. *Journal of the Mechanics and Physics of Solids*, **96**, 29–47, 2016.

[91] W. Xu and W. Wang. Single-negative properties based on the bandgaps of one-dimensional phononic crystal. *Applied Mechanics and Materials*, **105-107**, 279–282, 2011.

[92] W. Xu, W. Wang, and T. Yang. Multi-objective optimization of layered elastic metamaterials with multiphase microstructures. *Journal of Vibration and Acoustics*, **135**(4), 041010, 2013.

[93] H. Jiang and Y. Wang. Phononic glass: A robust acoustic-absorption material. *Journal of the Acoustical Society of America*, **132**(2), 694–699, 2012.

[94] L. Li, Z. Zhang, Q. Huang, and S. Li. A sandwich anechoic coating embedded with a micro-perforated panel in high-viscosity condition for underwater sound absorption. *Composite Structures*, **235**, 111761, 2020.

[95] R. J. Bobber. *Underwater Electroacoustic Measurements*. 1970.

[96] B. Zeqiri, W. Scholl, and S. P. Robinson. Measurement and testing of the acoustic properties of materials: a review. *Metrologia*, **47**, 156–171, 2010.

[97] J. C. Piquette. Technique for detecting the presence of finite sample-size effects in transmitted wave measurements made on multilayer underwater acoustic panels. *Journal of the Acoustical Society of America*, **90**(5), 2831–2842, 1991.

[98] C. Audoly. Scattering from thin elastic screens. *Journal of the Acoustical Society of America*, **83**(S1), S104, 1988.

[99] C. Audoly and C. Giangreco. Improvement of the measurement of the transmission coefficient of panels at normal incidence using surface receivers. *Journal Acoustique*, **3**(4), 369–379, 1990.

[100] J. D. Smith. Diffraction from the edge of a thin elastic half plane and implications for panel measurements. *Journal of the Acoustical Society of America*, **128**(3), 973–988, 2010.

[101] J. C. Piquette. An analytical technique for reducing the influence of edge diffraction in reflection measurements made on thin acoustical panels. *Journal of the Acoustical Society of America*, **80**(1), 19–27, 1986.

[102] J. C. Piquette. An extrapolation procedure for transient reflection measurements made on thick acoustical panels composed of lossy, dispersive materials. *Journal of the Acoustical Society of America*, **81**(5), 1246–1258, 1987.

[103] J. C. Piquette. Direct measurements of edge diffraction from soft underwater acoustic panels. *Journal of the Acoustical Society of America*, **95**(6), 3090–3099, 1994.

[104] J. P. Szabo and A. D. Bent. Reduction in edge effects for small panels characterized by a parametric array source. *Journal of the Acoustical Society of America*, **145**(2), 795–804, 2019.

[105] V. F. Humphrey. The measurement of acoustic properties of limited size panels by use of a parametric source. *Journal of Sound and Vibration*, **98**(1), 67–81, 1985.

[106] P. J. Westervelt. Parametric acoustic array. *Journal of the Acoustical Society of America*, **35**(4), 535–537, 1963.

[107] V. F. Humphrey, S. P. Robinson, J. D. Smith, M. J. Martin, G. A. Beamiss, G. Hayman, and N. L. Carroll. Acoustic characterization of panel materials under simulated ocean conditions using a parametric array source. *Journal of the Acoustical Society of America*, **124**(2), 803–814, 2008.

[108] J. C. Piquette. The ONION method: A reflection coefficient measurement technique for thick underwater acoustic panels. *Journal of the Acoustical Society of America*, **85**(3), 1029–1040, 1989.

[109] J. C. Piquette. Transmission coefficient measurement and improved sublayer material property determination for thick underwater acoustic panels: A generalization and improvement of the ONION method. *Journal of the Acoustical Society of America*, **92**(1), 468–477, 1992.

[110] T. Brunet, O. Poncelet, and C. Aristégui. Negative-index metamaterials: is double negativity a real issue for dissipative media? *EJP Applied Metamaterials*, **2**, 3–8, 2015.

[111] A.-C. Hladky-Hennion, J. O. Vasseur, G. Haw, C. Croënne, L. Haumesser, and A. N. Norris. Negative refraction of acoustic waves using a foam-like metallic structure. *Applied Physics Letters*, **102**(14), 144103, 2013.

[112] B.-I. Popa, W. Wang, A. Konneker, S. A. Cummer, C. A. Rohde, T. P. Martin, G. J. Orris, and M. D. Guild. Anisotropic acoustic metafluid for underwater operation. *Journal of the Acoustical Society of America*, **139**(6), 3325, 2016.

[113] T. Rossing. *Springer handbook of acoustics*. 2007.

[114] C. Audoly and C. Giangreco. Global characterization of multilayer panels for underwater applications. *Journal of Wave-Material Interaction*, **5**(1), 55–72, 1991.

[115] K. Deb and T. Goel. Controlled elitist non-dominated sorting genetic algorithm for better convergence. In *Proceedings of the First International Conference on Evolutionary Multi-Criterion Optimization*, Zurich, Switzerland, 7-9 March 2001.

[116] A.-C. Hennion, R. Bossut, J. N. Decarpigny, and C. Audoly. Analysis of the scattering of a plane acoustic wave by a periodic elastic structure using the finite element method: Application to compliant tube gratings. *Journal of the Acoustical Society of America*, **87**(5), 1861–1870, 1990.

[117] C. Audoly. Evaluation of sound velocity inside underwater acoustic materials using test panel acoustic measurements. In *Proceedings of 10th Anglo-French Physical Acoustics Conference (AFPAC 2011)*, Frejus, France, 19-21 January 2011,.

[118] L. Roux, M. Pouille, C. Audoly, and A.-C. Hladky. Panel measurement method for the determination of scattering coefficients and edge diffraction in an open water tank. *Journal of the Acoustical Society of America*, **147**(2), 1104–1112, 2020.

[119] ATILA Finite Element Software Package for the analysis of 2D & 3D structures based on smart material. ISEN, Acoustics Laboratory, Lille, France, 2010.

[120] G. Gaunaurd. Comments on 'absorption mechanisms for waterborne sound in Alberich anechoic layers'. *Ultrasonics*, **23**, 90–91, 1985.

[121] L. Roux, C. Croënne, C. Audoly, and A.-C. Hladky-Hennion. Homogenization of acoustic metamaterials using retrieval methods. *Journal of Applied Physics*, **127**(22), 225102, 2020.

[122] S. H. Lee and O. B. Wright. Origin of negative density and modulus in acoustic metamaterials. *Physical Review B*, **93**(2), 024302, 2016.

[123] V. C. Fedotovskii. A porous medium as an acoustic metamaterial with negative inertial and elastic properties. *Acoustical Physics*, **64**, 548 – 554, 2018.

[124] J. D. Achenbach and M. Kitahara. Reflection and transmission of an obliquely incident wave by an array of spherical cavities. *Journal of the Acoustical Society of America*, **80**, 1209–1214, 1986.

[125] J. D. Achenbach, Y. C. Lu, and M. Kitahara. 3-d reflection and transmission of sound by an array of rods. *Journal of Sound and Vibration*, **125**(3), 43–476, 1988.

[126] S. Ivansson. *Reflection from steel plates with doubly periodic anechoic coatings*, pages 89–98. Theoretical and Computational Acoustics, 2005.

[127] S. M. Ivansson. Sound absorption by viscoelastic coatings with periodically distributed cavities. *Journal of the Acoustical Society of America*, **119**(6), 3558–3567, 2006.

[128] S. Robert, J.-M. Conoir, and H. Franklin. Propagation of elastic waves through two-dimensional lattices of cylindrical empty or water-filled inclusions in an aluminum matrix. *Ultrasonics*, **45**, 178–187, 2006.

[129] K. Zong, H. Franklin, O. Lenoir, and M. V. Predoi. Effects of periodicity perturbations on the transmission by underwater phononic crystals. *Journal of the Acoustical Society of America*, **132**(4), 2834–2841, 2012.

[130] D. A. Frickey. Conversions between S, Z, Y, H, ABCD, and T parameters which are valid for complex source and load impedances. *IEEE Transactions on Microvave theory and techniques*, **42**(2), 205–211, 1994.

[131] S. Kumar, P. Bhushan, O. Prakash, and S. Bhattacharya. Double negative acoustic metastructure for attenuation of acoustic emissions. *Applied Physics Letters*, (112), 2018.

[132] Z. Wang, C. Zhou, V. Khaliulin, and A. Shabalov. An experimental study on the radar absorbing characteristics of folded core structures. *Composite Structures*, **194**, 199–207, 2018.

[133] Y. Duan, J. Luo, G. Wang, Z. H. Hang, B. Hou, J. Li, P. Sheng, and Y. Lai. Theoretical requirements for broadband perfect absorption of acoustic waves by ultra-thin elastic meta-films. *Scientific Reports*, **5**(1), 1–9, 2015.

[134] J. Z. Song, P. Bai, Z. H. Hang, and Y. La. Acoustic coherent perfect absorbers. *New Journal of Physics*, **16**(3), 033026, 2014.

[135] P. Wei, C. C. ans Sai Tak Chu, and J. Li. Symmetrical and anti-symmetrical coherent perfect absorption for acoustic waves. *Applied Physics Letters*, **104**(12), 121902, 2014.

Abstract

Designing efficient hull coatings for acoustic stealth of submerged vehicles remains a challenge that evolves along with improvements in sonar performance. Low frequency performance is particularly important for military applications, due to the long range propagation properties of low frequency signals in the sea. Acoustic metamaterials are now widely recognised as promising candidates for such underwater coatings. The aim of this research is to study metamaterials for underwater applications, from theoretical analysis to experimental characterisation.

This thesis presents analytical or semi-analytical models based on a transfer matrix formalism to homogenise periodic structures. These methods are then used in a computationally efficient optimisation approach to obtain metamaterial designs that meet a goal in terms of their anechoism coefficient, hull decoupling coefficient, or both. The entirety of this approach is first carried out for multilayered structures then extended to metamaterials with macro-inclusions to which a degree of complexity is added. Finally, measurement methods in a water tank facility are implemented and validated. They are then used for the experimental characterisation of panels manufactured within the framework of the thesis.

Résumé

Concevoir des revêtements de coque pour la furtivité acoustique des véhicules submergés deumeure un défi évoluant constament avec l'amélioration des performances sonar. Les performances à basses fréquences sont particulièrement importantes pour les applications militaires, en raison des propriétés de propagation à longue distance dans l'eau des signaux à basses fréquences. Les métamatériaux acoustiques sont désormais largement reconnus comme des candidats prometteurs pour de tels revêtements. L'objectif de cette recherche est d'étudier les métamatériaux pour des applications sous-marines, de l'analyse théorique à la caractérisation expérimentale.

Cette thèse présente des modèles analytiques et semi-analytiques basés sur un formalisme de matrices de transfer pour homogénéiser des structures périodiques. Ces méthodes sont ensuite utilisées dans une approche d'optimisation peu couteuse en temps de calculs pour obtenir des designs de métamatériaux qui répondent à des objectifs en termes de coefficient d'anéchoïsme, de masquage, ou les deux. L'ensemble de cette approche est d'abord réalisée pour des structures multicouches puis étendue aux métamatériaux à macro-inclusions auxquels s'ajoute un degré de complexité. Enfin, des méthodes de mesure pour bassin acoustique sont mises en œuvre et validées. Elles sont ensuite utilisées pour la caractérisation expérimentale de panneaux fabriqués dans le cadre de la thèse.